PACIFIC EARTHQUAKE ENGINEERING
RESEARCH CENTER

Performance-Based Seismic Demand Assessment of Concentrically Braced Steel Frame Buildings

Chui-Hsin Chen
Stephen A. Mahin
Department of Civil and Environmental Engineering
University of California, Berkeley

PEER 2012/103
DECEMBER 2012

Performance-Based Seismic Demand Assessment of Concentrically Braced Steel Frame Buildings

Chui-Hsin Chen

Stephen A. Mahin

Department of Civil and Environmental Engineering
University of California, Berkeley

PEER Report 2012/103
Pacific Earthquake Engineering Research Center
Headquarters at the University of California, Berkeley

December 2012

ABSTRACT

The highly nonlinear behavior associated with buckling and nonductile fracture of braces reduces the ability of the special concentrically steel braced frame (SCBF) system to dissipate energy, resulting in undesirable modes of behavior. We analyzed archetype buildings of SCBFs and buckling restrained braced frames (BRBFs). The seismic demands of the system and structural elements were computed and interpreted for 3-, 6-, and 16-story SCBFs and BRBFs under various hazard levels. The analysis results show large seismic demands for the 3-story SCBF, which may result in unexpected damage of structural and nonstructural elements.

We performed evaluations of seismic design parameters for 2-, 3-, 6-, 12-, and 16-story SCBFs and BRBFs, which demonstrated that short-period braced frame systems, especially SCBFs, had higher probabilities of collapse than longer-period braced frame systems. The response was substantially improved by lowering the response reduction factor of the 2-story SCBF building; this reduced the collapse risk at the hazard level of 2% probability of exceedance in 50 years.

The investigation of system performance and member behavior provides seismic demands to more accurately assess the socioeconomic losses of SCBFs and BRBFs for performance-based earthquake engineering.

ACKNOWLEDGMENTS

Many professors, graduate students, and engineers assisted this work. Special thanks are due to Professors Bozidar Stojadinovic and Haiyan Huang for serving on Dr. Chen's dissertation committee and providing valuable advice and guidance, as well as to Professors James Kelly and Sanjay Govindjee for their assistance on various aspects of this work. Sincere appreciation is given to Dr. Patxi Uriz, who provided considerable assistance in developing numerical models, implementing them on the Berkeley computer cluster, and interpreting data from his tests of braces and braced frames. Rafael Sabelli, Director of Seismic Design at Walter P Moore, provided advice related to interpretation of code requirements for the SCBF and BRBF structures considered herein. Mr. Sabelli's efforts greatly contributed to the success of this work.

The assistance of Drs. Andreas Schellenberg, Matthew Dryden, Yuli Huang, Tony Yang, Frank McKenna and Silvia Mazzoni in developing various aspects of the OpenSees models is gratefully acknowledged. The authors are thankful for Claire Johnson's effort in proofreading the manuscript, and the technical assistance from Charles James, the PEER/NISEE Library Director.

The authors would like to acknowledge the financial support provided by the National Science Foundation under Grants CMS-0600625 and CMS-0619161, and by the University of California at Berkeley through the Byron and Elvira Nishkian Endowed Chair in Structural Engineering. Some of the work reported herein was prepared as part of a report prepared for the Building and Fire Research Laboratory of the National Institute of Standards and Technology under contract number SB134107CQ0019, Task Orders 67344 and 68002. Dr. Chen was also aided by funds from the Dr. and Mrs. James C.Y. Soong Fellowship provided through UC Berkeley Graduate Division, and financial support through Taiwan Merit Scholarship TMS-094-2-A-025.

The opinions, conclusions and recommendations contained in this report are those of the authors alone and do not necessarily reflect the views of the National Science Foundation, National Institute of Standards and Technology, Pacific Earthquake Engineering Research Center, the Regents of the University of California, or others associated with this project.

CONTENTS

LIST OF FIGURES

LIST OF TABLES

1 Introduction

1.1 MOTIVATION

Special steel moment-resisting frame (SMRF) systems were once considered to be one of the best structural systems for use in areas of high seismicity. The simple configuration of structural elements and straightforward design criteria of this structural system increased its popularity among engineers, architects, and owners. However, the 1994 Northridge, 1995 Hyogo-ken Nanbu, and other recent earthquakes have shaken the confidence of engineers in these systems due to widespread brittle fractures that occurred in special welded steel beam-to-column connections [FEMA 2000a]. The Federal Emergency Management Agency (FEMA) initiated a six-year program of investigation and guideline development by the SAC Joint Venture comprising the Structural Engineers of Northern California, Applied Technology Council, and California Universities for Research in Earthquake Engineering [FEMA 1997a, 1997b, 1997c, 2000b, 2000c, 2000d].

Although the resulting guidelines have restored the confidence of engineers and the public in the use of SMRF systems, requirements and restrictions are now more stringent for designs using this structural system, and more rigorous checks are stipulated for quality control to achieve the required ductility of beam-to-column connections. Research on SMRF systems has also demonstrated that very large story drift may occur during a severe earthquake, leading to serious damage to structural and nonstructural components. Because the design of SMRF systems is usually controlled by code-designated story drift limits, the member sizes may be much larger than those designed solely on the basis of force. This has resulted in cost increases and complex construction configurations, and engineers and owners now seek more efficient and economical systems.

The special concentrically steel braced frame (SCBF) system is one of the candidates that are simple to design, effective in resisting lateral forces, and efficient in limiting lateral deformation. Currently, SCBF systems make up about 40% of the market for office and hospital buildings in California, and the trend is believed to be increasing [Ferch 2004]. Although SCBFs are now widely used, damage to concentrically braced frames observed during past earthquakes, including the 1985 Mexico [Osteraas and Krawinkler 1989], 1989 Loma Prieta [Kim and Goel 1992], 1994 Northridge [Tremblay et al. 1995; Krawinkler et al. 1996], and 1995 Hyogo-ken Naubu [Architectural Institute of Japan 1995; Hisatoku 1995; Tremblay et al. 1996] events, should be noted. The failure mode generally observed was fracture of the braces at the locations of local buckling or plastic hinges. In some cases, fractures were observed at the weld of the connections to the gusset plate or the weld in the boundary of the gusset plates. Research demonstrated that this structural system is prone to concentrating the damage to a single story,

which results in significant story drift and floor acceleration [Khatib et al. 1988], and design codes have been updated to reduce such common forms of damage.

Despite these code updates, the seismic performance of concentrically braced frames is not considered as robust as it should be. Several factors may degrade the performance of SCBF systems:

- Braces dissipate energy by yielding in tension and by inelastic buckling in compression. Buckling of braces often decreases their ductility and energy-dissipating capacity under cyclic loading [Black et al. 1980; Tang and Goel 1989; Kim and Goel 1992]. It is observed that braces fracture after only a few cycles due to the limited ductility capacity.
- The nonlinear behavior of braces as well as braced frames is complex. Therefore, the intensity and distribution of forces, and deformations over the building are difficult to predict numerically. The failure of braces can result in large story drift and frame instability. Some damage occurs because of the unexpected concentration of deformation or force at a few stories [Aguero et al. 2006].
- There are a variety of failure modes for SCBF systems. From the observations of previous earthquakes and experiments, damage occurs in braces, gusset plates, beam-column connections, brace-to-framing connections, and beams and columns. The occurrence of failure modes is sensitive to characteristics of earthquakes, structural configurations, proportions of structural members, and detailing of the connections.

Several experiments have been conducted in recent years to assess the seismic responses of concentrically braced frame systems. Despite the available experimental and field data, it is difficult to establish confidence in current design methods. Research efforts have long strived to develop quantitative probabilistic methods to evaluate the performance of structures [Hamburger et al. 2003; Moehle et al. 2005]. These are quite versatile in terms of addressing engineering-centric goals, such as continued occupancy or collapse prevention, or in terms of societal-centric goals such as maximum probable losses (or down time or injuries) over the life of a structure or given the occurrence of a scenario event (see, for example, Miranda and Aslani [2003]). Thus, a significant opportunity exists to validate and improve design methods for concentrically braced frame structures by developing and validating realistic numerical models and using these models in combination with modern performance-based evaluation frameworks [Moehle 2003].

Most previous analytical studies investigated the behavior of structural components in a braced frame or the behavior of tested specimens. Such preliminary studies indicate the need for additional system studies. Studies are still limited regarding system performance [Uriz and Mahin 2008].

1.2 OBJECTIVES

The objectives of this study were to:

- Investigate the sensitivity of global and local engineering demands to parameters used in the design and analysis of concentrically braced frames
- Develop further understanding of the seismic behavior of concentrically braced frame systems in terms of the engineering demand parameters

- Use performance-based evaluation concepts to understand the trade-offs between the stiffness, strength, and ductility, and the global and local demands associated with various performance goals

The objectives were achieved by:

- Evaluating and improving numerical models to predict the response of concentrically braced frames consistent with the efficiency and accuracy needs of performance-based earthquake engineering (PBEE)
- Studying the sensitivity of seismic demands to seismic hazard and structural characteristics
- Examining various engineering demand parameters to characterize performance
- Applying a probabilistic PBEE framework to the assessment of structural performance
- Assessing the design parameters of current codes for steel braced frames using the methodology of FEMA P695 (ATC-63)
- Identifying the global and local seismic demands for performance-based design
- Developing schemes to improve system performance

1.3 SCOPE

Performance-based earthquake evaluation criteria have been developed by several researchers to assess the seismic hazard, structural responses, expected damage, and possible losses for various hazard levels and structural systems. Figure 1.1 illustrates the framework of PBEE as developed by the Pacific Earthquake Engineering Research Center (PEER) of the University of California, Berkeley [Moehle 2003]. By constructing an appropriate conditional probability function, the relationship between ground motion intensity and socioeconomic variables is established using the total probability theorem.

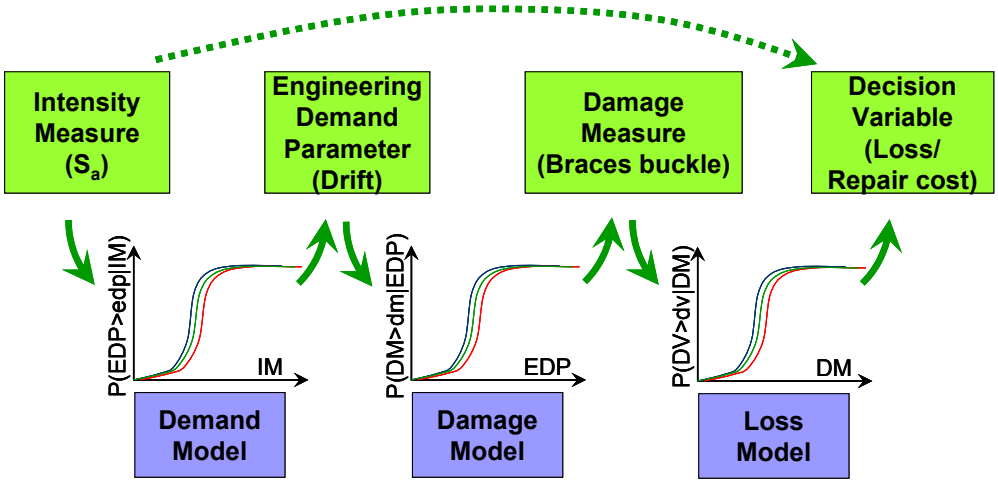

Figure 1.1 Illustration of PBEE framework.

The engineering demand parameter (EDP) model relies on extensive numerical simulations to characterize the relationship between the intensity measure and the EDPs. The damage model, which relates the EDPs to the damage measures, is usually constructed by summarizing the observations from test data and field work to relate EDPs to damage. The loss model defines the relationship between the damage measure and the decision variables, which are usually expressed in terms of death, dollar losses, and downtime; the construction of this model requires efforts from industry to help estimate the possible losses.

The research presented here emphasizes the demand model for braced frame systems. We constructed efficient and accurate nonlinear numerical models, and then carefully calibrated them with existing test data for braces and two-story braced frames. To determine the accuracy of the extensive nonlinear dynamic analyses performed for simulations for system behaviors, we compared the results for system performance of the numerical models with results from a more sophisticated but more computational expensive finite-element model, which has been proved to accurately simulate global and local failure of braced frames.

The investigated braced frame systems included SCBF systems conforming to current building codes [ASCE 2005] as well as previous versions of the codes, and BRBF systems. Because of the large variety of possible brace configurations, it was not practical to include all configurations. We discuss only structures with a double-story X configuration, which is currently one of the most efficient and commonly used configurations.

To verify the capacity of the braced frame systems to resist collapse under extreme ground motion excitations, we evaluated the design parameters detailed in the current code for SCBF and BRBF systems. Structures with different numbers of stories, representing various period ranges, were analyzed with the selected ground motions. The response reduction factor (R-factor) was the primary design parameter evaluated, but the discussion also includes overstrength factor and the deflection amplification factor C_d.

To understand how the collapse-resisting capacity of braced frame buildings can be improved, our study evaluated the effects of changing the response reduction factor. In this report we propose new design parameters to better control the deformation concentration observed in high-rise SCBF buildings.This research also identifies the global and local force and deformation demands of SCBF and BRBF for various hazard levels using the SAC ground motion set [Somerville 1997], representing various hazard levels. Simple methods to estimate the out-of-plane deformation of buckling braces and column axial force demands are proposed.

This report is organized as follows. Chapter 2 reviews recent studies on the numerical simulation of braced system behavior and the evaluation of design parameters of braced frame systems. Chapter 3 describes the construction of the numerical models and their calibration using test data and results of more detailed finite-element models. Chapter 4 examines in detail the performance of a 3-story SCBF designed with different criteria and a 3-story BRBF. Chapter 5 evaluates the seismic performance factors (R-factor, Ω_0, and C_d factor) found in current design codes using the methodology of FEMA P695 [2009]. Chapter 6 presents the global force and deformation demands of SCBF and BRBF systems having different number of stories; the effects of changing the design criteria to improve the system performance of SCBF are evaluated. Chapter 7 examines the force and deformation demands of braces, beams, and columns under various hazard levels; this chapter also proposes simple methods to estimate the out-of-plane deformation of buckling braces and column axial force demands. Concluding remarks and recommendations are given in Chapter 8.

2 Literature Review

The typical failure modes experienced by SCBF buildings due to earthquake excitation include damage to braces, brace-to-framing connections, columns, and base plates [Kato et al. 1980; Hanson and Martin 1987; Osteraas and Krawinkler 1989; Architectural Institute of Japan 1995; Tremblay et al. 1995; Bonneville and Bartoletti 1996; WJE 1998; Naeim 1997, 1998; Kelly et al. 2000]. Much experimental and analytical research has been conducted on the performance of braces [Tremblay 2002; Lee and Bruneau 2005; Yang and Mahin 2005], gussets [Astaneh-Asl 1998; Roeder et al. 2005; Chambers and Ernst 2005] and frames [Khatib and Mahin 1988; Fukuta et al. 1989; Wallace and Krawinkler 1989; Bertero et al. 1989; Tremblay et al. 1995, 1996; Sabelli 2000; Tremblay et al. 2003; Uriz and Mahin 2008]. Recent research on SCBF and BRBF buildings has focused on the experimental and numerical performance of braces [Han et al. 2007; Tremblay et al. 2008; Fell et al. 2009], brace-to-framing connections [Packer 2006; Willibald et al. 2006; Lehman et al. 2008; Shaw et al. 2010; Wigle and Fahnestock 2010] and systems [Fahnestock et al. 2007a, 2007b; Tsai et al. 2008; Broderick et al. 2008; Annan et al. 2009; Tremblay et al. 2009] in response to updated design codes (ASCE/SEI 7-05 [2005]) or using construction details that are similar to those in the United States.

This chapter discusses research that has focused mainly on numerical simulations of system performance of SCBF and BRBF systems. Studies that evaluate design parameters—ductility, overstrength, and response modification factors—are also examined. Because of the considerable amount of literature on this topic, this section provides a brief synopsis of recent work.

2.1 LITERATURE ON SYSTEM PERFORMANCE OF BRACED FRAME SYSTEM USING NUMERICAL SIMULATIONS

Several researchers have used numerical simulations to investigate the behavior of braced frame systems [Sabelli 2000; Ding 2006; Uriz and Mahin 2008; Yoo et al. 2008; Khandelwal et al. 2009; Huang and Mahin 2010]. Seismic demands of several prototypes of SCBF and BRBF buildings were investigated by Sabelli et al. [2000; 2003] using phenomenological models in SNAP-2DX [Rai et al. 1996]. The model buildings were designed to assess the design and analysis procedures of the then-current design, National Earthquake Hazard Reduction Program (NEHRP) Recommended Provisions for Seismic Regulations for New Buildings and Other Structures [FEMA 1997b, 1997c]. The structural configurations included are shown in Figure 2.1. Table 2.1 lists the analytical results of the model buildings with chevron configuration subjected to a suite of 20 ground motion records with 10% exceedance in 50 years. The 1997 NEHRP provisions allowed the unbalanced tension/compression capacity of braces to be

disregarded in the design of beams on the roof level; therefore, the inelastic response was concentrated at the roof level for almost all ground motions considered. Fracture of braces, which was observed in many of the analyses, occurred mostly at the roof level and early in the record. In this study, the 6-story SCBF was designed based on the performance of the 3-story SCBF, such that the roof beams of the 6-story SCBF were stronger and stiffer than the requirement in the 1997 NEHRP provisions; the damage was less concentrated and smaller peak story drift ratios were observed (see Table 2.1). In the double-story X configuration of 6-story SCBF, the 1997 NEHRP provisions did not require a vertical unbalanced load for the design of the beams, and no significant beam hinging was observed when subjected to all ground motions.

Analytical results of the model BRBF buildings studied show that the BRBF effectively reduced the damage concentration and the vertical unbalanced load in beams. In addition, the response of BRBFs was more sensitive to proportioning rather than to varying the design R-factors ranging from 6 to 8. Table 2.1 shows that the maximum story-drift ratios of 3- and 6-story BRBF were similar. Also, the drift ratio of BRBFs was similar to that of the 6-story SCBF, but much less than that of the 3-story SCBF, which had relatively weaker roof beams. While the study identified some important parameters associated with structural configurations, proportioning, and modeling, it was suggested that the confidence of the results would be improved by calibrating the analytical model with experimental research and employing more detailed models that account for bending and shear forces in the braces.

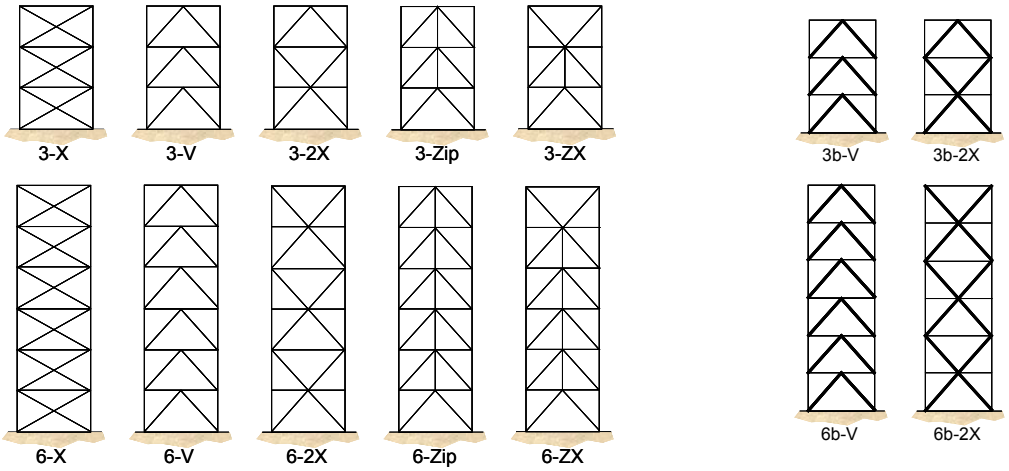

Figure 2.1 **Considered structural configurations of 3- and 6-story SCBF and BRBF in Sabelli et al. [2003].**

Table 2.1 **Response summary for 10% in 50 year events (after Sabelli [2000]).**

	Frame	Story drift ratio (%)		Residual story drift ratio (%)	
		Mean	+1σ	Mean	+1σ
6-Story	BRBF (6b-V, R = 8)	1.6	2.2	0.7	1.1
	SCBF (6-V)	1.8	2.6	0.4	0.7
3-Story	BRBF (3b-V, R = 8)	1.4	2.1	0.5	1.0
	SCBF (3-V)	3.9	7.0	2.5	5.6

Using OpenSees models [McKenna 1997], Uriz and Mahin [2008] conducted a series of experimental and analytical studies on SCBFs and BRBFs to assess the performance of chevron-braced frame structures with improved simulation models. Braces were modeled considering large local displacements; fiber sections were used to model plastic hinge behavior including low-cycle fatigue effects. The effects of fatigue did not account for true fracture mechanics; rather, Rainflow cycle counting and Manson-Coffin fatigue criteria were used to fail individual fibers at a plastic hinge. Eventually, all fibers at a section would fail under severe loading conditions. The investigation examined many parameters, including the net section reinforcement at brace connections, the effects of fatigue modeling parameters, and the dynamic characteristics of SCBFs and BRBFs, as well as the responses of low-rise and mid-rise braced frame buildings. Table 2.2 summarizes some of the response quantities of 3-story and 6-story chevron SCBF and BRBF designs. The brace proportions and details are identical to the buildings found in Sabelli [2000].

Table 2.2 Median (and standard deviation) of drifts for 3- and 6-story SCBFs and BRBFs at various hazard levels (after Uriz and Mahin [2008]).

ID	Hazard level (% in 50 years)	Peak story drift ratio at any level (%)	Residual roof drift (%)
3VF (SCBF)	50	0.4 (0.7)	0 (0.1)
	10	1.6 (0.9)	0 (0.2)
	2	5.7 (2.4)	0.7 (1.0)
3VB (BRBF)	50	0.6 (0.6)	0 (0.1)
	10	1.3 (0.7)	0.1 (0.4)
	2	3.8 (2.1)	2.1 (2.2)
6VF (SCBF)	50	0.4 (0.3)	0.02 (0.1)
	10	1.1 (0.6)	0.06 (0.15)
	2	4.4 (2.2)	0.7 (1.1)
6VB (BRBF)	50	0.4 (0.3)	0.08 (0.1)
	10	1.4 (0.8)	0.3 (0.7)
	2	4.4 (2.5)	1.37 (2.2)

The results showed that the drift demands of low-rise SCBFs were slightly greater than those of BRBFs at various hazard levels. Nonetheless, out-of-plane deformation of buckling braces was observed even at the 50% probability of exceedance in 50-year hazard level. The performance of the mid-rise SCBF was poorer than the low-rise SCBF in some aspects; the residual displacement at the 50% probability of exceedance in 50 year hazard level was greater in the 6-story model, while the demand on the braces was also greater at the 10% probability of exceedance in 50-year hazard level. Also, the damage was concentrated in the lower stories in low-rise and mid-rise SCBFs. Compared to the SCBF system, the BRBFs showed a consistent tendency to distribute deformation more uniformly along the height of the building at various hazard levels. Moreover, no brace fracture was observed for the BRBFs and no incidence of collapse was found.

In general, the response of SCBFs demonstrated large variation under severe earthquake excitation. Variations also exist for different numerical models. The results of SNAP-2DX and

OpenSees simulations show a range of difference in predicting engineering demands for the same model buildings.

Finite-element models overcome the limitations of phenomenological models (such as the SNAP-2DX model) and physical-theory models (such as the OpenSees fiber-based model) and are able to simulate local damage in braced frame buildings. Khandelwal et al. [2009] developed macro-models to conduct progressive collapse analysis of 10-story SCBF and EBF buildings, which were the combination of beam-column and discrete spring finite elements. These models were implemented and run on LS-DYNA. A few assumptions and limitations were chosen in developing this model: the gusset plates and beam-column connections in the model were simulated with simplification. The gusset plates were assumed to remain elastic and designed to be so. The beam-column connections were simulated as fully restrained, and the panel zones were assumed to be elastic, even under collapse conditions. Additional factors were not included by Khandelwal et al. [2009], such as the strain rate effect, debris impact during collapse, and the uplift of the foundation. Nonetheless, the study successfully simulated the collapse behavior of the selected steel braced frame buildings.

Also utilizing LS-DYNA, Huang and Mahin [2010] developed a new continuum damage mechanics material model to capture the inelastic behavior and deterioration of mechanical properties. The model was implemented for SCBF buildings with the parameters calibrated from test data of braces and braced frames [Yang and Mahin 2005; Uriz and Mahin 2008]. Shell elements were employed in the model building with selected meshes that were determined from a sensitivity study. The beam-column connections, gusset-to-framing connections, and gusset-to-brace connections were modeled in detail and the connected bolts were modeled as springs. Under extensive analysis of a preliminary case study, the seismic demand of a 3-story, double-story X-braced frame building was examined for PBEE. In recognition of the detailed and accurate information provided by the finite-element model as well as the excess of computational cost for the study of PBEE, Chapter 3 discusses the results from the finite-element and fiber-element based models.

Yoo et al. [2008] conducted nonlinear finite-element analyses to investigate the behavior of multistory X-braced frames and their gusset plate connections. ANSYS [2005] models with four-node quadrilateral shell elements were used for members, and bilinear kinematic hardening material was adopted to simulate the nonlinear behavior of test specimens. The numerical model was calibrated with test data from a single story, one-bay diagonal braced frame [Lehman et al. 2008] and then used to investigate the parameters affecting the local and global behavior of 2-story double-story X-braced frame specimens that were then tested under cyclic loading. The results illustrated that the proposed methodology for designing gusset plates was economical and effective in reducing premature gusset-plate buckling. It was also noted that neglecting the composite effects of concrete slabs in numerical models resulted in underestimating the stress and strain demands of the mid-span gusset plates. Also, the potential damage was reduced by adopting the proposed details of gusset plates. Yoo et al.'s research also suggested that the double-story X-SCBF configuration has the potential to decrease deformation concentration in a single story

A performance evaluation of three-dimensional (3D) SCBF structures under earthquake excitations was conducted by Ding [2006]. The study investigated the redundancy of a SCBF system, where 3-, 8-, and 12-story chevron braced frame buildings were designed as model buildings. The responses of structures were simulated in ABAQUS [2003]. Beams and columns were modeled as 3D Euler beams. The modeling scheme of the brace connections is illustrated in

Figure 2.2 considering the rigid-end zones and three times the thickness of the gusset plates for the flexibility of global brace buckling and gusset bending. For each brace, 20 beam elements were used in the models and brace fracture was simulated with user-defined elements. In these simulations, brace fracture caused torsion of the buildings resulting in large displacements. For some ground motion excitations, brace fracture was observed even after the ground motion peak. Ding's research also recognized the high computational costs for numerical simulations for refined analytical models and recommended that numerical models for system performance evaluation should be simplified.

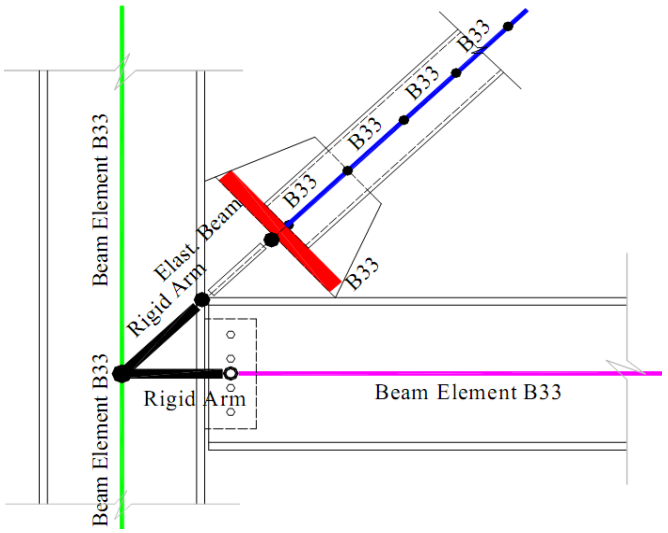

Figure 2.2 Modeling scheme of the brace connections by Ding [2006].

Consideration of numerical models for PBEE has been discussed in two other studies. Chenouda and Ayoub [2009] conducted a probabilistic analysis of the collapse of a degrading multiple-degree-of-freedom (MDOF) system on steel moment-resisting frame (MRF) buildings and identified the impact of degradation on displacements of MDOF systems because the degradation strongly affected the higher-mode responses, especially for short-period structures. Chenouda and Ayoub also demonstrated that while an equivalent first-mode SDOF system with degrading properties might not collapse, a MDOF counterpart could collapse. This study highlights the benefits and necessity of including the degradation of properties when studying the collapse potential of MDOF systems. Ruiz-García and Miranda [2009] conducted seismic demand analyses of residual drift on one-bay generic frame buildings of steel MRF and noted several issues when computing residual drift demand hazard curves. Using the lumped plasticity approach might result in larger residual drift when using a fiber-element modeling [Yazgan and Dazio 2008]. Also, a degrading element model might lead to large uncertainty for residual drift demand when estimated by different software packages. Ruiz-García and Miranda concluded that besides the lateral-load resisting structural system, the fundamental period of the structure also had great influence on residual drift demand.

Based on its computational efficiency and accuracy, this study used the OpenSees analysis framework [McKenna 1997] as an analytical tool. Fatigue properties were adopted from Uriz and Mahin [2008]. The realism of local failure modes were assessed by comparison with test results and predictions using LS-DYNA [LSTC 2007] numerical models [Huang 2010].

2.2 LITERATURE ON THE EVALUATION OF DESIGN PARAMETERS

Some recent studies have evaluated the effect of design parameters on the performance of building structures. A few of them use nonlinear dynamic analyses to investigate SCBF and BRBF buildings, designed according to current seismic codes (ASCE 7-05) for regions of high seismic hazard, over a wide period range.

The ductility and overstrength factors of structural systems were investigated by Balendra and Huang [2003]. The model buildings were 3-, 6-, and 10-story MRF and CBF buildings conforming to the British BS 5950 code [BSI 1990], which does not have any seismic provisions. Nonlinear pushover analyses and the N2 method [Fajfar 2000] were conducted to evaluate the performance of these structures. Balendra and Huang concluded that the steel frames currently being designed according to the BS 5950 code were able to resist the base shear caused by the "design earthquake" for Singapore. The data in Table 2.3 also show that the overstrength of braced frame buildings is about 70% of that of MRF for various numbers of stories. The ductility capacity of the investigated CBF systems is about 1.5 for various numbers of stories. In general, the smaller overstrength of CBF systems results in smaller effective R factors (the ratio of computed capacity to elastic demand) in CBF systems compared to MRF systems. The trend also shows the *R* factors were smaller as the number of stories increased. Chapter 6 presents a similar discussion related to SCBF and BRBF systems designed for seismic design category D of current U.S. codes.

Table 2.3 Overstrength, ductility, response modification, and effective R for steel frames under most common vertical load combinations [after Balendra and Huang 2003].

Type of steel frame	Number of stories	Overstrength	Ductility	R
MRF	3	8	1.95	15.6
	6	4.66	1.94	9.04
	10	3.77	1.67	6.30
CBF	3	5.57	1.53	8.52
	6	3.33	1.57	5.23
	10	2.48	1.51	3.74

Similarly, Kim and Choi [2004] evaluated the overstrength, ductility and response modification factors of SCBF and OCBF. A variety of model buildings was investigated, including 3-, 6-, 9-, 12-, 15-, 18-, and 21-story SCBF systems and 3-, 6-, and 9-story OCBF systems, that were designed in accordance with IBC2000 (ICC 2000) and AISC Seismic Provisions [2002]. Static nonlinear pushover analyses were conducted to evaluate the design parameters for all model buildings, and an incremental dynamic analysis (IDA) was performed on the 6-story SCBF model structure. Six ground motion records that adequately matched with the design spectrum were selected from the SAC project ground motion library to perform the IDA. In general, the IDA results showed smaller overstrength factors, but greater ductility demand. The response modification factors obtained from the IDA and static pushover approaches were similar. The pushover analysis revealed that the overstrength factors were greater in the lower-rise SCBFs, and for the cases studied the overstrength factors were greater than the code (Ω_0) value of 2.0. The results also showed that the lower-rise SCBFs tended to have greater effective response modification factors. It was suggested that further research was

required to define the effective response modification factors at various performance levels accounting for seismic hazard levels, number of stories, target ductility ratios, etc.

Hines and Grynuik [2006] assessed the performance of low-ductility chevron braced frame buildings in moderate seismic regions. The model buildings included the design of 3-, 6-, 9-, and 12-story buildings in the Boston area with $R = 3$. Frame analyses were conducted using 14 ground motion records that matched closely the IBC2003 [ICC 2003] MCE-level earthquake spectrum for Site Class B and scaled to simulate Site Class D conditions. The results showed that the 9- and 12-story model buildings were more vulnerable to collapse than the 3- and 6-story counterparts. Higher mode effects were believed to contribute to the collapse potential in the upper stories. Similarly, Hines and Appel [2007] investigated a 9-story chevron braced frame with R = 3 but brace connection fracture capacity that corresponded to systems with R ranging from 2 to 7, according to ASCE 7-02. In the case study, the braced frame with brace connection fracture capacity of $R = 3$ experienced more collapse instances than frames with other R values. Increasing the strength of the brace connections was not a guarantee of reduction in the potential for collapse, because the drift and damage tended to concentrate in a few stories while other stories still provided substantial strength and stiffness. The concentration of drift and damage was one of the primary factors influencing the collapse performance.

Asgarian and Shokrgozar [2009] conducted research on ductility, overstrength, and response modification factors of BRBF buildings. To investigate these design parameters, OpenSees two-dimensional (2D) models were subjected to nonlinear static pushover analysis, nonlinear IDA, and linear dynamic analysis. The material characteristics were modeled as being bilinear without degrading properties. The model building designs conformed to the Iranian Earthquake Resistant Design Code [BHRC 2005] and Iranian National Building Codes for Structural Steel Design. Structural configurations included two braced bays having double-story X, chevron, and V bracings for 4-, 6-, 8-, 10-, 12-, and 14-story buildings. The results showed that the overstrength factors ranged between 1.5 and 2.0, and the resulting effective response modification factors for ultimate limit state design method were between 4.5 and 16. The effective R-factors decreased as the number of stories increased.

Evaluating the design parameters of both conventional braced frames (CBF) and BRBFs in Iran, Mahmoudi and Zaree [2010] performed static nonlinear analyses on single and double bracing bays in 3-, 5-, 7-, 10-, and 12-story model buildings. Different configurations, such as chevron, V, and X bracings, were included. The CBFs were designed according to the Iranian Earthquake Resistant Design Code where R = 6 for CBF. For BRBFs, an R of 8 was used. All the beam connections in the CBFs and BRBFs were assumed to be pinned, and the braces were designed to take 100% of the lateral loads. The effective R-factors of both CBF and BRBF decreased (results corroborated in other research, e.g., Asgarian and Shokrgozar [2009]) with increasing structural height. Also, the effective non-collapse increased as the number of bracing bays increased. In conclusion, because R-factors varied among different structural configurations, number of bracing bays, and building height, and as the constant R-factors in design codes did not reflect these variations, it was suggested that the R-factors for both CBF and BRBF buildings in codes be modified.

In recognition of the lack of rationale to determine R-factors in current seismic design codes, Lee and Foutch [2006] investigated the issue by designing 3-, 9-, and 20-story steel MRFs with different R-factors (8, 9, 10, 11, and 12). Static nonlinear pushover analyses with displacement controlled loading were conducted to evaluate the strength capacity and post-yielding performance; IDA was also performed to analyze the seismic drift capacity. In addition,

nonlinear dynamic analyses were carried out to investigate the seismic demands using 20 SAC ground motion records representing 2% probability of exceedance in 50 years. The results showed that the 20-story steel MRF model buildings tended to concentrate drift in the lower stories. For the 3- and 9-story model buildings designed for an R-factor of 12, the buildings provided 95% confidence of avoiding global collapse and better than 50% confidence for avoiding local connection failure (determined according to FEMA 350). In conclusion, current seismic design that adopts R-factors and minimum bounds on design base shear (C_s factor) provides adequate protection against dynamic instability for high-rise buildings where P-Δ effects have greater impact on dynamic responses of structures.

2.3 SUMMARY

Previous research suggests that SCBF and BRBF buildings covering a range of building heights should be designed as per ASCE 7-5 and AISC 2005 and evaluated numerically. Nonlinear static pushover analysis, nonlinear dynamic analysis, and IDA should be conducted to investigate the system's performance. Results suggest that numerical models should incorporate strength degrading and stiffness softening properties as well as element fracture behavior. In addition to PBEE studies for different hazard levels, FEMA P695 [2009] provides a good basis for such evaluations of design parameters (R-factor, overstrength factor, and C_d-factor) related to collapse potential.

3 Preliminary Numerical Simulation

Performance-based earthquake engineering depends on numerical simulation of structural responses to future seismic events. As such, analytical models should represent structural behavior realistically and numerical procedures should be efficient enough to permit a large number of events to be simulated. In braced frames, the brace characteristics dominate seismic behavior. As the braces yield in tension or buckle in compression, they provide lateral load resistance and energy dissipation. The complex nonlinear behavior of the braces results in the complex response of the structural system. It is thus essential to model the braces as accurately as possible. In this chapter we constructed numerical models of braces and braced frames and tested their accuracy by comparing the model with the test data. We also compared the numerical models developed here with high-fidelity (but computationally expensive) finite-element numerical models. A preliminary PBEE study of a 3-story SCBF was performed to assess capabilities of different analytical models and to understand better the effects of these models on demand parameters. The results are presented in terms of the EDPs to identify the system performance.

3.1 SIMULATION TOOL

OpenSees was employed as the primary simulation tool. The brace models used for the numerical simulations were based on the previous work by Uriz and Mahin [2008] with some simplifications considering the large number of analysis to be performed. The OpenSees framework (Figure 3.1) is an object-oriented software framework used mostly for structural and geotechnical engineering simulations; most of its modules are developed on an open-source basis and implemented in C++. The Tcl command language [Ousterhout 1994; Welch et al. 2003] is used to define and execute the analysis. Users construct their models from the module *ModelBuilder*, and the program adds the related objects to the *Domain* module. In *Domain*, the program holds the state of the model at each time step. In the meantime, users can use the *Recorder* module to record these states to monitor response. The *Analysis* module analyzes the responses of the model as it moves from the current state to the next state.

Figure 3.2 illustrates the beam-column element for modeling the structural members. In this study, a model consisted of beam, column, and brace members. Each element was modeled by either a displacement-based beam-column element or a force-based beam-column element [Neuenhofer and Filippou 1997]. For each element, the number of integration points selected was based on a previous parametric study [Uriz and Mahin 2008]. Cross sections at each integration point were represented by an assembly of uniaxial fibers. For each fiber, the uniaxial stress-strain relationship was used considering material properties that account for failure due to

low-cycle fatigue [Uriz and Mahin 2008]. The material was modeled by the Menegotto-Pinto model with isotropic strain hardening. The co-rotational geometric transformation was adopted here to account for local and global geometric nonlinearities. As such, the effects of lateral buckling of braces were explicitly taken into account.

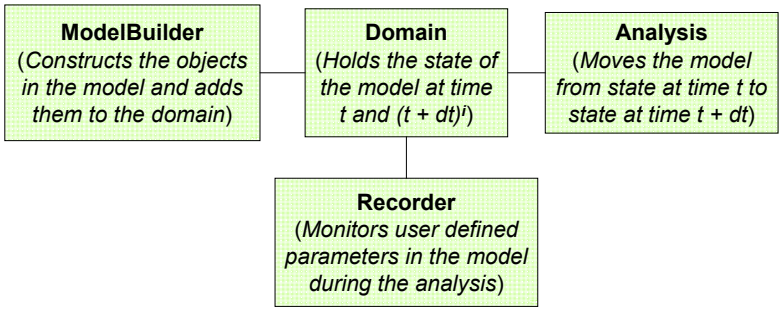

Figure 3.1 Framework of OpenSees.

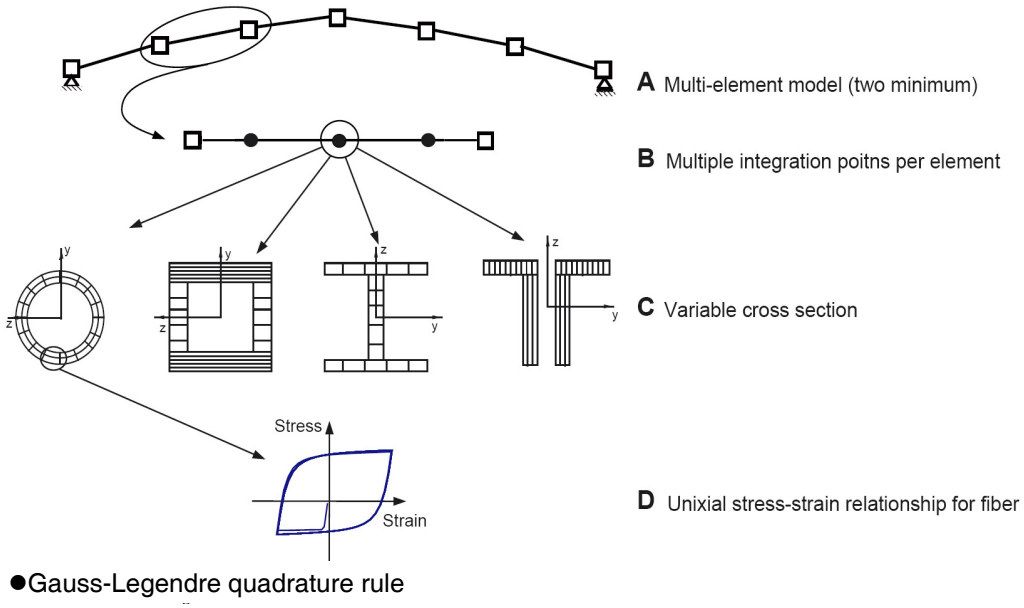

Figure 3.2 Illustration of the beam-column element for modeling the braces (after Uriz and Mahin [2008]).

The numerical model in Figure 3.3 shows the geometric parameters of the brace member model. An initial camber is imposed along the middle of the brace to induce buckling. To better capture the behavior of the brace, the brace models have denser element distribution in the middle, where the inelastic behavior is more likely to occur if the brace buckles. Summarized in Table 3.1, the study by Uriz and Mahin [2008] investigated the sensitivity of cyclic response to the initial camber, the number of elements, the number of integration points per element, and the number of fibers at each section chosen to accurately estimate the inelastic strains at the critical sections in braces.

Table 3.1 Suggested modeling parameters of braces in OpenSees [Uriz and Mahin 2008].

Parameter	Initial camber	Number of elements	Number of integration points	Number of fibers
Suggestion	0.05% to 0.1% of brace length	4, 7, 10, 30	Minimum of 3	10 to 15 layers

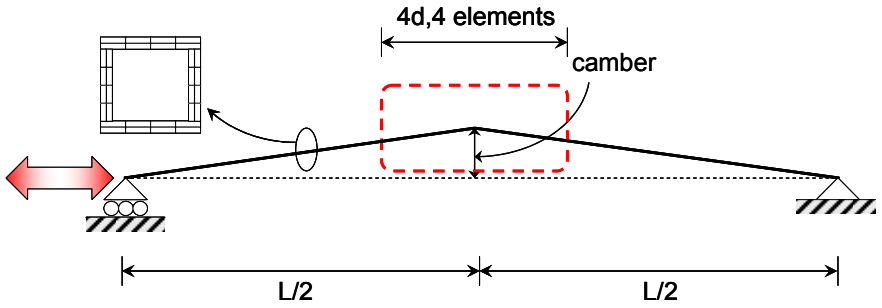

Figure 3.3 Illustration of brace model.

3.2 MODELING FATIGUE BEHAVIOR UNDER CYCLIC LOADING

Low-cycle fatigue was explicitly simulated using an approach suggested by Uriz and Mahin [2008] and implemented in OpenSees models. As noted previously, fracture of braces due to low-cycle fatigue has a profound impact on the global and local behavior of an SCBF system. The mechanics of fatigue is as follows.

Basquin [1910] observed that the stress amplitude and number of cycles to failure are linearly related when plotted on a log-log graph. The relation can be expressed as Equation 3.1:

$$\frac{\Delta\sigma}{2} = \sigma_f^{'}(2N_f)^b \tag{3.1}$$

where

$\frac{\Delta\sigma}{2}$ = the constant stress amplitude applied to the material; $\Delta\sigma$ is the stress range.

$\sigma_f^{'}$ = fatigue strength coefficient.

N_f = fatigue life, or number of cycles the material can sustain before the failure occurs. $2N_f$ in the equation means the number of reversals to failure (1 reversal = 1/2 cycle).

b = fatigue strength exponent (Basquin's exponent), which usually varies between –0.05 and –0.12.

In the 1950s, Coffin [1954] and Manson [1953] proposed that the plastic strain amplitude and fatigue life also had a linear log-log relationship. The relation is expressed in Equation 3.2:

$$\frac{\Delta\varepsilon_p}{2} = \varepsilon_0 (2N_f)^m \tag{3.2}$$

where

$\frac{\Delta\varepsilon_p}{2}$ = the constant plastic strain amplitude applied to the material. $\Delta\varepsilon_p$ is the plastic strain range.

ε_0 = fatigue ductility coefficient.

N_f = fatigue life, or number of cycles the material can sustain before failure occurs.

m = fatigue ductility exponent, which usually varies between –0.5 and –0.7.

From the relation of stress amplitude and elastic strain amplitude, and from Equation 3.1, the relationship between elastic strain amplitude and fatigue life can be written as Equation 3.3:

$$\frac{\Delta\varepsilon_e}{2} = \frac{\Delta\sigma}{2E} = \frac{\sigma_f^{'}(2N_f)^b}{E}, \tag{3.3}$$

where the total stain $\Delta\varepsilon$ is the summation of elastic strain and plastic stain. In terms of strain amplitude, the relation is shown in Equation 3.4:

$$\frac{\Delta\varepsilon}{2} = \frac{\Delta\varepsilon_e}{2} + \frac{\Delta\varepsilon_p}{2}. \tag{3.4}$$

If we substitute Equation 3.2 and Equation 3.3 into Equation 3.4, then the strain-life relation can be written as Equation 3.5:

$$\frac{\Delta\varepsilon}{2} = \frac{\sigma_f^{'}}{E}(2N_f)^b + \varepsilon_0 (2N_f)^m. \tag{3.5}$$

Figure 3.4 is the graphic expression of Equation 3.5. The low-cycle fatigue behavior is the primary failure mode in the braces. In the low-cycle fatigue range, the total strain amplitude is relatively large, and the plastic strain amplitude reflects most of the total strain amplitude. As such, Equation 3.5 can be approximated as Equation 3.6:

$$\frac{\Delta\varepsilon}{2} \approx \frac{\Delta\varepsilon_p}{2} = \varepsilon_0 (2N_f)^m. \tag{3.6}$$

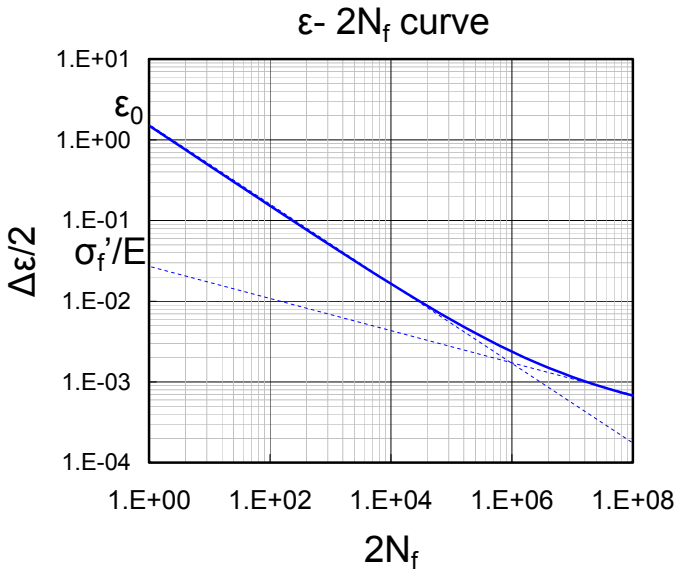

Figure 3.4 Relationship between strain amplitude and fatigue life.

3.2.1 Rainflow Cycle Counting

The strain-life of a material is counted in terms of the number of cycles it can sustain under constant strain amplitude. Although this is an efficient way to define the fatigue life of a material in the laboratory, the earthquake response does not emulate a constant strain range in structural members. To identify the fatigue life of a material under varying strain amplitude, the Rainflow cycle counting algorithm (Figure 3.5) is employed, where the number of cycles having a particular strain range is counted through the whole seismic ground excitation. Water flows down a pagoda-like structure representing the strain history with a vertical time axis. Specific rules have been developed to quantify the amplitude and number of cycles [ASTM 2003].

Earlier research by Matsuishi and Endo [1968] using Rainflow cycle counting required a complete loading history. As such, failure of a member could not be simulated during an analysis run. Other studies [Downing and Socie 1982; Glinka and Kam 1987; Hong 1991; Anthes 1997; Uriz and Mahin 2008] proposed the "one-pass" algorithm where the cycles are counted before the entire loading history is acquired.

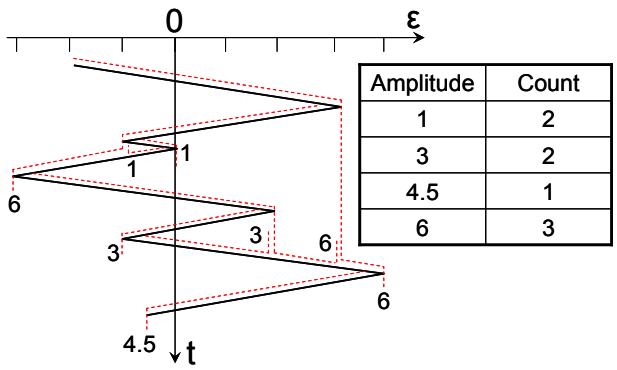

Amplitude	Count
1	2
3	2
4.5	1
6	3

Figure 3.5 Illustration of Rainflow cycle counting.

As cycle counting proceeds, the fatigue life of a material is estimated by counting the cycles of various amplitudes during a complex loading history. One of the most popular approaches to identify the damage progress is the linear damage rule proposed by Palmgren [1924] and Miner [1945]. The damage index *DI* in Equation 3.7 ranges from 0 to 1, in which 0 means there is no damage and 1 means the fatigue life is exhausted:

$$DI = \Sigma \frac{n_i}{N_{fi}}, \tag{3.7}$$

where n_i is the number of cycles applied at a stress level corresponding to failure in N_{fi} cycles. N_{fi} is calculated from Equation 3.6 given the fatigue parameters ε_0 and m. The history of $\Delta\varepsilon$ is calculated from Rainflow cycle counting algorithm and substituted into Equation 3.6 to determine N_{fi} [Uriz and Mahin 2008].

OpenSees incorporated the Rainflow cycle counting algorithm in the fatigue material module. When the damage index of a fiber exceeds unity, the fatigue life of that fiber is flagged as being exhausted and the fiber is removed from the cross section by reducing its strain and stress to zero.

3.2.2 Fatigue Material Parameters

The fatigue parameters ε_0 and m for the OpenSees model were obtained by calibrating the model with test data. To illustrate this, an HSS6x6x3/8 brace with slenderness ratio KL/r = 51.9 was analyzed. Test results are from Yang and Mahin [2005]. Different combinations of ε_0 ranging from 0.03 to 0.3 and m ranging from –0.5 to –0.70 were analyzed, and the dissipated energy of the analytical result was compared with that of the test results. By observing the correlation of test and analysis results, the optimal combination of fatigue parameters relevant to this study was calculated to be ε_0 = 0.09 and m = –0.6, which are similar to values obtained by Uriz and Mahin [2008]. The analytical results of the behavior of a brace were compared with the experimental results in Figure 3.6. The tensional and compressional strength of the brace hysteresis characteristics and the fracture points were generally captured by the analysis.

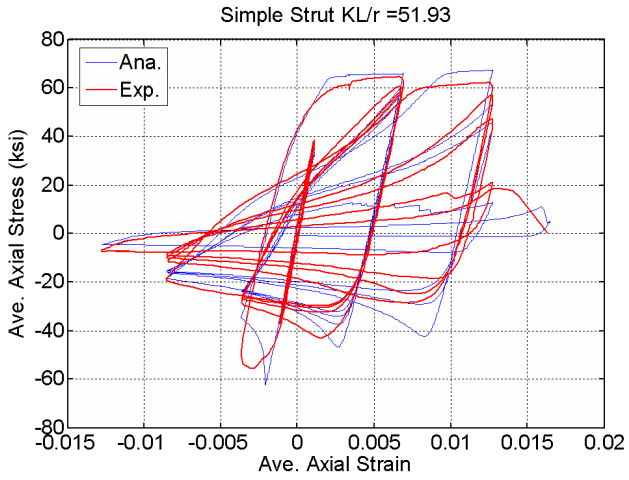

Figure 3.6 Comparison of analytical and experimental responses of an HSS6×6×3/8 brace with KL/r = 51.93.

It is important to note that the fatigue model only considers unidirectional material properties, and the OpenSees beam-column model does not consider local buckling. As such, the fatigue life prediction requires careful calibration to test results representing the members being modeled.

3.3 TWO-STORY TESTED SCBF

The previous research [Uriz and Mahin 2008] conducted a test on a large-scale, two-story conventional chevron braced frame (Figure 3.7). The test results were simulated in a 3D model that captured the responses of the specimen satisfactorily. To reduce the computational effort, we simplified this model to a 2D frame model with the modeling parameters discussed earlier, and the brace members were modeled with ideal pin-ended connections. In the 2D model, the out-of-plane deformation was constrained. As such, only the in-plane failure modes were accounted for and the braces were arranged to buckle in the plane of the frame by aligning the orientation of the pin ends.

The 2-story model—a total story height of 20 ft with a 20-ft span—is illustrated in Figure 3.8. Lateral force was applied at only the upper level to achieve a desired cyclic displacement history. Because the lateral force was applied only on the upper level, the story shears of both upper and lower levels were the same. Because the braces made up the majority of the story shear, the design and size of braces in both stories were identical. The column size was W10×45; the beam size was W24×117; and the brace size was HSS 6×6×3/8. No axial load was applied to the column during the test. The beams were designed to take the unbalanced force induced by the buckling of the braces and the drag force transferred by column and braces from the actuator.

Several studies [Neuenhofer and Filippou 1997; Scott et al. 2004] have demonstrated the advantages of a force-based over a displacement-based beam-column element; thus the force-based nonlinear beam-column element was chosen. Beams were represented by two force-based beam-columns. Columns were modeled by single force-based beam-column; they were continuous and assumed fixed at their base. The hysteretic characteristics of the braces were modeled using an approach developed by Uriz and Mahin [2008]. Each brace was subdivided into 10 force-based beam-column elements, with fibers used to model the shape and hysteretic characteristics of the brace at the integration points along each element.

The beam-to-column connections were fully constrained in the numerical model. At connections with gusset plates, the behavior was considered to be very nearly fixed, even if such connections were not detailed as being fully restrained. Although finite-element analyses [Huang and Mahin 2010] and tests [Uriz and Mahin 2008] suggested that shear-tab-only connections may rupture in the presence of large lateral story drifts or the effects of unbalanced forces applied to a beam when a brace connected to its mid-span ruptures, this mode of failure is difficult to model without more test data; therefore, all beam-to-column connections in the braced bay were assumed to be fully restrained in the OpenSees fiber-based models.

For the sake of simplicity, and consistent with recommendations of Uriz and Mahin [2008], the beam-column connections and the region between the fold line in the gusset plate and the center of the beam-column connections were idealized as being rigid due to the high stiffness and strength of these regions compared to adjacent members.

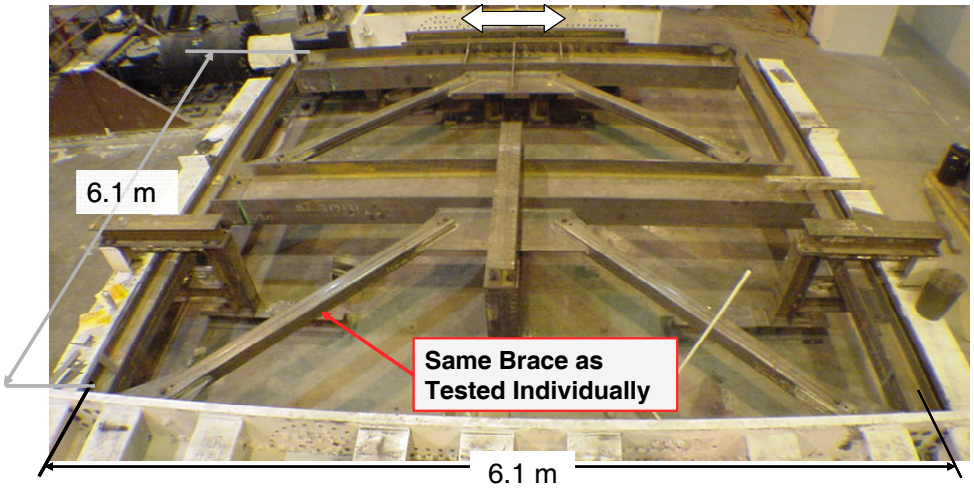

Figure 3.7 Test specimen of two-story chevron braced frame [Uriz and Mahin 2008].

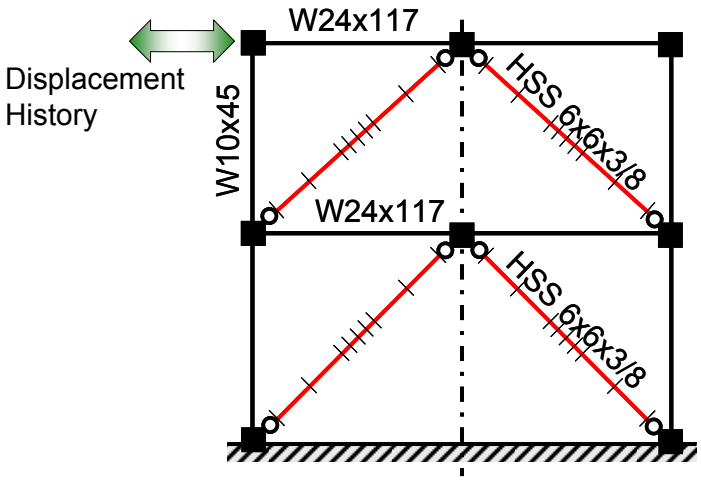

Figure 3.8 Numerical model of two-story chevron braced frame.

For the fatigue-sensitive models, the strain history in each fiber in the braces, beams, and columns was tracked and a Rainflow cycle counting algorithm was used to determine the amplitude of each inelastic cycle. A Manson-Coffin relation, calibrated to multiple tests of HSS6×6×3/8 braces and other sections, was used to characterize low-cycle fatigue damage to each fiber during a particular cycle of response. Miner's rule was used to cumulate cyclic damage throughout the response. If a fiber's fatigue life was exceeded during the analysis, that fiber was removed from the numerical model. This approach has been successfully used to model yielding, buckling, and low-cycle fatigue rupture of braces and braced frames [Uriz and Mahin 2008].

The actual material strength (shown in Table 3.2) was used to model the frame members. The measured yielding stresses for all the structural components were greater than the nominal values. For the braces, the yielding stress for modeling was 32% higher than the nominal stress.

Table 3.2 Material properties of two-story chevron braced frame test.

Member	Average F_y (ksi)	Average F_u (Ksi)	Elongation (%)
Column (W10×45)	55.8 (Gr. 50)	73.7	23.9
Beam (W24×117)	58 (Gr. 50)	74.5	26
Brace (HSS 6×6×3/8)	60.6	65.9	36

The analytical and experimental results are compared in Figures 3.9 and 3.10. Figure 3.9 presents the hysteretic loops of the braces in the lower level. The strength degrading and the fracture of the braces were estimated to a satisfactory degree. Figure 3.10 depicts the roof displacement–base shear relation and shows that the computed initial elastic stiffness of the braced frame was almost identical to the experimental stiffness. Also, the analytical maximum strength of the braced frame approximates the experimental results. The pinching behavior of the braced frame due to the buckling of the braces was well captured. Note that the fracture of the braces leading to a sudden observed drop of strength was also reasonably accurate. At the end of the test, the remaining strength of the braced frame was primarily from the contribution of the moment resisting frame, and that strength was well captured.

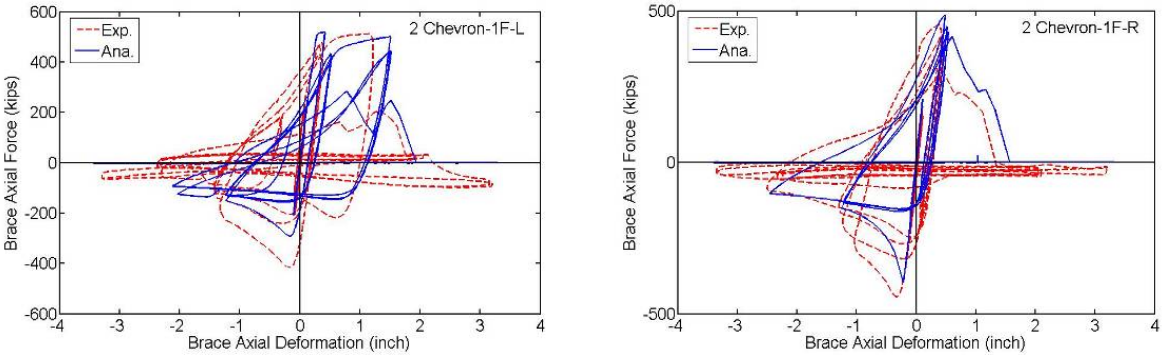

Figure 3.9 Comparison of analytical and experimental responses of braces in the first story.

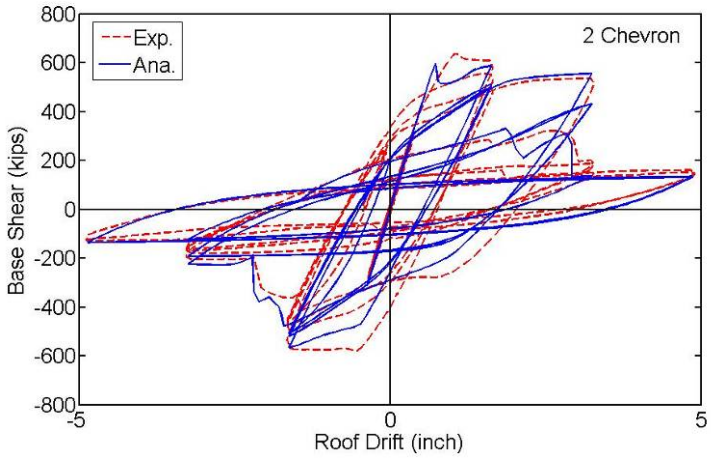

Figure 3.10 Comparison of analytical and experimental response of two-story chevron braced frame.

3.4 PRELIMINARY STUDIES OF A THREE-STORY MODEL BUILDING

The performance of a typical 3-story steel braced building was assessed. The previous modeling approach was used and the sensitivity of performance to material and global modeling assumptions was examined. No test results were available for this model. As shown in Figure 3.11, the model building has regularly spaced gravity-resisting frames (continuous columns with ideal pin connections to the beams and foundation); the lateral earthquake-load resistance is provided by special concentric braced frames located on the perimeter of the building. Designed to conform to the provisions of ASCE/SEI 7-05 [DASSE 2007], this building was located in downtown Los Angeles, California, for use as a commercial office building. Table 3.3 lists some of the principal attributes of the structure and the key parameters used in the seismic design.

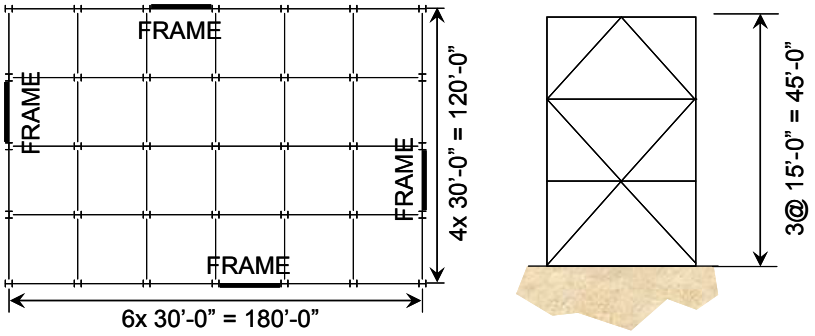

Figure 3.11 Model building floor plan and elevation.

Table 3.3 Design parameters of model buildings.

Code	ASCE/SEI 7-05
Building location	Los Angeles, CA
Seismic design category	D
Occupancy category	II (Office)
Importance factor	1.0
Short period spectral acceleration, S_s	2.2g
1 sec. period spectral acceleration, S_1	0.74g
F_a	1.0
F_v	1.5
R	6
Design base shear	0.24W
Code approximated period (T_a)	0.35 sec

Table 3.4 lists the member sizes used in the model. The same size column was used over the whole height of the building. Note that the roof beam was heavy compared to the lower two floor beams, because the configuration of the braces adopted results in small unbalance forces in the lower two levels. Where braces intersected along the length of the beam in the chevron braced frames, the beam was typically designed for the vertical component of the maximum unbalanced load produced by the tension and compression braces, in addition to axial and other

forces associated with the applied earthquake forces. The tension brace was assumed to carry a load of $R_y P_y$ while the compression brace was assumed to carry the post-buckling load of only 0.3 $\varphi_c P_n$.

Table 3.4 Member sizes.

Floor/Story	Braced frame columns	Braced frame beams	Brace size
Roof/3	W14×176	W36×210	HSS 10.0×0.375
3rd/2	W14×176	W30×116	HSS 11.25×0.50
2nd/1	W14×176	W27×84	HSS 12.5×0.50

3.4.1 Design Spectra

The design response spectrum (ASCE 7-05) used in the archetype structure's design is shown in Figure 3.12. The vertical line on the plot represents the structure's computed elastic fundamental period (0.5 sec) in numerical models.

The structure was analyzed considering 60 ground motion records taken from the SAC ground motion ensembles developed consistent with 1997 NEHRP seismic hazard curves for Los Angeles [Somerville 1997]. The 60 records represent three different hazard levels: the service-level earthquake (50% probability of exceedance in 50 years, 50/50), the design-level earthquake (10% probability of exceedance in 50 years, 10/50), and the MCE-level earthquake (2% probability of exceedance in 50 years, 2/50). Median pseudo-acceleration and displacement spectra for the 20 ground motion records corresponding to each hazard level are shown in Figure 3.12. Note that for the period of this archetype building, the median spectral values for the 20 records corresponding to the design-level event are less than the corresponding ASCE/SEI 7-05 code spectra. Thus, the records used in this study are smaller on average than those that correspond to the seismic hazard at the site.

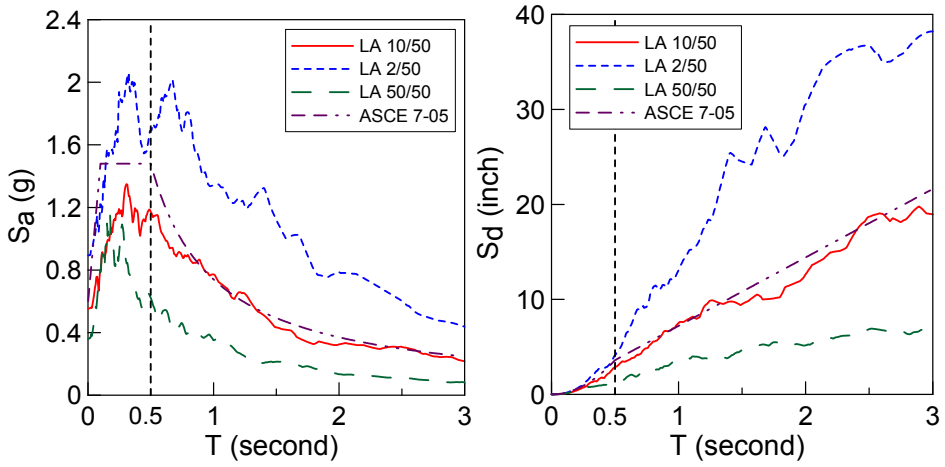

Figure 3.12 Response spectra.

Rather than using the median values of results for records corresponding to that hazard level, in this case we used the spectral displacement corresponding to the basic site hazard curve and structural fundamental period, in conjunction with a regression analysis of the responses for the parameters of interest, to interpret the response at a particular hazard level. The median

elastic spectral displacements corresponding to the computed fundamental period of the SCBF structure are shown in Table 3.5 for the three hazard levels.

Table 3.5 Median of $S_{d,\text{Elastic}}$ (in.).

Fundamental period	Hazard level		
	50% in 50 yrs	10% in 50 yrs	2% in 50 yrs
T = 0.50 sec	1.70	2.74	4.13

3.4.2 Numerical Models at Phase I

Several variations of numerical models were considered, and analyses were conducted in two phases. The parameters varied in Phase I for a single ground motion were:

- First-story height
- Mass considered in vertical direction
- Effect of rigid end zone in the mid-span of beams
- Beam-column connection type
- Effect of fatigue material
- Comparison of force-based and displacement-based beam column elements

These results were compared with one another and to results of a full finite-element model implemented in LS-DYNA and used to refine the OpenSees model. The numerical models were further refined in Phase II by comparing their responses to a single ground motion as well as statistical responses to the ground motion set. For both phases, the basic assumptions for the models were the same. The parameters varied were:

- Axial load modeling in beams
- The viscous damping ratios
- Fatigue material parameters

Fiber-based models of the archetype structure were used for the OpenSees analyses and shell-based finite-element models were used for the LS-DYNA [LSTC 2007]. Although two separate software packages were used, the modeling was conducted to be as identical as possible. In both cases, only one braced bay was considered, subjected to vertical gravity dead loads and with in-plane horizontal seismic excitations applied at the base. Half of the tributary reactive mass of the building was assigned to a single frame; the torsional response of the structure about a vertical axis was not considered. The gravity-load-only framing was idealized as a leaning column; therefore, it provided no structural strength or stiffness, but it resulted in appropriate geometric nonlinearity effects. For the sake of clarity and simplicity, the vertical component of seismic excitation and the mechanical characteristics of the floor slabs were ignored.

3.4.2.1 OpenSees model

Figure 3.13 illustrates the numerical models, including the braced frame and the leaning column. The numerical models were based on the parameters previously discussed with improved details in the brace-to-frame connections. Additional parameters for dynamic analysis are discussed in this section.

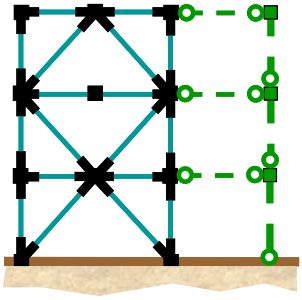

Figure 3.13 Sketch of basic OpenSees model.

The vertical floor mass tributary to the braces intersecting a beam or column was included in the models. Earlier studies [Khatib et al. 1988] have shown that this vertical mass has a significant effect on dynamic response during brace buckling.

Because only mass-proportional viscous damping could be modeled with the current implicit solver version of LS-DYNA, an OpenSees model with mass-proportional damping was used for some of the analyses for comparison. For mass-proportional viscous damping, the damping coefficient was selected to produce viscous damping equal to 4% of critical at the computed first mode period (T) of the structure. Rayleigh damping, based on the mass and tangent stiffness proportional damping, was used in most of the OpenSees analyses, with the damping coefficients selected to give viscous damping of 4% of critical at the first and third mode periods.

P-Δ effects were represented using either one or two leaning columns. Each leaning column was constrained to have the same lateral displacement as the nearest adjacent column at the same level in the braced bay. The axial stiffness and flexural stiffness of the columns were assumed to be large, but a pin was introduced at the bottom of the column in each story. Thus, bending of the gravity-load-only columns did not contribute to the lateral stiffness or strength of the structure. Applied axial loads on the leaning column were taken as half or one-quarter of the total dead load of each floor (less the dead load directly tributary to the braced bay) depending on whether one or two leaning columns were included in the model. A co-rotational formulation was used to simulate P-Δ effects for these columns. A single leaning column was commonly used to represent gravity-only framing. Because axial deformability and axial load-moment interaction are considered in the OpenSees model for the beams, the axial forces introduced in the beams in the braced bay by the leaning columns can significantly alter behavior. Thus, cases with one or two leaning columns were considered. For the plan configuration shown in Figure 3.11, two leaning columns would be the most realistic case.

Instead of being modeled as ideal pins, the fold line in the gusset plate of the brace ends was modeled by one force-based beam-column element with fiber section. The dimension of this element was (L × W × t) = ($2t_g \times b_g \times t_g$), where t_g is the thickness of the gusset plate and b_g is the width of the gusset at the central location of the folding line. This provided adequate

modeling constraint to the braces of the braced frames with fully restrained brace-to-gusset connections.

Although the OpenSees fiber-based elements accounted for many aspects of the behavior of braces (and beams and columns), they did not explicitly account for the effects of local buckling and fracture-mechanics-related phenomena. Three-dimensional related behavior modes (such as the torsion and twist of beams, columns, braces, and gussets) were not simulated in the OpenSees model. No attempt was made in this study to model potential in-plane or out-of-plane buckling of columns (although comparison of peak column axial forces suggests that column lateral buckling was unlikely). Although these effects were of interest to the current study, it is unclear whether the low-cycle fatigue damage parameters, used and derived on the basis of the behavior of small and mid-sized square HSS braces, are entirely appropriate for the size and shape of braces used in the archetype structure.

3.4.2.2 LS-DYNA model

The finite-element models [Huang and Mahin 2010] of the archetype structure were formulated in three dimensions using LS-DYNA. The analysis models explicitly simulate local buckling and evolution of damage due to low-cycle fatigue [Huang and Mahin 2008]. To be consistent with the OpenSees models, lateral-torsional response of beams and lateral buckling of columns were neglected.

Based on an assessment of computational effectiveness, we chose shell elements instead of solid or beam elements. Mesh convergence was examined using progressively refined finite-element meshes. Our final choice of a shell element size corresponding to about the shell thickness achieved an overall model that we believed to be simple with reasonable accuracy. Unlike the case in the OpenSees model, the gusset plates and connection regions in the LS-DYNA model were fully represented using shell elements. Net reduced sections at the connections of the braces to gusset plates were adequately reinforced per AISC [2005] requirements so that premature rupture at those locations was avoided. A significant difference between the fiber and shell element models was that the beam-to-column connections away from gusset plates were modeled in LS-DYNA as welded shear tab connections, rather than as the moment connections used in OpenSees.

Crack initiation and propagation were modeled by element erosion (shell element removal) using a cyclic damaged plasticity material model developed by Huang and Mahin [2008, 2010]. This mechanics-based approach simulates materials that follow a Manson-Coffin model and Miner's rule. Material property specifications similar to those of the OpenSees model were used. The plasticity and damage properties of steel material were calibrated against braces and validated with a SCBF subassembly experiment conducted at the University of California, Berkeley [Yang and Mahin 2005; Uriz and Mahin 2008]. A comparison of experiment and numerical results is shown in Figure 3.14; note that buckling and fracture of braces is accurately modeled (Figures 3.14d and 3.8e). In addition, the simulated damage and fracture at the beam-column connections match the experiment (Figures 3.14c and 3.14f). These simulations show that the cyclic damaged plasticity model is reasonable and useful for damage evaluation in steel structures.

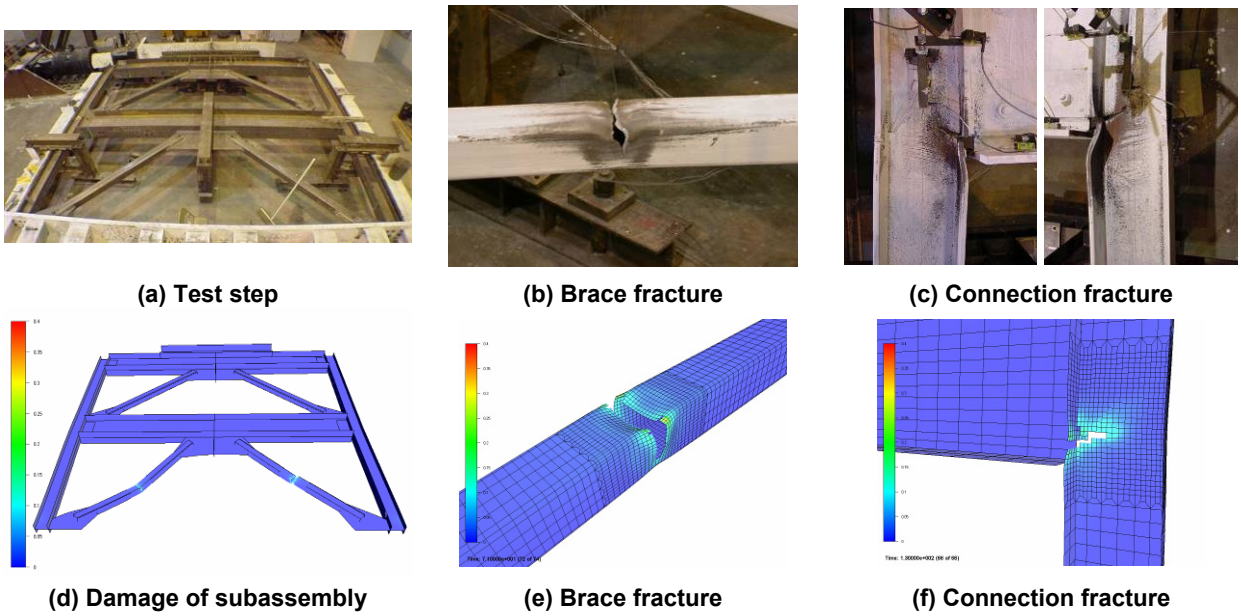

(a) Test step (b) Brace fracture (c) Connection fracture

(d) Damage of subassembly (e) Brace fracture (f) Connection fracture

Figure 3.14 Comparison of experiment and LS-DYNA simulation results.

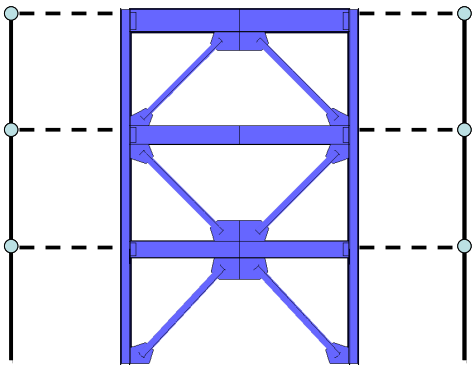

Figure 3.15 Sketch of basic LS-DYNA model.

The SCBF columns were fixed at the base. Although the top and bottom flanges of all beams were laterally restrained to prevent lateral-torsional motion and out-of-plane buckling, the columns were unrestrained between floors so in-plane and out-of-plane column buckling could be detected.

The finite-element model for the 3-story SCBF archetype is shown in Figure 3.15. All components except the leaning columns incorporated the damaged plasticity material model and were modeled as shell elements. No rigid elements were incorporated in the model. Similar to the OpenSees model, the vertical floor mass tributary to the braces and the dual pin-connected leaning column were modeled on each floor level to account for P-Δ effects. The beams in the gravity-only system were disregarded.

3.4.3 Phase I Analysis

A basic numerical model was developed to monitor the sensitivity of response to variations in model characteristics and ground motions. The displacement time histories of the structural response to SAC ground motion LA32 (simulated time history for a magnitude 7.1 earthquake on the Elysian Park fault) shows pulses in both positive and negative directions; we chose this record in this section to compare with results from various models. Eleven OpenSees models were compared to determine the sensitivity to geometric configuration, boundary conditions, and the analytical element types. The models were all 3-story, double-story X SCBFs designed following the building code of ASCE/SEI 7-05 (Model B). The detailed parameters of the models are listed in Table 3.6. Model names beginning with 3BF represent the 3-story model with Fixed beam-column connections, with gusset plates modeled in the brace ends, and with non-lateral-resisting leaning columns. The model name beginning with 3BP is similar to 3BF except that the beam-column connections are Pin ended. In model names with H and R, the story height of the first story is taller than the other stories because the work point in the column base is actually under the ground; however, in real practice the first-story height is sometimes counted from the ground level. Both the H and R models were analyzed to account for the influence of the story height. The difference between H and R models is that R models include the rigid end region in the mid-span of the beams while H models do not. Model names with V mean the assigned effective vertical mass is greater than the tributary mass and equal to the effective mass in the horizontal direction; model names without V have the assigned effective vertical mass equal to the tributary mass. Models with subscript "d" represent that the displacement-based nonlinear beam-column element was employed, and models without subscript "d" used the force-based nonlinear beam-column element. The responses are shown in Figures 3.16 to 3.27. The influence of changing parameters is discussed next.

Table 3.6 Model names and their properties in Phase I analysis.

Model	Fix-ended beam	Pin-ended beam	Taller first story	Same vertical mass as horizontal mass	Tributary vertical mass	Rigid end region in the mid-span of beam	No fatigue	Displacement-based element	Force-based element
$3BFHV_d$	X		X	X				X	
$3BFRV_d$	X		X	X		X		X	
$3BFV_d$	X			X				X	
$3BFH_d$	X		X		X			X	
$3BFR_d$	X		X		X	X		X	
$3BF_d$	X				X			X	
3BFHV	X		X	X					X
3BFRV	X		X	X		X			X
3BFR	X		X		X	X			X
$3BPR_d$		X	X		X	X		X	
3BFRN	X		X		X	X	X		X

3.4.3.1 Effect of first-story height

The effect of uniform story height can be seen by comparing models $3BFV_d$ and $3BF_d$ with the other models that have taller first stories. The taller first story tends to concentrate the story drift in the first story, whereas the lateral deformation of the models with uniform story height tends to concentrate in both the first and second stories. The energy-dissipating mechanism is different for models with taller first stories. Models $3BFV_d$ and $3BF_d$ dissipated energy due to the nonlinear behavior of the first- and second-story structural members, while the other models dissipated energy largely via first-story structural members. Models $3BFV_d$ and $3BF_d$ had smaller maximum story drift among all levels compared to all other models.

3.4.3.2 Effect of rigid end zone in the mid-span of beams where braces meet

Comparison of model $3BFHV_d$ with $3BFRV_d$, $3BFH_d$ with $3BFR_d$, and 3BFHV with 3BFRV demonstrates the effect of a rigid end region in the mid-span of beams. For models $3BFHV_d$ and $3BFRV_d$, brace fracture occurred at different times and therefore the permanent story drifts were different. For model $3BFH_d$, the permanent story drift was positive and different compared to the other models. Model $3BFR_d$, with a rigid end zone, had negative permanent story drift, and the response was smoother compared to model $3BFH_d$. For models 3BFHV and 3BFRV, the shape of the hysteretic loops was similar. Generally, the effect of the rigid end region at the mid-span of beams where braces intersect was less significant compared to the effect of story height.

3.4.3.3 Effect of vertical mass

The effect of vertical mass on story drifts was investigated by comparing model $3BFHV_d$ with $3BFH_d$ and $3BFRV_d$ with $3BFR_d$. Larger vertical mass did not necessarily result in a larger story drifts under horizontal excitation. In model $3BFHV_d$ the larger vertical mass caused large permanent story drift on the first story, while in model $3BFRV_d$ the story drift on the second story was less compared to model $3BFR_d$. Comparing $3BFRV_d$ with $3BFR_d$, the model with larger vertical mass had jagged response, which was due to the dynamic effect of the vertical mass.

3.4.3.4 Effect of analytical element types

The different responses of displacement-based and force-based elements can be seen by comparing $3BFHV_d$ with 3BFHV and $3BFRV_d$ with 3BFRV. The results of models $3BFRV_d$, 3BFHV, and 3BFRV were similar, but in general the force-based models had smoother responses. The force-based model was improved by using smaller time steps. The time step changes during the dynamic analysis until convergence occurs. For example, model 3BFR used a time step as small as 10^{-6}.

The story drift of 3BFR was similar to the results obtained using LS-DYNA, which employed shell elements to capture detailed responses. The major difference between 3BFR and LS-DYNA results was that the fracture of braces in 3BFR resulted in a sudden drop of strength, which was similar to what occurred in earlier experimental results. In LS-DYNA, strength still degraded, but because the braces did not completely fracture there was no sudden drop of strength.

These results show that a force-based beam-column element accurately estimates the nonlinear responses of the 3-story, double-story X braced frame. In addition, the use of a smaller time step is recommended not only to increase the accuracy but also to improve the convergence. As to the vertical mass, the results demonstrate that it is not as significant a factor in the response compared to the other parameters, such as the story height and the element type.

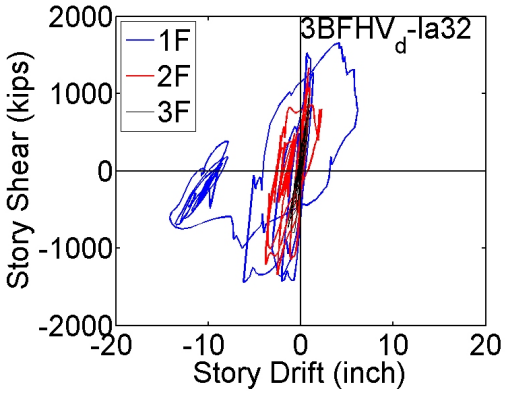

Figure 3.16 **Taller first-story height with same vertical mass as horizontal mass (displacement-based element).**

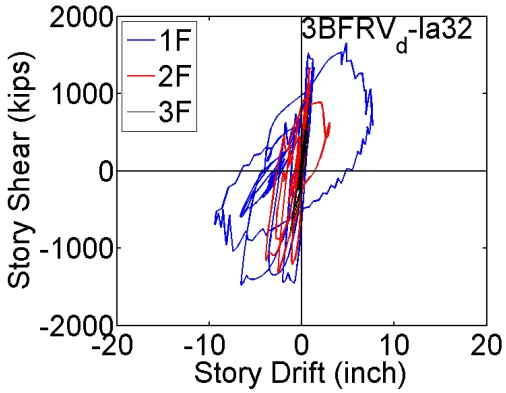

Figure 3.17 **Taller first-story height with same vertical mass as horizontal mass and rigid end region in the mid-span of beam (displacement-based element).**

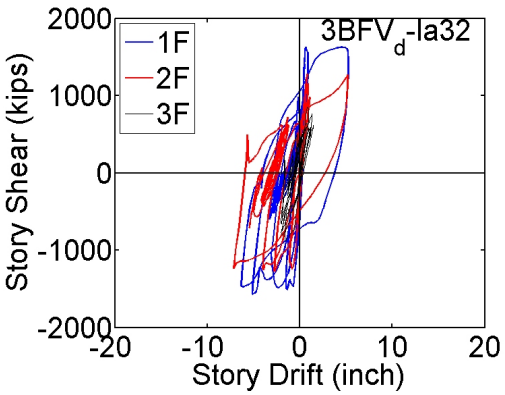

Figure 3.18 **Uniform story height with same vertical mass as horizontal mass (displacement-based element).**

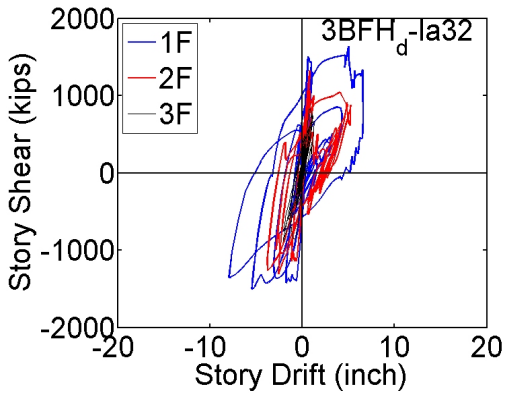

Figure 3.19 **Taller first-story height with less vertical mass than horizontal mass (displacement-based element).**

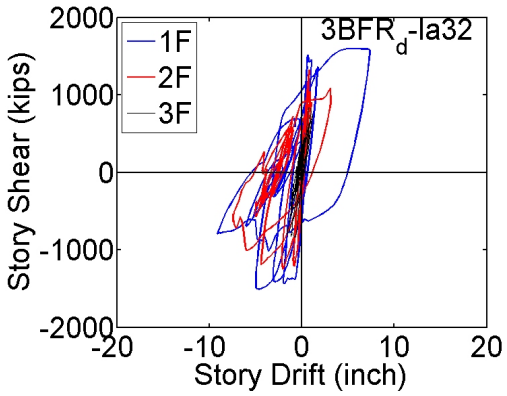

Figure 3.20 **Taller first-story height with less vertical mass than horizontal mass and rigid end region in the mid-span of beam (displacement-based element).**

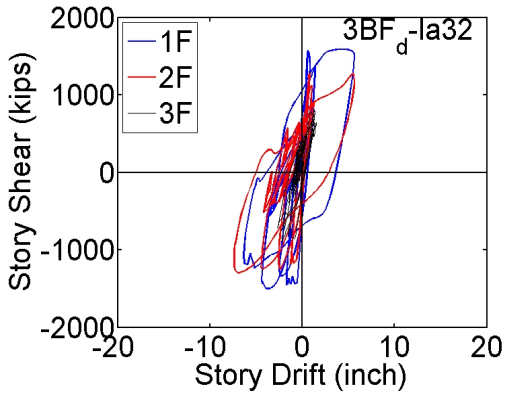

Figure 3.21 **Uniform story height with less vertical mass than horizontal mass (displacement-based element).**

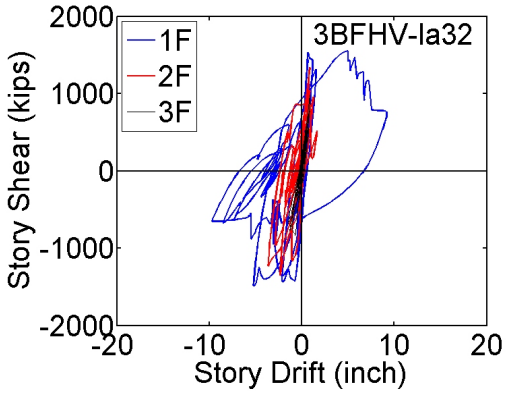

Figure 3.22 **Taller first-story height with same vertical mass as horizontal mass (force-based element).**

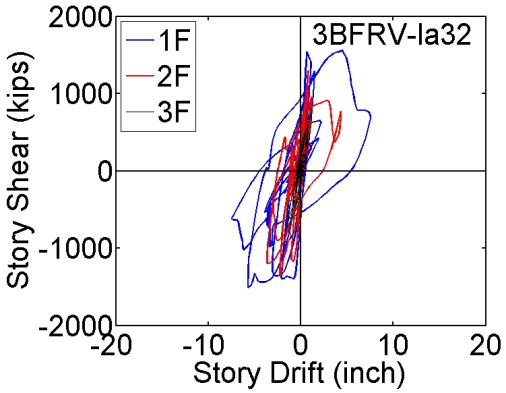

Figure 3.23 **Taller first-story height with same vertical mass as horizontal mass and rigid end region in the mid-span of beam (force-based element).**

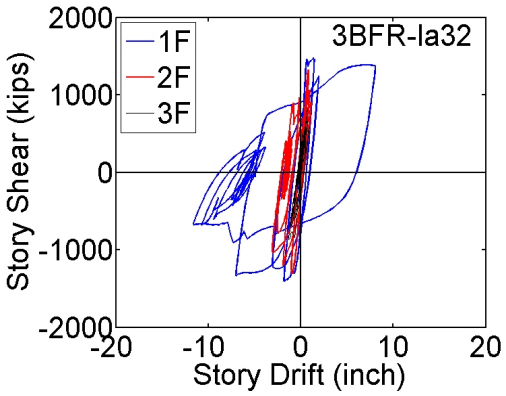

Figure 3.24 **Taller first-story height with less vertical mass than horizontal mass and rigid end region in the mid-span of beam (force-based element).**

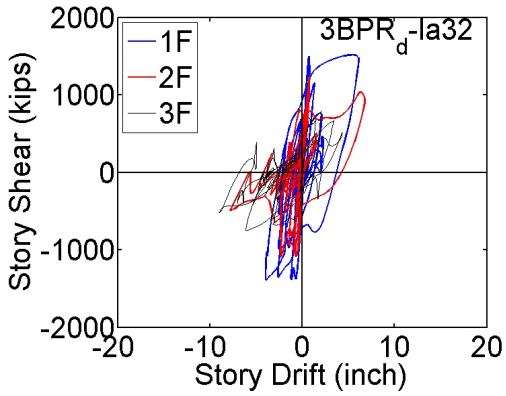

Figure 3.25 **Taller first-story height with less vertical mass than horizontal mass, rigid end region in the mid-span of beam and pin-ended beams (displacement-based element).**

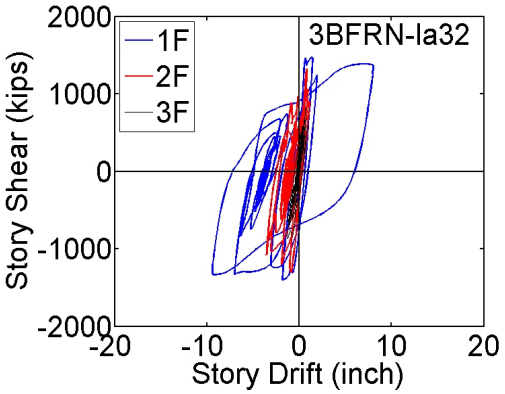

Figure 3.26 **Taller first-story height with less vertical mass than horizontal mass, rigid end region in the mid-span of beam and non-fatigue materials (force-based element).**

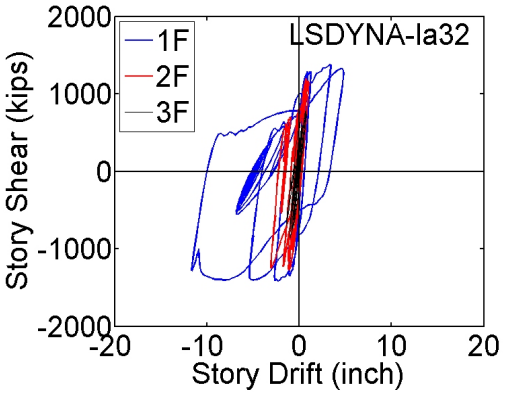

Figure 3.27 **Finite-element model of archetype structure in LS-DYNA.**

3.4.4 Phase II Analysis

This section presents results for the five 2D (planar) models. These models allowed for comparison of the effects of (1) mass proportional viscous damping versus combined mass and tangent stiffness proportional viscous damping, (2) the number of leaning columns used to represent geometric nonlinearities, and (3) whether rupture due to low-cycle fatigue is considered or not.

These models were designated 3BF1L, 3BF2L, 3BF2LN, 3BF2LM, and 3BF2LMN, according to the naming convention shown in Table 3.7. For example, model 3BF2LMN was a 3-story, double-story X SCBF designed to comply with ASCE/SEI 7-05, with fully constrained beam-column connections, with two leaning columns (one on each side of the frame), with mass-proportional damping, and with fatigue disregarded in the modeling of all structural components. We investigated responses to pushover analyses (nonlinear static analyses) and to nonlinear dynamic analyses under a single ground motion and large ensembles of ground motions. Results obtained with LS-DYNA were used to further study the differences between fiber-based and finite element-based models.

Table 3.7 OpenSees model names.

Abbreviation	Denotation
B	Double-story X SCBF designed to comply with ASCE/SEI 7-05
F	Model building with fully constrained beam-column connections
1L or 2L	1 leaning column or 2 leaning columns
M	Mass-proportional damping (Rayleigh damping otherwise)
N	Non-fatigue material (fatigue material otherwise)

3.4.4.1 Pushover analysis of Phase II models

Nonlinear pushover analyses were carried out on the models. Lateral forces were distributed over height according to the models' elastic first mode shape. The resulting relations between roof lateral displacement and base shear are shown in Figure 3.28. The initial loading stiffnesses of the OpenSees model and LS-DYNA models were similar. At a roof drift index (roof lateral displacement divided by the roof elevation) of about 0.3%, one of the braces at the ground story buckled globally in the OpenSees model, resulting in a sudden loss of frame strength and an overall negative tangent lateral stiffness. In the LS-DYNA model, stiffness decreased gradually before reaching the brace's buckling load, and the peak system strength was slightly smaller compared to the OpenSees prediction. This gradual decrease in initial stiffness was associated with several possible factors: e.g., frame action, resulting in greater initial stress and sway in the braces, local stress concentrations resulting in earlier local yielding throughout the frame, and initiation of minor local buckling prior to global brace buckling.

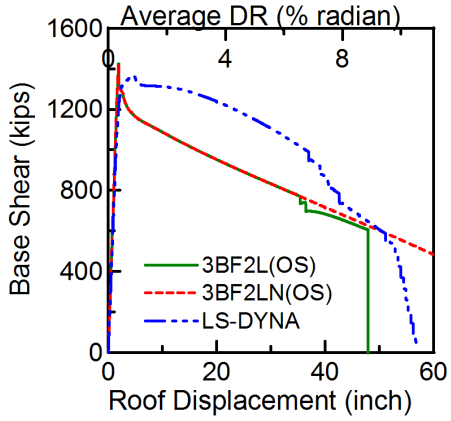

Figure 3.28 Base shear as a function of roof displacement for three models.

After the brace-buckling load was reached, the base shear dropped rapidly in the OpenSees model, while reducing much more gradually in the LS-DYNA model. The greater post-buckling strength of the LS-DYNA model was attributed to increased post-buckling contributions of the braces through in-plane bending to the overall structural stiffness and strength. For the planar OpenSees model, the braces were pinned to the connections and their contribution to frame response was thus only associated with their axial load-axial deformation characteristics. However, in the finite-element model, additional strength contributed to counter the deteriorating axial load capacity of the buckled brace(s) by (1) the moment capacity of the gusset plate to out-of-plane motion of the braces, slowing the deterioration of brace axial load capacity, and especially (2) by the gusset plates developing brace bending in the plane of the SCBF.

The OpenSees models exhibited steady reduction of base shear capacity with increasing lateral roof displacement. This is associated with the post-buckling characteristics of the braces, but also with the effects of geometric nonlinearities. The damage was concentrated almost entirely in the ground story, with buckling occurring in one of the ground-story braces, followed by tensile yielding of the other brace in the ground story. Limited tension yielding of the second-story brace was predicted. The third story remained essentially elastic in the OpenSees model.

For the OpenSees models including low-cycle fatigue rupture of individual fibers, a small additional reduction of shear capacity was seen at a roof drift index of about 6.5%. This is associated with the compression brace at the ground story brace losing all of its capacity. A final loss of capacity was observed at a roof drift index of about 8.5%. This is associated with rupture of the tension brace. As noted in Uriz and Mahin [2008], the Rainflow cycle counting approach counts tension and compression cycles equally, so that failures may occur in tension or compression cycles. Even under compression loading, one side of a plastic hinge in a brace is actually loaded in tension. The Manson-Coffin relation used in both the OpenSees and LS-DYNA models resulted in much larger drift capacity under monotonic loading than would be expected during cyclic or earthquake loading.

For the LS-DYNA analysis, buckling of the ground story brace occurred quite early, followed by tension yielding of the brace in the same level. There was minor yielding in the second-story tension brace. Although this was similar to the progression of events in OpenSees, brace fracture was not predicted. However, at about 7–8% roof drift ratio, the tension column began to fracture near the bottom of the shear tab at the end of the lowest beams. At a roof drift ratio of about 9–10%, the connection of the bottom tension brace to the gusset plate failed. This is associated with combined tension, in-plane bending, and stress concentration at the tip of the gusset plate. These two modes of failure were not modeled in OpenSees. The base shear went to zero gradually in LS-DYNA, which was due to the residual capacity of the compression side column and compression brace. In OpenSees, the failure of both braces at the bottom level led to numerical instability.

The results showed that the roof drift index (roof lateral displacement divided by the roof elevation) was about 0.30% at the first buckling of a brace, about 6% to 8% at rupture of the first brace, and 8.5% for numerical instability due to excessive damage to the structure. Because the connections in OpenSees model were idealized, their failure was not explicitly simulated in the analysis. It was assumed that the connections remained intact under the seismic demand analyzed.

3.4.4.2 Individual case studies of dynamic response of the Phase II models

The six model buildings were subjected to the 60 SAC ground motions described previously. Before looking at a statistical analysis of the sensitivity of key EDPs to ground motion intensity, it is useful to examine in more detail the response of the systems to an individual ground motion. In this section we examine time histories of critical story drift and vertical mid-span beam displacement, and hysteretic loops for critical braces and for the frame roof displacement-base shear for SAC record LA32 (a simulated time history for a magnitude 7.1 earthquake on the Elysian Park fault), which is part of the ensemble scaled to be representative of the MCE hazard level. This ground motion caused the largest displacement responses in the model buildings.

Figure 3.29 plots the story drift and brace axial deformation time histories at the first (bottom) story for record LA32. The bottom story suffered the largest story drifts for this (and most other) records, while the upper two stories remained essentially elastic.

For all five OpenSees models in Figure 3.29, the response to LA32 is characterized by a single very large story displacement excursion to about 14 to 20 in. in the first story, corresponding to story drift ratios of around 8 to 11%. Permanent lateral roof displacements at the end of the record ranged from about 6 to 16 in. This level of permanent lateral displacement is difficult to repair. The displacement time histories for models 3BF1L, 3BF2L, and 3BF2LM, all of which included material models accounting for low-cycle fatigue, are similar. For models 3BF2LN and 3BF2LMN, which disregarded fatigue, the time history responses were similar, but they had smaller story drifts and residual story drifts then the other models. On the contrary, story drifts in the fatigue-sensitive models increased significantly once fracture occurred and had larger residual deformations. The strength response of the LS-DYNA model was decreased gradually; this is more similar to the OpenSees models that did not include fatigue material properties.

Due to the slight sag of the beam at the brace-to-beam intersection, the brace axial deformation time histories show that the tension braces tended to have smaller axial deformation than the compression braces (comparing the absolute values). Thus, the damage in the OpenSees models was greater in compression than in tension (see Figure 3.29).

Figure 3.30 shows the vertical displacement at the mid-span of the beams for different stories. Because the responses in the second and third stories were essentially elastic, the vertical displacement in these stories was relatively small. For models 3BF2LN and 3BF2LMN without fatigue-sensitive materials and for the LS-DYNA model, the peak mid-span vertical displacements were about 3.5 to 4 in., and the residual mid-span vertical displacements were about 1.5 to 3 in. For models 3BF1L, 3BF2L, and 3BF2LM, the peak mid-span vertical displacement was between 1.8 and 2.3 inches. The residual mid-span vertical displacements of OpenSees models with fatigue-sensitive materials were similar to those without fatigue materials, while the LS-DYNA model had the largest vertical residual displacement among all the models.

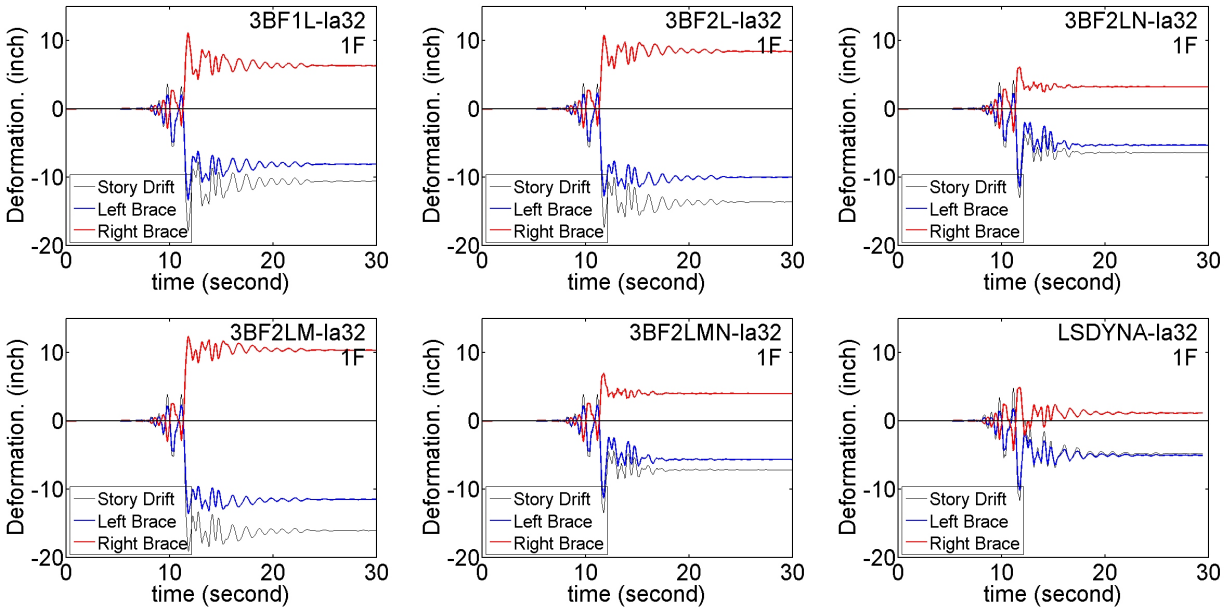

Figure 3.29 **Time history of story drift and brace axial deformation in the ground story due to LA32.**

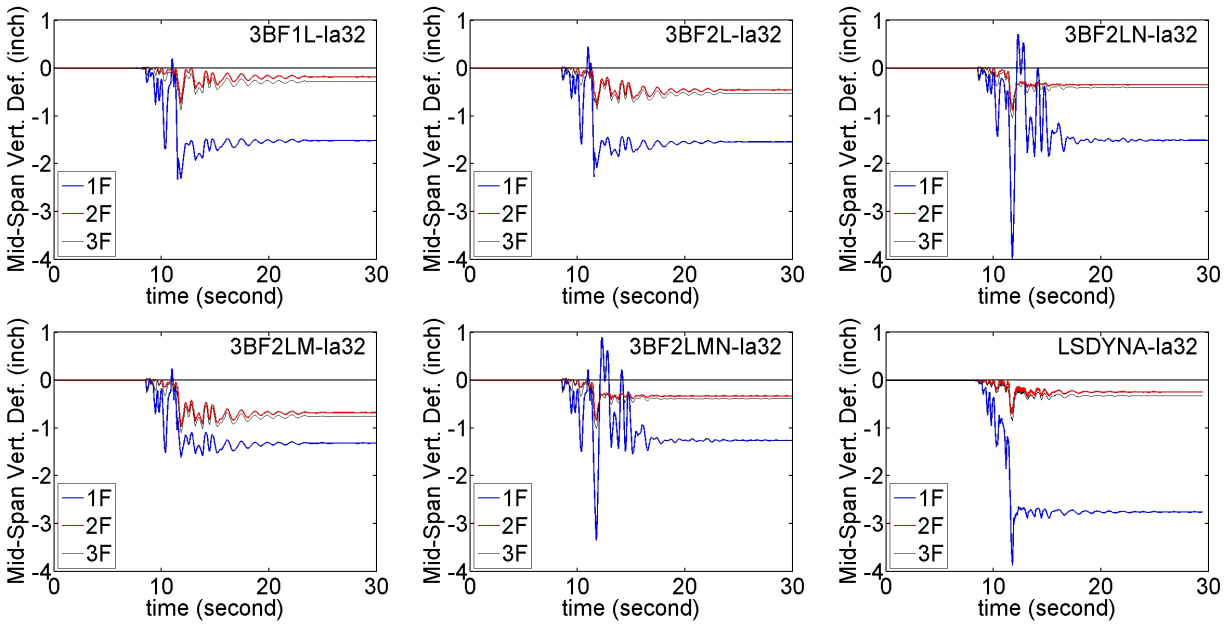

Figure 3.30 **Time history of vertical displacement at mid-span of beams on each level.**

The hysteresis loops of braces in the first story are depicted in Figure 3.31. The buckling and yielding behavior of all the models before initiation of fracture was similar. Models with the same damping type responded similarly; i.e., 3BF1L was similar to 3BF2L and 3BF2LN, while 3BF2LM was similar to 3BF2LMN. The OpenSees models with fatigue-sensitive material properties had their braces fracture at about the same time (although some variations exist, which reflect differences in other modeling parameters). Complete fracture of the braces in the first story did not occur for the LS-DYNA model, which might reflect the fact that the LS-DYNA model distributes yielding and damage throughout the structure to a greater degree compared to the OpenSees models.

The lateral drift–story shear hysteresis loops of each story are depicted in Figure 3.32, providing a direct comparison of the global behavior. Initially, all stories had similar drifts, but once a brace buckled, drifts tended to be concentrated in the bottom story, with only minor inelastic drifts in the second story. The third story remained nearly elastic during the excitation. The behavior of the OpenSees fiber models with material models including low-cycle fatigue was typified by fracture of the tension brace in the bottom level. The resulting vertical displacement at the mid-span of the second floor beam increased the story drift considerably compared to a story drift calculated from the brace elongation alone. The models with fractured braces tended to have greater residual drifts compared to models without fractured braces. The hysteretic responses showed that the strength and stiffness were reduced significantly after brace fracture occurred.

Although the braces in the bottom story fractured during record LA32, they did not fracture under some MCE ground motions, even if fatigue-sensitive material was included. In such cases, the hysteresis loops were more similar to those in models without fatigue, and the hysteresis behavior was more similar to that in the LS-DYNA simulation.

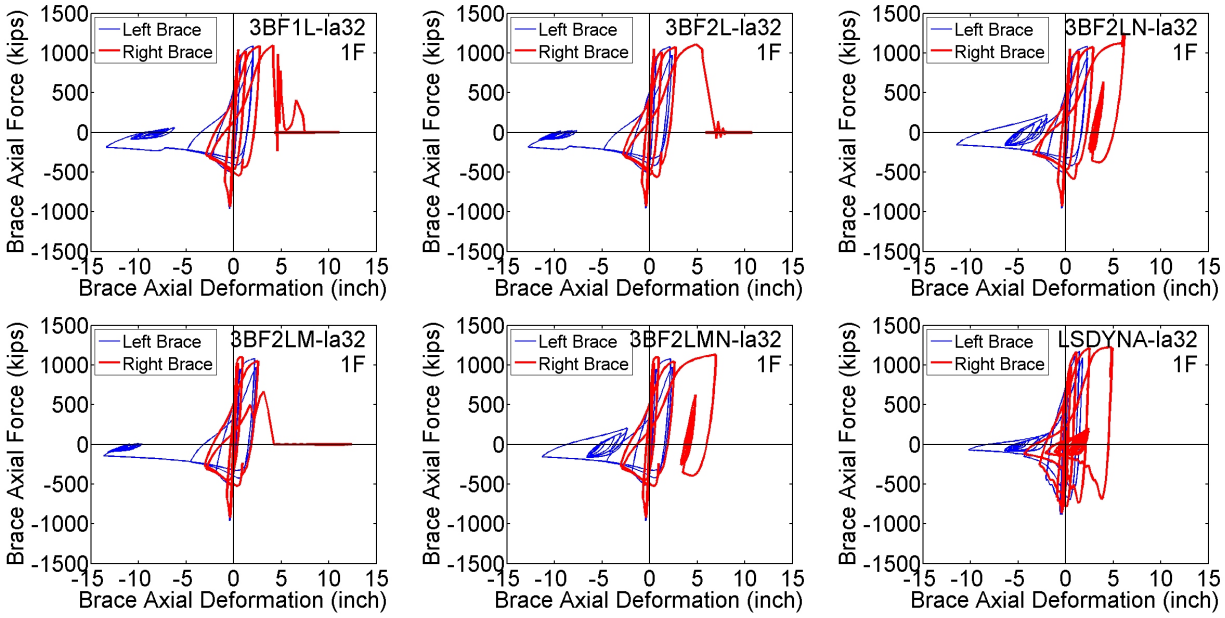

Figure 3.31 Relationship between axial force and axial deformation of braces on the first story due to LA32.

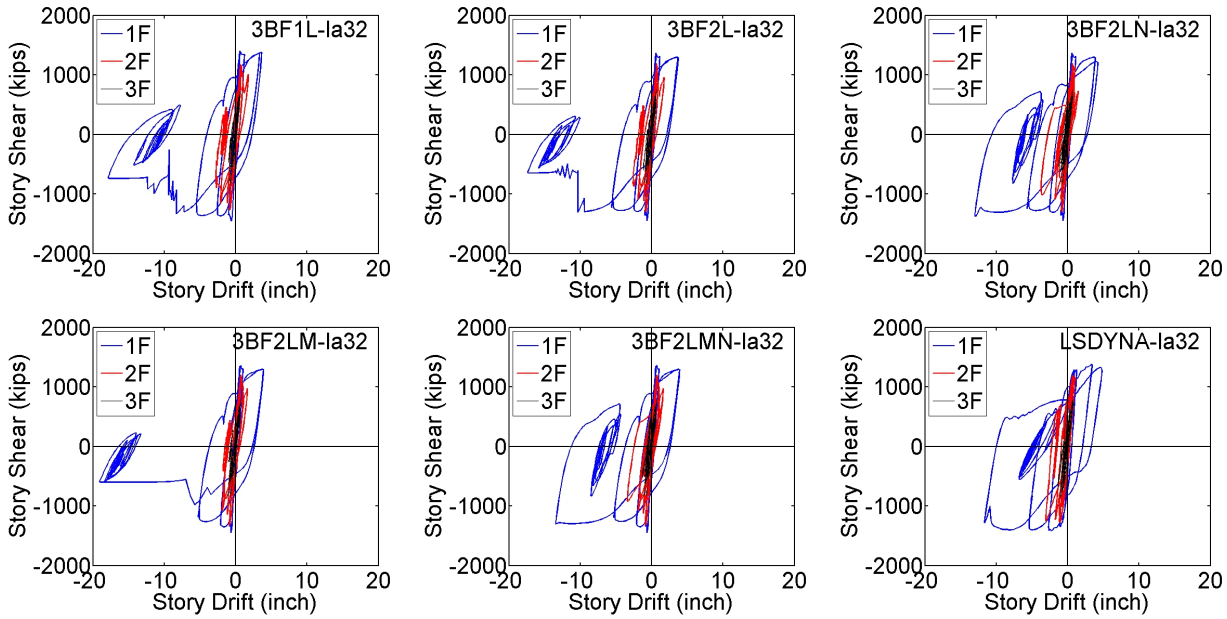

Figure 3.32 Relationship between story shear and story drift due to LA32.

In general, we investigated the effect of beam axial forces on response by comparing the responses of models with one and two leaning columns (models 3BF1L and 3BF2L); Figure 3.29 demonstrates that the braces fracture at different times and that response time histories show slight differences. The difference of peak story drift on the first story was less than 2%. The effect of low-cycle fatigue was investigated by comparing models 3BF2L with 3BF2LN and 3BF2LM with 3BF2LMN. The displacement time histories were different as well as the residual story strength after the braces fractured. The post-fracture stiffness was also different for different models. The damping effect was investigated by comparing 3BF2L with 3BF2LM and 3BF2LN with 3BF2LMN. The story drifts were similar for the mass-only and Rayleigh (mass and stiffness) damping models. Fracture of the braces had a greater impact on the responses of different models than the type of damping adopted in the models.

3.4.4.3 Statistical evaluation of story drift demands of Phase II models

Figures 3.33 through 3.37 show the relationship of peak story drift ratio to $S_{d,\text{Elastic}}$ for each record used in the analysis, where $S_{d,\text{Elastic}}$ is the elastic spectral displacement for the record used in the analysis at the fundamental period of the model being simulated. In these plots, DR1 is the peak story drift ratio of the first story for each record considered; DR2 is that of the second story; DR3 is that of the third story; DRave is the peak roof displacement divided by the total height of the model building (which is thus the average story drift ratio); and DRmax is the maximum story drift ratio occurring at any of the three stories. The ratio of DRmax/DRave is regarded as the index of the tendency of the system to form a soft story: the higher the ratio, the more concentrated the damage is in a single story.

Linear regression analyses were performed considering all of the results for a particular model in the lognormal form $\ln(DR) = b + m \cdot \ln(S_{d.\text{Elastic}})$. Table 3.8 lists the slope m and the intercept b of the regression for all the models, and σ^2 denotes the variance of the lognormal distribution of DRmax.

The regression parameters were so similar that the differences of m and b between each model were within 3%. Consequently, the regression lines plotted in the figures are also very similar. Although the trends are similar, several data points show large inelastic demands when $S_{d,\text{Elastic}}$ becomes large. For the case study, ground motion record LA32 is among the cases that produced demands larger than predicted by the regression relation. To account for this increased response at large $S_{d,\text{Elastic}}$ values, a nonlinear regression model may be more suitable for these structures. Improved results obtained using an intensity measure based on inelastic spectral displacement are presented later in this report.

Figure 3.33 compares regression analysis results for models 3BF1L and 3BF2L, which differ in the number of leaning columns. The data of DR1 shows more dispersion than DR2 and DR3, because the first story experienced more nonlinear deformation. The peak drifts on the first story contributed most of the maximum DR values, but the dispersion was slightly less for the DRmax values. The dispersion on the average DR was even smaller due to the less scattered data on DR2 and DR3. DRmax/DRave plots show that all the ratios were below 3.0, and most of them were below 2.0.

Table 3.8 Slope, intercept, and standard deviation of the regression relation of DRmax and $S_{d,\text{Elastic}}$ for all OpenSees models.

Model	*m*	*b*	σ^2
3BF1L	1.58	–5.78	1.08
3BF2L	1.55	–5.67	1.12
3BF2LN	1.53	–5.66	1.19
3BF2LM	1.56	–5.68	1.06
3BF2LMN	1.53	–5.62	1.19

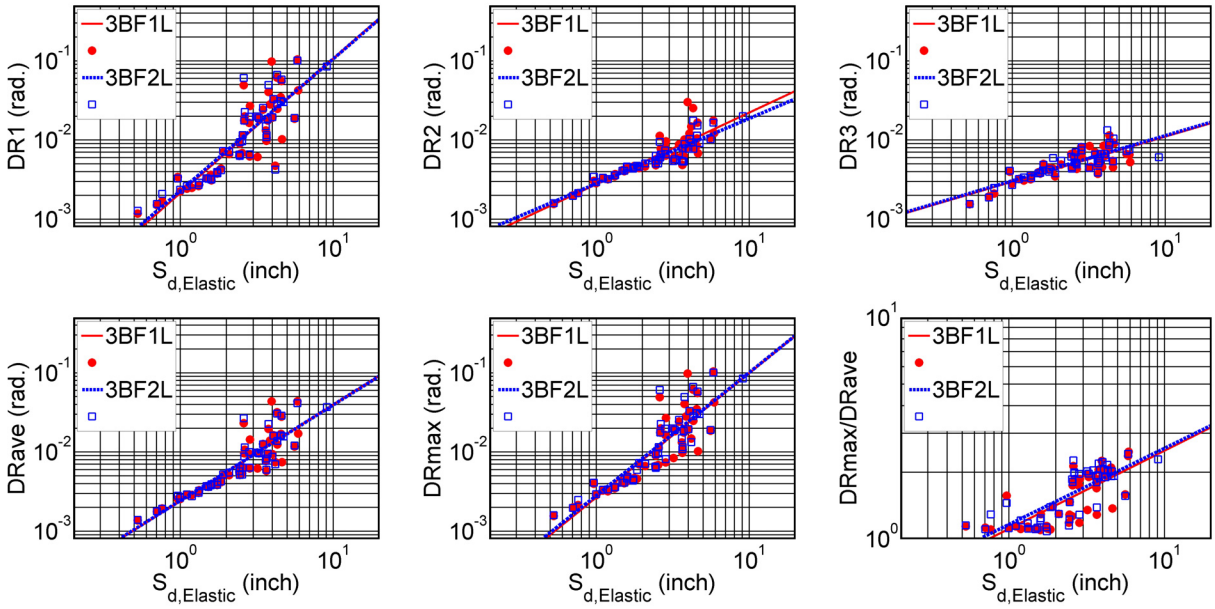

Figure 3.33 Comparison of story drift ratios between one-leaning-column model (3BF1L) and two-leaning-column model (3BF2L).

Table 3.9 Median expected EDPs corresponding to different hazard levels based on elastic displacement spectra.

EDPs	Hazard Level	3BF1L	3BF2L	3BF2LN	3BF2LM	3BF2LMN
DRmax (radian)	50/50	0.73%	0.78%	0.78%	0.79%	0.81%
	10/50	1.58%	1.64%	1.62%	1.66%	1.69%
	2/50	3.01%	3.10%	3.04%	3.14%	3.17%
DRave (radian)	50/50	0.52%	0.54%	0.54%	0.53%	0.55%
	10/50	0.96%	0.96%	0.97%	0.96%	0.99%
	2/50	1.57%	1.57%	1.60%	1.59%	1.63%
DRmax/DRave	50/50	1.39	1.46	1.44	1.47	1.48
	10/50	1.66	1.72	1.68	1.73	1.71
	2/50	1.92	1.97	1.90	1.98	1.94
Residual DR (radian)	50/50	0.04%	0.05%	0.05%	0.05%	0.05%
	10/50	0.24%	0.31%	0.22%	0.28%	0.23%
	2/50	1.06%	1.40%	0.77%	1.29%	0.89%

The EDPs predicted from these regression lines corresponding to different hazard levels are listed in Table 3.9. These were determined from the regression lines identified in Figures 3.33 to 3.37, and the values of $S_{d.\text{Elastic}}$ in Table 3.5 corresponding to the hazard spectra for the site and the computed fundamental period of the structure. For the most severe hazard level (the 2/50 or MCE-level event), the median expected maximum DR values were slightly over 3.0%. For the design-level event, the expected median maximum DR were over 1.5%. Using the story drift index at the onset of brace buckling (about 0.3%) as the yield displacement of the structure, these maximum DRs correspond to story drift ductility of more than 10 and 5 for the MCE- and design-level events, respectively.

Note that for all the models, the expected median maximum story drift ratio at the service-level event (50/50, or 50% probability of exceedance in 50 years) exceeded the drift that will cause a brace to buckle (about 0.3%). Thus, following a frequent (service-level) earthquake, the analyses show that at least one brace is likely to buckle, and it will be necessary to replace one or more braces and repair nonstructural damage in the adjacent elements.

Figures 3.34 and 3.35 compare responses for the different types of damping for models with and without fatigue-sensitive materials. Figures 3.36 and 3.37 compare the effect of fatigue-sensitive materials. Statistically, the results exhibit very little difference. Although the case study of the response to the LA32 record indicated that responses of different models could differ significantly, regression curves based on responses to many records were quite similar.

For the application of performance-based design, a relation was developed from the regression analyses that included the probability that a value of DRmax would be exceeded for a given value of $S_{d.\text{Elastic}}$. In Figure 3.38, fragility curves are presented for maximum story drifts ratios of 0.3% and 2.5%. These values are simplified proxies for the initiation of brace buckling and the maximum drift accepted by standard code design methods for a Design Basis Event (ASCE/SEI 7-05).

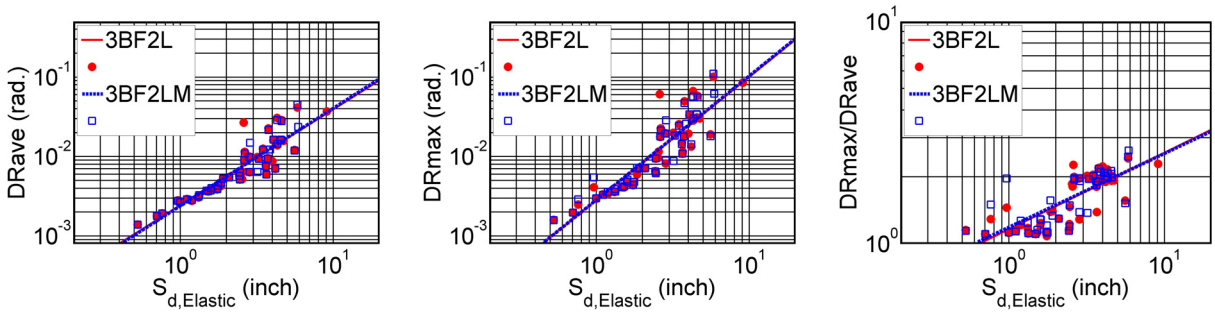

Figure 3.34 **Comparison of story drift ratios between Rayleigh damping model (3BF2L) and mass-proportional model (3BF2LM).**

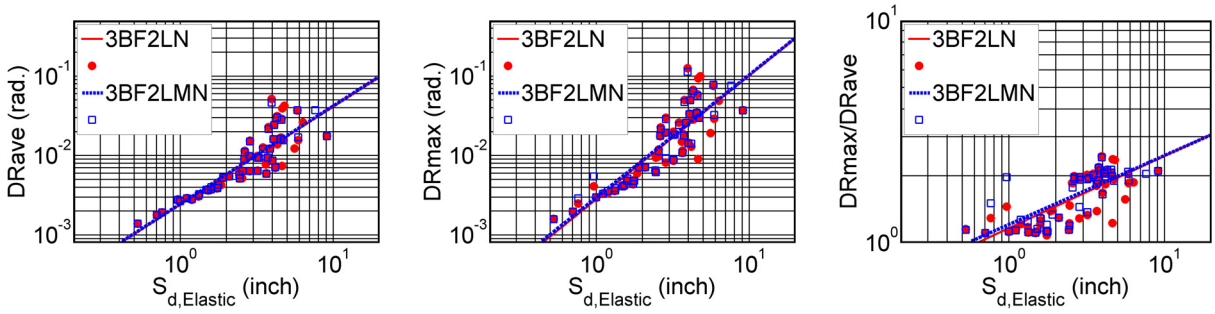

Figure 3.35 **Comparison of story drift ratios between Rayleigh damping model (3BF2LN) and mass-proportional model (3BF2LMN) without braces fatigue.**

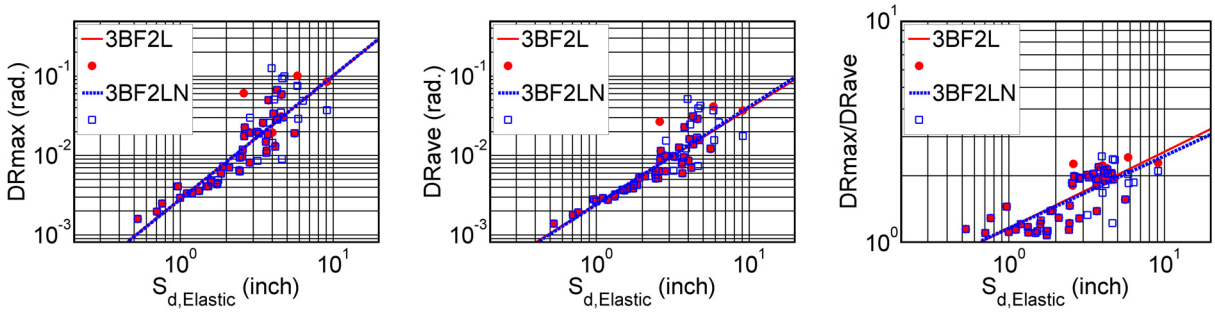

Figure 3.36 **Comparison of story drift ratios between fatigue model (3BF2L) and non-fatigue model (3BF2LN) with Rayleigh damping.**

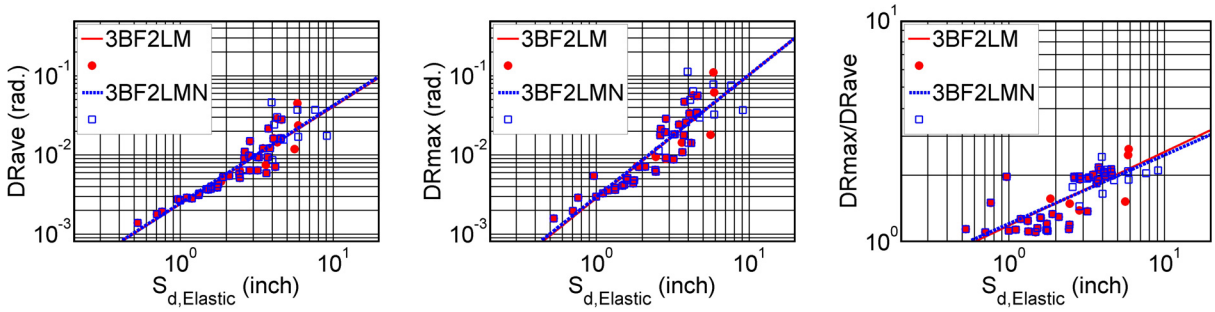

Figure 3.37 Comparison of story drift ratios between fatigue model (3BF2LM) and non-fatigue model (3BF2LMN) with mass-proportional damping.

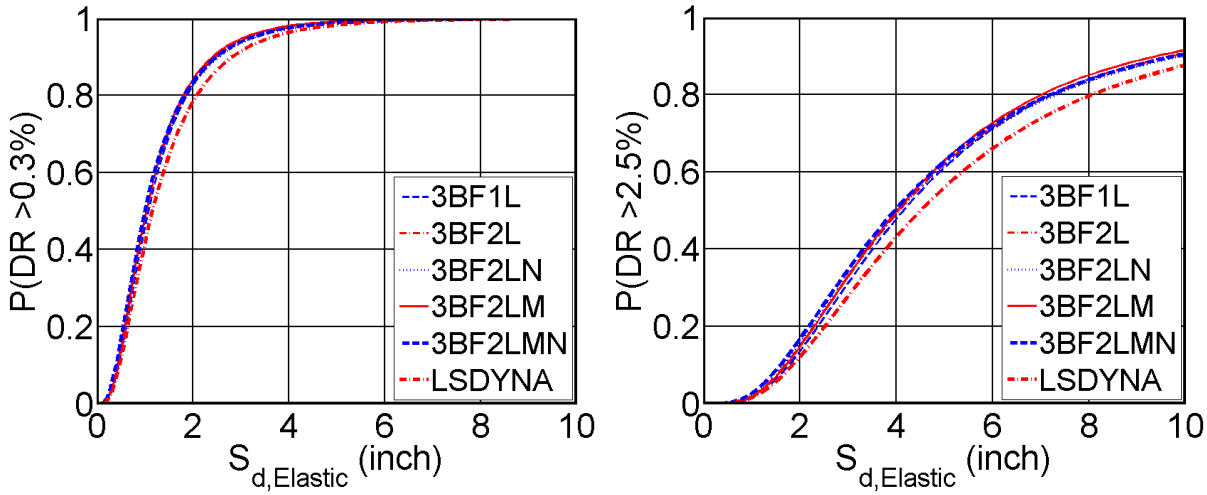

Figure 3.38 Probability of exceeding critical drifts for different models.

Obtained from Figure 3.38, Table 3.10 lists the probability that the maximum story drift ratio will exceed 0.3% and 2.5% for earthquakes with a given probability of exceedance for each OpenSees model. For the MCE-level event, the OpenSees models all have more than a 57% probability of developing maximum story drifts greater than 2.5%. For the design-level event, these probabilities drop to 33%. Considering the service-level event, the models have more than 80% probability of buckling a brace on one or more stories. Obviously, to minimize significant local nonstructural damage during service-level events, the likely motion of the brace in the buckled configuration must be considered, along with the possibility of replacing braces following such events due to permanent lateral offsets.

Figure 3.39 illustrates the displacement time histories of different models. Among all analyses for the 60 ground motions, record LA32 shows the peak value of maximum DR. LA28 and LA40 show the maximum positive and negative difference between OpenSees model 3BF2L and the LS-DYNA model.

In most analyses under the same ground motion, the OpenSees models tended to have larger story drift because of the characteristics of the low-cycle fatigue and brace models used, as demonstrated in Figure 3.39 for the LA32 (left) and LA28 (middle) time histories. The differences between the OpenSees and LS-DYNA models were evident at the peak response, leading to different residual floor drift. Given that, it is also possible that the peak floor drift

predicted by LS-DYNA might be larger than that of OpenSees if the peak response is less severe, as shown for the LA40 time history.

Table 3.10 Probability of exceeding critical DR values for different models based on elastic displacement spectra.

Model		Hazard level		
		50% in 50 yrs	10% in 50 yrs	2% in 50 yrs
3BF1L, T = 0.50 sec	P(DR > 0.3%)	80.4%	94.6%	98.7%
	P(DR > 2.5%)	11.7%	33.0%	57.1%
3BF2L, T = 0.49 sec	P(DR > 0.3%)	81.8%	94.6%	98.6%
	P(DR > 2.5%)	13.6%	34.5%	58.0%
3BF2LN, T = 0.49 sec	P(DR > 0.3%)	81.0%	93.9%	98.3%
	P(DR > 2.5%)	14.4%	34.6%	57.1%
3BF2LM, T = 0.49 sec	P(DR > 0.3%)	82.4%	95.1%	98.8%
	P(DR > 2.5%)	13.1%	34.5%	58.8%
3BF2LMN, T = 0.49 sec	P(DR > 0.3%)	81.9%	94.3%	98.5%
	P(DR > 2.5%)	15.2%	36.0%	58.6%

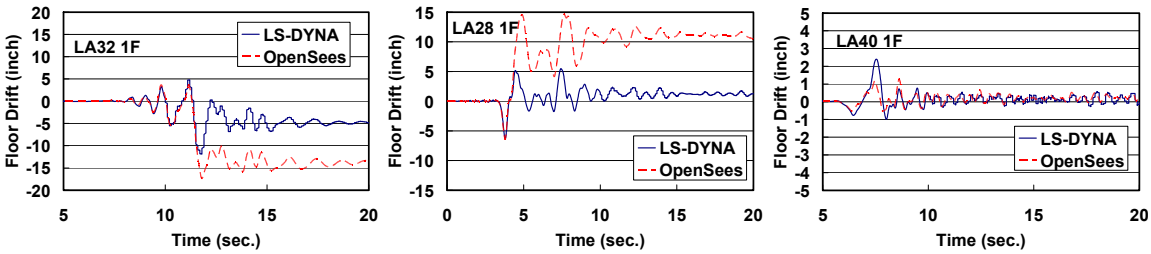

Figure 3.39 Floor displacement time histories of OpenSees model 3BF2L and LS-DYNA model under three SAC time histories.

3.4.4.4 Statistical evaluation of residual story drift demands of Phase II models

Another response parameter of interest is the residual displacement in a structure, which is used to determine whether it is feasible or cost-effective to repair a structure after an earthquake. Figures 3.40 to 3.44 are similar to those presented in Figures 3.33 to 3.37, except the vertical axes are related to the maximum residual story drift remaining at the end of the earthquake. Plots are presented for the roof residual displacement (left), the peak residual drift index at any floor (middle), and the ratio of the peak residual displacement to the maximum displacement at that story (right). The points on the plots are data for individual records. Two lines are superimposed for the plot of maximum residual drift index, one representing the median linear regression analysis result for the residual story drift ratio (Res. DR) and the other representing the previously reported maximum story drift ratio (DRmax).

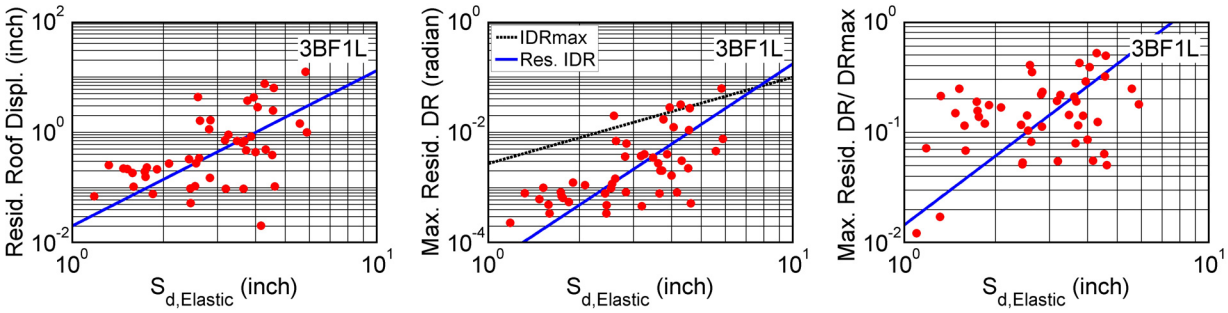

Figure 3.40 Relationship between residual deformation and $S_{d,Elastic}$ of model 3BF1L.

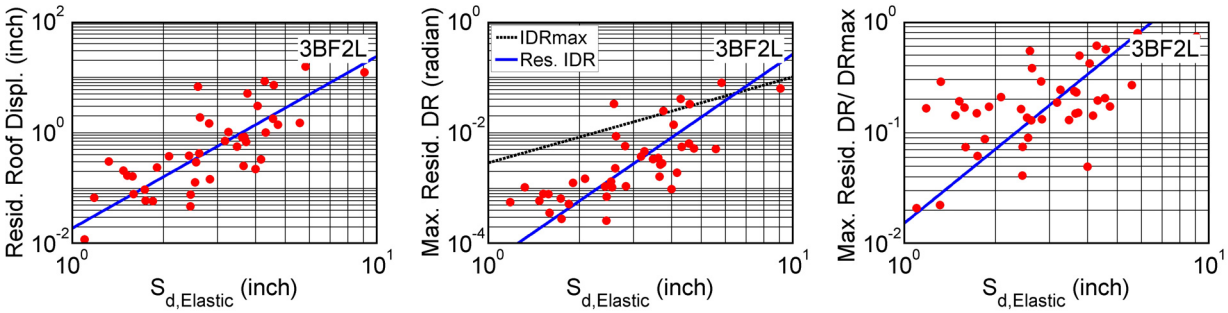

Figure 3.41 Relationship between residual deformation and $S_{d,Elastic}$ of model 3BF2L.

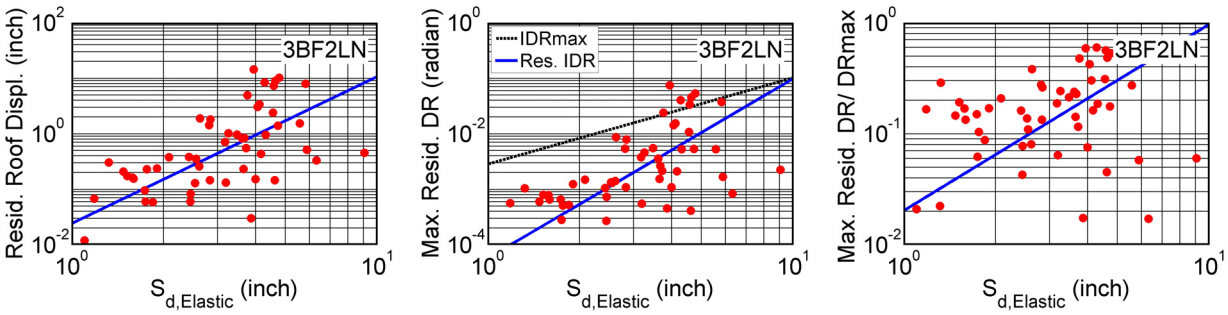

Figure 3.42 Relationship between residual deformation and $S_{d,Elastic}$ of model 3BF2LN.

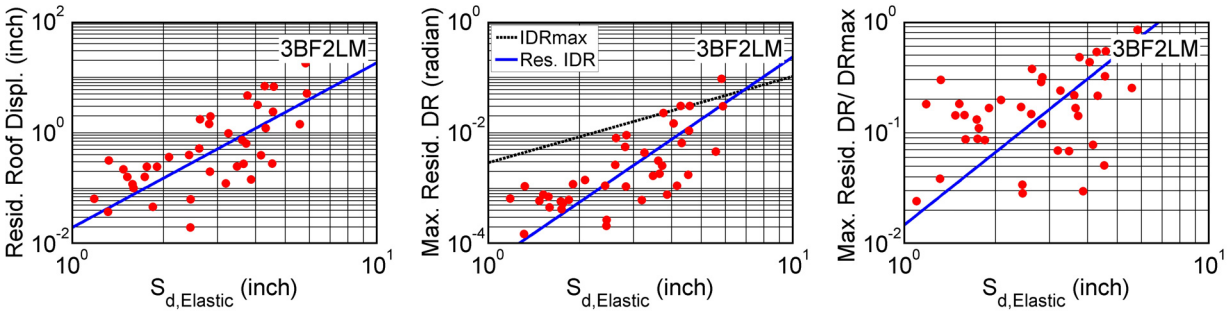

Figure 3.43 Relationship between residual deformation and $S_{d,Elastic}$ of model 3BF2LM.

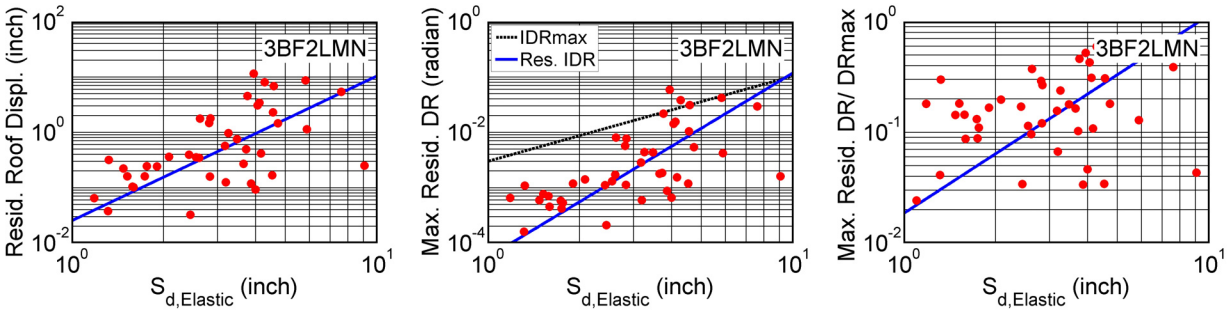

Figure 3.44 Relationship between residual deformation and $S_{d,\text{Elastic}}$ of model 3BF2LMN.

In Figures 3.40 to 3.44 it is obvious that there is tremendous scatter in the peak story residual displacements. In some cases, the residual displacement significantly exceeded the median expected maximum displacement at a particular value of $S_{d.\text{Elastic}}$, while in other cases the residual displacement was quite small.

In the plots of maximum residual DR/maximum DR, the residual displacement became a more significant fraction of the peak story drift for larger intensity shaking. The models without fatigue included tended to have smaller residual displacements, although the maximum and average story drifts do not show much difference among all the models.

For the models in which the braces may fracture, considering the spectral displacement corresponding to this structure at the MCE and design levels, the expected median maximum residual story drifts listed in Table 3.9 were about 1.25% and 0.28%, respectively. For the models without fatigue incorporated, the expected median maximum residual story drifts were reduced to about 0.83% and 0.22% for the MCE- and design-level events, respectively.

3.4.4.5 Inelastic spectrum displacement as ground motion intensity measure

To investigate whether the substantial dispersion of the results plotted in Figures 3.33 through 3.44 can be reduced, we considered alternative ground motion intensity measures. Results are shown below for the case where an inelastic spectrum displacement was used as the ground motion intensity measure.

The inelastic spectrum displacement was based on the first mode characteristics of the model building and generated from the software application *BiSpec* [Hachem 2005]. The strength and stiffness properties of the equivalent single-degree-of-freedom system were based on the static pushover analyses results (Figure 3.28) using the procedure outlined by Chopra [2006]. A bilinear model was used to represent the hysteretic behavior of the structure. Inelastic displacements were computed for each of the 60 ground motions used in the study, and the peak displacements $S_{d,\text{Inel}}$ were used instead of $S_{d,\text{Elastic}}$ to plot the peak EDPs.

As can be seen in Figure 3.45, the scatter of the results for peak DR was significantly reduced compared to previously plotted cases using $S_{d,\text{Elastic}}$. Table 3.11 presents the R-square of the fit of the DRmax–$S_{d,\text{Inel}}$ relation. The inelastic spectrum displacement substantially improved the dispersion of the DRmax–$S_{d,\text{Inel}}$ relation, and the tendency of the DR to exceed the regression curve for high-intensity shaking was no longer apparent. It appears that this discrepancy may be thus associated with the "energy preserved" tendency that has been noted for single-degree-of-freedom inelastic structures with relatively short periods [Chopra 2006]. This is captured by the

nonlinear analysis for the single-degree-of-freedom systems used to obtain $S_{d,\text{Inel}}$. This may not be appropriate for systems for systems having greater contributions of higher modes to response or for systems with longer periods.

Table 3.12 shows the expected EDPs based on the inelastic displacement spectra. The values for the service-level and design-level events are generally smaller in the EDP–$S_{d,\text{Inel}}$ relation than in the EDP–$S_{d,\text{Elastic}}$ relation (see Table 3.9); however, for the MCE-level event, the expected EDPs are larger in the EDP–$S_{d,\text{Inel}}$ relation than in the EDP–$S_{d,\text{Elastic}}$ relation.

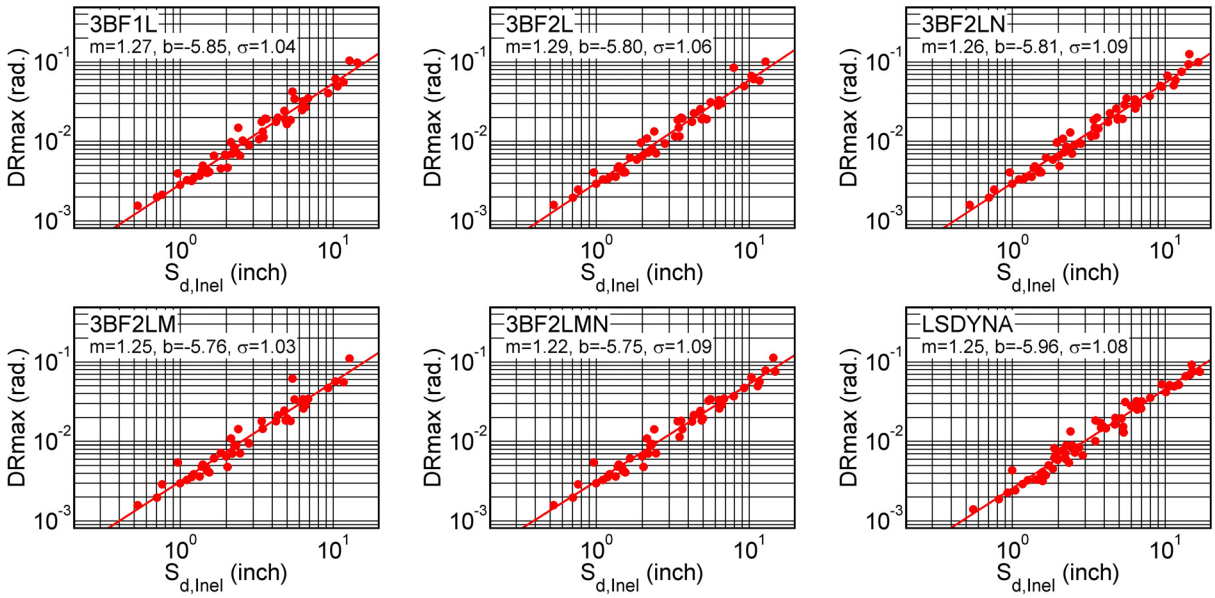

Figure 3.45 Relationship between maximum story drift ratio and inelastic spectrum displacement for different models.

Table 3.11 *R*-square of the fit of DRmax and S_d relation for different models.

Model	3BF1L	3BF2L	3BF2LN	3BF2LM	3BF2LMN	LS-DYNA
R-square of DRmax vs. $S_{d,\text{Elastic}}$ relation	0.7531	0.8021	0.7473	0.8246	0.8059	0.7577
R-square of DRmax vs. $S_{d,\text{Inel}}$ relation	0.9588	0.9618	0.9728	0.9438	0.9662	0.9642

A comparison of different models with intensity measures based on elastic and inelastic displacement spectra is shown in Figure 3.46. The period of the LS-DYNA model is 0.52 sec while that of OpenSees model is 0.5 sec; the values of S_d for the OpenSees and LS-DYNA models are virtually the same. The difference in expected DRmax values for OpenSees and LS-DYNA models is less than 10%.

Table 3.12 Median expected engineering demand parameters corresponding to different hazard levels based on inelastic displacement spectra.

EDPs	Hazard Level	3BF1L	3BF2L	3BF2LN	3BF2LM	3BF2LMN
DRmax (radian)	50/50	0.66%	0.69%	0.68%	0.70%	0.70%
	10/50	1.42%	1.52%	1.45%	1.50%	1.46%
	2/50	4.72%	5.15%	4.80%	4.91%	4.67%
DRave (radian)	50/50	0.48%	0.49%	0.49%	0.49%	0.49%
	10/50	0.88%	0.90%	0.89%	0.89%	0.88%
	2/50	2.24%	2.33%	2.27%	2.26%	2.22%
DRmax/DRave	50/50	1.36	1.42	1.39	1.44	1.43
	10/50	1.62	1.69	1.64	1.69	1.66
	2/50	2.11	2.21	2.11	2.18	2.10
Residual DR (radian)	50/50	0.03%	0.04%	0.04%	0.04%	0.04%
	10/50	0.18%	0.24%	0.17%	0.21%	0.17%
	2/50	2.44%	3.97%	1.79%	3.09%	1.87%

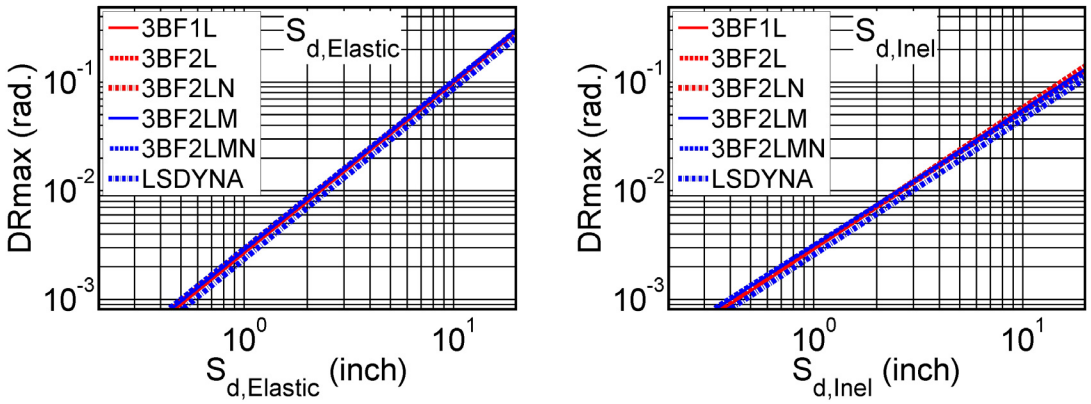

Figure 3.46 Trend lines of DRmax and S_d for different models.

3.5 SUMMARY

Analytical studies of a 3-story SCBF building were conducted using fiber-based models from the computational platform OpenSees and using shell elements from the finite-element software program LS-DYNA. Analytical results of each model were interpreted and compared in terms of nonlinear static pushover analyses, a case study under a single earthquake record, and a probabilistic analysis of results using 60 ground motions representative of different hazard levels.

In the Phase I analysis, the force-based beam-column element was recommended to better estimate the nonlinear responses of the 3-story double-story X-braced frame. In addition, a relatively small time step was employed to improve the accuracy of the results and the convergence of the analysis. An adequate working point at the column base should be defined so

that the taller first story may be included in the numerical model and reflect the more realistic structural behavior.

In the Phase II analysis, the pushover analysis showed that the braces in the ground story began to buckle globally at a story drift ratio of about 0.3% in both the OpenSees and LS-DYNA models. The LS-DYNA model, being more sensitive in capturing localized stress concentrations and local buckling, showed a more gradual change in strength before and after reaching the peak strength. The OpenSees fiber model exhibited a sudden drop in strength at the initiation of buckling or fracture. The LS-DYNA model suggested an ultimate failure mode that is different than the fiber models in OpenSees. Both identified a soft first-story response, but OpenSees suggested a failure by severe buckling of the compression brace and fracture of the tension brace. The shell element model in LS-DYNA suggested that final failure is associated with fracture in the column at the top of the first-story tension-side column, and in-plane deformation related fracture of the brace-to-gusset plate connection at the bottom of the tension brace.

The case study of structural behavior under ground motion record LA32 showed that adding low-cycle fatigue to the OpenSees fiber models resulted in larger story drifts (for records where a brace fractures) and led to larger residual story drifts. The vertical displacement at mid-span of beams predicted results in the tension braces having smaller axial deformations than the compression braces. In OpenSees models with fatigue-sensitive materials, when the braces fractured, the overall strength and stiffness of the structure were reduced after the fracture. The drift demands increased significantly whenever fracture occurred. Comparing the effects of beam axial forces, fatigue materials, and damping types, we found that material properties that fail in low-cycle fatigue affected the response more so than in the case of the other phenomena.

The OpenSees analyses suggest that as the number of cases where fracture occurs is small on a statistical basis, fatigue-sensitive materials do not change the overall response significantly. However, when examining the response to a single ground motion, fracture of a brace has an important impact on structural response. OpenSees results show that the expected median maximum story drift ratio at the service-level event (about 0.75%) exceeded the drift needed to cause buckling of a brace (about 0.3%). OpenSees models predicted that for this hazard level, there is more than 80% probability of buckling a brace at one or more stories. For a 2%-in-50-year hazard level, the OpenSees models had more than a 57% probability of developing maximum story drifts greater than 2.5%. For the design-level event, the probability dropped to 33%.

Results for this short-period SCBF system demonstrate that using inelastic spectral displacements instead of those based on elastic analysis substantially reduced dispersion of the results, especially for large-intensity events. The predicted story drifts for maximum considered hazard levels increased, however, when inelastic spectral displacements were used as the intensity measure. Additional research is needed on this topic.

OpenSees fiber models suggest that residual displacement becomes a more significant fraction of the peak story drift for larger intensity shaking. However, according to observations from the analyses, the relationship between residual displacements and ground motion durations did not show clear trends. The effect of fatigue-sensitive materials was more important for the residual displacement than for the peak displacement. For the OpenSees models that employed fatigue-sensitive materials, the expected median maximum residual story drifts were about 1.25% and 0.28% for the MCE-level and design-level events, respectively.

Comparison of inelastic behavior predicted by fiber models with OpenSees and shell elements with LS-DYNA for individual ground motion records shows that the difference between beam-element and shell-element models can be significant for some ground motion excitations. For the ground motions used in this study, shell-element models in LS-DYNA predicted smaller maximum story drift and residual story drift, but larger maximum vertical displacement at mid-span of the beam and stiffness reduction. Moreover, the ultimate failure modes may differ significantly for the two models. On the other hand, from a statistical perspective (when inelastic spectrum displacement is used as the intensity measure), the difference between OpenSees beam-element model and LS-DYNA shell-element model results was less than the dispersion for different ground motions by the same model. For the case considered here, if inelastic spectrum displacements are used to predict the structural responses, corresponding inelastic properties can be obtained from analysis using beam- or shell-element models, resulting in equally accurate median response prediction.

In general, the parameters in Phase II models did not result in any statistically significant differences. For the final models considered in Chapter 4, the one-leaning column and two-leaning column options were used and the fatigue-sensitive material was included. Because the scatter in statistical data was reduced by using the inelastic spectrum displacement, the probability relation was generated based on inelastic spectrum displacement.

4 Performance Evaluation of Braced Frame Buildings

We next conducted a detailed performance evaluation for 3-story braced frame buildings. The SCBF buildings were designed according to both older and current codes to investigate the impact of code change on structural response. A BRBF building was also analyzed to evaluate the advantages and disadvantages of different braced frame systems. To improve the system performance of the SCBF, the response reduction factor for design using code approaches was reduced to limit the demands in the building; we also investigated the effectiveness of this strategy. This chapter compares statistically the drift demands of four structures based on the numerical models developed and evaluated in Chapter 3.

4.1 DESIGN CRITERIA

We investigated seismic responses of 3-story tall steel buildings with lateral earthquake-load resistance provided by SCBFs or BRBFs located on the perimeter of the building (Figure 4.1). These buildings were designed by others [Sabelli 2000, DASSE 2007]. Model A was designed in conformance with the provisions of the 1997 NEHRP seismic design provisions, and Model B and Model C were designed to comply with the provisions of ASCE/SEI 7-05. Model B is the same model building as discussed in Chapter 3. The importance factor and redundancy factor were assumed to be unity for all designs. Table 4.1 lists some of the principal attributes of the structures and the key parameters used in the seismic design.

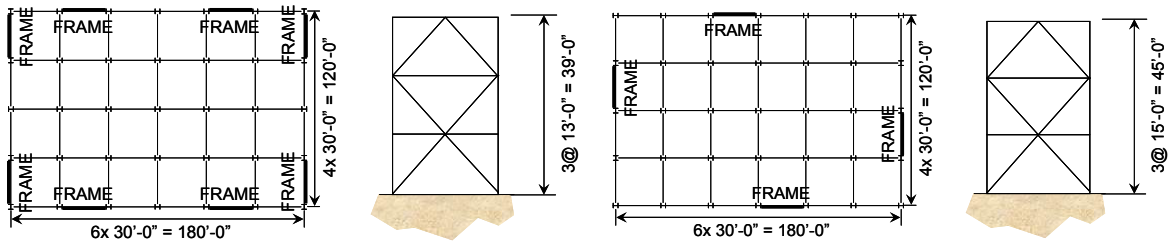

(a) Model A (b) Model B and C

Figure 4.1 Model building floor plan and elevation.

Table 4.1 Design parameters of model buildings.

Model	A	B (SCBF), C (BRBF)
Code	1997 NEHRP	ASCE/SEI 7-05
Building location	Los Angeles, CA	Los Angeles, CA
Seismic design category	D	D
Occupancy category	II (Office)	II (Office)
Importance factor	1.0	1.0
Short period spectral acceleration, Ss	2.09 g	2.2 g
1 sec period spectral acceleration, S1	0.77 g	0.74 g
Fa	1.0	1.0
Fv	1.5	1.5
R	6	6 (SCBF), 8 (BRBF)
Design base shear	0.23W	0.24W (SCBF), 0.13W (BRBF)

4.2 MODEL BUILDINGS

Table 4.2 lists the member sizes used in the models. Model A represents the typical SCBF bent designed based on 1997 NEHRP provisions, while Models B and C represent SCBF and BRBF systems designed based on ASCE/SEI 7-05. The configuration of lateral load-resisting frames were also different, with Model A having twice as many lateral load-resisting bents. The story height for Model A was 13 feet, whereas that for Models B and C was 15 feet. Model B is the same building as modeled in Section 3.4.

Table 4.2 Member sizes.

Floor	Model	Braced frame columns	Braced frame beams	Brace size
Roof	A	W12×96	W18×46	HSS 6×6×3/8
	B	W14×176	W36×210	HSS 10.0×0.375
	C	W14×132	W24×76	4 $in.^2$
3rd	A	W12×96	W27×84	HSS 8×8×1/2
	B	W14×176	W30×116	HSS 11.25×0.50
	C	W14×132	W24×76	6 $in.^2$
2nd	A	W12×96	W30×90	HSS 8×8×1/2
	B	W14×176	W27×84	HSS 12.5×0.50
	C	W14×132	W24×76	7.5 $in.^2$

The roof beam of Model A was particularly light compared to the lower two floor beams because the 1997 AISC Seismic Provisions [AISC 1997] contain an exception to the normal strong beam design requirement at the roof of chevron SCBF systems. The beams are typically designed to account for the unbalanced load produced by the tension and compression braces (described in Section 3.4). According to 1997 AISC seismic provisions, this provision was not required for the roof, so the roof beam was significantly smaller than at the other levels. In contrast, the roof beam of Model B is considerably heavier than the second and third floor

girders. This is because the unbalanced loads induced from the buckling of braces on the top story were considered in accordance with the 2005 AISC Seismic Provisions [AISC 2005]. The tension force used to compute the unbalanced load on the beam was based on $R_y P_y$ instead of P_y, and the unbalance loads in the lower two stories were small. In Model C, the member sizes are typically smaller because of the greater R value, the reduced brace unbalanced forces, and the longer fundamental period and therefore smaller design acceleration.

Table 4.3 Member sizes.

Floor	Model	Braced frame columns	Braced frame beams	Brace size
Roof	A	W12×96	W18×46	HSS 6×6×3/8
	B	W14×176	W36×210	HSS 10.0×0.375
	C	W14×132	W24×76	4 in.^{2}
3rd	A	W12×96	W27×84	HSS 8×8×1/2
	B	W14×176	W30×116	HSS 11.25×0.50
	C	W14×132	W24×76	6 in.^{2}
2nd	A	W12×96	W30×90	HSS 8×8×1/2
	B	W14×176	W27×84	HSS 12.5×0.50
	C	W14×132	W24×76	7.5 in.^{2}

4.3 OPENSEES NUMERICAL MODELS

Four model buildings, designated 3AF, 3BF, $3BF_3$, and 3CF, were analyzed and discussed. The notation used for the model names is listed in Table 4.3. All the beams were considered to be rigidly connected to the columns in all models, including the beams with braces connected in the middle span and in the ends. Model $3BF_3$ was similar to Model 3BF, except twice as many braced bents were used, thus a effective force reduction factor R of 3 (rather than 6) was used for model $3BF_3$; therefore, the member sizes of model $3BF_3$ were the same as those of model 3BF, but the effective seismic mass of model $3BF_3$ was half that of model 3BF. Model 3CF was also similar to model 3BF except for the use of buckling-restrained braces. The OpenSees modeling parameters of model 3CF were essentially the same as those for the SCBF models, except for the modeling of the braces. Adopting the fatigue model, model 3CF was modeled to conform to the code requirement on the ductility capacity for testing of braces. (The BRBs were required to achieve a cumulative inelastic axial deformation of at least 200 times the yield deformation.) Fracture occurred when the fatigue life in BRBs was exhausted. Compared to the SCBF model, the modeling of braces in BRBFs was more straightforward because there was no need to apply the initial camber to the BRBs. Only one force-based nonlinear beam-column element was used for each BRB. The modeling properties were calibrated from test data (BRBs had the cyclic deformation capacity conforming to the code minimal requirement). Rigid end zones were used to increase the stiffness, which was computed using only the steel core, to get more accurate stiffness of BRBs that accounted for the stiffness contribution from tapered and connection areas of an actual BRB.

Table 4.4 Model names.

Abbreviation	Denotation
A	Double-story X SCBF designed to comply with 1997 NEHRP
B	Double-story X SCBF designed to comply with ASCE/SEI 7-05
C	Double-story X BRBF designed to comply with ASCE/SEI 7-05
F	Model building with fully constrained beam-column connections
Subscript 3	Model building designed with R = 3 instead of R = 6 for SCBF

4.4 DESIGN SPECTRA

The seismic spectra considered in the design of the three model buildings are shown in Figure 4.2. The spectra are quite similar, although in the constant amplified acceleration range, the ASCE/SEI 7-05 spectrum is slightly larger than that in the 1997 NEHRP provisions.

The SAC ground motion suite that is used to conduct nonlinear dynamic analysis is the same as the suite described and used in Chapter 3. The medians of the pseudo-spectral acceleration (S_a) and spectral displacement (S_d) corresponding to a particular hazard level are shown in Figure 4.2. The median elastic spectral displacements corresponding to the fundamental period of the various models for the three hazard levels considered are summarized in Table 4.4.

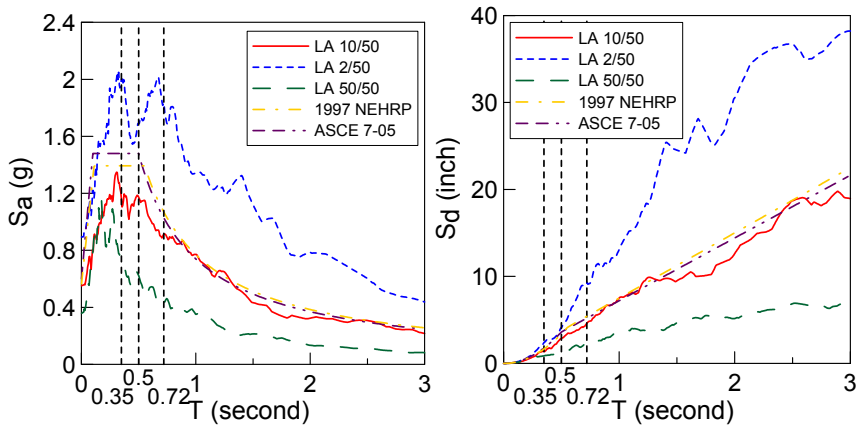

Figure 4.2 Response spectra.

Table 4.5 Median elastic spectral displacement $S_{d,\text{Elastic}}$ (in.).

Model	Hazard level		
	50% in 50 yrs	10% in 50 yrs	2% in 50 yrs
3AF, T_1 = 0.36 sec	1.12	1.63	2.44
3BF, T_1 = 0.49 sec	1.70	2.74	4.13
$3BF_3$, T_1 = 0.35 sec	1.07	1.56	2.30
3CF, T_1 = 0.72 sec	2.86	4.67	9.31

4.5 STATISTICAL EVALUATION OF STORY DRIFT DEMANDS

4.5.1 Story Drift Ratio

Figure 4.3 compares the responses of structures (models 3AF and 3BF) that were designed under different design codes. The regression lines of the story drift ratios in the first story (DR1) were similar for models 3AF and 3BF. For the second story (DR2), the regression curve of model 3BF was slightly steeper than that of model 3AF. In the plot of DRave, the slopes of both models were similar but the regression curve of 3BF fell below that of 3AF. Similar observations were noted in the plot of DRmax, but the regression curves were more parallel. The data in the DRmax/DRave plot were less scattered for model 3BF, with the ratios mostly less than 3.0.

While the trend lines offer a general comparison regardless of the intensity of the ground motions, the comparison of the EDPs with respect to different hazard levels should take into account the difference of the fundamental periods. As shown in Table 4.5, model 3BF has larger maximum DR than model 3AF for all three hazard levels; in particular, for the MCE-level event the maximum DR of 3BF was almost twice that of 3AF. This difference is primarily due to the longer period of 3BF and also the resulting larger $S_{d,\text{Inel}}$. Nonetheless, for the MCE-level event the soft-story index (DRmax/DRave) of 3BF was only slightly greater than that of 3AF. For the service-level event, the soft-story index of 3BF was smaller than that of 3AF. The weaker roof beam in 3AF may contribute to this difference.

Figure 4.4 compares results for models 3BF and $3BF_3$ for different hazard levels corresponding to the inelastic displacement spectra. Model $3BF_3$ was twice as stiff and strong as model 3BF. Thus, the fundamental period and spectrum displacement for model $3BF_3$ are significantly less than those for model 3BF (see Table 4.4). The regression curves at all levels (except for the top story)—the average DR and maximum DR—were almost identical for models 3BF and $3BF_3$. In the DRmax/DRave plot, the regression curves of the two models are similar, but because the spectrum displacement of model $3BF_3$ is smaller, the tendency to form a soft story is actually reduced. The median story drift ratios listed in Table 4.5 show that reducing the R value decreases the drift demand of SCBF. In the service-level event, the maximum story drift ratio is about 0.3%, and the braces may not buckle at this hazard level. For the other hazard levels, the drift demand is lower and therefore the deformation demand of braces is smaller.

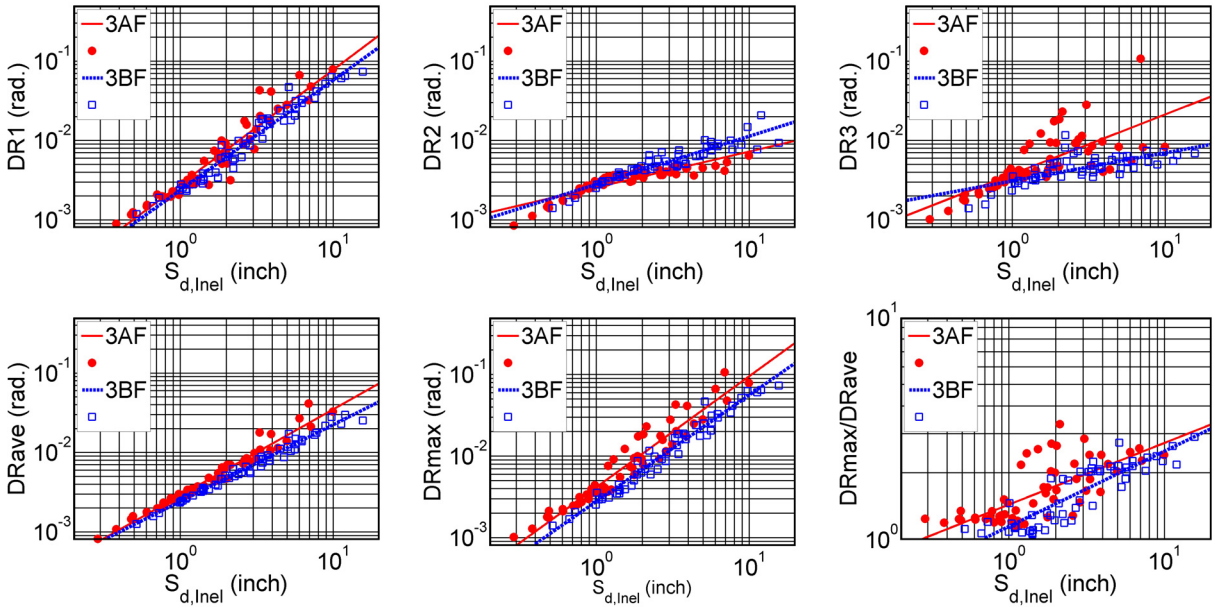

Figure 4.3 Story drift ratio for models 3AF (1997 NEHRP) and 3BF (ASCE/SEI 7-05).

Table 4.6 Median expected EDPs corresponding to different hazard levels based on inelastic displacement spectra.

EDPs	Hazard level	3AF	3BF	$3BF_3$	3CF
$S_{d,\text{Inel}}$ (in.)	50/50	1.08	1.90	1.12	2.63
	10/50	1.67	3.24	1.63	6.00
	2/50	3.60	8.36	2.82	16.20
DRmax (radian)	50/50	0.46%	0.69%	0.31%	0.84%
	10/50	0.84%	1.52%	0.51%	1.95%
	2/50	2.38%	5.15%	1.04%	5.37%
DRave (radian)	50/50	0.32%	0.49%	0.26%	0.61%
	10/50	0.50%	0.90%	0.38%	1.37%
	2/50	1.16%	2.33%	0.65%	3.68%
DRmax/DRave	50/50	1.47	1.42	1.20	1.39
	10/50	1.66	1.69	1.34	1.42
	2/50	2.05	2.21	1.59	1.46

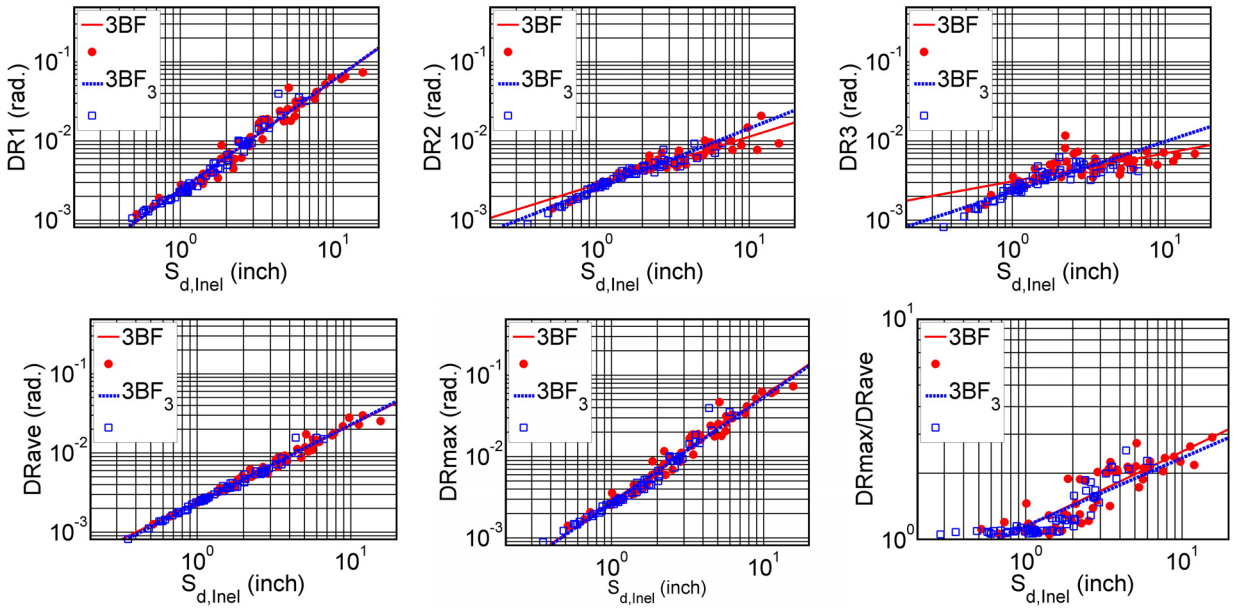

Figure 4.4 Story drift ratio for models 3BF (R = 6) and 3BF$_3$ (R = 3).

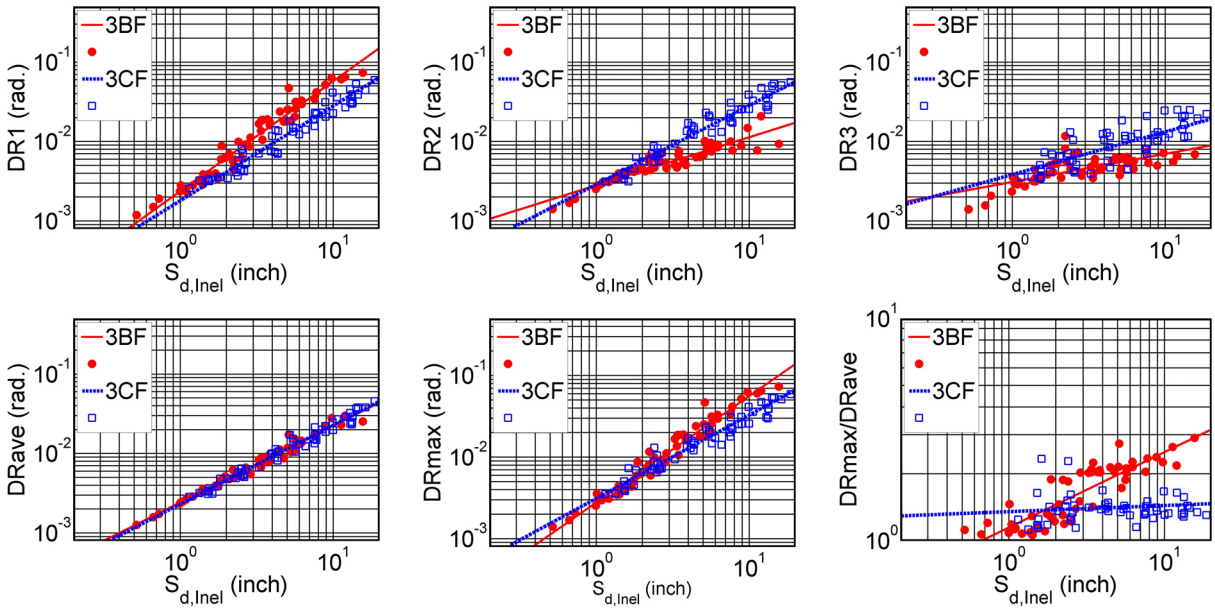

Figure 4.5 Story drift ratio for models 3BF (SCBF) and 3CF (BRBF).

A comparison of the regression curve of DRave for models 3BF and 3CF shows that both models are rather similar (Figure 4.5). The DRs for each story, however, show differences between models 3BF and 3CF, demonstrating that the BRBF tends to have a more uniform DR throughout the whole building, as the braces do not buckle and deteriorate. As shown in Figure 4.5, the tendency to form a soft story is much less than with the SCBF. Considering the difference of spectrum displacement, the maximum DR of model 3CF is greater than that of model 3BF at different hazard levels (see Table 4.5). The shift in fundamental period greatly increases the spectrum displacement, resulting in high drift demands for different hazard levels.

The data allow us to develop a relation describing the probability that a maximum story drift ratio is exceeded for a given inelastic spectrum displacement. The probability that the maximum story drift ratio will exceed 0.3% and 2.5% radian is shown in Figure 4.6, which is representative of initiation of buckling and the maximum drift accepted by standard code design methods for a design-basis event. The probability curves show different results for models 3AF and 3BF. However, it is not clear whether this difference is due to the differences in code provisions or simply the sizes and shapes of the members selected. Thus, the response of a SCBF designed according to a particular code may be very sensitive to designer selection of member sizes, slenderness ratios, and degree of compactness. A comparison of models 3BF and $3BF_3$ demonstrates that the probability curves are similar. However, if the structure is designed with R = 3, the stiffness usually increases resulting in a shorter fundamental period, smaller displacement demand, and lower probability of exceeding the critical drift levels. Similar observations are noted when models 3BF (SCBF) and 3CF (BRBF) are compared. Because the code prescribes an R of 8 for BRBFs, the fundamental period of a BRBF is usually longer.

Considering the service-level event, models 3AF, 3BF, and $3BF_3$ have 65.6%, 76.6%, and 51.6% probabilities of buckling a brace at one or more levels, respectively (see Table 4.6). This illustrates the need to consider likely local nonstructural damage during service-level events, and the possible need to replace braces following such events due to permanent lateral offsets. Considering the MCE-level event, models 3AF, 3BF, $3BF_3$, and 3CF have 48.1%, 70.8%, 16.4%, and 81.8% probabilities of exceeding 2.5% drift, respectively. Severe damage is expected for the models with high probabilities of exceeding the critical drifts.

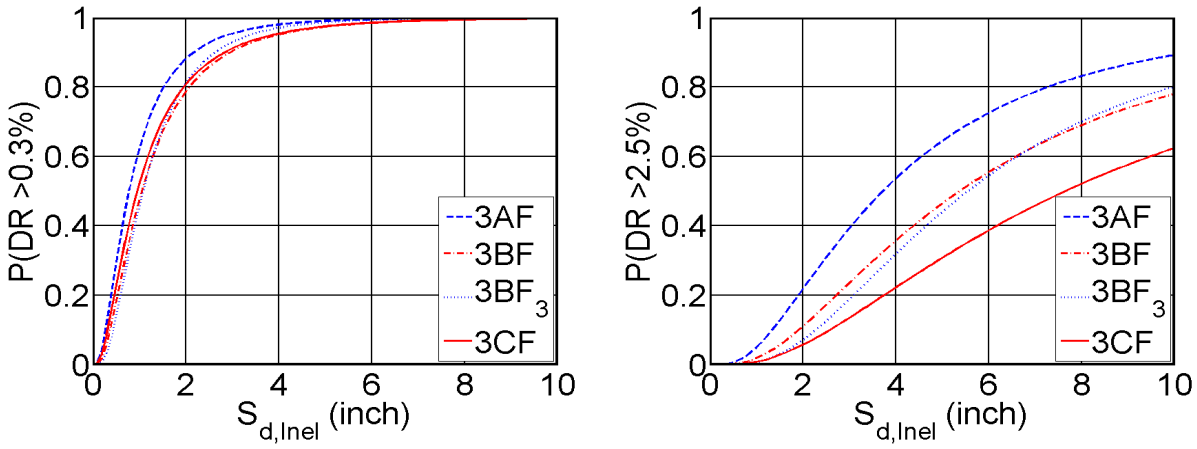

Figure 4.6 Probability of exceeding critical drift level for different models.

Table 4.7 Probability of exceeding critical DR values for different models based on inelastic displacement spectra.

Model		Hazard level		
		50%, 50 yrs	10%, 50 yrs	2%, 50 yrs
3AF, T = 0.36 sec	P(DR > 0.3%)	65.6%	82.8%	97.2%
	P(DR > 2.5%)	6.0%	15.6%	48.1%
3BF, T = 0.49 sec	P(DR > 0.3%)	76.6%	91.8%	99.5%
	P(DR > 2.5%)	9.7%	26.4%	70.8%
$3BF_3$, T = 0.35 sec	P(DR > 0.3%)	51.6%	72.1%	91.5%
	P(DR > 2.5%)	1.0%	3.9%	16.4%
3CF, T = 0.72 sec	P(DR > 0.3%)	88.3%	98.5%	100.0%
	P(DR > 2.5%)	10.4%	38.7%	81.1%

4.5.2 Residual Story Drift Ratio

Another response parameter of interest is the residual displacement in a structure, which is used to determine whether it is feasible to repair a structure following an earthquake. The residual story drift ratios of each model corresponding to different hazard levels are listed in Table 4.7. Figures 4.8 to 4.10 present the relations of the maximum residual story drift remaining at the end of the earthquake and spectrum displacement. The dots represent data points related to residual drift ratios. Two lines are superimposed, one representing the median linear regression analysis result for the residual story drift ratio and the other representing the previously reported maximum story drift ratio. The trend for residual displacements is such that the residual drifts become a larger fraction of the maximum drifts as the intensity of shaking increases.

Table 4.8 Median expected residual story drift ratio corresponding to different hazard levels based on inelastic displacement spectra.

EDPs	Hazard level	3AF	3BF	$3BF_3$	3CF
Residual DR (radian)	50/50	0.02%	0.04%	0.01%	0.10%
	10/50	0.07%	0.24%	0.03%	0.39%
	2/50	0.56%	3.97%	0.15%	1.95%

Figure 4.7 shows the residual drift for model 3AF. The median expected maximum residual displacement became a larger fraction of the peak story drift as the intensity of shaking increased. Although no data points show the residual displacements exceeding the median peak story drift ratio, some show them rather close. Considering the spectral displacement corresponding to model 3AF for the service-level and design-level events, the expected median maximum residual story drifts were 0.02% and 0.07%, respectively. For the MCE-level event, the expected median maximum residual story drift ratio was 0.56% radian.

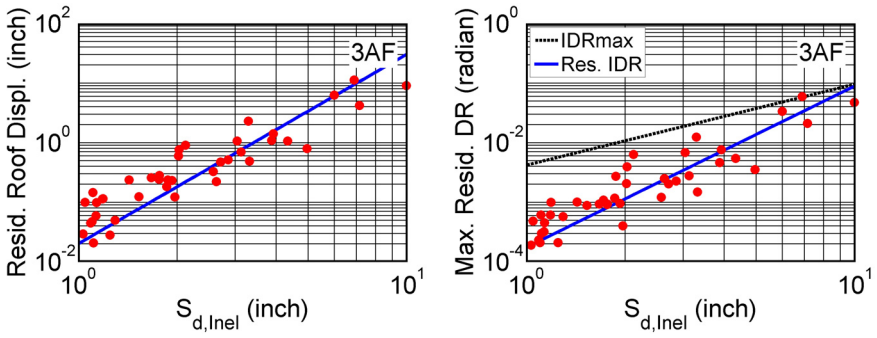

Figure 4.7 Relationship between residual deformation and $S_{d,\text{Inel}}$ for model 3AF.

For model 3BF (Figure 4.8), no data points show the residual displacement exceeding the median peak story drift ratio. Compared to model 3AF, the residual displacement was a smaller fraction of the peak story drift, although the residual displacement of model 3BF was larger for the three hazard levels. For the design-level and MCE-level events, the expected median maximum residual story drift ratios were 0.24% and 3.97% radian, respectively. For the service-level event, the expected median maximum residual story drift ratio was 0.04%.

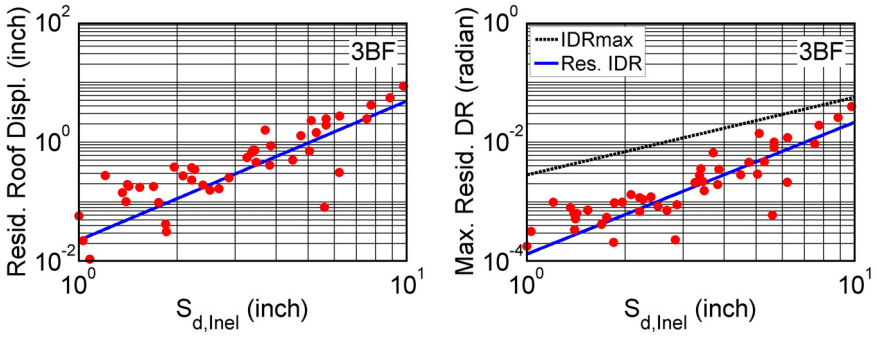

Figure 4.8 Relationship between residual deformation and $S_{d,\text{Inel}}$ for model 3BF.

For model $3BF_3$, the maximum residual story drifts were considerably smaller than for model 3BF (Figure 4.9). For the MCE-level event, the median expected maximum drift was on the order of 0.15% radian. This was in part due to smaller lateral displacements, but also because the stronger and stiffer braces remained intact even under this level of excitation.

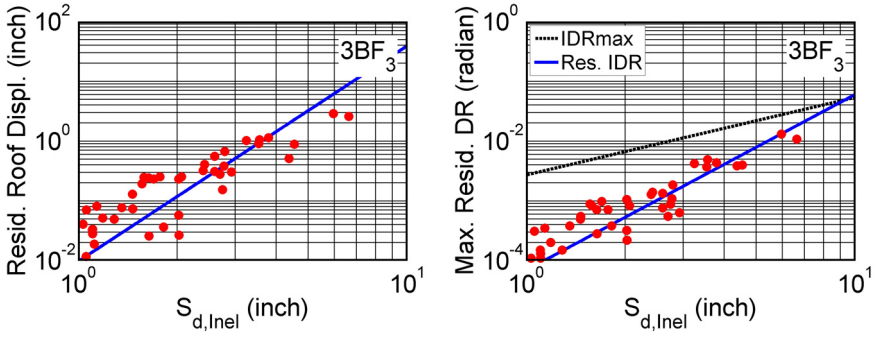

Figure 4.9 Relationship between residual deformation and $S_{d,\text{Inel}}$ for model $3BF_3$.

For model 3CF, the residual drifts became a larger fraction of the maximum drifts with increased intensity of shaking than for the other models, but this trend was less pronounced because the regression lines were more parallel (Figure 4.10). In addition, model 3CF tended to have larger residual displacement than the other models partly because of the longer fundamental period and partly because of the properties of the buckling-restrained braced frames. The braces yielded rather than buckled under severe events, because more energy was required to reverse the displacement as the yielding strength was normally greater than buckling strength. Consequently, model 3CF exhibited larger residual displacement; we believe its larger period and inelastic deformation to be the cause of this increase. For the service-, design-, and MCE-level events, the expected median maximum residual story drift ratios were 0.10%, 0.39%, and 1.45% radian, respectively.

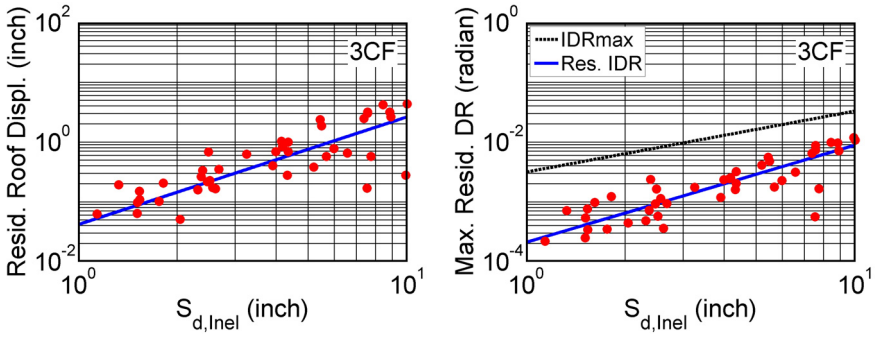

Figure 4.10 Relationship between residual deformation and $S_{d,Inel}$ of model 3CF.

4.6 SUMMARY

According to our analyses, the performance of SCBFs designed in compliance with ASCE/SEI 7-05 and 1997 NEHRP are quite similar.

Generally, the expected median maximum story drift ratios of SCBF with R of 6 exceeded values likely to cause buckling of the braces considered at the service-level event. Thus, after a frequent (service-level) earthquake, it would be necessary to replace one or more braces and repair nonstructural damage to adjacent elements. The expected median maximum story drift ratios were also likely to exceed 2.5% radian for the MCE-level event, whereby the integrity of the beam-to-column connections can be assessed with confidence.

In contrast, model $3BF_3$ resulted in median expected maximum DRs less than those needed to initiate buckling for the service-level event and less than those likely to fracture the beam-to-column connections for the MCE-level event.

To provide a more useful indication of the response characteristics of the various models, the fragility curves were integrated with respect to the seismic hazard to obtain the probability for a given hazard level that the maximum DR exceeds some key threshold. For the MCE-level event, models 3AF and 3BF had 48.1% and 70.8% probabilities, respectively, of developing maximum story drifts greater than 2.5%. In model $3BF_3$, the probability was 16.4%. For the design-level event, these probabilities dropped to 15.6%, 26.4%, and 3.9% for models 3AF, 3BF, and $3BF_3$, respectively. Interestingly, considering the service-level event, models 3AF, 3BF, and $3BF_3$ had 65.6%, 76.6%, and 51.6% probabilities, respectively, of having a brace buckle in one or more stories. The likely motion of the brace in the buckled configuration must be considered

to minimize significant local nonstructural damage during the service-level event. It is also necessary to consider replacing braces following service-level events due to the buckling of braces.

Residual lateral drifts were considered for all models as the intensity of ground shaking increased. In model $3BF_3$, the residual drifts were in the reasonable range for post-earthquake repair for different hazard levels. The residual story drift ratio was 0.15% radian for the MCE-level event. The BRBF model had the largest residual drift, partly because of the longer fundamental period and partly because of the characteristics of the buckling-restrained braced frames.

Finally, the tendency to form a soft story was reduced for different seismic hazard levels when the R value is reduced from 6 to 3. Although the cost of constructing SCBFs with an R of 3 would be higher and significant elastic response would be expected, the demands would be more consistent with the capacity of the connections and buckling braces considered here. In the case of BRBFs, although higher maximum drift demands and residual drift demands were expected, the tendency to form a soft story was less than for SCBFs.

5 Evaluation of Seismic Performance Factors Using FEMA P695 (ATC-63) Methodology

5.1 INTRODUCTION TO FEMA P695 (ATC-63) METHODOLOGY

The FEMA P695 (ATC-63) project "Quantification of Building System Performance and Response Parameters" (FEMA P695 2009) developed a methodology to quantify building system performance and response parameters that can be used in seismic design. One of the key parameters investigated is the response modification coefficient (R-factor). Other related design parameters, including the system overstrength factor (Ω_0) and deflection amplification factor (C_d), were also addressed.

5.1.1 Seismic Performance Factors

Seismic performance factors are the key parameters for designing buildings. Figure 5.1 visually depicts these factors:

R: Response modification factor

Ω: Effective overstrength factor

C_d: Deflection amplification factor

V_{Ela}: Base shear of elastic system under design earthquake ground motions

V_{max}: Maximum base shear of the yielded system

V: Design base shear from building codes

Δ_{Ela}: Roof drift of elastic system under design earthquake ground motions

Δ_u: Roof drift corresponding to 80% of the maximum base shear after building yields

Δ_y: Idealized yielding roof drift

Δ_{des}: Roof drift corresponding to the design base shear

Δ: Roof drift of yielded system under design earthquake ground motions

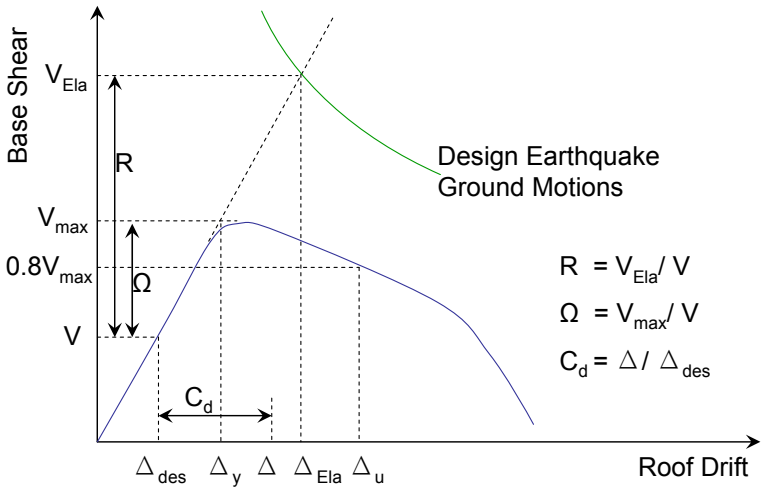

Figure 5.1 Illustration of seismic performance factors.

FEMA P695 (ATC-63) quantified the system performance and response parameters considering the collapse-level response of buildings. The seismic performance factors (R, Ω ,C_d) are illustrated in Figure 5.2 in terms of single-degree-of-freedom spectral parameters (S_A, S_D) instead of base shear and roof drift. The conversion to spectral coordinates assumes that 100% of the effective seismic weight of the structure, W, participates in fundamental mode at the fundamental period, consistent with Equation 5.1:

$$V = C_s\, W. \tag{5.1}$$

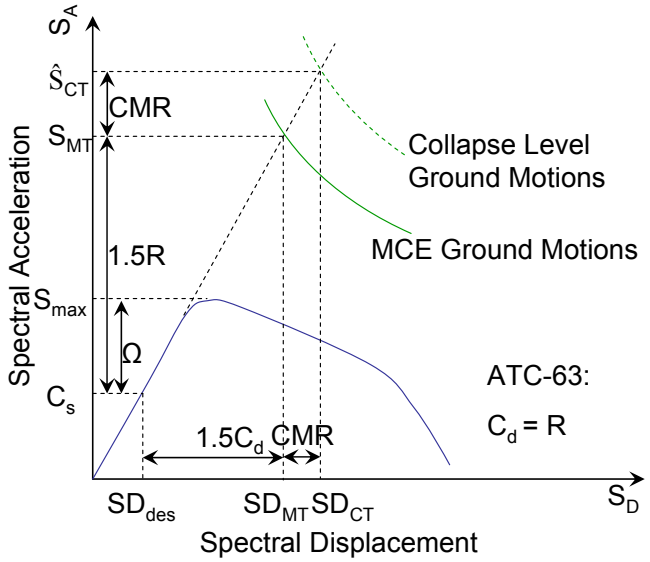

Figure 5.2 Illustration of seismic performance factors as defined by FEMA P695.

Figure 5.2 defines the seismic performance factors used in FEMA P695. The following terms are used:

$\hat{S}_{CT}$: Median spectral acceleration of collapse level earthquakes at the fundamental period of the building

S_{MT}: Spectral acceleration of maximum considered earthquake (MCE) at the fundamental period of the building
S_{max}: Maximum lateral force of the yielded system normalized by the effective seismic weight of the building, *W*
C_s: Seismic response coefficient as determined in Section 12.8.1.1 of ASCE/SEI 7-05
SD_{CT}: Median spectral displacement of collapse level earthquakes at the fundamental period of the building corresponding to spectral response acceleration $\hat{S}_{CT}$
SD_{MT}: MCE spectral displacement at the fundamental period of the building corresponding to spectral acceleration S_{MT}
SD_{des}: Spectral displacement at the fundamental period of the building corresponding to seismic response coefficient C_s
CMR: Collapse margin ratio

The relation in Equation 5.2 is illustrated in Figure 5.2. The factor of 1.5 accounts for the definition of design earthquake ground motions in ASCE/SEI 7-05 as being two-thirds of MCE ground motions.

$$1.5R = S_{MT}/C_s \tag{5.2}$$

The overstrength parameter Ω in Figure 5.2, which is calculated from a pushover analysis, is different from the overstrength factor Ω_0 of ASCE/SEI 7-05, which is used for design of nonductile elements. Naturally, different designs of a building have different Ω values, and most appropriate Ω for a specific design can be considered to be Ω_0. The notation follows the definition of FEMA P695.

FEMA P695 (ATC-63) assumes the displacement of the yielded system in the MCE-level event is equal to $1.5C_d$ times SD_{des} and is equal to the MCE elastic system displacement, SD_{MT}. This relationship leads to:

$$C_d = R. \tag{5.3}$$

Note that Equation 5.3, instead of the prescribed values in ASCE/SEI 7-05, is used later in this chapter in the design of archetype buildings to evaluate system collapse resistance.

5.1.2 Collapse Margin Ratio

FEMA P695 (ATC-63) defined the collapse level ground motions as the intensity that would result in median collapse of the archetype building of interest. Nonlinear dynamic analyses were conducted by scaling up the intensity of 22-pair ground motion records until the median collapse intensity ($\hat{S}_{CT}$) was reached, where one-half of the ground motions caused collapse of the archetypes. The collapse margin ratio (CMR) was defined as the ratio of $\hat{S}_{CT}$ to the maximum considered earthquake ground motion demand (S_{MT}, determined directly from the response spectrum) at the fundamental period *T*. As shown in Figure 5.2, the collapse level intensity is greater than the MCE-level intensity. The CMR defined in Equation 5.4 is an index of the probability that a building will collapse from the MCE-level ground motion.

$$CMR = SD_{CT}/SD_{MT} = \hat{S}_{CT}/S_{MT} \tag{5.4}$$

5.2 OVERVIEW OF FEMA P695 (ATC-63) METHODOLOGY

The methodology of FEMA P695 (ATC-63), illustrated in Figure 5.3, requires the use of a ground motion set, analysis methods, test data, design requirements, and a peer review.

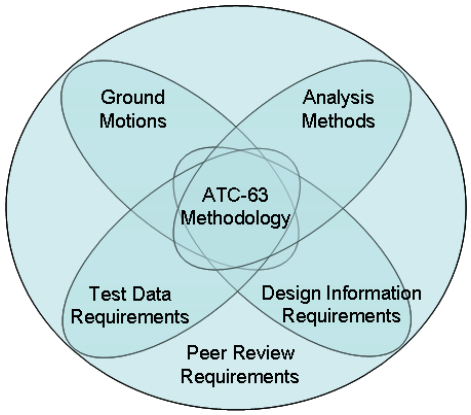

Figure 5.3 Illustration of FEMA P695 (ATC-63) methodology.

Generally, FEMA P695 is used to evaluate the design requirement of existing structural systems and also the newly developed systems. This chapter uses FEMA P695 to evaluate SCBFs and BRBFs designed according to the design provisions in ASCE/SEI 7-05. Our application of the FEMA P695 approach consisted of acquiring the system information, developing archetype buildings, constructing numerical models, performing nonlinear analysis, and evaluating the collapse resistance of the structural system (Figure 5.4). The next sections follow the FEMA P695 process step-by-step to evaluate current design requirements for SCBF and BRBF systems. Systems studied ranged from 2 to 16 stories. The archetypes were not redesigned to improve their collapse resisting force where needed.

The archetype buildings were designed to cover a selected range of structural geometry and design parameters including structural configurations, seismic design categories, fundamental periods, etc. These archetypes were assembled into "performance groups" reflecting major changes in structural behaviors within the archetype design space.

The numerical models were developed with the calibration of available test data. The CMR was determined from the nonlinear dynamic analyses. Because the methodology in FEMA P695 is a generalized procedure using a constant set of ground motions for different sites, hazard levels, and structural periods of interest, we modified the CMR to account for the frequency content (spectral shape) of the set of ground motions [Baker 2005; Baker and Cornell 2006] by simplified spectral shape factors (SSF). The adjusted collapse margin ratio (ACMR) was computed by multiplying CMR by SSF (ACMR = SSF × CMR). The SSF depended on fundamental period, period-based ductility, and seismic design category of the building and was tabulated in Table 7-1 of FEMA P695.

Performance of each archetype and each performance group was evaluated by comparing the ACMR to the acceptable ACMR. The acceptable ACMR was determined based on the uncertainty factors of the structural system. The quality of design requirements, test data, numerical modeling, and a prescribed set of ground motions contributed to the total system collapse uncertainty, denoted as $\beta_{TOT} = \sqrt{\beta_{RTR}^2 + \beta_{DR}^2 + \beta_{TD}^2 + \beta_{MDL}^2}$, where β_{RTR} is the record-to-

record uncertainty, β_{DR} is the design requirement-related uncertainty, β_{TD} is the test data-related uncertainty, and β_{MDL} is the modeling-related uncertainty. Quality ratings for design requirements, test data, and numerical modeling were quantified by the following scale: (A) superior, $\beta = 0.10$; (B) good, $\beta = 0.20$; (C) fair, $\beta = 0.35$; and (D) poor, $\beta = 0.50$. The details to determine these uncertainty factors were described in FEMA P695.

The total system collapse uncertainty was used to determine the acceptance criteria, which are conditional probabilities of collapse (under MCE ground motions) of 10% in average for a performance group and 20% for individual archetypes. The acceptable $ACMR_{10\%}$ and $ACMR_{20\%}$ were tabulated in Table 7-3 of FEMA P695 based on the total system uncertainty and the acceptable probability of collapse. If an individual archetype or a performance group failed the evaluation (ACMR < Acceptable ACMR), the archetypes needed to be redesigned with modified seismic performance factors. The iterative process continued until adequate seismic performance factors were identified to provide a structural system with adequate collapse resistance.

The evaluation was conducted for both SCBF and BRBF systems; however, the evaluation in this section was not a complete study of the braced frames as there are a variety of structural configurations and design options. Here, only a few representative braced frames were investigated. In the analyses, the global buckling behavior and possible rupture of the braces were explicitly considered in the computational models. Based on available test data, other critical non-simulated collapse modes were indirectly accounted for in beams, columns, and other components based on available test data.

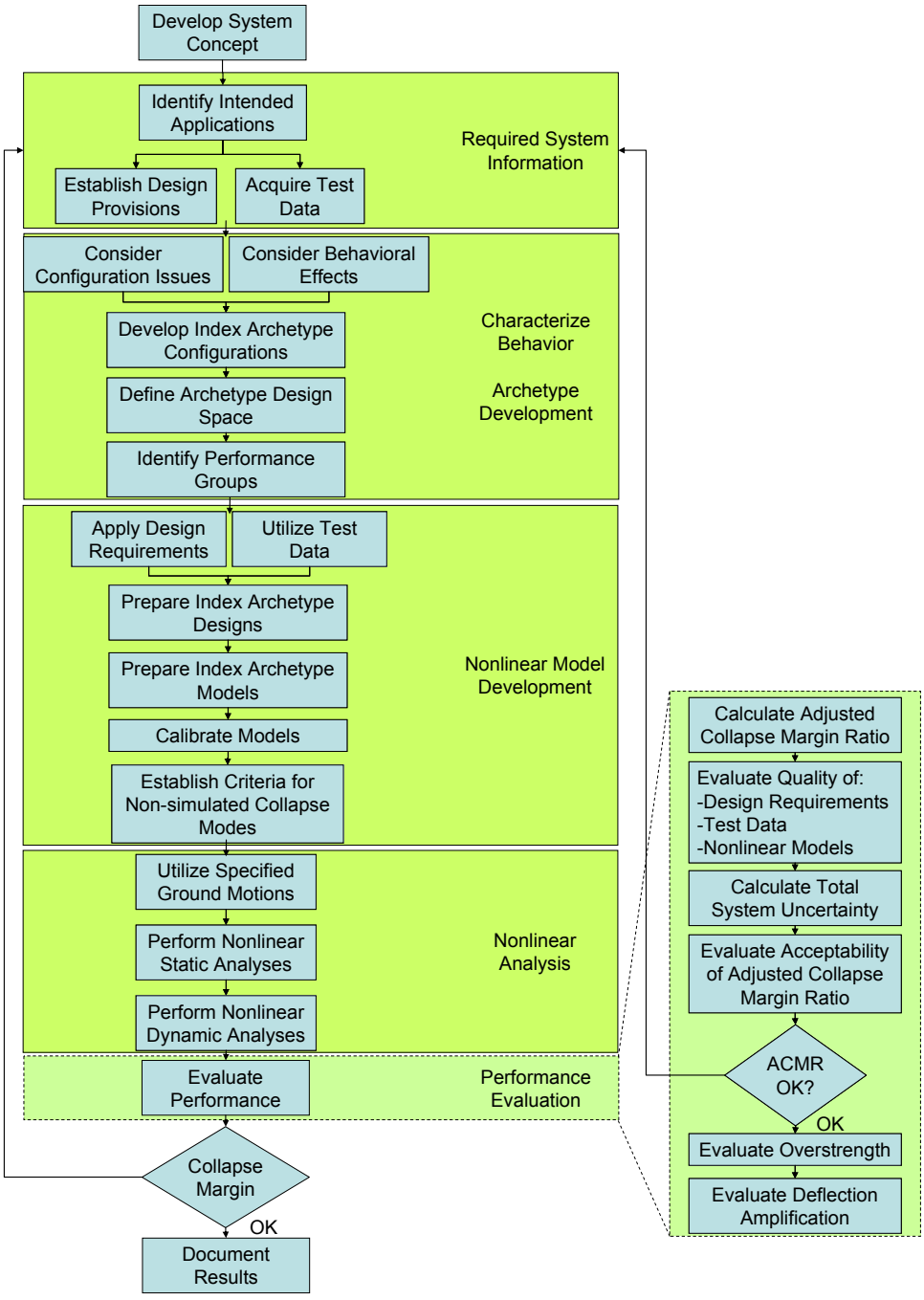

Figure 5.4 Process of evaluating seismic performance factors of buildings using FEMA P695 (ATC-63) methodology.

5.3 STRUCTURAL SYSTEM INFORMATION

5.3.1 Design Requirements

The archetype design, described in Appendix A, carefully followed the ASCE/SEI 7-05 design requirements. The beam-column connections and brace-to-framing connections of the archetypes were not designed in detail. It was assumed that they had adequate stiffness and strength and

were detailed such that they would not fail before the braces fractured. The ASCE/SEI 7-05 requirements mainly focused on braces, beams, and columns; therefore, many assumptions were used to design the beam-column connections, gusset-to-framing connections, and brace-to-gusset connections with the understanding that these assumptions might have an effect on the overall behavior of the system. Therefore, these design requirements should not be categorized as "A-Superior" according to the FEMA P695 methodology; however, a designation of "B-Good" reflects the degree of confidence in the design requirements for the SCBF and BRBF archetypes.

5.3.2 Test Data

Testing of braces, braced frame components, and braced frames has a long history [Black et al. 1980; Zayas et al. 1980; Tremblay 2002, 2008; Black et al. 2004; Yang and Mahin 2005; Powell et al. 2008; Yoo et al. 2008; Uriz and Mahin 2008]. The material properties derived from these tests may vary depending on the date and location of the tests. To calibrate the numerical models used here, data from recent tests conducted on braces and braced frames [Yang and Mahin 2005; Uriz and Mahin 2008] at the Pacific Earthquake Engineering Research Center were adopted. The test data included the cyclic responses of tube braces, pipe braces, buckling-restrained braces, conventional buckling chevron braced frames, and chevron BRB frames. Although considerable test data are available, important limitations need to be considered:

1. Variations in member sizes: The brace size of the SCBF test specimens and conventional braces were similar, around 6 inches across the section. The archetypes may incorporate heavier or lighter sections, which might affect local and global cyclic responses. In addition, the beam and column sizes likely differ from those encountered in the archetypes.
2. Variations in loading conditions: Due to the limitations of the test setup for laboratory tests, the SCBF and BRBF were not subjected to gravity loads during the tests. Also, the cyclic load was applied only on the roof level. The idealized load pattern reduced the complexity in order to examine the component responses, hence the uniform force distribution may or may not be representative of seismic loading.
3. Absence of slabs: The concrete slabs were not included in the test specimens; therefore, changes in stiffness and strength because of the intended or accidental composite behavior were not reflected in the test results used to calibrate the models.
4. Variations in drift range: The frame specimens tested were subjected to large story drifts able to significantly damage the critical elements. For the safety and protection of the experimental facilities, the tests did not continue until the specimens collapsed; therefore, the structural response between the stages of significant damage and total collapse remains largely unknown.

In sum, although test data are available for SCBF and BRBF elements and frames, due to limitations and variations of experimental procedures and intentions, the test data cannot provide the exact requirements of model parameters and behavior. Accordingly, for the purpose of assessing the total uncertainty, the test data are categorized as "B-Good" in FEMA P695.

5.4 IDENTIFICATION OF ARCHETYPE CONFIGURATIONS

The double-story X configuration was adopted for the archetypes because of its cost benefit and because compared to chevron or inverted V braced frames, the loading path in double-story X braced frames is more straightforward. The unbalanced load in beams due to the buckling or fracture of braces in chevron and inverted V braced frames can be avoided if the double-story configuration is used, allowing for a reduction the size of the beam. In addition, the double-story X configuration does not have the braces intersect within a story as the single-story X configuration does, and the potential failure in the brace-to-brace connections can be avoided. This configuration reflects current design trends in real practice.

We designed 10 archetypes for SCBFs (summarized in Table 5.1) and 10 for BRBFs (summarized in Table 5.2). The archetypes represented the combination of two seismic demand intensities and five building heights, namely 2, 3, 6, 12, and 16 stories. Figure 4.1(b) shows the typical layout of the archetypes. The braced bays (for both SCBFs and BRBFs) were located at the perimeter of the structures. For the 2-, 3-, and 6-story archetypes, one bay of braced frame was used in each side of the perimeter. For the 12- and 16-story archetypes, two nonadjacent bays of braced frame were used in each side of the perimeter. The story height for all archetypes was 15 ft, except for the 2-story series, which had a story height of 10 ft. The floor plan was 180 ft by 120 ft. Beam spans were 30 ft typically, except for the 2-story where the span was 20 ft.

Tables 5.1 and 5.2 also show the performance groups of SCBF and BRBF archetypes, respectively. The archetypes were intended to cover braced frames in both the short- period and long-period range, and they were evaluated for high and low seismic demands. The performance groups are summarized as follows:

- Maximum seismic design criteria (SDC D_{max}), short period
- Maximum seismic design criteria (SDC D_{max}), long period
- Minimum seismic design criteria (SDC D_{min}), short period
- Minimum seismic design criteria (SDC D_{min}), long period

The high and low seismic demands were represented by the minimum and maximum demands possible in Seismic Design Category (SDC) D. The archetypes were designed for a Site Class D soil conditions and design lateral loads of $S_s = 1.5\ g$ and $S_1 = 0.6\ g$ for SDC D_{max}, and $S_s = 0.55\ g$ and $S_1 = 0.13\ g$ for SDC D_{min}.

Table 5.1 Performance groups for evaluation of special steel concentrically braced frame archetypes.

Group No.	Grouping criteria				Number of archetypes
	Basic configuration	Design load level		Period domain	
		Gravity	Seismic		
PG-1SCB	Double-story X-braces	Typical	SDC D_{max}	Short	2[1]
PG-2SCB				Long	3[2]
PG-3SCB			SDC D_{min}	Short	2[1]
PG-4SCB				Long	3[2]

1. Short-period performance groups, PG-1 and PG-3, include 2-story and 3-story archetypes.
2. Long-period performance groups, PG-2 and PG-4, include 6-story, 12-story, and 16-story archetypes.

Table 5.2 Performance groups for evaluation of buckling-restrained brace frame archetypes.

Group No.	Grouping criteria				Number of archetypes
	Basic configuration	Design load level		Period domain	
		Gravity	Seismic		
PG-1BRB	Double-story X-braces	Typical	SDC D_{max}	Short	2[1]
PG-2BRB				Long	3[2]
PG-3BRB			SDC D_{min}	Short	2[1]
PG-4BRB				Long	3[2]

1. Short-period performance groups, PG-1 and PG-3, include 2-story and 3-story archetypes.
2. Long-period performance groups, PG-2 and PG-4, include 6-story, 12-story, and 16-story archetypes.

Tables 5.3 and 5.4 summarize the properties of the SCBF and BRBF archetype designs needed to evaluate SDC D, including code-calculated structural period, fundamental period of numerical model, and the design base shear. The building height limit for steel braced frames was 240 ft in this evaluation, which was extended from the 160-ft limit prescribed in ASCE/SEI 7-05. Diaphragms were assumed to be constructed with concrete filled metal deck with a length-to-width ratio less than 3. The structures were assumed to have no horizontal irregularities, allowing them to be idealized as being rigid in plane. The archetypes were regular in plan and the braced frames were located at the perimeter of the buildings. The redundancy factor (ρ) was equal to 1.0 for the archetypes as determined by analysis. The analytical procedures used in the design of the archetypes were equivalent lateral force (ELF) analysis and modal response spectrum analysis (RSA). The selection of analytical procedures followed ASCE/SEI 7-05. The design of the archetypes was not governed by P-Δ effects according to design analyses.

Table 5.3 Special steel concentrically braced frame archetype design properties.

Archetype design ID number	No. of stories	Key archetype design parameters						
		Analysis procedure	Seismic design criteria					$S_{MT}(T)$ (g)
			SDC	*R*	*T* (sec)	T_1 (sec)	*V/W* (g)	
Performance group no. PG-1SCB								
2SCBFDmax	2	ELF	D_{max}	6	0.26	0.40	0.167	1.50
3SCBFDmax	3	ELF	D_{max}	6	0.49	0.58	0.167	1.50
Performance group no. PG-2SCB								
6SCBFDmax	6	ELF	D_{max}	6	0.82	1.02	0.122	1.10
12SCBFDmax	12	ELF	D_{max}	6	1.38	1.91	0.073	0.65
16SCBFDmax	16	RSA	D_{max}	6	1.71	3.16	0.059	0.53
Performance group no. PG-3SCB								
2SCBFDmin	2	ELF	D_{min}	6	0.28	0.55	0.083	0.75
3SCBFDmin	3	ELF	D_{min}	6	0.52	0.80	0.064	0.58
Performance group no. PG-4SCB								
6SCBFDmin	6	ELF	D_{min}	6	0.88	1.51	0.038	0.34
12SCBFDmin	12	ELF	D_{min}	6	1.47	2.64	0.023	0.20
16SCBFDmin	16	RSA	D_{min}	6	1.83	4.67	0.022	0.16

Table 5.4 Buckling-restrained brace frame archetype design properties

Archetype design ID number	No. of stories	Key archetype design parameters						
		Analysis procedure	Seismic design criteria					$S_{MT}(T)$ (g)
			SDC	*R*	*T* (sec)	T_1 (sec)	*V/W* (g)	
Performance group no. PG-1BRB								
2BRBFDmax	2	ELF	D_{max}	8	0.40	0.50	0.125	1.50
3BRBFDmax	3	ELF	D_{max}	8	0.73	0.80	0.103	1.23
Performance group no. PG-2BRB								
6BRBFDmax	6	ELF	D_{max}	8	1.23	1.35	0.061	0.73
12BRBFDmax	12	RSA	D_{max}	8	2.06	2.82	0.044	0.44
16BRBFDmax	16	RSA	D_{max}	8	2.56	3.73	0.044	0.35
Performance group no. PG-3BRB								
2BRBFDmin	2	ELF	D_{min}	8	0.43	0.68	0.059	0.70
3BRBFDmin	3	ELF	D_{min}	8	0.78	1.25	0.032	0.38
Performance group no. PG-4BRB								
6BRBFDmin	6	ELF	D_{min}	8	1.31	2.34	0.022	0.23
12BRBFDmin	12	RSA	D_{min}	8	2.21	3.49	0.022	0.14
16BRBFDmin	16	RSA	D_{min}	8	2.74	4.83	0.022	0.11

Braces in the SCBF and BRBF models were assumed to have pin connections to the framing. Rigid-in-plane offsets were assumed at the beam-column connections and brace-to-framing connections. The effective length of the braces corresponded to 70% of the work-point-to-work-point length. The effective stiffness of the BRBs was modified to 1.4 times the stiffness computed using only the steel core to account for the stiffness contribution from tapered and connection areas of BRBs.

Fully restrained connections were adopted in designing the beams, which were assumed to be laterally supported at quarter points along the span. In addition to the typical load combinations, axial forces due to the yielding and fracture of braces were applied to the beams where the braces intersect at the ends. The axial forces conservatively accounted for the overstrength and strain hardening of the brace under tension and neglected the compression strength of the other brace. According to the current code, those beams where the braces intersect at the mid-span were not explicitly required to be designed to take the unbalanced axial loads from differences in tension and compression of the braces. As such, the beam sizes on the even-numbered stories were usually greater than those at the odd-numbered stories.

Columns of the braced frames are fixed at the base. They were oriented to resist lateral force by strong-axis bending. Overstrength factors for the seismic load were taken from ASCE/SEI 7-05. The gravity systems were idealized as leaning columns, and P-Δ effects were considered by applying gravity load on the leaning columns. The gravity systems were assumed to be axially rigid and (as stipulated in FEMA P695) to have no lateral resisting capacity. Their failure was not considered in analyses of the archetypes.

Two-dimensional frames were designed disregarding possible lateral-torsional behavior of structural members. It was assumed that the frame members are adequately supported laterally. Also, global torsion effects due to mass and stiffness eccentricities were not accounted for in the design.

5.5 ARCHETYPE ANALYSIS MODELS

The numerical models were developed based on the parameters discussed in Chapters 3 and 4. OpenSees fiber models were used considering the fatigue material property, Rayleigh damping, and one leaning column.

5.5.1 Collapse Modes Simulation

The evaluation in FEMA P695 uses non-simulated collapse limit states to consider the significant failure modes that are not possible or not practical to be directly simulated. Non-simulated collapse limit states were established in cooperation with the FEMA P695 peer review panel. In the analytical models of the archetypes, the collapse modes due to the damage of the braces were well calibrated with test data. Although the brace failure was one of the most critical indices to identify if the archetypes collapse, there were other collapse modes that were not explicitly simulated but the force and deformation were tracked (i.e., non-simulated collapse modes) for limit state checks; these collapse modes needed to be incorporated in this evaluation through post-processing or adequate capacity design. These failure modes considered in the numerical models are summarized in Table 5.5; all the failure modes listed were incorporated in the evaluation for limit state checks except for the neglected failure modes.

Many non-simulated collapse modes and neglected failure modes can be avoided by detailed design and quality control during construction. The global buckling of columns was not explicitly modeled, but the force and deformation demand of columns were tracked to check if the columns failed.

Table 5.5 Critical deterioration modes of steel braced frame buildings.

Critical deterioration modes	Explicitly modeled	Non-simulated	Neglected in model	Empirical criteria
Braces				
Local buckling		×		
Global buckling	×			
Net-section failure			×	
Low-cycle fatigue fracture	×			
Beam				
Lateral torsional buckling			×	
Column				
Torsion			×	
Fracture				× (10% drift)
Tension failure (at splice/base plate)		×		
Global buckling		×		
Connections			×	
3D torsion of system			×	

Earlier tests [Newell and Uang 2006] on wide flange columns under cyclic interactions of axial and lateral loading demonstrated that the columns begin to loss their capacity after 7% to 9% story drift ratio. The member sizes of the column test specimens in that study were similar to those of the archetypes. The critical story drift capacity of columns was modified to be incorporated in component limit state checks for collapse modes. Because the boundary conditions of the test specimens were more constrained than those of the archetypes studied here, the story drift capacity for the non-simulated collapse of columns was modified to 10% radian and used in the evaluation as the collapse criteria. If the numerical model of these archetypes did not show collapsing responses at large ground motion intensity, it was assumed to collapse if the drift exceeded 10% due to the high probability of column failure.

5.5.2 Uncertainty Due to Model Quality

For the purpose of assessing uncertainty, this modeling is rated as "B-Good." The brace behavior is believed to control the failure modes of the SCBFs and BRBFs. The brace models were calibrated with test data to capture the failure responses satisfactorily. Moreover, the braced

frame models incorporated with the brace models matched the test data of two-story braced frames. Although some non-simulated collapse modes were not explicitly included in the analysis models, they were taken into consideration based on the test data. Although the fiber-based element had limited capacity to simulate the local buckling behavior, the modeling capacity of capturing the local buckling behavior can be improved. Also, the 3D effects were not explicitly modeled. Essentially, this modeling approach was well calibrated to large amounts of data and able to simulate structural response up to collapse, but there was still room for improvement. As such, the model quality in this study is rated as "B-Good" in FEMA P695 (ATC-63) as approved by the peer review panel.

5.6 NONLINEAR STRUCTURAL ANALYSES

Nonlinear static and dynamic analyses were performed with OpenSees models to identify the system behavior for the evaluation. To compute the system overstrength factor (Ω_0) and to help verify the structural model, we used a monotonic static pushover analysis based on the lateral load pattern prescribed in ASCE/SEI 7-05. Figure 5.5 shows examples of the pushover curve for the 3-story archetypes.

For archetype 3SCBFDmax, buckling of braces occurred at about 0.002 roof drift ratio, which was also the drift ratio of the maximum strength; the corresponding base shear was V_{max} = 730 kips. The strength then dropped quickly, because the braces rapidly lose compression capacity. The P-Δ effect contributed to the observed negative stiffness. The overstrength factor can be computed as $\Omega = V_{max}/V$, and the period-based ductility can be computed as $\mu_T = \Delta_u/\Delta_y$, where V_{max} is the maximum base shear strength at any point on the pushover curve, V is the design base shear in Equation 5.1, Δ_u is the roof displacement at the point of 20% strength loss ($0.8V_{max}$), and Δ_y is effective yield displacement (see Figure 5.1). For 3SCBFDmax, Ω = 730 (kips)/519 (kips) = 1.41, and μ_T = 0.012 (radian)/0.002 (radian) = 6.01. The overstrength factor and ductility capacity of all SCBF archetypes are listed in Table 5.6.

For archetype 3BRBFDmin, the braced frame yielded at about 0.003 roof drift ratio. The maximum strength of 210 kips occurred at around 0.01 roof drift ratio with the negative stiffness coming from the P-Δ effect. The overstrength factor and ductility capacity of BRBF archetypes are listed in Table 5.7.

To compute the collapse capacity for each archetype design, the incremental dynamic analysis (IDA) approach was implemented using the far-field ground motion set and ground motion scaling method. Figure 5.6 illustrates how IDA was used to compute the collapse capacity of archetype 3SCBFDmax. The spectral acceleration at collapse (S_{CT}) was computed for each of the 44 ground motions of the far-field set, and then the median collapse level ($\hat{S}_{CT}$) was computed, which was 2.4 *g* for 3SCBFDmax. The collapse margin ratio (CMR) was 1.60 (see Table 5.6) for archetype 3SCBFDmax.

Static pushover analyses were completed and the IDA method was applied to each of the ten archetype designs for SCBFs and ten for BRBFs. Tables 5.6 and 5.7 summarize the results of these analyses. These IDA results showed that the two-story SCBFs and BRBFs had lower CMR than the other archetypes. Generally, the 12-story SCBF and 3-story BRBF had higher CMR. The trend also showed that although the SCBFs designed for lower seismic demand had higher CMR, this trend was not obvious for BRBFs.

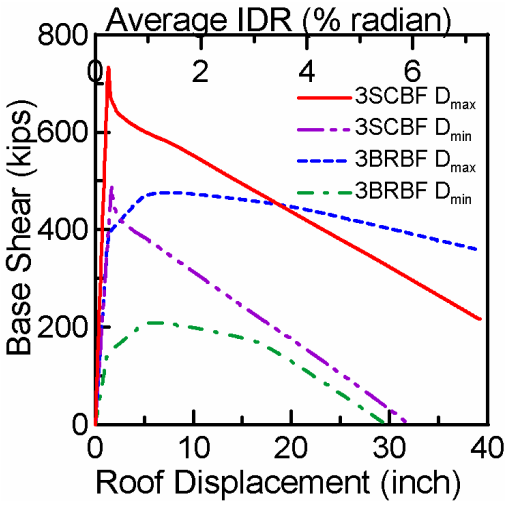

Figure 5.5 Pushover curve for 3-story archetypes.

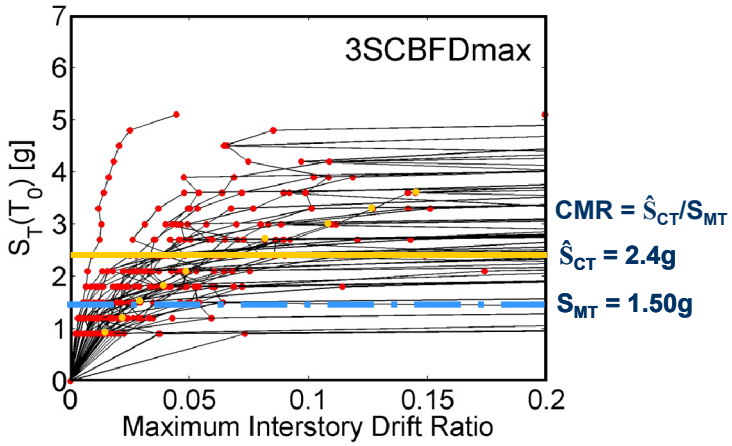

Figure 5.6 IDA of archetype 3SCBFDmax.

5.7 PERFORMANCE EVALUATION

Tables 5.8 and 5.9 show the final results and acceptance criteria for each of the SCBFs and BRBFs, respectively. The summary includes the CMR computed from the IDA, the spectral shape factor (SSF), and the adjusted collapse margin ratio (ACMR); Section 5.2 summarized the definition of these parameters.

The results in Table 5.8 show that, generally, the SCBF archetypes with short periods had lower ACMR values and may have unacceptable collapse resistance. The 16-story archetypes were designed using the RSA procedure and had acceptable ACMR values. The two-story SCBF designed for the highly seismic scenario (SDC D_{max}) did not satisfy the FEMA P695 criteria. Although archetypes with long periods were more likely to pass the acceptance criteria, 6-story and 3-story SCBF archetypes had similar ACMRs. The results also show that the archetypes designed for the highly seismic scenario (SDC D_{max}) tended to have lower ACMRs than those designed for the low seismic scenario (SDC D_{min}).

The results for BRBFs in Table 5.9 show more variation, but the BRBF archetypes with short periods generally had lower ACMR values and had the highest collapse probability. The two-story BRBFs had especially low ACMRs compared to the other BRBF archetypes. For the long-period performance group, the 12-story archetypes had lower ACMRs. The results of two-story and 6-story BRBF archetypes show that the archetypes designed for the highly seismic scenario (SDC D_{max}) did not necessarily have lower ACMRs. The ACMRs for the 3-story BRBFs designed for D_{max} and D_{min} demands were similar.

Comparing the results for SCBF and BRBF archetypes, the SCBFs had smaller ACMR values compared to BRBFs. The two-story SCBF designed for SDC D_{max} did not pass the FEMA P695 criteria, and an adjustment in the design requirements may be necessary. Because of the low ACMR values of the two-story SCBF designed for SDC D_{max}, the mean ACMR of the short-period performance group of SCBF designed for SDC D_{max} was too low to pass the acceptance criteria. All other SCBF and BRBF archetypes and performance groups satisfied the collapse resistance criteria.

Table 5.6 Summary of collapse results for special steel concentrically braced frame archetype designs.

Archetype design ID number	Design configuration			Pushover and IDA results			
	No. of stories	Gravity loads	Seismic SDC	Static Ω	S_{MT} (T) (*g*)	S_{CT} (T) (*g*)	CMR
Performance group no. PG-1SCB							
2SCBFDmax	2	Typical	D_{max}	1.44	1.50	1.5	1.00
3SCBFDmax	3	Typical	D_{max}	1.41	1.50	2.4	1.60
Performance group no. PG-2SCB							
6SCBFDmax	6	Typical	D_{max}	1.34	1.10	1.8	1.64
12SCBFDmax	12	Typical	D_{max}	1.60	0.65	2.1	3.23
16SCBFDmax	16	Typical	D_{max}	2.11	0.53	1.4	2.64
Performance group no. PG-3SCB							
2SCBFDmin	2	Typical	D_{min}	1.38	0.75	1.3	1.73
3SCBFDmin	3	Typical	D_{min}	2.41	0.58	2.1	3.62
Performance group no. PG-4SCB							
6SCBFDmin	6	Typical	D_{min}	1.86	0.34	1.2	3.53
12SCBFDmin	12	Typical	D_{min}	2.20	0.20	1.2	6.00
16SCBFDmin	16	Typical	D_{min}	1.56	0.16	0.7	3.53

Table 5.7 Summary of collapse results for buckling-restrained braced frame archetype designs.

Archetype design ID number	Design configuration			Pushover and IDA results			
	No. of stories	Gravity loads	Seismic SDC	Static Ω	S_{MT} (T) (*g*)	S_{CT} (T) (*g*)	CMR
Performance group no. PG-1BRB							
2BRBFDmax	2	Typical	D_{max}	1.31	1.50	2.6	1.73
3BRBFDmax	3	Typical	D_{max}	1.48	1.23	5.7	4.63
Performance group no. PG-2BRB							
6BRBFDmax	6	Typical	D_{max}	1.47	0.73	2.4	3.29
12BRBFDmax	12	Typical	D_{max}	1.17	0.44	1.0	2.27
16BRBFDmax	16	Typical	D_{max}	1.00	0.35	1.1	3.14
Performance group no. PG-3BRB							
2BRBFDmin	2	Typical	D_{min}	1.44	0.70	1.2	1.71
3BRBFDmin	3	Typical	D_{min}	2.11	0.38	2.1	5.53
Performance group no. PG-4BRB							
6BRBFDmin	6	Typical	D_{min}	1.28	0.23	0.7	3.04
12BRBFDmin	12	Typical	D_{min}	1.44	0.14	0.4	2.86
16BRBFDmin	16	Typical	D_{min}	1.15	0.11	0.5	4.55

\

Table 5.8 Summary of collapse performance evaluations of special steel concentrically braced frame archetypes.

Arch. design ID no.	Design configuration		Computed overstrength and collapse margin parameters					Acceptance check	
	No. of stories	SDC	Static Ω	CMR	μ_T	SSF	ACMR	Accept. ACMR	Pass/ fail
Performance group no. PG-1SCB									
2SCBFDmax	2	D_{max}	1.44	1.00	4.3	1.22	1.22	1.56	Fail
3SCBFDmax	3	D_{max}	1.41	1.60	6.1	1.28	2.05	1.56	Pass
Mean of performance group:			1.42	1.30	5.2	1.25	1.63	1.96	Fail
Performance group no. PG-2SCB									
6SCBFDmax	6	D_{max}	1.34	1.64	6.6	1.36	2.23	1.56	Pass
12SCBFDmax	12	D_{max}	1.60	3.23	3.2	1.32	4.26	1.56	Pass
16SCBFDmax	16	D_{max}	2.11	2.64	1.8	1.21	3.20	1.56	Pass
Mean of performance group:			1.69	2.50	3.8	1.30	3.23	1.96	Pass
Performance group no. PG-3SCB									
2SCBFDmin	2	D_{min}	1.38	1.73	5.8	1.12	1.94	1.56	Pass
3SCBFDmin	3	D_{min}	2.41	3.62	3.0	1.08	3.91	1.56	Pass
Mean of performance group:			1.90	2.68	4.4	1.10	2.93	1.96	Pass
Performance group no. PG-4SCB									
6SCBFDmin	6	D_{min}	1.86	3.53	3.9	1.15	4.06	1.56	Pass
12SCBFDmin	12	D_{min}	2.20	6.00	3.4	1.23	7.38	1.56	Pass
16SCBFDmin	16	D_{min}	1.56	3.53	1.2	1.06	4.64	1.56	Pass
Mean of performance group:			1.87	4.63	2.8	1.15	5.36	1.96	Pass

Table 5.9 Summary of collapse performance evaluations of buckling-restrained braced frame archetypes.

Arch. design ID no.	Design configuration		Computed overstrength and collapse margin parameters					Acceptance check	
	No. of stories	SDC	Static Ω	CMR	μ_T	SSF	ACMR	Accept. ACMR	Pass/ fail
Performance group no. PG-1BRB									
2BRBFDmax	2	D_{max}	1.31	1.73	11.9	1.33	2.31	1.56	Pass
3BRBFDmax	3	D_{max}	1.48	4.63	22.7	1.39	6.44	1.56	Pass
Mean of performance group:			1.40	3.18	17.3	1.36	4.37	1.96	Pass
Performance group no. PG-2BRB									
6BRBFDmax	6	D_{max}	1.47	3.29	15.5	1.53	5.03	1.56	Pass
12BRBFDmax	12	D_{max}	1.17	2.27	4.0	1.4	3.18	1.56	Pass
16BRBFDmax	16	D_{max}	1.00	3.14	3.1	1.32	4.15	1.56	Pass
Mean of performance group:			1.21	2.90	7.5	1.42	4.12	1.96	Pass
Performance group no. PG-3BRB									
2BRBFDmin	2	D_{min}	1.44	1.71	6.6	1.13	1.94	1.56	Pass
3BRBFDmin	3	D_{min}	2.11	5.53	10.5	1.2	6.63	1.56	Pass
Mean of performance group:			1.77	3.62	8.5	1.17	4.28	1.96	Pass
Performance group no. PG-4BRB									
6BRBFDmin	6	Dmin	1.28	3.04	6.4	1.28	3.90	1.56	Pass
12BRBFDmin	12	Dmin	1.44	2.86	3.1	1.21	3.46	1.56	Pass
16BRBFDmin	16	Dmin	1.15	4.55	2.0	1.15	5.23	1.56	Pass
Mean of performance group:			1.29	3.48	3.8	1.21	4.19	1.96	Pass

5.8 EVALUATION OF Ω

The overstrength factors Ω for each archetype, given in Table 5.6 for SCBF and Table 5.7 for BRBFs, show no specific identifiable trends. In general, the overstrength factors varied between 1.3 and 2.4 for SCBFs and were not necessarily correlated to SDC. For BRBF archetypes, the overstrength factors varied between 1.0 and 2.1.

Some of the overstrength factors were observed to be low. It appeared this was because the damage was concentrated in a certain story of the archetypes from first-mode pushover analysis. The overstrength factors could even be lower than 1.0. Figure 5.7 illustrates the relationship between story shear demand and capacity; although the story shear capacity of each story was greater than the design story shear, the design story shear demand and capacity were similar in the 9th story. Under the first-mode pushover loads, the 9th story was the first story to reach capacity. As such, the damage was concentrated in the 9th story under the first-mode pushover loads, resulting in the peak base shear being associated with the story shear capacity of

the 9th story. The resulting peak base shear was less than the design base shear, and therefore the overstrength factor was less than 1.0. The capacity of the story where the damage was concentrated under the first-mode pushover analysis dominated the maximum strength of the building. When the deformation under the first-mode pushover loads was more uniform along the height of the building or was concentrated in the lower stories, the overstrength factor was more likely to be large.

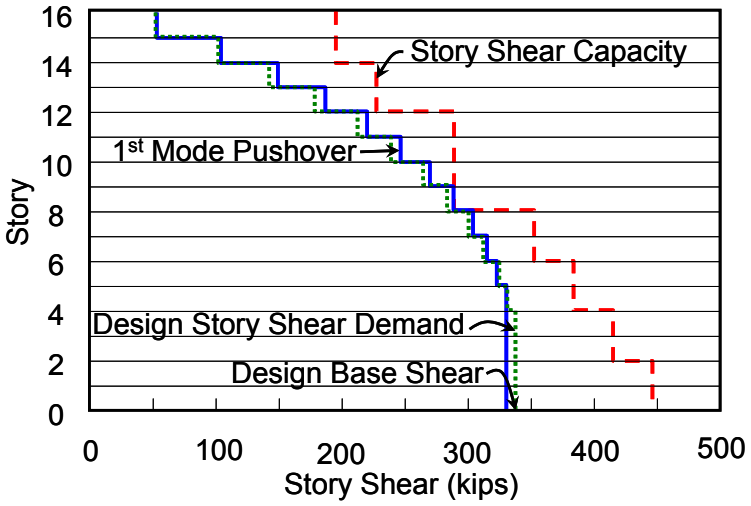

Figure 5.7 Illustration of story shear demand and capacity.

5.9 SUMMARY

The BRBF archetypes passed the evaluation, but the two-story SCBF designed for SDC D_{max} failed the FEMA P695 criteria. As such, the seismic performance factors of ASCE/SEI 7-05 seem appropriate for BRBFs based on the methodology and the archetypes, but may need adjusting for short-period SCBFs.

5.9.1 Observations on the FEMA P695 Methodology

The spectral shape factors (SSFs) are dependent on the ductility established by nonlinear static analysis. For the untypical pushover curve of SCBFs with negative post-yield tangent stiffness, FEMA P695 may underestimate the ductility demand of the system and may err in determining the ACMR. The evaluation is likely on the conservative side. The quality ratings are based on subjective judgment; therefore it is important to study the reviews and comments from engineers and researchers to have confidence in the quality ratings.

Although we designed all the archetypes on the basis of design requirements of current codes, variations exist between designers as the same design codes can be satisfied with different selections of structural layout, member size, and detailing. The subjectivity of the design process warrants that design alternatives be thoroughly studied. The evaluation provided here gave a preliminary assessment of the implementation of our methodology to SCBFs and BEBFs.

Most of the SCBF and BRBF archetypes passed the evaluation, although some performed better than others. The seismic performance factors of ASCE/SEI 7-05 seem appropriate for BRBFs, but may need adjusting for SCBFs based on our methodology and the archetypes. Those

archetypes that barely passed the evaluation may fail if the uncertainty is larger. One reason why certain archetypes fail or come close to failing is that the R-factors may be too large for low-rise archetypes. Because drift may control the design, in the taller archetypes member sizes are typically increased to obtain more stiffness; with the increase in stiffness comes an increase in strength. Low-rise archetypes typically satisfy drift requirements, and members sizes need not be increased beyond those required for strength. They thus have less reserve capacity to resist collapse.

5.9.2 Observations on System Performance

The Equivalent Lateral Force Analysis (ELF) and modal Response Spectrum Analysis (RSA) had a greater effect on the member size for higher-rise braced frames than lower-rise braced frames. In the low-rise archetype 6SCBFDmax, for example, the difference of force demand in the members determined by ELF and RSA was within 10%. For the higher archetype 16SCBFDmax, the difference increased to 50%. For structures where the force governs the design criteria, the maximum difference of design lateral force between ELF and RSA was 15% according to the current code; for structures where the drift governs the design criteria, the design lateral force calculated from the RSA could be much smaller compared to the ELF. For high-rise SCBF and BRBF archetypes, because of the selected design configurations (number of bays of braced frames, SDC, gravity, etc.), the ELF resulted in uncommonly large member sizes, therefore the RSA was used for the design of the archetypes to be representative of the evaluation on the structural systems.

The pushover curve demonstrated that the buckling of braces for some SCBFs caused a sudden global drop of strength. This kind of response resulted in a small period-based ductility using the PEMA P695 methodology and an overestimation in the overstrength factor. In the numerical model adopted here, the buckling strength and drift were affected by the initial imperfection applied in the middle of braces. A constant initial imperfection was adopted for modeling purpose, implying that the braces were fabricated with the same degree of quality. In real practice, however, the initial imperfection varies for each brace, thus the pushover responses may or may not be the same as the one shown in numerical models. Although the responses of the frame under larger deformations or after cyclic responses were less sensitive to initial imperfections, the simulated peak strength and buckling (yielding) drift from the pushover analysis should be interpreted with caution.

The first-mode pushover analysis showed that instead of distributing deformation uniformly, braced frames tended to concentrate damage in certain stories. When the damage was concentrated in higher stories, the overall strength of the braced frames was dominated by the damaged level, which may underestimate the base shear capacity. The overstrength factor, therefore, may be as low as 1.0 or even smaller.

Some of the analyses demonstrated that the archetype frames showed no evidence of collapse response even after the braces ruptured, with loss in their capacity in tension and compression. The moment-resisting frames in the model might contribute more than was expected to resist collapse. The models of the braced frames included fiber elements, which were able to capture strength degradation effects associated with brace buckling; however, the responses associated with deterioration of the beams due to plastic hinging were not explicitly simulated. As such, these evaluation results were more representative if the connections were detailed and able to reach the required ductility and strength demand.

5.9.3 Recommendations for Further Experimental or Analytical Investigation

This evaluation was intended to examine the appropriateness of the seismic performance factors for typical SCBFs and BRBFs designed for SDC D_{max}. Because of the large amount of design choices, such as different floor plans, different vertical configurations, and different numbers of braced bays, a limited set of typical braced frames were analyzed. More efforts were required to reduce the uncertainty of seismic performance factors.

Some of the designs of SCBFs used large brace sizes that were not quantified in the previous tests. Because the local and global behavior of large braces is believed to be different from that of regular braces, more testing is needed to improve the confidence on the quality of test data.

The archetypes used only the double-story X configuration. Other braced frames with different vertical configurations, or chevron braced frames designed with larger beams to resist the unbalanced load from braces and with different load paths, may exhibit other failure modes not obvious in double-story X braced frames. Further investigation on the different brace configurations should cover a wider range of samples to improve the confidence of the evaluation.

For the taller buildings, it may be not efficient to use only braced frames to resist the lateral load. Designs incorporating outriggers or multiple bays of braced frames are common. Analyses of such buildings will provide meaningful comparison to the typical archetypes.

A 3D model can be constructed to account for the 3D related failure modes. The torsional effect of the building is important for the braced frames, especially when the structure is subject to near-field ground motions in two orthogonal directions, which may show obvious asymmetric excursions.

6 Evaluation of Global Seismic Demands and Design Parameters of Braced Frame Buildings

6.1 INTRODUCTION

According to the FEMA P659 evaluation results presented in Chapter 5, low-rise braced frame archetypes have higher probabilities of collapse at the MCE-level event (2% probability of exceedance in 50 years, or 2/50) than taller ones. The simulation results for the 3-story, code-conforming braced frame buildings show that the probability of fracturing at least in one brace at the MCE-level event is over 70% in SCBF buildings and over 80% in BRBF buildings. Fracture of braces significantly reduced the lateral strength and stiffness of the buildings and increased the probability of the collapse of these buildings [also see Uriz and Mahin (2008)]. Although taller braced frame buildings more easily satisfied FEMA P695 collapse prevention safety criteria, the damage tended to be concentrated in just a few stories.

To further investigate how the braced structural systems perform under earthquakes, we selected several of the archetypes for more detailed study. The 3-, 6-, and 16-story tall archetypes 3SCBFDmax, 6SCBFDmax, 16SCBFDmax, 3BRBFDmax, 6BRBFDmax, and 16BRBFDmax were chosen to represent SCBF and BRBF systems with both short and long periods. Examined in this chapter are the drift and force demand. In addition, we report the collapse and damage characteristics of the two-story SCBF system. The numerical models were established according to the parametric studies and results presented in Chapter 3 and 4.

As in Chapters 3 and 4, the SAC ground motions [Somerville 1997] corresponding to the service (50/50), design (10/50), and MCE (2/50) hazard levels for downtown Los Angeles were used to assess likely demands at different hazard levels. Figure 6.1 shows the medians of SAC ground motions. Note that the median of the 10/50 records is similar to the design spectral acceleration of FEMA P695 at SDC Dmax.

This chapter presents global demands related to story drift, shear, and floor acceleration. EDPs related to local or member behavior are presented in Chapter 7.

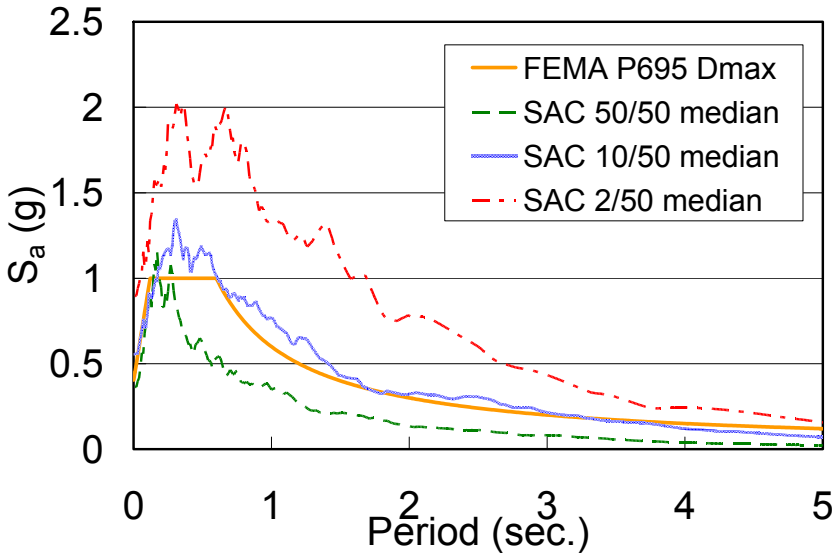

Figure 6.1 **Design spectral acceleration of FEMA P695 at SDC Dmax and the median spectral acceleration of SAC ground motions.**

6.2 GLOBAL DRIFT DEMAND

Drift demands are discussed here in terms of the maximum story drift that occurs during the response to the seismic excitation and the residual (permanent) story drift ratio present at the end of the record. These EDPs can be related to local structural damage (see Chapter 7), to damage to displacement-sensitive nonstructural components, and to difficulty in restoring a structure to operational status.

6.2.1 Story Drift Demands

Figure 6.2 presents the median and 84th percentile of the maximum story drift (the maximum value of the peak story drift at any story) of the three SCBF archetypes at three hazard levels. These values are also summarized in Table 6.1. It is assumed that the distribution of the DRmax is lognormal. The number of cases where the buildings collapsed for these records is also shown in this figure; there are 20 records at each hazard level. The results shown are generated from the non-collapse results. If the DRmax of the collapse results were also included, the median and 84th percentile of DRmax would significantly increase, especially for the archetypes with more collapse cases.

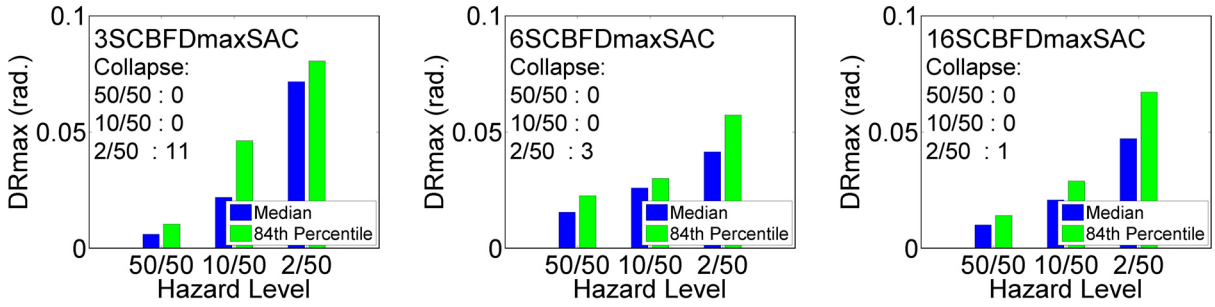

Figure 6.2 **Maximum story drift ratios of SCBF archetypes under SAC ground motions corresponding to three hazard levels.**

Table 6.1 **Summary of maximum story drift ratios of SCBF and BRBF archetypes under SAC ground motions corresponding to three hazard levels.**

Model	50/50		10/50		2/50	
	Median	84th Percentile	Median	84th Percentile	Median	84th Percentile
3SCBFDmaxSAC	0.61%	1.05%	2.19%	4.63%	7.16%	8.06%
6SCBFDmaxSAC	1.56%	2.26%	2.59%	3.01%	4.14%	5.73%
16SCBFDmaxSAC	1.01%	1.41%	2.08%	2.89%	4.71%	6.71%
3BRBFDmaxSAC	0.68%	1.23%	1.95%	3.86%	4.82%	7.96%
6BRBFDmaxSAC	0.89%	1.07%	1.93%	2.70%	3.65%	8.11%
16BRBFDmaxSAC	1.05%	1.38%	1.78%	2.48%	3.27%	5.28%

At the service-level event, the median DRmax of model 3SCBFDmaxSAC was the smallest among the SCBF archetypes compared. At the design-level event, the median DRmax values of the three SCBF archetypes were similar, between 2% and 2.6%. The 84th percentile value for this model was greater than the other two cases, owing to some near-collapse cases at the design-level event. At the MCE-level event, this model showed 11 cases of collapse, far more than the other two archetypes. The median DRmax for the nine excitations where it did not collapse was 7.16% whereas for models 6SCBFDmaxSAC and 16SCBFDmaxSAC it was 4.14% and 4.71%, respectively. In general, for 3SCBFDmaxSAC, the DRmax responses changed more from one hazard level to another than the other two cases; that is, even if DRmax of 3SCBFDmaxSAC at the service-level event is smaller than that of other archetypes, it is larger than theirs at the MCE-level event and contributes to a higher risk of collapse than the other archetypes.

Figure 6.3 shows the median and 84th percentile value of the maximum story drift of the BRBF archetypes for three hazard levels. The median DRmax values for a given hazard level of different BRBF archetypes were more similar than with the SCBFs. The 84th percentile value for model 3BRBFDmaxSAC was greater than the other models for service-level and MCE-level events. A similar trend for SCBFs is evident where the median DRmax of 3BRBFDmaxSAC was smaller than for the other BRBF archetypes at the service-level event, but greater at the MCE-level event.

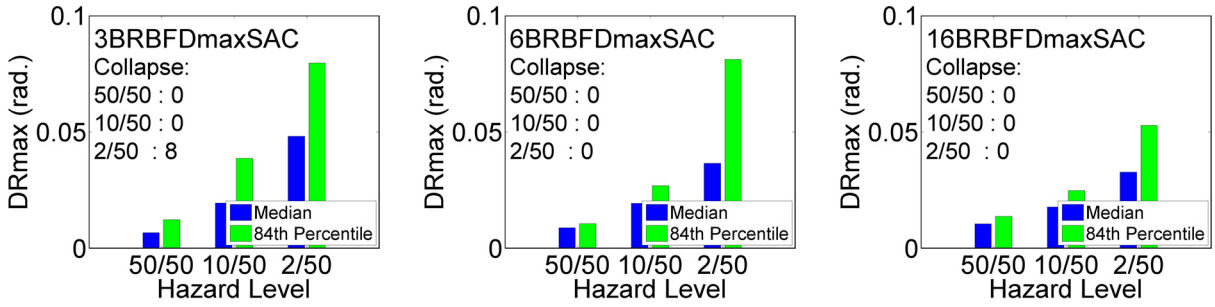

Figure 6.3 Maximum story drift ratios of BRBF archetypes under SAC ground motions corresponding to three hazard levels.

In general, for 6-story and 16-story archetypes, the median DRmax was slightly greater for the SCBFs than for the BRBFs at all three hazard levels. The median DRmax for model 3SCBFDmaxSAC for non-collapse cases of the MCE-level event was 7.16% while that of model 3BRBFDmaxSAC was 4.82%. The difference between 84th percentile and median is an estimate of standard deviation under normal assumptions, giving an indication of dispersion. For all the archetypes, this dispersion was greater at the MCE-level event than at the other hazard levels.

Figure 6.4 plots the distribution of the median and 84th percentile of DRmax over the height of the SCBF archetypes. For the service-level event, the top story of model 6SCBFDmaxSAC had the largest median service level DRmax (1.56%) among the compared models. For the design-level event, 3SCBFDmaxSAC tended to concentrate deformation at the bottom level, while the other archetypes had a more uniform drift profile. For 16SCBFDmaxSAC, the median drifts increased gradually with elevation, but the 84th percentile at the 13th story was unusually large. The drifts at the bottom two stories were small because the available brace sections at these stories were much larger than required and provided extra strength and stiffness. For the MCE-level event, the DRmax profiles were larger than those for the design-level event, but maximum drifts and especially the 84th percentile values tended to be concentrated in a few stories.

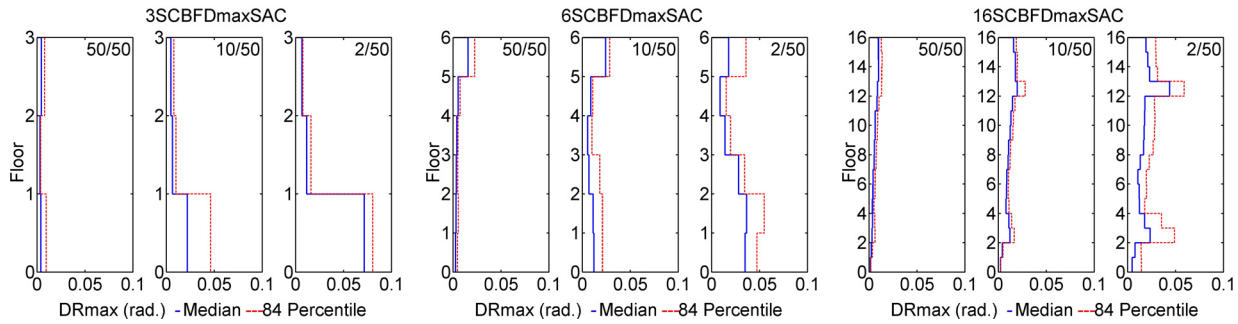

Figure 6.4 Profiles of the maximum story drift ratios of SCBF archetypes under SAC ground motions corresponding to three hazard levels.

The median and 84th percentile values of DRmax over the height of the BRBF archetypes are shown in Figure 6.5. The median drifts for the MCE-level event show that the drifts of BRBF archetypes changed more gradually than the SCBF archetypes (see Figure 6.6), without abrupt increases of DRmax at a few stories. For the service-level event, the median DRmax of any story of 3BRBFDmaxSAC was greater than that of 3SCBFDmaxSAC and the

median DRmax of any story of 16BRBFDmaxSAC was similar to that of 16SCBFDmaxSAC. In 16BRBFDmaxSAC, although the maximum of median DRmax occurred at middle floors, the change was gradual from the adjacent floors, unlike the case in 16SCBFDmaxSAC. The uniform distribution of deformation contributed to a more efficient pattern of energy dissipation for BRBFs.

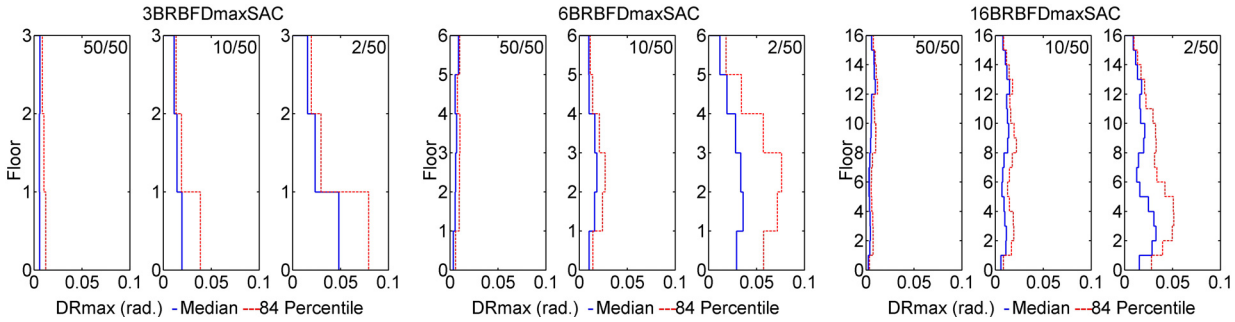

Figure 6.5 **Profiles of the maximum story drift ratios of BRBF archetypes under SAC ground motions corresponding to three hazard levels.**

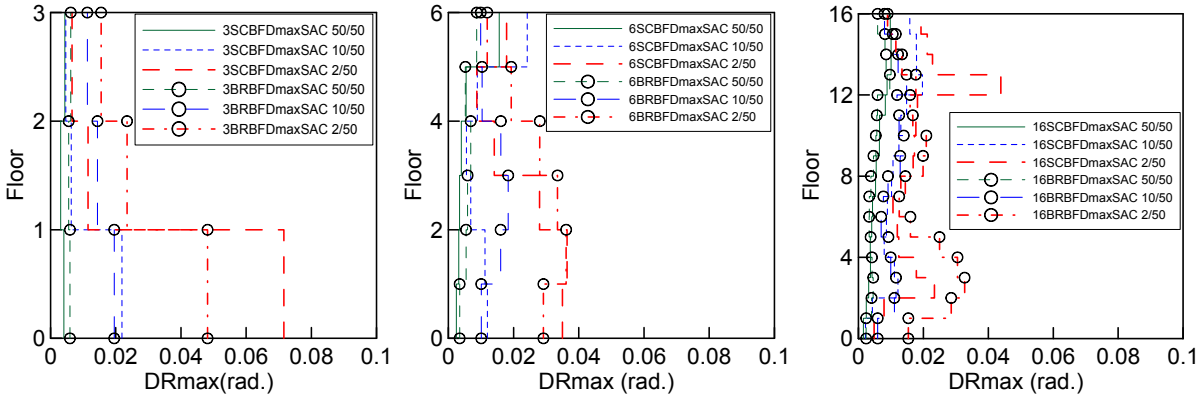

Figure 6.6 **Comparison of profiles of maximum story drift ratios of different archetypes under SAC ground motions corresponding to three hazard levels.**

6.2.2 Residual Story Drift Demands

The median residual DRs of SCBF archetypes were less than 0.1% for the service-level event for all three archetypes (see Figure 6.7). For the design-level event, although the median residual DR of 3SCBFDmaxSAC was 0.52% at the first story, the 84th percentile was more than 2.84%. The median residual DRs of 6SCBFDmaxSAC and 16SCBFDmaxSAC at the design-level event were less than 0.3%, representing buildings that may be repairable after earthquakes. For the MCE-level event, the residual DRs were especially large at the levels where the median DRmax values were concentrated for all three archetypes. The residual DRs of SCBF archetypes with fewer stories tended to be greater than in those with more stories. Although the median residual DRs of 16SCBFDmaxSAC were the smallest among the three archetypes (0.06%, 0.24%, and 1.44% for the service-, design-, and MCE-level events, respectively), the 84th percentile value

for the MCE-level event exceeded 3.9 at the stories where the median DRmax was concentrated, a level that represents damage making repairs problematic.

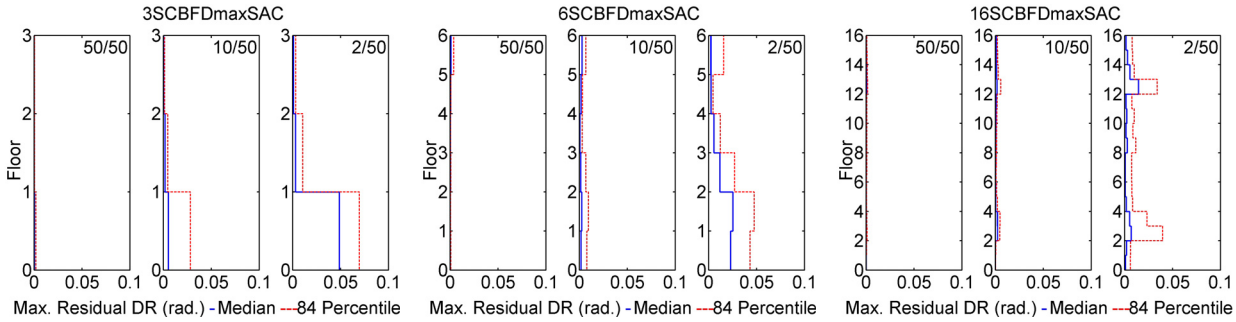

Figure 6.7 Profiles of the maximum residual story drift ratios of SCBF archetypes under SAC ground motions corresponding to three hazard levels.

The residual DRs of BRBF archetypes were less than 0.12% for the service-level event for the three archetypes (see Figure 6.8). For the design-level event, the median residual DRs in BRBFs were 0.61%, 0.53%, and 0.29% for the 3-, 6-, and 16-story archetypes, respectively. For the MCE-level event, the residual DRs were especially large at the stories where the median DRmax values were concentrated. The maxima of the median residual DR of the three BRBF archetypes at the MCE-level event were 2.88%, 1.82%, and 2.47% for the 3-, 6-, and 16-story archetypes, respectively. Note that it is not a given that the taller BRBF archetypes have smaller median residual DRs, as was the case with the SCBF archetypes.

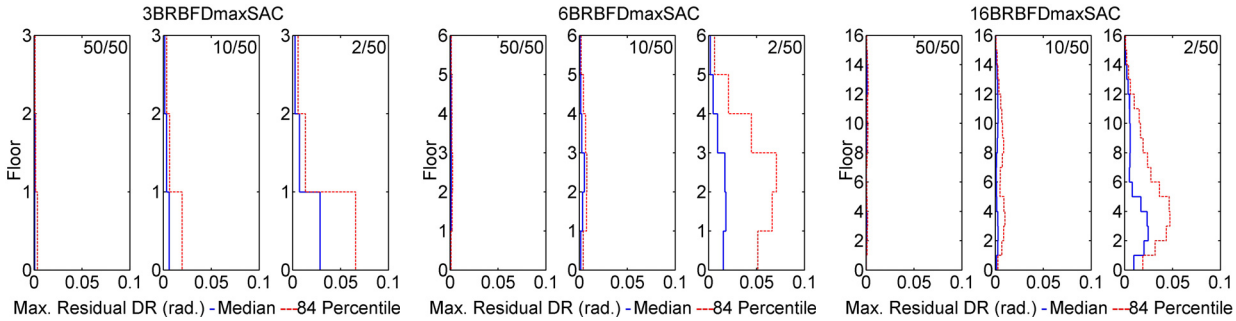

Figure 6.8 Profiles of the maximum residual story drift ratios of BRBF archetypes under SAC ground motions corresponding to three hazard levels.

A comparison of the residual DRs for the service-level and design-level events finds that they are similar for the SCBFs and BRBFs at most of the stories (see Figure 6.9). For the MCE-level event, the median residual DR of 3BRBFDmaxSAC was smaller than that of 3SCBFDmaxSAC at the first story, but greater at the other stories. The difference of the 84th percentile and the median residual DR of 6BRBFDmaxSAC for the MCE-level event was about 5.23%, which is greater than the difference for 6SCBFDmaxSAC (2.24%). The maximum median residual DR of 16BRBFDmaxSAC for the MCE-level event was about 2.5% and distributed in a few stories while that of 16SCBFDmaxSAC was 1.44% and only occurred in one story. The difference between the median and 84th percentile of residual DR was generally greater in 16BRBFDmaxSAC than in 16SCBFDmaxSAC; that is, there were more cases of large residual DR in 16BRBFDmaxSAC than in 16SCBFDmaxSAC.

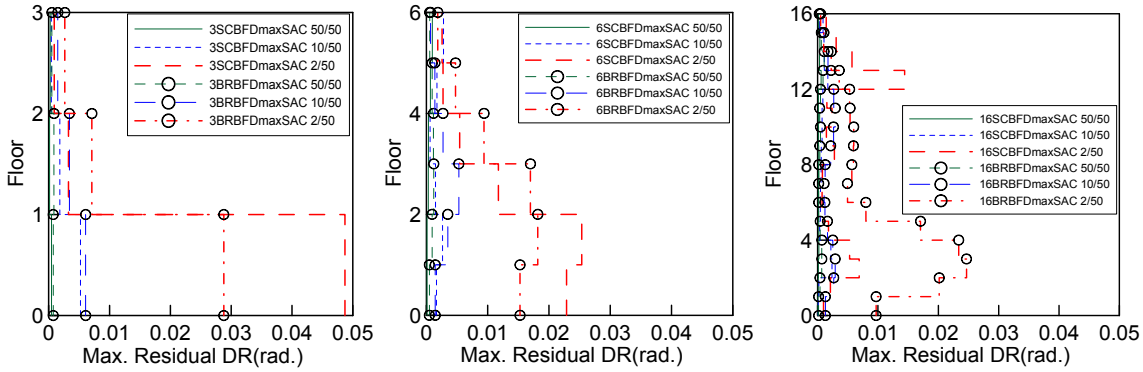

Figure 6.9 Comparison of profile of the maximum residual story drift ratios of different archetypes under SAC ground motions corresponding to three hazard levels.

6.3 GLOBAL FORCE DEMAND

The global force demand examined was the story shear, which identifies the maximum force demand at each story under various hazard levels. The story shear profile illustrates the story shear strength pattern under dynamic loadings.

The R-factor is the force reduction between an elastic system and a nonlinear system. It is bounded by the ductility capacity of the structure. Given the limited ductility of the braced frame system, we considered it important to investigate this force-related parameter. After examining the distribution of median and the 84th percentile values of story shear, we interpreted these in terms of the effective R_{Sa} value of the archetypes and base shear overstrength.

6.3.1 Story Shear

Figure 6.10 shows the story shear distribution of SCBF archetypes over the height of the buildings for the service-, design-, and MCE-level events. For 3SCBFDmaxSAC, the shape and values of the profile of maximum story shear were similar at all three hazard levels. The median of maximum base shears were 744 kips, 749 kips, and 753 kips at the service-, design-, and MCE-level events, respectively. While similar trends were observed in 6SCBFDmaxSAC, in 16SCBFDmaxSAC the distribution of story shear in upper stories was not necessarily smaller than the lower floor for two adjacent stories. The higher mode effects seemed to be reflected in the profile. For the design-level and MCE-level events, the median story shears at ground levels were 1544 kips and 1652 kips, respectively, while the story shears from the 3rd story to 12th story were about 1000 kips. The ground levels were subjected to much higher story shear demands.

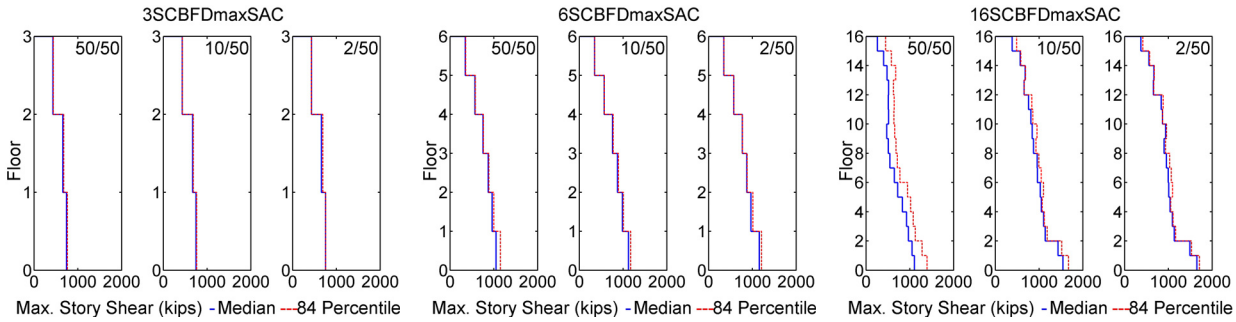

Figure 6.10 Profiles of the maximum story shear of SCBF archetypes under SAC ground motions corresponding to three hazard levels.

Figure 6.11 plots the story shear distribution for BRBF archetypes over the height of the buildings at the service-, design-, and MCE-level events. The story shears for 3BRBFDmaxSAC and 6BRBFDmaxSAC tended to increase consistently in each story as the hazard level increased. For 3BRBFDmaxSAC the median of maximum base shears were 453 kips, 522 kips, and 566 kips for the service-, design-, and MCE-level events, respectively. For 6BRBFDmaxSAC the median of maximum base shears were 618 kips, 788 kips, and 1019 kips for the service-, design-, and MCE-level events, respectively. For 16BRBFDmaxSAC, increasing the hazard intensity increased shear demand on the lower levels while the shear demands in the 4th story and above did not change as much as the lower levels did. The median of maximum base shears were 481 kips, 597 kips, and 825 kips for the service-, design-, and MCE-level events, respectively, for 16BRBFDmaxSAC. The story shears in the higher stories did not undergo significant change as the hazard intensity increased. In the lower stories, the differences between the median and 84th percentile value of story shears were also greater than the difference in the higher stories.

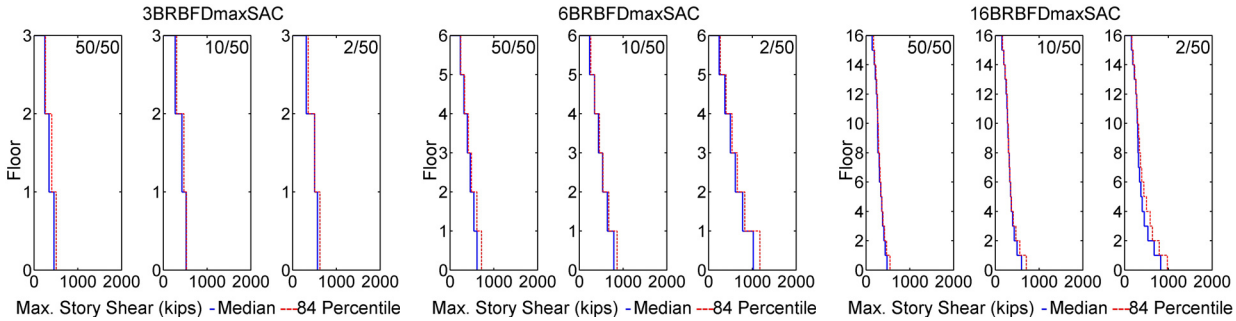

Figure 6.11 Profiles of the maximum story shear of BRBF archetypes under SAC ground motions corresponding to three hazard levels.

In each archetype, the median story shears were similar to the 84th percentile values for the design-level event. For many cases, the story shears approached the yielding capacity of each story for 3- and 6-story archetypes. Several of the story shears were greater than the story yielding capacity due to the deformation hardening of the yielding components or the additional lateral force resistance from the mechanism of beams and columns. In 16SCBFDmaxSAC, the difference between the median and 84th percentile was greater for the service-level event. The archetype still remained essentially elastic; the variation of story shear for elastic structural response was larger than that for nonlinear structural response because as long as the buildings experienced nonlinear structural response, the maximum story shear demands were near capacity. For the design-level and MCE-level events, however, most stories experienced nonlinear behavior; therefore, the story shear demands were similar to the capacity of each story.

If a story experienced extensive nonlinear behavior, the profile of story shear demand was similar to that of the capacity. Because most of the archetypes experienced nonlinear response at each story—especially for the design-level and MCE-level events—and the story shear capacity of BRBF archetypes were smaller than the SCBF counterparts, the story shear demands in BRBFs were generally smaller than those in SCBFs (see Figure 6.12). The base shear of 3SCBFDmaxSAC was almost 1.5 times that of 3BRBFDmaxSAC, and the base shear of 16SCBFDmaxSAC was almost 2 times that of 16BRBFDmaxSAC. Three primary factors that affected the larger base shear demand and capacity of SCBF archetypes:

1. The shorter fundamental period of SCBF archetypes: The shorter fundamental period of 3SCBFDmaxSAC relative to 3BRBFDmaxSAC corresponded to larger design spectral acceleration and, therefore, resulted in larger design lateral force. Although the design spectral acceleration in the long-period range varied less, the design spectral acceleration corresponding to the fundamental period of 16SCBFDmaxSAC was about 1.2 times that of 16BRBFDmaxSAC.
2. The greater design R-factor of BRBF archetypes: The design R-factor for SCBFs and BRBFs was 6 and 8, respectively. The difference resulted in a 1.33 times larger design force for SCBFs given the same design spectral acceleration in both systems.
3. Selection of member sections: Because it is more convenient to customize the brace sizes of BRBFs, the capacity of the BRBF is usually close to the design force. In contrast, the selection of brace sizes for SCBFs is constrained to available sections, and these can be more than 10% stronger than required. Moreover, because member sizes are based on the design compression force in a brace, and most braces have tensile capacity greater than their compressive capacity, the ultimate capacity of a system where the tension brace yields and the compression brace buckles is greater than the capacity calculated based on first buckling of braces.

The characteristics of materials also affect the ultimate capacity of the structure. Nonetheless, we assumed that the difference in material properties in the analyses have negligible effects on the ultimate capacity. The initial tangent and Bauschinger effect parameters were set to be the same for all the material in the analyses.

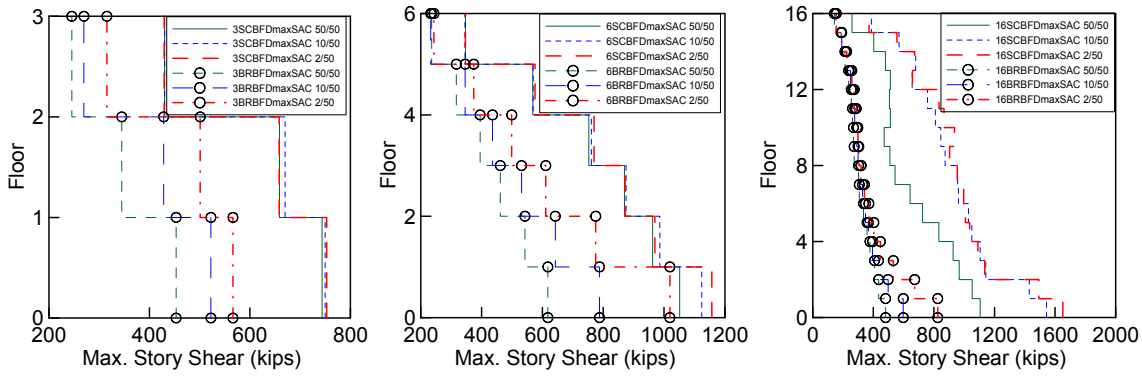

Figure 6.12 Comparison of profile of the maximum story shear of different archetypes under SAC ground motions corresponding to three hazard levels.

6.3.2 Effective R-factor

This section investigates the appropriateness of the code response modification factors (R-factor) for the archetypes. Code R-factors consider the ductility and overstrength of a structure and are generally expressed in the following form [Uang 1991]:

$$R = R_{\mu}\Omega \tag{6.1}$$

where R_μ is the ductility reduction factor and Ω is structural overstrength factor.

For a single-degree-of-freedom (SDOF) system, the relationship between ductility (μ) and R_μ was well established (Newmark and Hall 1982; Riddell et al. 1989). The relationship is period dependent and expressed in Equations 6.2, 6.3, and 6.4. Linear interpolation was used for different period ranges.

$$R_{\mu}^{NH} = 1.0 \text{ (T} < 0.03 \text{ sec)} \tag{6.2}$$

$$R_{\mu}^{NH} = \sqrt{2\mu - 1} \text{ (0.125} < \text{T} < \text{about 0.4 sec depending on } \mu) \tag{6.3}$$

$$R_{\mu}^{NH} = \mu \text{ (T} > \text{about 0.6 sec depending on damping ratio)} \tag{6.4}$$

Overstrength usually accounts for the beneficial effects from other factors such as the material overstrength and the strain rate effect during earthquake excitation. This section identifies response modification factors of the archetypes and examines the Code R-factors.

The overstrength, ductility, and response modification factors of the archetypes obtained from the analyses in Chapter 5 are summarized in Table 6.2, which also includes archetype 2SCBFDmaxSAC. Note that the definitions of Ω and Ω_0 in this chapter are commonly used in other literature [Uang 1991], but are different from those in Chapter 5. The overstrength factor Ω was obtained from the computed Ω_0, with nominal material properties times the material overstrength 1.05 and strain-rate factor 1.1 [Uang 1991; Ellingwood et al. 1980]). R_μ^{NH} was calculated from Newmark-Hall R_μ^{NH}–μ relationships given computed structural ductility in Chapter 5 and fundamental period. Conceptually, if the ratio $R_{code}/(\Omega * R_\mu^{NH})$ is greater than 1.0, it means that the overstrength and ductility capacity of the archetype designed with R_{code} are insufficient. The 2-story SCBF and 16-story SCBF and BRBF archetypes have $R_{code}/(\Omega * R_\mu^{NH})$ ratios greater than 1.0. However, for 16-story archetypes, the estimation of overstrength factors was affected by more uncertain factors, and Ω and $\Omega * R_\mu^{NH}$ may be underestimated in some cases. This issue is discussed next.

Table 6.2 Overstrength (Ω_0, Ω), ductility (μ), and response modification factors (R_μ^{NH}, R_{code}) of the archetypes.

Archetypes	Ω_0	Ω	μ	R_μ^{NH}	R_{code}	$\Omega * R_\mu^{NH}$	$R_{code}/(\Omega * R_\mu^{NH})$
2SCBFDmaxSAC	1.44	1.67	4.29	2.75	6	4.59	1.31
3SCBFDmaxSAC	1.41	1.62	6.09	3.78	6	6.14	0.98
6SCBFDmaxSAC	1.34	1.55	6.57	6.57	6	10.19	0.59
16SCBFDmaxSAC	2.11	2.44	1.77	1.77	6	4.31	1.39
3BRBFDmaxSAC	1.48	1.71	22.67	16.26	8	27.85	0.29
6BRBFDmaxSAC	1.47	1.70	15.45	15.45	8	26.25	0.30
16BRBFDmaxSAC	1.00	1.16	3.13	3.13	8	3.61	2.22

The trend in which the 16-story archetypes have a smaller ductility capacity than the 3- and 6-story archetypes is obvious in Table 6.2 due to drift concentration and more severe P-Δ effect occurring in high-rise archetypes. The values of Ω_0 and μ obtained from pushover analysis should be interpreted with caution for high-rise archetypes because the force and deformation responses of the first-mode nonlinear static pushover analyses are not representative of the responses obtained from nonlinear dynamic analyses.

Nonlinear dynamic analyses obtain values of base shear and ductility capacity that differ from those from the pushover analyses. Table 6.3 shows the median base shear demands of the archetypes at the design-level event ($V_{10/50}$) and the maximum base shear from first-mode pushover analyses (V_{max}). Because the archetypes experienced nonlinear behavior for the design-level event, the corresponding base shear demands were similar to the capacity; the static pushover analyses resulted in smaller base shear compared to dynamic analyses. This difference was more obvious for 16-story archetypes. For 16SCBFDmaxSAC, the mechanism caused by first-mode pushover occurred in the third story, whereas during SAC ground motion excitations the mechanism mostly occurred in the first story; V_{max} (1035 kips) was associated with the story shear capacity of the third story and was smaller than $V_{10/50}$ (1544 kips) Thus Ω_0 and Ω calculated from first-mode pushover were smaller than overstrength calculated from the base shear in dynamic analyses (Ω').

Table 6.3 Median base shear demands at the design-level event of the archetypes and maximum base shear from pushover analyses.

Archetypes	First-mode pushover maximum base shear (V_{max}) (kips)	Median base shear demand at the design-level event ($V_{10/50}$) (kips)	$V_{10/50}/V_{max}$
3SCBFDmaxSAC	730	749	1.03
6SCBFDmaxSAC	1020	1124	1.10
16SCBFDmaxSAC	1035	1544	1.49
3BRBFDmaxSAC	475	522	1.10
6BRBFDmaxSAC	558	788	1.41
16BRBFDmaxSAC	365	597	1.64

The SDOF constant ductility spectra for the design-level event and the Newmark-Hall relation are compared in Figure 6.13. The SDOF constant ductility spectra were constructed from the 20 SAC ground motion records representing the events of 10% probability of exceedance in 50 years. The post-yielding stiffness ratio was assumed to be 5% for a bilinear SDOF system, and a damping ratio of 4% was used for the system. Note that the Newmark-Hall approach provides lower R_μ^{NH} than the effective $R_\mu^{10/50}$ factors calculated from SAC ground motions. For example, for target ductility of 6.0, R_μ^{NH} factors calculated using the Newmark-Hall approach was 82%, on average, of the effective $R_\mu^{10/50}$ factors for periods from 0 to 5 sec.

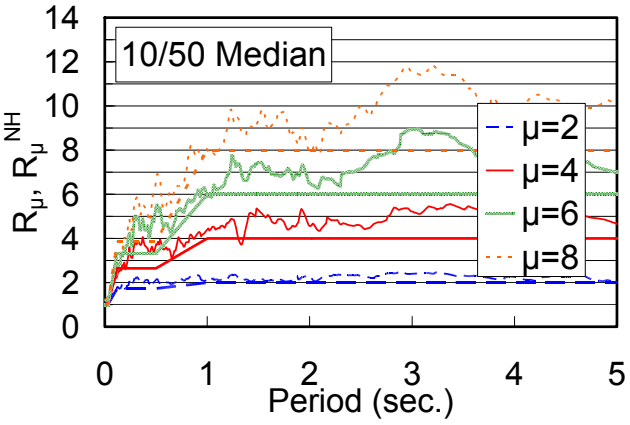

Figure 6.13 Constant ductility spectra of SAC ground motions.

For 16-story archetypes, because the dynamic responses exhibited higher overstrength (Ω') than the overstrength factor Ω estimated from first-mode static pushover analysis, the $\Omega' * R_\mu^{10/50}$ factor representing dynamic response was greater than $\Omega * R_\mu^{NH}$ obtained from first-mode static pushover analysis. Therefore, although the $\Omega * R_\mu^{NH}$ was less than R_{code} for 16-story archetypes, only one collapse was observed when they were subjected to the SAC ground motion excitations of the MCE-level event.

In contrast, for 2SCBFDmaxSAC, because the Ω factor was less affected by the difference between the static and dynamic analyses, the large $R_{code}/(\Omega * R_\mu^{NH})$ ratios simply resulted from insufficient strength and ductility capacity of the archetypes. To reduce the probability of damage and collapse of 2SCBFDmaxSAC, it is necessary to either improve the ductility and strength capacity of the archetype or reduce the ductility and strength demands on the archetype.

6.4 EFFECTIVE R-FACTORS FOR DESIGN OF TWO-STORY SCBF TO RESIST COLLAPSE

To take advantage of structural overstrength and ductility, the current code specifies an R-factor. The short-period archetype 2SCBFDmaxSAC, designed conforming to the current codes, did not have sufficient overstrength and ductility to resist collapse in the MCE-level event. We designed two-story SCBFs with various R-factors, and we discuss the collapse resistance in this section.

In current code for SCBFs, a design R-factor of 6 is too large for low-rise SCBF archetypes to resist collapse in the MCE-level event, in which the probability of collapse is more than 20% (see Chapter 5). Table 6.4 summarizes the number of collapses and DR responses of

two-story SCBF archetypes with design R-factors of 6, 4.5, 3.3, and 3. The archetype with the design R-factor of 6 resulted in one collapse for the design-level event, but the archetype exhibited collapse behavior for almost all the ground motion records for the MCE-level event. In the case with a design R-factor of 4.5, the collapse cases were reduced to eight for the MCE-level event, but the collapse risk was still high. At design R-factors of 3.3 and 3, no collapse cases were observed for the design-level event and the numbers of collapse cases for the MCE-level event were three and one for the R = 3.3 and R = 3 archetypes, respectively.

Table 6.4 also shows the median of maximum DR for these two-story archetypes. Note that the median DRmax for a design R-factor of 6 for the MCE-level event is not shown because only two non-collapse cases remained and the statistical results are not representative. The results demonstrated that considering design R-factors of 3.3 or 3.0 for two-story SCBF archetypes successfully reduces the drift demand at various hazard levels as well as the probability of collapse in the MCE-level event.

Table 6.4 Summary of responses of two-story SCBF archetypes with different R-factor for design.

R (design)	T_1 (sec)	Number of collapses (out of 20 records)		Median DRmax (non-collapse)	
		10/50	2/50	10/50	2/50
6	0.4	1	18	0.028	--
4.5	0.35	0	8	0.016	0.033
3.3	0.30	0	3	0.007	0.017
3	0.28	0	1	0.006	0.019

6.5 DEMAND-TO-CAPACITY RATIO

Damage concentration is common in the analyses of braced frame archetypes. It causes severe nonlinear behavior in a few stories in high-rise archetypes, while other stories still remain elastic. This section highlights the relationship between damage concentration and the demand-to-capacity ratio (DCR) of the building.

6.5.1 Capacity

The story shear capacity at the yielding point of the SCBF archetypes is based on the brace capacity alone. The typical pushover response of SCBFs from OpenSees analyses shows that the response is elastic until the first global buckling of the brace(s). For the double-story X braced frame archetypes before the buckling occurs, the tension and compression braces have forces of about the same magnitude but opposite sign. The story shear contributed by columns and other structural elements is generally small (less than 10% of total story shear) at the range of elastic responses. Therefore, it is assumed the major story shear contribution is due to the brace capacity. This is illustrated in Equation 6.5:

$$
\begin{aligned}
V_{br,SCBF} &= \left|P_{compression}\right| \cdot \cos(\theta + \theta') + \left|P_{tension}\right| \cdot \cos(\theta - \theta') \\
&\cong P_{cr} \cdot \cos(\theta) + P_{cr} \cdot \cos(\theta) \\
&= 2P_{cr} \cdot \cos(\theta)
\end{aligned} \tag{6.5}
$$

where P_{cr} is the compression capacity of the buckling braces at one level, θ is the incline angle of the brace with respect to the horizon, and θ' is the story drift angle at the yielding point, which is small compared to θ and may be neglected.

The story shear capacity at the yielding point of the BRBF archetypes is estimated similarly and expressed in Equation 6.6:

$$
\begin{aligned}
V_{br,BRBF} &= \left|P_{compression}\right| \cdot \cos(\theta + \theta') + \left|P_{tension}\right| \cdot \cos(\theta - \theta') \\
&\cong P_{y} \cdot \cos(\theta) + P_{y} \cdot \cos(\theta) \\
&= 2P_{y} \cdot \cos(\theta)
\end{aligned} \tag{6.6}
$$

where P_y is the tension capacity of the BRB at one level.

6.5.2 Demand-to-Capacity Ratio Profile

The story shear demand at the yielding point is based on the first-mode pushover analysis. The demand in Figure 6.14 is normalized to the shear capacity of the story where the DCR is at maximum considering all stories of an archetype; that is, the maximum DCR is 1.0 (see Figure 6.14).

Figure 6.14 provides indices to predict precisely where the first yielding will occur under the first-mode pushover analysis. The base shear demand at the yielding strength of the structure is not always near the story shear capacity of the base level. Instead, it is estimated given the story shear capacity and the location of the level where the largest DCR occurs. The 3-story and 6-story archetypes demonstrated relatively more uniform profile of DCR along the height of the buildings; all the DCR values were greater than 0.8. For the 16-story archetypes, the DCR of 1.0 occurred in the middle stories. Under the first-mode pushover analysis, it is expected that the levels with higher DCRs will yield earlier and experience more nonlinear behavior, with the likelihood of damage being concentrated in those stories.

Figure 6.15 plots the DCR of the braced frame archetypes under dynamic excitations; μ and σ shown in the figure are the mean and variance among all the stories in the archetype. The distribution of the DCR of dynamic responses differs from the results from static pushover results in being more uniform and close to 1.0, because most of the stories experienced nonlinear responses and the story shear demands approached the "yielding" capacity in each story. Therefore, it was difficult to identify which story yielded first and which story experienced more inelastic behavior from the DCR of dynamic responses. Although using the first-mode load pattern in static pushover analyses to represent the dynamic responses of structures had uncertain accuracy, the DCR of static pushover analyses exhibited a distribution that was possibly associated with the drift concentration. Therefore we used the DCR of pushover analyses as an indicator to investigate the initiation of yielding and the consequent deformation concentration.

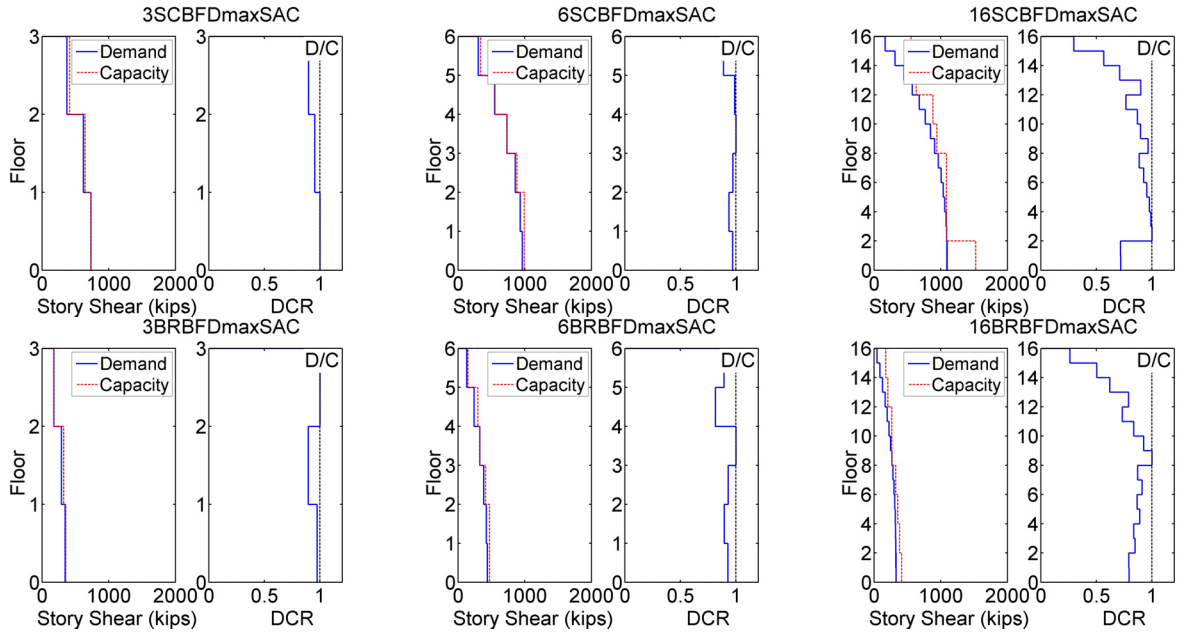

Figure 6.14 Story shear capacity and demand of first-mode pushover analysis and normalized demand-to-capacity ratio of braced frame archetypes.

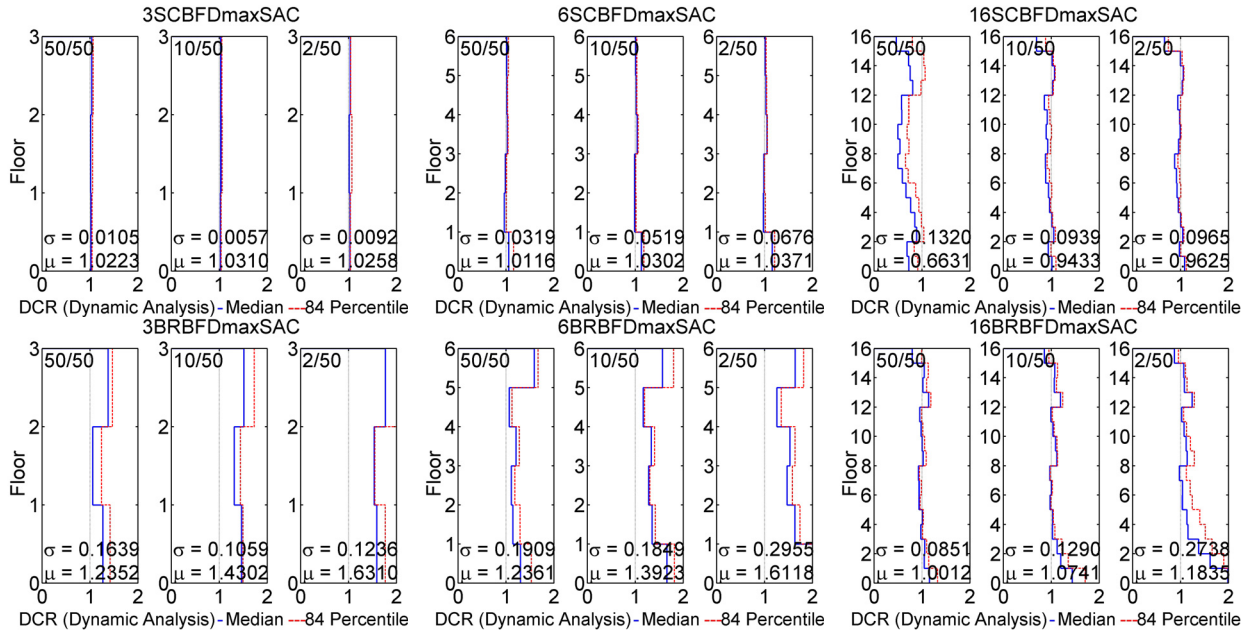

Figure 6.15 Demand-to-capacity ratios of braced frame archetypes with respect to various hazard levels.

For pushover analysis, the contribution from the P-Δ effect, manifested as the force of a leaning column, was greater after buckling occurred (see Figure 6.16). After the peak loading when the brace buckled, the column force increased rapidly while the contribution from the P-Δ effect also increased. Although both of these two components increased, they are of opposite signs, canceling out a possible increase in story shear. Generally, the total story shear was reduced more when the P-Δ effect was more obvious at larger drift, whereas the column force

did not increase much and approached the plastic capacity of the columns. As a result, the pushover curve demonstrated a negative slope after a peak force around the occurrence of brace buckling.

For the MCE-level event in the dynamic analyses, DRmax values were about 5%, whereas the contribution from the P-Δ effect was about 10% of the peak story shear from static pushover analysis; the mechanisms under dynamic excitations were observed in several stories, mostly lower stories. While the capacity of a story was estimated considering only the brace capacity, seismic loading resulted in nonlinear responses and plastic hinges at the columns and beams, contributing to a large component of the story shear. Therefore, Figure 6.15 shows that the median of story shear demands was close to the yielding capacity of each level (i.e. the DCR was about 1.0); in some stories, especially lower ones, the DCR varied between 1.0 and 2.0.

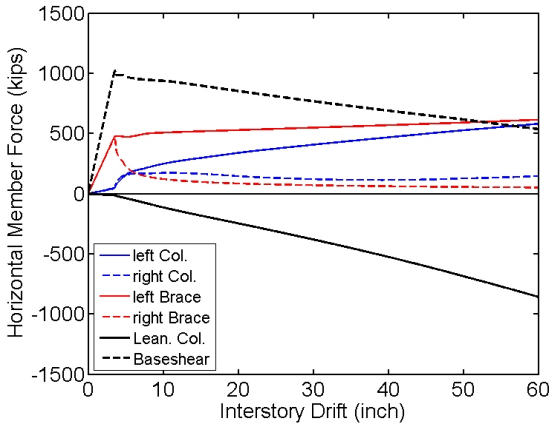

Figure 6.16 Typical pushover curve and force contribution from various structural elements.

6.6 CONSIDERING DEMAND-TO-CAPACITY RATIO PROFILE FOR DESIGNING A 16-STORY SCBF ARCHETYPE

For high-rise archetypes, damage was concentrated in several stories. One reason is that the difference in stiffness or strength at adjacent floors is too large, giving rise to a soft story/weak story mechanism. The proportion of the structural components in the archetypes is not appropriate, and, therefore, although the structural deformation along the building height is within the design limits for service-level and design-level events, the damage concentration becomes more obvious with the MCE-level event which corresponds to the higher nonlinear demand.

The first-mode static pushover analysis of archetype 16SCBFDmaxSAC illustrated that the DCR was greater for some stories than for others. The results from dynamic analysis also showed a similar possible trend of drifts being greater in the stories where these static DCRs were greater. However, the relationship between DCR and drift was not obvious. To simply estimate the relationship between the dynamic responses of a story and the DCR from first-mode pushover analysis, we assumed that the energy dissipation ratio of two stories is comparable to the pushover DCR ratio for the two stories. For the stories where the pushover DCR is larger, they were assumed to dissipate more energy during the dynamic excitations because yielding may occur there earlier than the other stories. Note that although DCR of pushover was used

here, more appropriate parameters need to be identified as an indication of the energy dissipation in each story subjected to dynamic excitations.

From the simplified bilinear story shear and DR relationship shown in Figure 6.17, the energy dissipated by story *i* and that dissipated by story *j* have a relationship in the form:

$$\frac{E_i}{E_j} = \frac{V_i \cdot DR_i - (1/2) \cdot V_i \cdot DR_y}{V_j \cdot DR_j - (1/2) \cdot V_j \cdot DR_y}, \tag{6.7}$$

with the primary assumption being

$$\frac{E_i}{E_j} = \frac{D_i / C_i}{D_j / C_j} (= \alpha). \tag{6.8}$$

By substituting Equation 6.8 into Equation 6.7, and by definition $V_i = C_i$ and $V_j = C_j$, we obtain:

$$\frac{C_i \cdot DR_i - (1/2) \cdot C_i \cdot DR_y}{C_j \cdot DR_j - (1/2) \cdot C_j \cdot DR_y} = \alpha . \tag{6.9}$$

For $\frac{C_i}{C_j} = \beta$,

$$\frac{\left(DR_i - (1/2) \cdot DR_y\right)}{\left(DR_j - (1/2) \cdot DR_y\right)} = \frac{\alpha}{\beta}. \tag{6.10}$$

Because DR_y is generally small if nonlinear behavior occurs, Equation 6.10 can be approximated as:

$$\frac{DR_i}{DR_j} \approx \frac{\alpha}{\beta} = \frac{D_i / C_i^2}{D_j / C_j^2}. \tag{6.11}$$

The relation in Equation 6.11 implies:

1. For those stories with similar force demand determined by static pushover analysis, if the story shear capacity of the story is greater, the DR during dynamic excitation is likely to be smaller. This situation usually occurs in adjacent bottom stories.
2. For those stories with similar story shear capacity, if the DCR from static pushover analysis is greater, the DR during dynamic excitation is likely to be greater. This comparison usually applies to adjacent stories along the height.
3. For those stories with similar DCR from static pushover analysis, if the capacity of the story is greater, the DR during dynamic excitation is likely to be smaller. The relation usually applies to the stories with DCR close to 1.0.

Figure 6.18 shows the relationship between D_i/C_i^2 (scaled with yielding capacity of the archetypes) and DR of 16SCBFDmaxSAC for three hazard levels. The regression is based on

zero intercept. The largest $D_i \cdot V_y/C_i^2$—corresponding to the largest median DRmax for the MCE-level event—was the response of the 13th story where the drift was concentrated. The data are summarized in Table 6.5. Note that although $D_i \cdot V_y/C_i^2$ on the third story was not especially large, dynamic analysis contends that the drift concentration was severe in this story, indicating that the changes of stiffness and strength in the adjacent stories may be too large. Given the proportional relationship between $D_i \cdot V_y/C_i^2$ and DR, not only $D_i \cdot V_y/C_i^2$ but also the change ratio of $D_i \cdot V_y/C_i^2$ at adjacent levels should be limited such that the DR in adjacent stories is not significantly altered. The constraint on the change of $D_i \cdot V_y/C_i^2$ in adjacent stories also confined the change of the stiffness at adjacent levels. Table 6.5 also lists the change ratio of $D_i \cdot V_y/C_i^2$ at two adjacent levels. The relatively large change ratios in the 3rd and 13th stories resulted in relatively large DR in these stories.

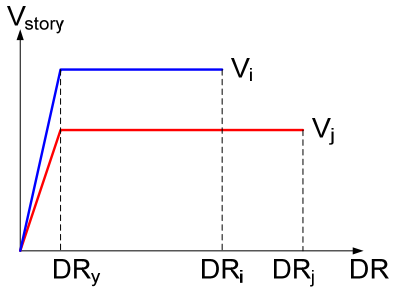

Figure 6.17 Simplified story shear and DR relationship.

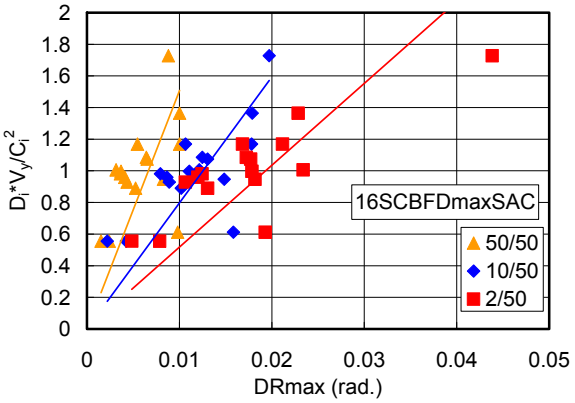

Figure 6.18 Relationship between $D_i \cdot V_y/C_i^2$ and median DRmax of 16SCBFDmaxSAC at different hazard levels.

Table 6.5 **$D_i \cdot V_y / C_i^2$, change ratio of $D_i \cdot V_y / C_i^2$ and median DRmax of 16SCBFDmaxSAC.**

Floor/Story		$D_i \cdot V_y / C_i^2$	Change Ratio of $D_i \cdot V_y / C_i^2$	Median DRmax		
				50/50	10/50	2/50
Roof	/16	0.63	0.52	0.98%	1.58%	1.93%
16	/15	1.21	0.81	1.00%	1.78%	2.12%
15	/14	1.48	0.79	1.00%	1.79%	2.28%
14	/13	1.88	2.00	0.88%	1.97%	4.38%
13	/12	0.94	0.88	0.83%	1.48%	1.82%
12	/11	1.06	0.95	0.65%	1.31%	1.77%
11	/10	1.12	0.93	0.64%	1.25%	1.72%
10	/9	1.20	1.36	0.55%	1.07%	1.68%
9	/8	0.88	0.96	0.53%	1.02%	1.31%
8	/7	0.92	0.97	0.43%	0.89%	1.07%
7	/6	0.95	0.98	0.41%	0.87%	1.20%
6	/5	0.97	0.98	0.36%	0.80%	1.24%
5	/4	0.99	0.99	0.37%	1.11%	1.79%
4	/3	1.00	2.15	0.32%	1.22%	2.34%
3	/2	0.46	1.00	0.24%	0.43%	0.79%
2	/1	0.47	—	0.15%	0.22%	0.49%

To reduce the drift concentration and the large DRmax of some stories for the MCE-level event, we redesigned the archetype as 16SCBFDmaxSACR. The target chosen was 0.025 radian, which was about the drift ratio to cause brace fracture, corresponding to $D_i \cdot V_y/C_i^2 = 1.3$ from the regression for the MCE-level event in Figure 6.18. The difference of $D_i \cdot V_y/C_i^2$ in two adjacent levels was selected to be within 30% to reduce stiffness irregularity. The member size and steel weight of the new design is shown in Table 6.6. Only the brace sizes were changed; the size in beams and columns remained the same as the previous design. The change in the total weight of the steel in the braced frames was less than 5%, and even less for the total weight of the whole building. Table 6.7 summarizes $D_i \cdot V_y/C_i^2$, the change ratio of $D_i \cdot V_y/C_i^2$, and median DRmax at various hazard levels of 16SCBFDmaxSACR; the relationship between $D_i \cdot V_y/C_i^2$ and DR is depicted in Figure 6.19. The median DRmax was effectively reduced and the DRmax profile under dynamic excitation was obviously more uniform along the height than the original design (see Figure 6.20).

Table 6.6 Member size and steel weight of 16SCBFDmaxSAC and 16SCBFDmaxSACR.

Floor/Story		Brace of 16SCBFDmaxSAC	Brace of 16SCBFDmaxSACR	Column	Beam
Roof	/16	HSS9-5/8×0.375	HSS10.75×0.375	W1×45	W18×65
16	/15	HSS9-5/8×0.375	HSS10.75×0.375	W12×45	W18×35
15	/14	HSS8-5/8×0.5	HSS10.75×0.5	W14×82	W18×71
14	/13	HSS8-5/8×0.5	HSS10.75x0.5	W14×82	W18×35
13	/12	HSS11-1/4x×0.5	HSS10×0.625	W14×120	W18×86
12	/11	HSS11-1/4×0.5	HSS10×0.625	W14×120	W18×35
11	/10	HSS10×0.625	HSS12.75×0.5	W14×176	W18×86
10	/9	HSS10×0.625	HSS12.75×0.5	W14×176	W18×35
9	/8	HSS11-1/4×0.625	HSS16×0.438	W14×233	W18×97
8	/7	HSS11-1/4×0.625	HSS16×0.438	W14×233	W18×35
7	/6	HSS11-1/4×0.625	HSS16×0.5	W14×283	W18×97
6	/5	HSS11-1/4×0.625	HSS16×0.5	W14×283	W18×35
5	/4	HSS11-1/4×0.625	HSS14×0.625	W14×342	W21×93
4	/3	HSS11-1/4×0.625	HSS14×0.625	W14×342	W18×35
3	/2	W12×96	W12×96	W14×370	W24×146
2	/1	W12×96	W12×96	W14×370	W18×35
Total Steel Weight (kips)		35130	29830	49530	30630

Table 6.7 $D_i \cdot V_y/C_i^2$, change ratio of $D_i \cdot V_y/C_i$, and median DRmax of 16SCBFDmaxSACR

Floor/Story		$D_i \cdot V_y / C_i^2$	Change ratio of $D_i \cdot V_y / C_i^2$	Median DRmax		
				50/50	10/50	2/50
Roof	/16	0.59	0.52	1.00%	1.85%	2.33%
16	/15	1.13	1.21	1.01%	1.88%	2.40%
15	/14	0.93	0.79	0.99%	1.86%	2.34%
14	/13	1.18	1.04	0.89%	1.70%	2.38%
13	/12	1.13	0.88	0.87%	1.62%	2.22%
12	/11	1.29	1.15	0.67%	1.43%	1.98%
11	/10	1.12	0.93	0.63%	1.42%	1.84%
10	/9	1.20	1.26	0.55%	1.14%	1.64%
9	/8	0.95	0.96	0.54%	1.10%	1.42%
8	/7	1.00	1.25	0.45%	1.00%	1.13%
7	/6	0.80	0.98	0.41%	0.93%	1.10%
6	/5	0.81	1.10	0.38%	0.84%	1.28%
5	/4	0.74	0.99	0.37%	0.79%	1.18%
4	/3	0.75	1.31	0.31%	0.67%	1.04%
3	/2	0.57	1.00	0.28%	0.61%	1.38%
2	/1	0.57	-	0.16%	0.52%	2.14%

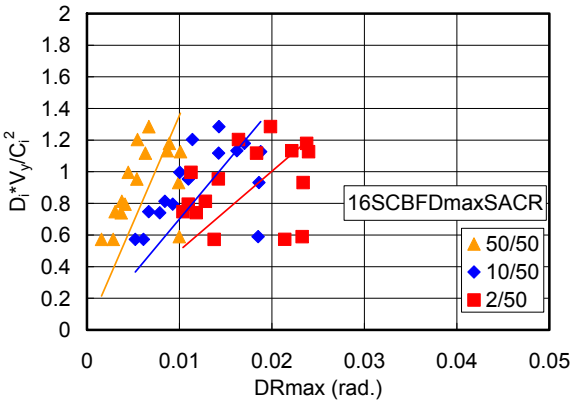

Figure 6.19 **Relationship between $D_i \cdot V_y/C_i^2$ and median DRmax of 16SCBFDmaxSACR at different hazard levels.**

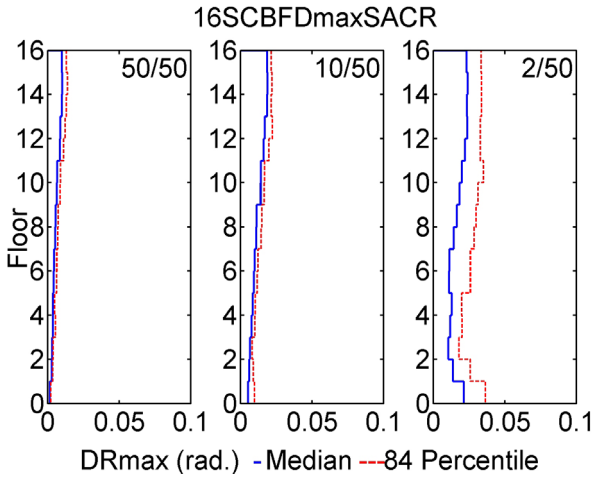

Figure 6.20 **Profiles of the maximum story drift ratios of 16SCBFDmaxSACR under SAC ground motions corresponding to three hazard levels.**

6.7 FLOOR ACCELERATION DEMAND

Life safety hazards can develop as a result of falling objects. The potential for nonstructural elements and contents falling is related to floor level accelerations. In addition to posing a life safety hazard, acceleration-sensitive objects can be dislodged or damaged, requiring considerable effort and funds to repair following an earthquake. For these reasons, we examined the maximum peak floor level accelerations (PFAs).

Figure 6.21 shows the median and 84th percentile of PFA of all the archetypes corresponding to various hazard levels. Figure 6.22 shows the median PFA of all the archetypes. Both figures only accounted for the non-collapse cases. The difference between the 84th percentile and the median shown in Figure 6.21 illustrates that these differences in BRBF archetypes are between 0.13*g* and 0.66*g* and those of SCBF archetypes are between 0.12*g* and 0.88*g*. The 6-story archetypes had greater differences than 3- and 16-story archetypes, which means that the PFAs had greater variation in the 6-story archetypes. Figure 6.21 also shows that

for all SCBF archetypes, the largest PFAs occurred on the bottom and roof floors (or the 5th story of 6SCBFDmaxSAC), but for all BRBF archetypes, the largest PFAs occurred on the bottom floors.

Figure 6.22 shows that median PFAs of low-rise archetypes were generally greater than those of high-rise counterparts. Note that PFAs for the MCE-level event were generally greater than those for the other hazard levels; this was especially true on the lower floors of 3-, 6-, and 16-story archetypes. For the 16-story BRBF archetype, median PFAs on the higher floors were similar for all three hazard levels, and for 16-story SCBF archetype, median PFAs on the higher floors were similar for the design-level and MCE-level events and greater than median PFAs for the service-level event. Median PFAs of the SCBF archetype 16SCBFDmaxSAC were greater than those of 16BRBFDmaxSAC along the height of the archetypes at three hazard levels due to the longer fundamental period and higher flexibility of BRBF archetypes. For 6-story archetypes, median PFAs of SCBF were greater than those of BRBFs on the top two floors at three hazard levels; for 3-story archetypes, median PFAs of SCBFs were greater than those of BRBFs along the height of the archetypes at three hazard levels, except on the roof for the MCE-level event. Generally, nonstructural damage associated with floor acceleration was more severe for SCBF archetypes than for BRBF archetypes at three hazard levels, and more severe for short-period archetypes than for long-period archetypes.

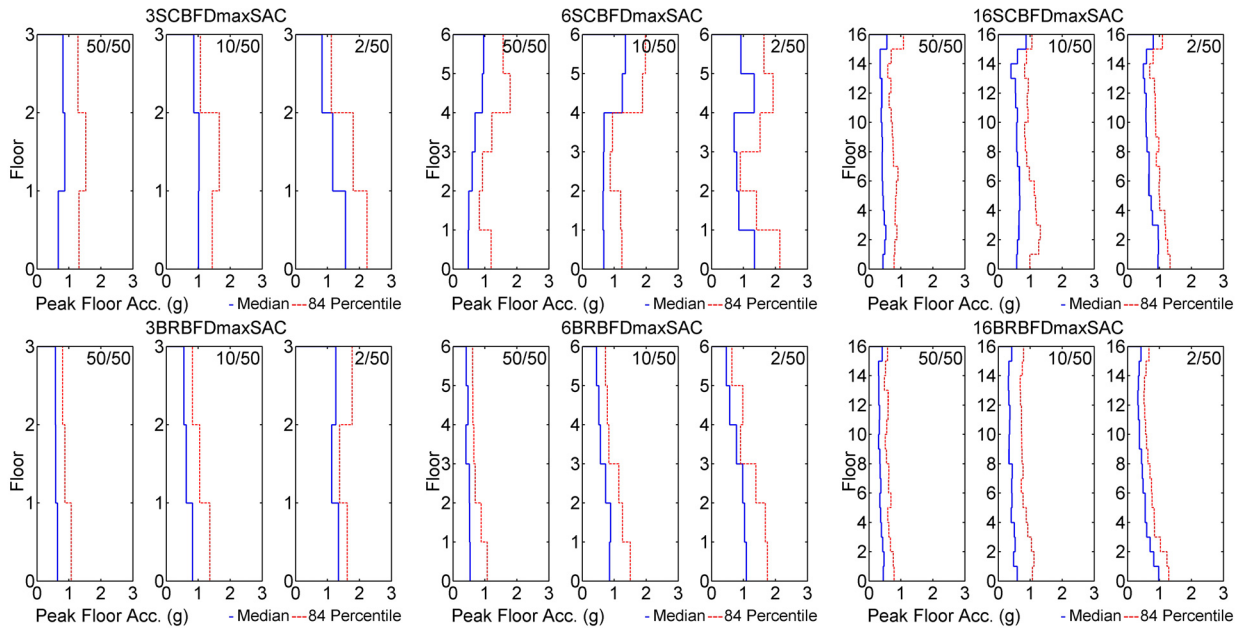

Figure 6.21 Peak floor accelerations of braced frame archetypes with respect to various hazard levels.

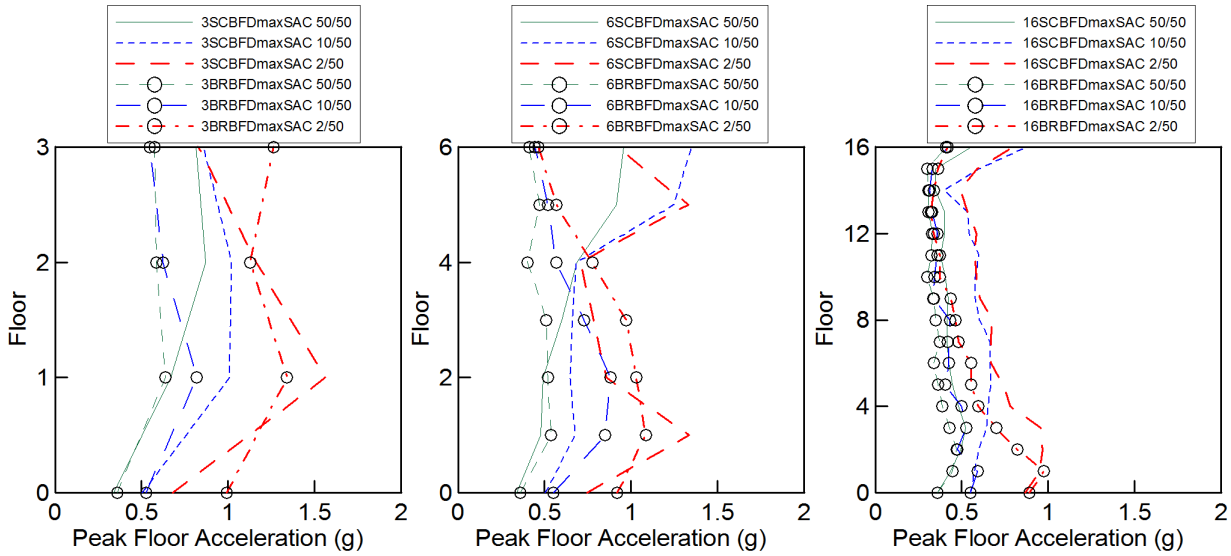

Figure 6.22 Comparison of peak floor accelerations of different archetypes under SAC ground motions corresponding to three hazard levels.

6.8 SUMMARY

Sixty SAC ground motion records representing three hazard levels were applied to evaluate the performance of 3-, 6-, and 16-story SCBF and BRBF archetypes. Low-rise SCBF archetypes showed a higher probability of collapse for the MCE-level event according to the evaluation in Chapter 5, while the high-rise SCBF archetypes had deformation concentrated in a few stories. The design R-factor of the two-story SCBF archetype was investigated for its high probability of collapse. To reduce the deformation concentration, the 16-story SCBF archetype was redesigned based on the proposed parameters. The results are summarized below.

- Drift Ratio: The deformation of archetype 3SCBFDmaxSAC tended to concentrate drift in the bottom story. For 16SCBFDmaxSAC, a few of the middle stories had larger median DRmax and 84th percentile. Deformation and damage concentration in those stories led to weak stories under dynamic excitations, especially for the MCE-level event. The BRBF archetypes generally had more uniform profile of DRmax than SCBF archetypes. In 16BRBFDmaxSAC, although the maximum of median DRmax occurred in the middle stories, the change was gradual between adjacent floors, a different response scenario compared to the sudden drift change displayed in 16SCBFDmaxSAC. The uniform distribution of drift contributed to a more efficient pattern for energy dissipation in BRBFs.
- Residual Drift Ratio: The median residual DRs of SCBF and BRBF archetypes at the service-level and design-level events were small (usually around 0.5% radian). For the MCE-level event, median residual DRs of all archetypes increased to 1.0% to 3.0%, signifying non-repairable damage to the buildings. The maximum median residual DR of 16BRBFDmaxSAC was about 2.5% and distributed across a few stories. For 16SCBFDmaxSAC, the maximum median residual DR was 1.44% and occurred in only one story.

- Story shear: In general, the median story shears were similar to the 84th percentile of story shears for each archetype. The story shears approached the yielding capacity of each story if the archetype had experienced nonlinear behavior. Because the strength capacities of SCBF archetypes were generally greater than those of BRBF archetypes, the story shear demands in BRBFs were smaller than those in SCBFs.
- Effective R-factor: The 2-story SCBF and 16-story archetypes had $R_{code}/(\Omega^*R_\mu)$ ratios greater than 1.0, which suggests that the overstrength and ductility capacity of the archetype designed with R_{code} are insufficient. The estimation of overstrength and R_μ needs to be modified to reflect the dynamic responses of archetypes and the characteristics of selected ground motions, respectively. After the modification, the code design parameters were appropriate for the 16-story archetypes. For the 2-story SCBF, the overstrength and ductility capacity were still insufficient. For archetype 2SCBFDmaxSAC, a smaller design R-factor (3.3 or 3.0) was more consistent with the ductility capacity of the structural system and more appropriate for the design. The code mandated R-factors appear to be unconservative for short-period archetypes. The R-factors of 3.3 and 3.0 successfully reduced the drift demand at various hazard levels as well as the probability of collapse in the MCE-level event. For collapse prevention in the MCE-level event, a period-dependent design R-factor may be more appropriate for the short-period SCBF archetypes designed for SDC Dmax.
- Demand-to-Capacity Ratio: The DCR provided indices to predict at which story the first yielding would occur in the first-mode pushover analysis. Although using the first-mode load pattern in static pushover analyses to represent the dynamic responses of structures had uncertain accuracy, the DCR of static pushover analyses exhibited a distribution that was possibly associated with the drift concentration. Therefore the DCR of pushover analyses was used here as an indicator to investigate the initiation of yielding and the consequent deformation concentration. Under the assumption that the energy dissipation profile over the height of the building during dynamic excitations is proportional to DCR distribution of the first-mode pushover analysis along the height, DR of each story was approximately proportional to D_i/C_i^2 (or $D_i \cdot V_y/C_i^2$). The analysis of the 16-story SCBF archetypes demonstrated that by limiting the $D_i \cdot V_y/C_i^2$ ratios, the target DR could be met at different hazard levels. The stiffness difference in adjacent stories should also be limited to reduce drift concentration. A difference of 30% for the $D_i \cdot V_y/C_i^2$ ratio in adjacent stories was adopted successfully reduced the stiffness irregularity of the 16-story SCBF archetype.
- Peak Floor Acceleration: The largest median PFAs occurred on the bottom or roof floors (or the 5th story of 6SCBFDmaxSAC) for SCBF archetypes; for all BRBF archetypes, the largest median PFAs occurred on the bottom floors. Analyses showed that the low-rise archetypes had greater median PFAs than the high-rise counterparts and that PFAs had greater variation in the 6-story archetypes than in the other archetypes. In general, median PFAs for the MCE-level event were greater than those at the other hazard levels, especially for the lower floors of all SCBF and BRBF archetypes. Median PFAs of 16SCBFDmaxSAC were greater than those of 16BRBFDmaxSAC along the height of the archetypes at three hazard levels due to the longer fundamental period and higher flexibility of BRBF archetypes. For 3-story and 6-story archetypes, however, the median PFAs of the BRBF archetypes were not always smaller than those of the SCBF counterparts. In general, nonstructural damage associated with floor acceleration was

expected to be more severe for SCBF archetypes than for BRBF archetypes at three hazard levels, and more severe for short-period archetypes than for long-period archetypes.

7 Seismic Demand Evaluation of Structural Members in Steel Braced Frame Buildings

7.1 INTRODUCTION

This chapter discusses the EDPs for structural members including the braces, beams, and columns corresponding to different hazard levels. These EDPs include out-of-plane deformation of braces in SCBFs, ductility demands of the braces, damage indices of braces, axial force and moment demands in beams and columns, and vertical deformation in the middle span of the beam where braces intersect. We propose simple and accurate approaches to estimate the out-of-plane deformation of braces and to estimate the column compressive axial forces.

7.2 BEHAVIOR AND DEMANDS FOR BRACES

This section discusses the demands of out-of-plane deformation and ductility of braces and damage of braces. Brace damage is expressed in terms of a damage index to represent the fatigue life of the braces under various hazard levels.

7.2.1 Out-of-Plane Deformation

In previous earthquakes, out-of-plane deformation of braces was commonly seen in SCBF buildings when gusset plates were oriented to allow braces to move out of the plane. The major concern of out-of-plane deformation of braces is the damage it may cause to adjacent walls and nonstructural components. A few design details can easily be employed so that the braces deform in-plane, although they are beyond the scope of this research. Although the numerical models presented here are two-dimensional assuming in-plane buckling of the braces, out-of-plane deformation of braces can be investigated by measuring the brace deformation transverse to its longitudinal axis. Figure 7.1 shows the out-of-plane deformation of braces for the SCBF archetypes for three hazard levels. The median out-of-plane deformation for the MCE-level event was 28.7, 22, and 19 inches for 3SCBFDmaxSAC, 6SCBFDmaxSAC, and 16SCBFDmaxSAC, respectively.

The distributions of the out-of-plane deformation along the height of the buildings were similar to the profile of the maximum DR, and their relationships were approximately proportional. Figure 7.2 illustrates the relationship between out-of-plane deformation and story drift. Story drift caused shortening of the compression braces, which led to out-of-plane deformation of the braces. It was assumed that the axial and flexural deformations of the braces were negligible and the deform shape was composed of straight lines.

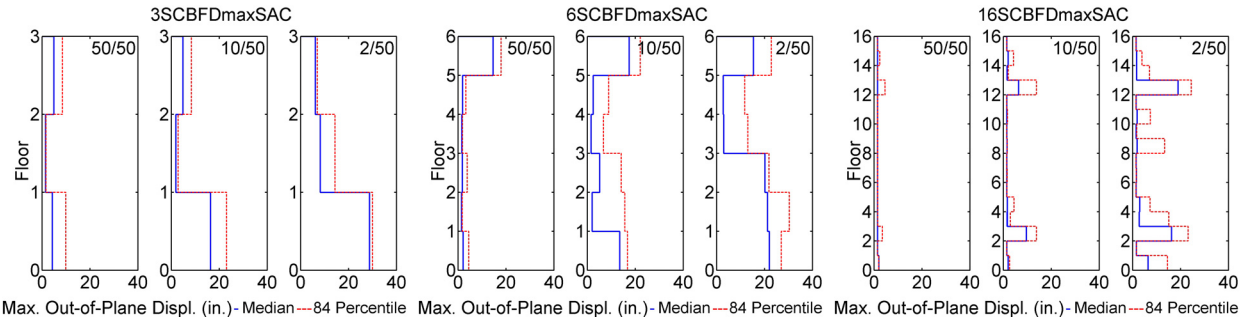

Figure 7.1 **Profiles of out-of-plane brace deformation of SCBF archetypes under SAC ground motions corresponding to three hazard levels.**

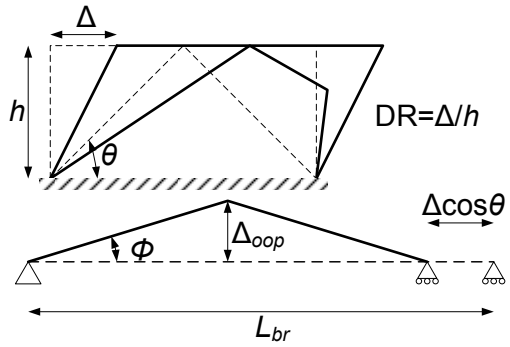

Figure 7.2 **Simplified relationship between story drift and out-of-plane brace deformation.**

The out-of-plane displacement can be expressed as:

$$\begin{aligned}\Delta_{oop} &= \frac{L_{br}}{2}\cdot\sin\phi \\ &= \frac{L_{br}}{2}\cdot\sin\left(\cos^{-1}\left(\frac{L_{br}-h\cdot\cos\theta\cdot DR}{L_{br}}\right)\right) \\ &= \frac{1}{2}\sqrt{2\cdot L_{br}\cdot h\cdot\cos\theta\cdot DR - h^2\cdot\cos^2\theta\cdot DR^2}\end{aligned} \tag{7.1}$$

where $\phi = \cos^{-1}\left(\frac{L_{br}-\Delta\cdot\cos\theta}{L_{br}}\right)$. The brace length is given by:

$$L_{br} = \eta\cdot\frac{h}{\sin\theta} \tag{7.2}$$

where η is the ratio of hinge-to-hinge length to workpoint-to-workpoint length of braces.

In this analysis, the effective brace length was assumed to be 70% of the workpoint-to-workpoint length and therefore η = 0.7. Substituting Equation 7.2 into Equation 7.1, the out-of-plane displacement can be rewritten and approximated as:

$$\Delta_{oop} = \frac{L_{br}}{2}\sqrt{DR \cdot \frac{\sin 2\theta}{\eta}\left(1 - \frac{\sin 2\theta}{4 \cdot \eta} \cdot DR\right)} \approx \frac{L_{br}}{2}\sqrt{\frac{\sin 2\theta}{\eta} \cdot DR} \tag{7.3}$$

The out-of-plane deformation is approximately proportional to the square root of DR. Note that when the DR is less than the DR that initiates buckling of the brace, the out-of-plane deformation has not yet occurred and Δ_{oop} should be zero. In that case we can modify Equation 7.3 as follows:

$$\Delta_{oop} = 0 \qquad \text{if } DR \leq DR_{buckle} \tag{7.4}$$

$$\Delta_{oop} \approx \frac{L_{br}}{2}\sqrt{\frac{\sin 2\theta}{\eta} \cdot (DR - DR_{buckle})} \qquad \text{if } DR > DR_{buckle} \tag{7.5}$$

where DR_{buckle} is the DR value that initiates buckling of the brace, which was about 0.25% radian in the analyses.

Tremblay et al. [2003] derived a simplified relationship between the brace axial deformation and out-of-plane deformation. The relation is rewritten in Equation 7.6:

$$\Delta_{oop,Tremblay} = 0.7\sqrt{\Delta \cdot \cos\theta \cdot L_{br}} \ . \tag{7.6}$$

This relation provides a conservative estimate for a low DR demand while yielding accurate estimations of large deformations [Tremblay et al. 2003]. Figure 7.3 compares these simplified estimations and the analytical responses for archetype 3SCBFDmaxSAC. Equation 7.5 provides accurate estimations of Δ_{oop} for various DR demands, especially small ones. In other words, Equation 7.5 gives precise information to evaluate damage and loss in SCBF systems at various hazard levels for PBEE.

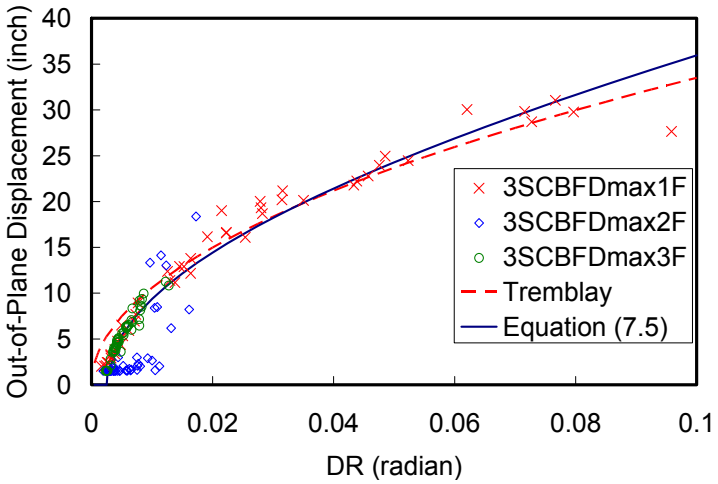

Figure 7.3 **Out-of-plane brace deformation of 3SCBFDmax under SAC ground motions versus predicted relationships.**

7.2.2 Ductility Demand

Local and global buckling of conventional braces results in damage concentration and limits the ductility capacity of the braces. We investigated the ductility demand of braces to aid the design of braced frame systems within the limitations of the brace ductility capacity. Figure 7.4 shows a typical hysteresis loop of a conventional buckling brace. In this section, the positive and negative ductility is defined and normalized by the yielding deformation of the brace.

Figure 7.5 shows the ductility demand of SCBF archetypes at various hazard levels. The data only included the non-collapse results. The distribution of the ductility demand was assumed to be lognormal. For the given SAC ground motions, most of the response of the SCBFs showed a larger ductility demand in the negative direction. For the MCE-level event, the maximum of negative median normalized brace ductility demand, exhibited by 3SCBFDmaxSAC, was 34.4. For the design-level event, this maximum was 14.9 and occurred in archetype 6SCBFDmaxSAC. The normalized median brace ductility demands of 6SCBFDmaxSAC were greater than those of 3SCBFDmaxSAC for the service-level and design-level events, but smaller for the MCE-level event. Archetype 16SCBFDmaxSAC had the smallest brace ductility demands for the three hazard levels; the normalized median brace ductility demand was 10.2 for the design-level event.

Figure 7.6 shows the ductility demands for the BRBF archetypes at various hazard levels. These show symmetrical responses in both the positive and negative directions. The median ductility demands of 3BRBFDmaxSAC and 6BRBFDmaxSAC were similar for the service-level and design-level events, but 3BRBFDmaxSAC demand exceeded 6BRBFDmaxSAC demand for the MCE-level event. The median brace ductility demands for the design-level event were 9.0 and 9.3 for archetypes 3BRBFDmaxSAC and 6BRBFDmaxSAC, respectively. Archetype 16BRBFDmaxSAC had the smallest brace ductility demand at all hazard levels. There was only a slight difference in median brace ductility demands for the service-level event, which were 3.18, 3.96, and 3.39 for 3-, 6-, and 16-story BRBF archetypes, respectively.

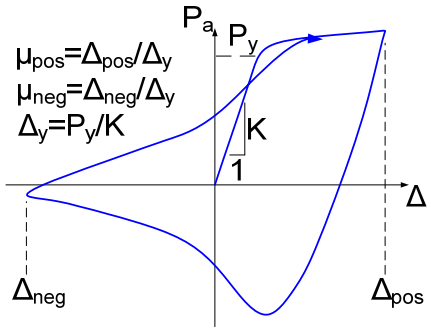

Figure 7.4 **Illustration of positive and negative ductility of a conventional buckling brace.**

A comparison of the SCBF and BRBF archetypes shows that the brace ductility demands of BRBFs were generally smaller at various hazard levels, with larger difference occurring between median and 84th percentile for the design-level and MCE-level events. The smaller brace ductility demands and better ductility performance of BRBFs may lead to a more reliable seismic resisting structural system for BRBFs compared to SCBFs.

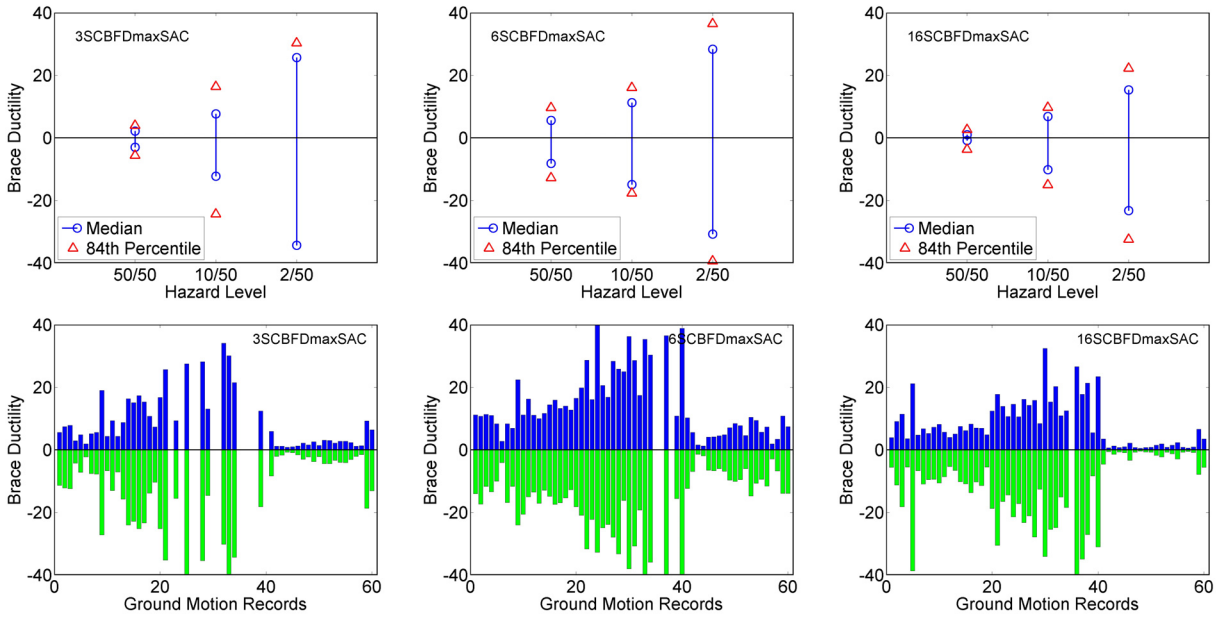

Figure 7.5 **Ductility demands of braces in SCBF archetypes under SAC ground motions corresponding to three hazard levels.**

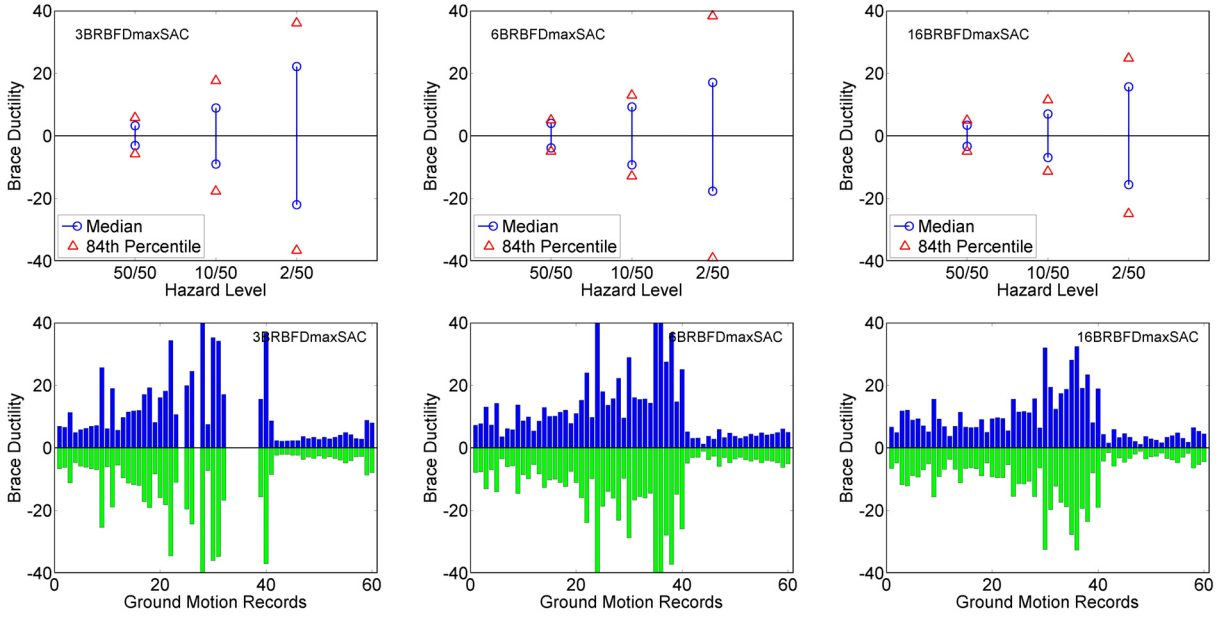

Figure 7.6 **Ductility demands of braces in BRBF archetypes under SAC ground motions corresponding to three hazard levels.**

7.2.3 Damage of Braces

The damage of each brace in the archetypes was monitored. The damage of each fiber at each modeled section was accumulated using the Rainflow cycle counting algorithm and Miner's rule, as discussed in Chapter 3. The normalized damage index DI [Uriz and Mahin 2008] at the modeled brace section is:

$$DI = \frac{\sum_{i=1}^{N} A_i \cdot DI_i}{\sum_{i=1}^{N} A_i}, \tag{7.7}$$

where A_i is the representative area of fiber i and DI_i is the damage index of fiber i. The maximum DI of the two braces in the same story is plotted in Figure 7.7. A DI of 1.0 represents the exhaustion of the fatigue life in a brace, that is, its complete rupture.

For 3SCBFDmaxSAC, the median brace damage indices were less than 0.04 for the service-level event in every story. For the design-level event, the median DI was 0.18 in the first story and less than 0.02 in the other stories. The variation of DI was large in the first story. The maximum DI in the first story for the design-level event was 0.87, meaning there was no complete rupture of the braces, but rupture was likely to have initiated. For the MCE-level event, the drift was concentrated more in the first story; therefore, the median DI in the first story was 1.0 but less than 0.05 for the other stories; the maximum DI values for the second and third story were smaller than those measured for the design-level event.

For 6SCBFDmaxSAC, the DI at the roof level was larger than at the other stories for the service-level and design-level events. Although the braces did not completely rupture in the service-level event, the median and maximum DI values for the 6th story were 0.22 and 0.89, respectively. The braces in the other stories had minor damage for the service-level event. For the design-level event, complete rupture of braces in the 6th story was observed during some earthquake excitations; therefore, the maximum DI for the 6th story was 1.0. The median DI values in all stories for the design-level event were similar to those for the service-level event, but they increased for all stories. For the MCE-level event, the median and maximum DI values for the 6th story were 0.16 and 1.0, respectively, similar to those for the design-level event (0.21 and 1.0, respectively). The damage was more concentrated in the lower stories, especially in the first story, where the median and maximum DI values were 0.77 and 1.0, respectively. The higher DI at the roof level showed that the deformation due to higher mode effects was greater for the 6-story SCBF archetype than for the 3-story SCBF archetype.

For 16SCBFDmaxSAC, the median DI values in all stories for the service-level and design-level events were less than 0.02. The maximum DI values occurred in the 3rd and 13th stories, where the story drift was concentrated. For the MCE-level event, some complete ruptures occurred at the 3rd and 4th stories; this was also the location where the DR was greater due to drift concentration. The maximum DI for the 13th story was 0.83; this level of damage may cause severe damage to braces in the event of an aftershock.

Compared to the SCBF archetypes, the BRBF archetypes showed more uniformly distributed DI in the braces along the height of the building. Also, the maximum DI among all the BRBF archetypes was less than 0.3, which occurred for the MCE-level event in the first story

of 3BRBFDmaxSAC. All DI values were less than 0.3 for 3BRBFDmaxSAC, 0.17 for 6BRBFDmaxSAC, and 0.1 for 16BRBFDmaxSAC for the MCE-level event.

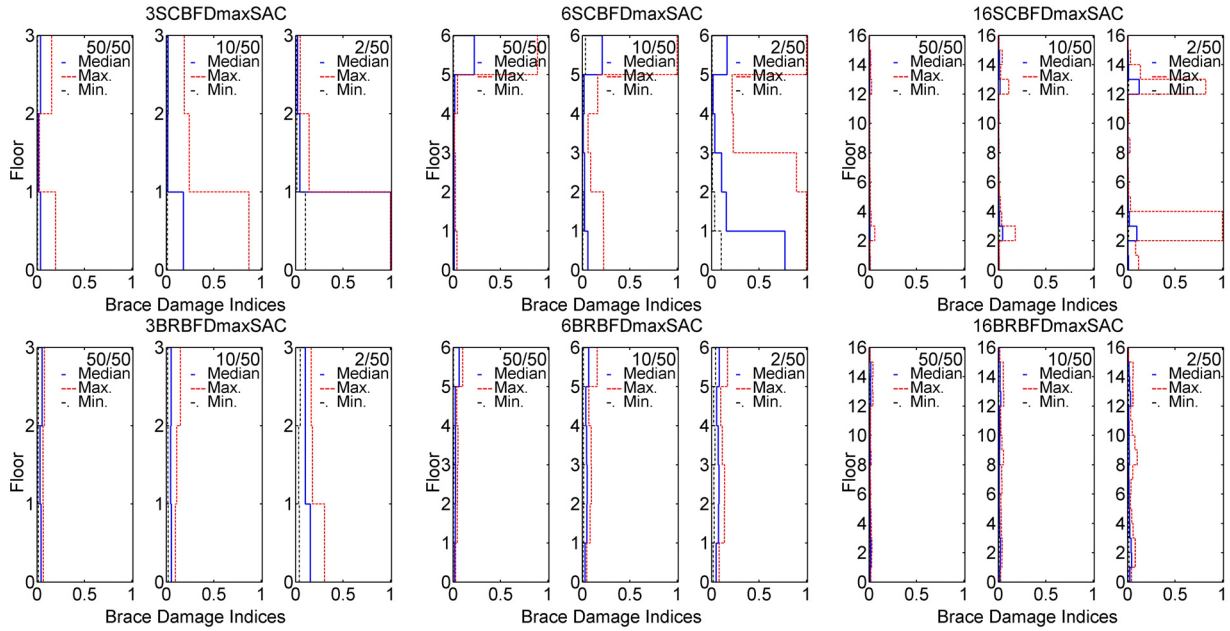

Figure 7.7 Profiles of brace damage indices of SCBF and BRBF archetypes under SAC ground motions corresponding to three hazard levels.

Figure 7.8 compares the damage indices for braces at the same story for various archetypes and hazard levels. Note that some values differ from the values of the envelope depicted in Figure 7.7 because the sample sizes were different for the two figures. The median DI values for the two braces in the same story were almost identical for most of the archetypes. The maximum DI profile of the BRBF archetypes was symmetric, but that of SCBF archetypes showed some asymmetric distribution. For those stories where one brace ruptured completely (DI = 1.0), the other brace usually also ruptured except for some instances in 16SCBFDmaxSAC. The right braces in the 3rd and 4th story of 16SCBFDmaxSAC ruptured completely, but the maximum DI in the left brace was only 0.27 for the 3rd story and 0.05 for the 4th story. The drift concentration for a few ground motions resulted in an asymmetric profile of the brace damage in the SCBF archetypes. For the BRBF archetypes, the brace damage distribution along the height showed a uniform and symmetric response at various hazard levels.

Figure 7.9 shows an approximately linear relationship between brace damage indices and DRmax for all archetypes; the responses from all stories were plotted together. The data demonstrate that few DI data points were between 0.3 and 0.6, with most readings below 0.3 or close to 1.0. In other words, in most cases, the braces had either not reached a 30% level of fatigue or were near rupture. For 6SCBFDmaxSAC, the DI values were usually less than 0.3 when DR was less than 2.0%, but when DR was greater than 2.0%, many DI values became 1.0.

Among the SCBF archetypes, 6SCBFDmaxSAC showed the steepest slope in the relationship between brace damage indices and DRmax. Data points where the brace damage indices were large but with small DRmax resulted in a steeper relationship, which usually occurred at the 6th story.

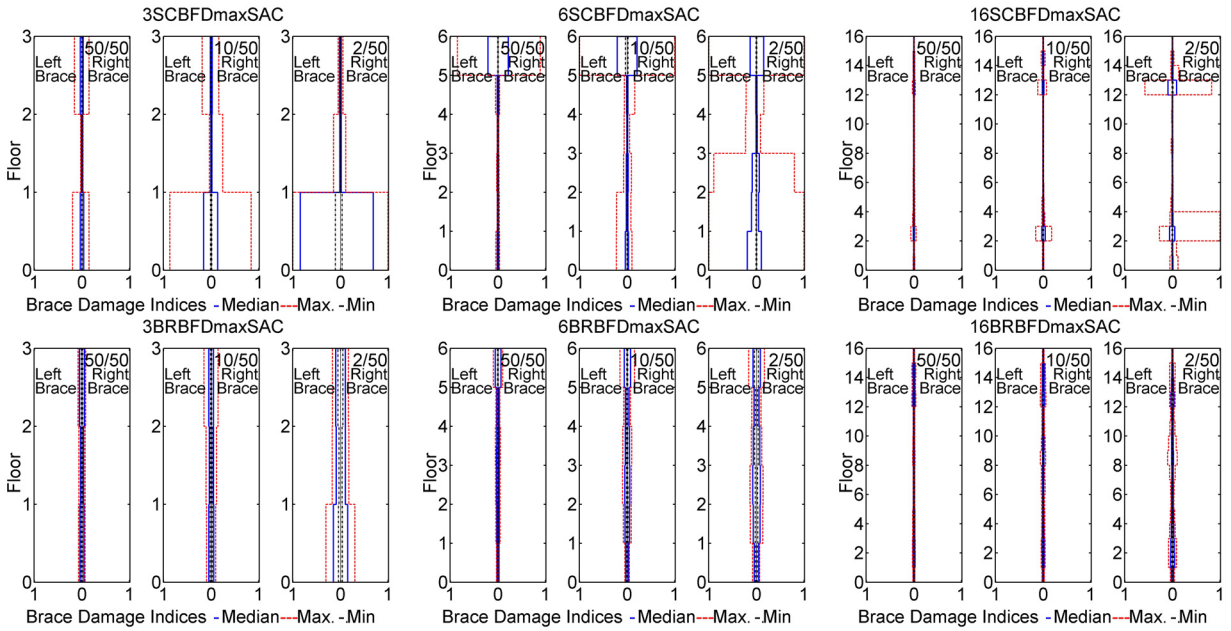

Figure 7.8 **Comparison of brace damage indices of two braces at the same level in SCBF and BRBF archetypes under SAC ground motions corresponding to three hazard levels.**

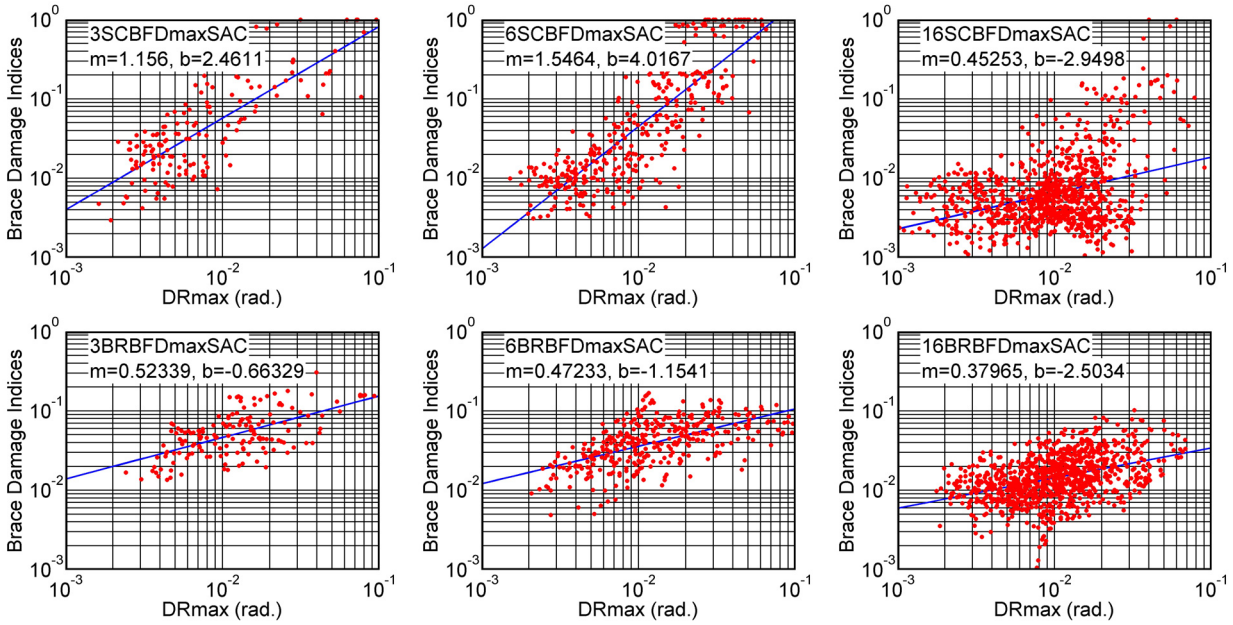

Figure 7.9 **Relationship between the maximum brace damage indices of a story and DRmax for all archetypes.**

Figure 7.10 shows the story drift histories and brace axial deformation histories of various SCBF archetypes under the excitation of LA09. In general, brace damage usually occurs as (1) damage with only few large excursions and several small ones, such as the response of the first story in 3SCBFDmaxSAC, the first story in 6SCBFDmaxSAC, and the third story in 16SCBFDmaxSAC; or (2) damage with several median-range excursions, such as the responses

of the 6th story in 6SCBFDmaxSAC. The brace axial deformation histories at the 6th story of 6SCBFDmaxSAC showed many excursions with about ±2 inch deformation range. These cycles resulted in severe damage to the braces (DI close to 1.0) without an extreme DRmax. Higher mode effects may contribute to such responses, as in the 6th story in 6SCBFDmaxSAC. The responses of the 3rd story in 3SCBFDmaxSAC and the 13th story in 16SCBFDmaxSAC showed higher-frequency and lower-frequency excitations, respectively, but the story drift was smaller than that in the 6th story in 6SCBFDmaxSAC and the brace damage indices were also smaller. Although DR is often used as a quick estimation of brace damage, the brace damage index is a more precise measurement.

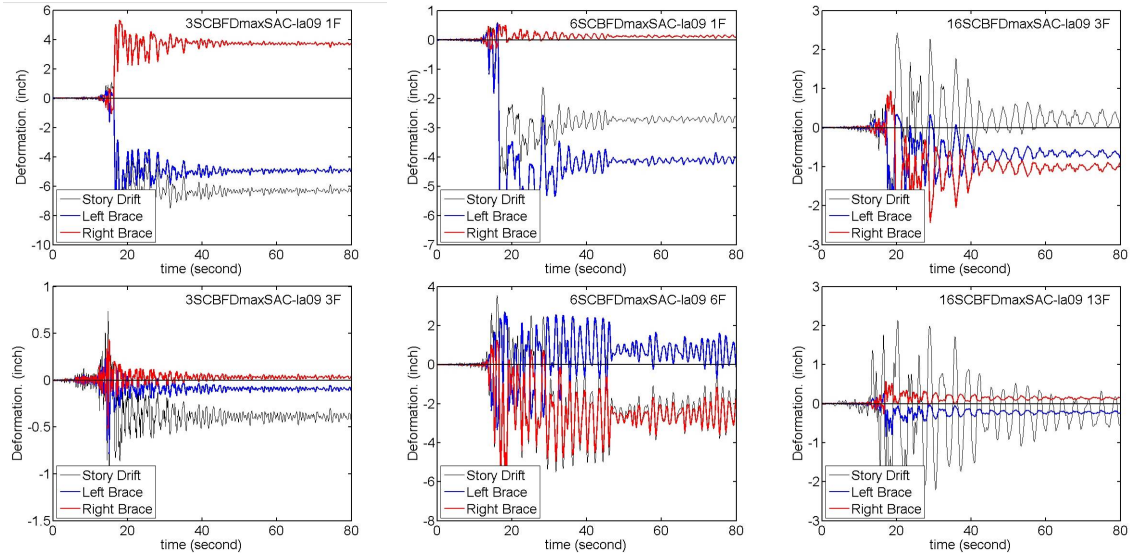

Figure 7.10 Story drift history and brace deformation history of SCBF archetypes subjected to ground motion LA09.

7.3 BEHAVIOR AND DEMANDS FOR BEAMS

For beams, the flexural moment demands are generally expected to be more critical than the axial force demand. The beam design for our archetype buildings considered the potential axial force demand from braces, such as unbalanced loads in chevron braced frames. The structural designs of the archetypes are described in Appendix A. This section discusses the axial force demands, flexural moment demands, and deformation demands in the middle span of the beams where the braces connect in the double-story X configuration.

7.3.1 Beam Axial Force Demand

The axial force demands in the beams of braced frames in the elastic range are expected to be small. The force demands come from the lateral forces (collectors) and the forces transferred from the braces. In the double-story X configuration, forces transferred from the braces are usually transferred to braces in adjacent stories or to columns rather than beams. Thus the design of these beams is usually not governed by the possible force demand or capacity of the braces and only accounts for the load combinations of dead load, live load, seismic load, etc. However,

when the braces yield, buckle, and degrade, the force of the braces in adjacent stories needs to be transferred by the beams.

Figure 7.11 shows the maximum axial force of the beams at different levels under different ground motion excitations for different archetypes. The beams of the odd stories have intersected braces in the middle span, and those of the even stories have braces connected in the beam-column connections.

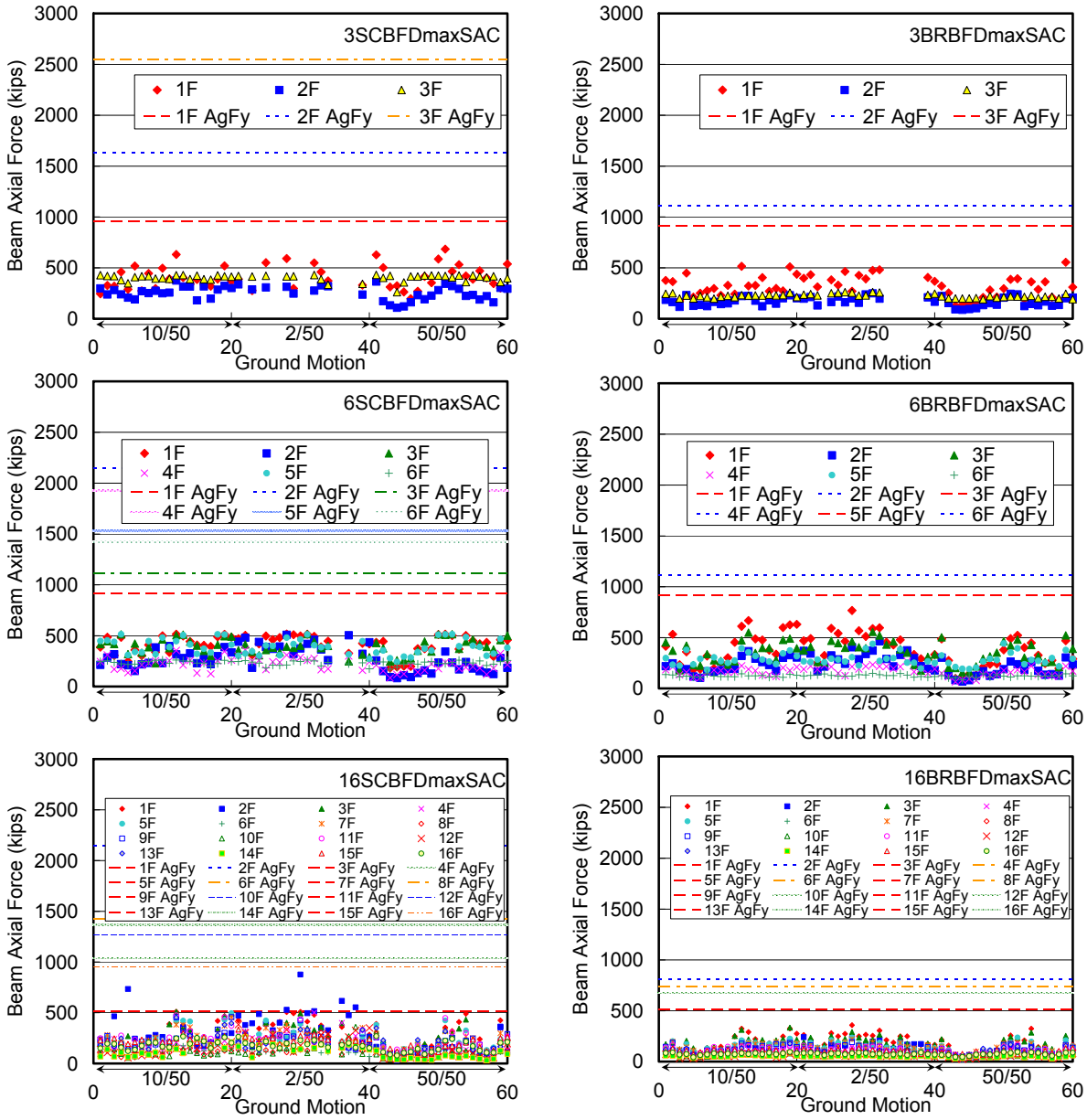

Figure 7.11 Maximum beam axial forces of SCBF and BRBF archetypes under SAC ground motions.

For the beams in odd stories, if the strength capacities of the braces on adjacent floors are similar, then the unbalanced load applied to the beams in design is canceled out. The force demands to consider when designing such beams are small. Because of the conservative design

of the archetypes, for beams in even stories large axial forces were developed to enable the complete yielding of the tension braces and 30% capacity of the compressive brace in two adjacent stories. For most of the responses of the archetypes, the beam axial forces did not exceed the capacity of the beams in odd stories where the demand for design was relatively small. The responses also showed that the axial force demands of beams were greater in the lower stories. Generally, the axial force demands in SCBF archetypes were slightly greater than in BRBF archetypes. For stories where the drift was concentrated, the demands were greater for both SCBF and BRBF archetypes. There were a few instances in 16SCBFDmaxSAC where the damage was concentrated in certain stories. Many of the maximum beam axial force demands in 16SCBFDmaxSAC approached the capacity of the second floor beam (first story, 1F), which was designed for relatively small demand. Some of the data from the 3rd floor beam (second story, 2F) showed a greater demand than the capacity of the second floor beam. In summary, for the design of beams in even stories, the estimation of beam axial forces demand was very conservative by considering the full capacity of braces on adjacent floors. For the design of beams in odd stories, the estimation of beam axial forces demand was appropriate by considering the full capacity of braces in adjacent stories unless severe drift concentration occurred.

Figure 7.12 shows the median and maximum of the beam axial force demands for SCBF and BRBF archetypes at different hazard levels. The median axial force demands were about 40% of capacity (A_gF_y) in the odd stories and about 10% to 15% in even stories for all archetypes. The beam design for all archetypes estimated the axial force demands by accounting for brace yielding and buckling at extreme conditions, which resulted in greater axial force demands of beams in even stories than those in odd stories. However, the profile of beam axial force demand under ground motion excitations showed a different trend. The estimations of beam axial force demand for design were much greater than the dynamic responses of the archetypes.

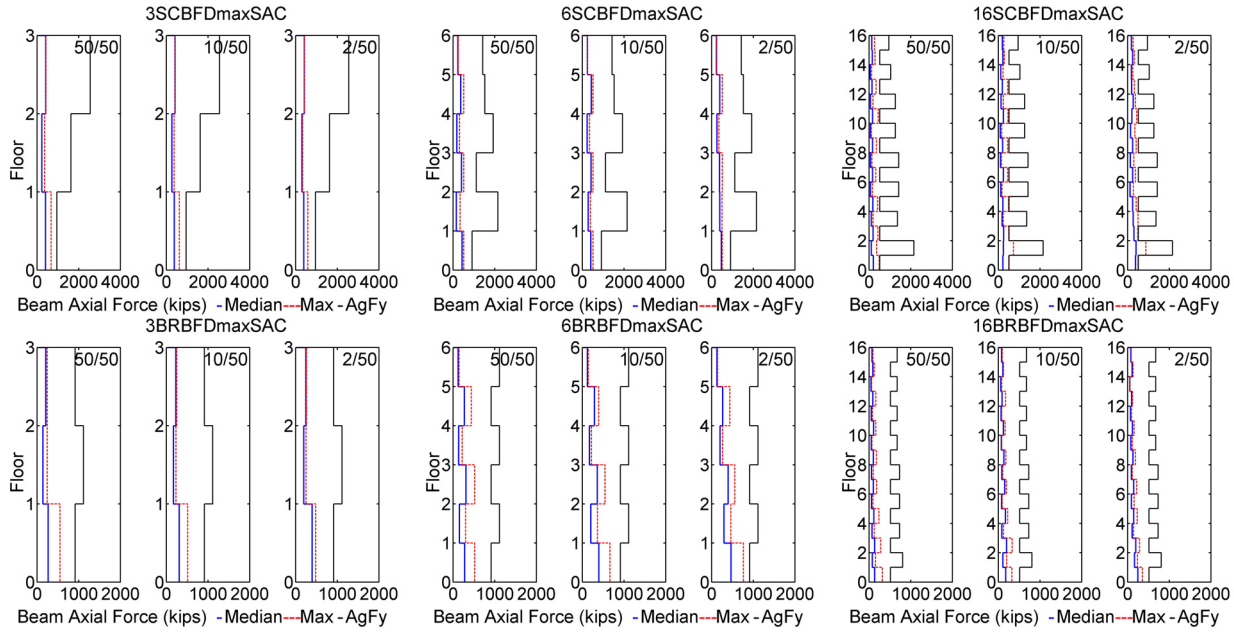

Figure 7.12 Profiles of beam axial forces of SCBF and BRBF archetypes under SAC ground motions corresponding to three hazard levels.

7.3.2 Beam Flexural Moment Demand

The profile of moment demands in beams of all the archetypes is shown in Figure 7.13. For 3SCBFDmaxSAC, the median and maximum of moment demands in the first story were approximately equal to the moment capacity of the first story for the design-level and MCE-level events, while those on the second and third stories were about 30% of the moment capacity. At various hazard levels for 6SCBFDmaxSAC, none of the beams reached their moment capacity because this design had a relatively uniform drift distribution and the force demands were also distributed more uniformly along the height. For 16SCBFDmaxSAC, the drift was concentrated in the 3rd and 13th stories for the design-level and MCE-level events, resulting in highly nonlinear behavior on those floors; the beam moment demands for these stories reached the beam capacity.

The properties of the beam moment demands profile for the BRBF archetypes differed from those of the SCBF archetypes. For 3BRBFDmaxSAC and 6BRBFDmaxSAC, these profiles were rather uniform at the three hazard levels; for the design-level and MCE-level events, the medians, maxima, and beam capacity were similar in the lower stories. For 16BRBFDmaxSAC for the design-level event, all the medians of beam moment demands were below the moment capacity, but the maxima of beam moment demands almost coincided with the moment capacity; for the MCE-level event, the medians, maxima, and beam moment capacity were almost identical except for the top few floors. Because of strain hardening, some of the maxima exceeded the capacity of the beam moments.

The difference between the maximum beam moment demand and capacity demonstrates that beam moment demand reached capacity in many stories for the BRBF archetypes for the design-level and MCE-level events. Given that, it would be expected that the BRBF archetypes experienced more nonlinear flexural behavior of beams, dissipating more energy through beam plastic rotations than their SCBF counterparts. The magnitude of beam moment demands were also greater in the BRBF archetypes.

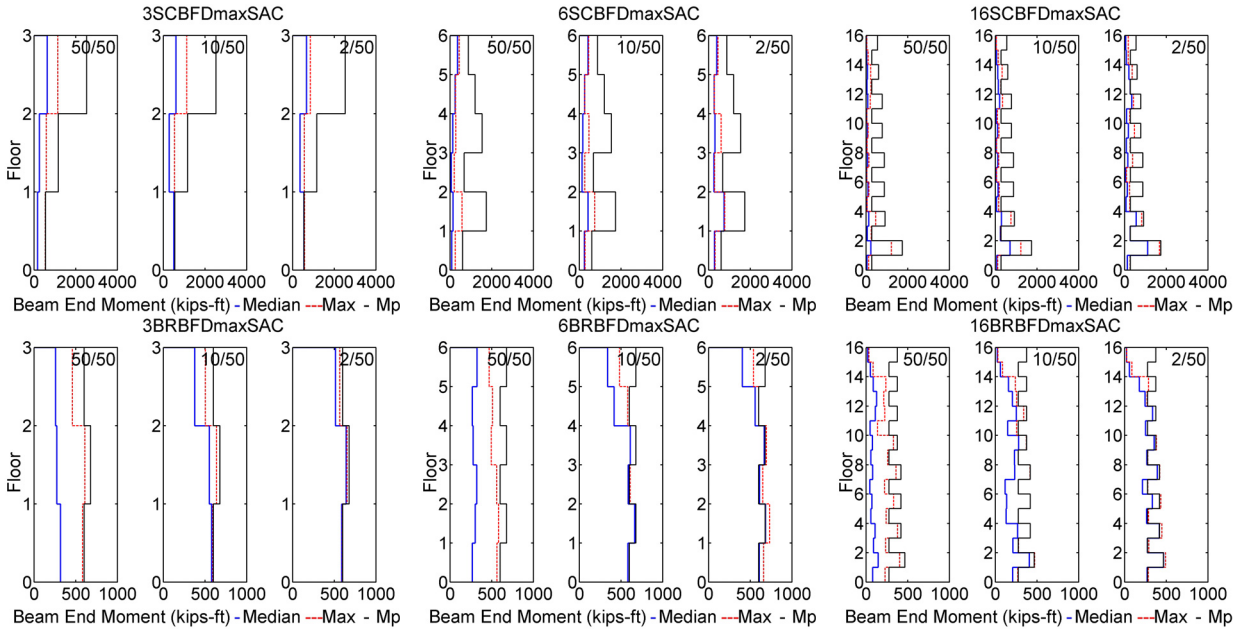

Figure 7.13 Profiles of beam end moments of SCBF and BRBF archetypes under SAC ground motions corresponding to three hazard levels.

7.3.3 P-M Relationship of Beams

While the medians and maxima of beam axial force and moment demands provided these peak responses independently, it was more common that the axial forces and moments interacted, and the peak responses of beam axial force and moment demands did not occur at the same time. Figure 7.14 shows examples of the P-M demands of beams in the first story for all archetypes under the excitation of LA09. In the first story of 3SCBFDmaxSAC, although the beam axial force was below 20% of the beam axial force capacity most of the time, at some instants it was more than 30% of capacity. The left beam at the left end, which is the beam-column connection, and the right beam in the middle span reached the moment capacity (M_p) in this example. In the first story of 6SCBFDmaxSAC, the responses of beam axial force demand were similar to those in 3SCBFDmaxSAC with one difference. The moment demands at all beam ends were about 50% of the beam moment capacity; the left beam at the left end and the right beam in the middle span had similar moment demands. In the first story of 16SCBFDmaxSAC, the beam axial force demand was about half that of 3SCBFDmaxSAC and 6SCBFDmaxSAC, and the beam moment demand was much smaller than in the 3- and 6-story counterparts; the beam moment demand was about 20% of the capacity. Clearly for 16SCBFDmaxSAC the beam moment demands were higher at beam-column connections (i.e. at the left end of the left beam and right end of the right beam) than the moment demand in the middle span of these beams.

The P-M responses of BRBF archetypes show more consistency among different archetypes; the beam axial force demands were all about 20% of capacity and beam moment demands all reached capacity in the three archetypes. For all BRBF archetypes, the inelastic behavior and moment demands were concentrated at beam-column connections rather than at the middle span of the beams.

The archetypes were designed with double-story X configuration, which reduced the unbalanced load in beams. In SCBF archetypes, although the unbalanced load was reduced, its effects still cannot be ignored in beam design. Under the unbalanced load, the moment demands in the middle span of the beams were about the same magnitude as the moment demand in the ends of the beams, as shown in the first story of 3SCBFDmaxSAC and 6SCBFDmaxSAC. For 16SCBFDmaxSAC, because the deformation and force demands were smaller, the unbalanced loads were usually small and the moment demands in the ends of the beams were greater than those in the middle span of beams; only the floors that had a higher deformation demand had similar beam moment demands in the middle and ends of the beams. In the BRBF archetypes, the unbalanced loads had little effect on the beam moment demands in the middle span of beams; all of these beam moment demands were far smaller than those in the ends of the beams.

Figure 7.15 shows the P-M relation of the beams on the second story. The beam axial force demands were about 10% of the capacity, and the beam moment demands dominated the behavior of the second story in all SCBF and BRBF archetypes. The response loops in the SCBF archetypes were relatively small because the capacity of these beams was much greater than the demands. In fact, the maximum beam moment demand of 6SCBFDmaxSAC was similar to that of 6BRBFDmaxSAC (about 700 kips-ft), the maximum beam moment demand of 3SCBFDmaxSAC was smaller than that of 3BRBFDmaxSAC, and the maximum beam moment demand of 16SCBFDmaxSAC was greater than that of 16BRBFDmaxSAC. For the even stories, the beam moment demands in SCBF and BRBF archetypes were similar.

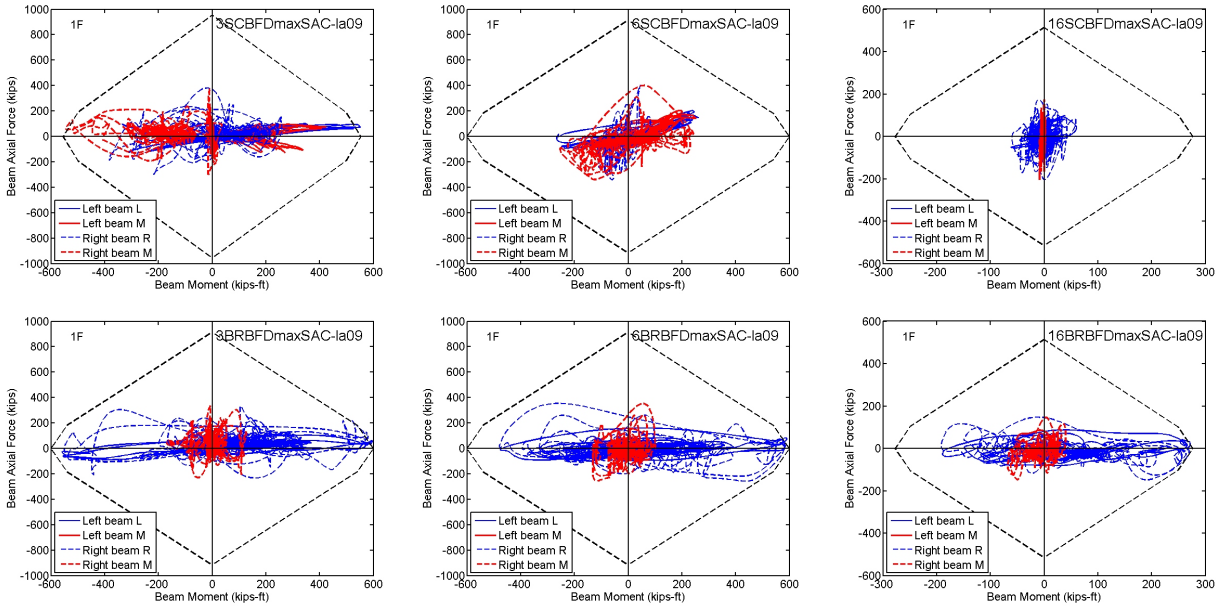

Figure 7.14 P-M interactions of the beams in the first story of SCBF and BRBF archetypes under the excitation of SAC ground motion LA09.

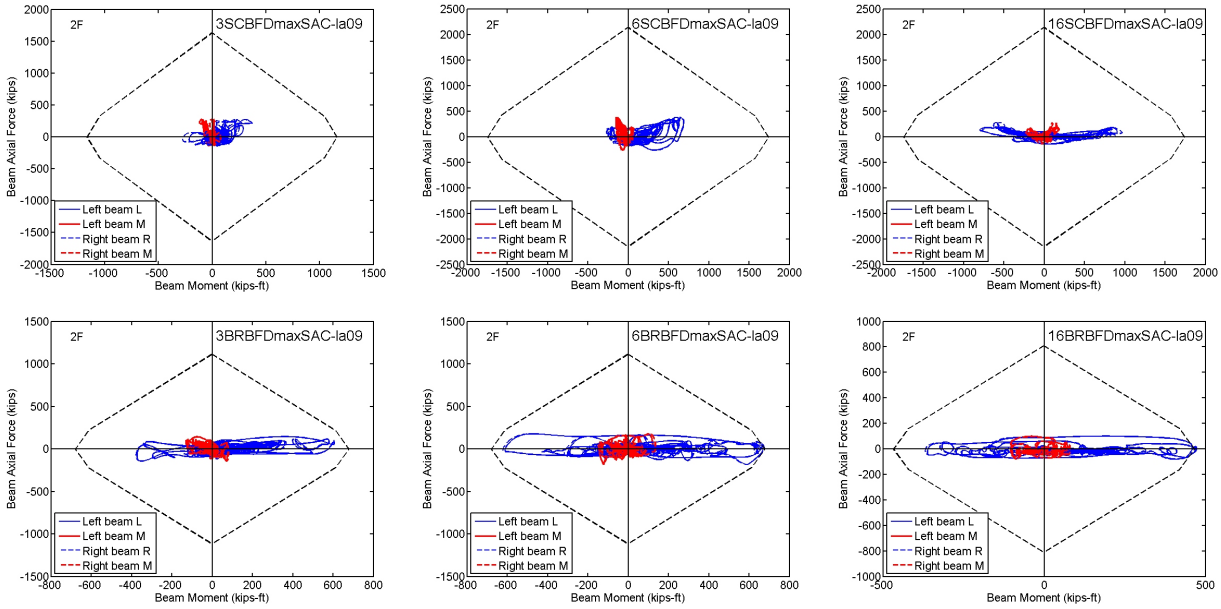

Figure 7.15 P-M interactions of the beams in the second story of SCBF and BRBF archetypes under the excitation of SAC ground motion LA09.

7.3.4 Vertical Displacement in the Middle Span

In chevron braced frames, beams are designed to resist the unbalanced loads due to yielding and buckling of the braces. In double-story X configuration, these unbalanced loads are expected to be small. However, some of the analytical results show that the vertical deformation in the middle span of beams where the braces intersect should not be neglected. These beams are

designed considering the brace capacity difference, which is small, on adjacent floors. However, when one of the braces intersected in a beam yields, buckles, or loses its strength capacity, the unbalanced loads in the beam increase leading to a large mid-span vertical displacement.

Figure 7.16 shows the median vertical deformation in the middle span of the beams in the odd stories for all SCBF and BRBF archetypes at different hazard levels. For the service-level event, the median vertical deformations were small, with the maximum deformation of about 0.2 inch occurring in the first and third stories of 3SCBFDmaxSAC.

For the design-level event, the median vertical deformations were more than 1.0 inch and 1.5 inches in the first story of 3SCBFDmaxSAC and 6SCBFDmaxSAC, respectively. The vertical deformation of 1.0 inch in the middle span of the beam corresponded to about 0.5% drift ratio in the beam-column connections. In such cases, the deformation demands of the beam-column connections increase by 0.5% radian. Note that the beam vertical deformations in 16SCBFDmaxSAC were relatively large in the stories where the DR was concentrated; the beam vertical deformations were 0.78 inch and 0.22 inch in the 3rd and 13th story, respectively, for the design-level event. Although this amount of vertical deformation in 16SCBFDmaxSAC may not increase the structural damage to a large extent, it may cause nonstructural damage that cannot be ignored.

For the MCE-level event, the median vertical deformation was as high as 3.93 inches on the first floor of 6SCBFDmaxSAC, which corresponded to about 2% drift ratio in the beam-column connections; this increased the deformation demands of the beam-column connections by a large amount, thereby increasing the risk of damage to them. Other large median vertical deformations in the middle span of beams for the MCE-level event occurred in the third story of 6SCBFDmaxSAC (2.15 inches), in the third story of 16SCBFDmaxSAC (1.82 inches), in the first story of 3SCBFDmaxSAC (1.45 inches), and in the 13th story of 16SCBFDmaxSAC (1.1 inches).

In general, the large median vertical deformations in beams occurred on the floors where the DI values of braces had greater differences between adjacent stories (see Figure 7.7). When one of the braces intersected in the beam yielded, buckled, or degraded, the unbalanced load was likely to cause large mid-span deformation in the beam.

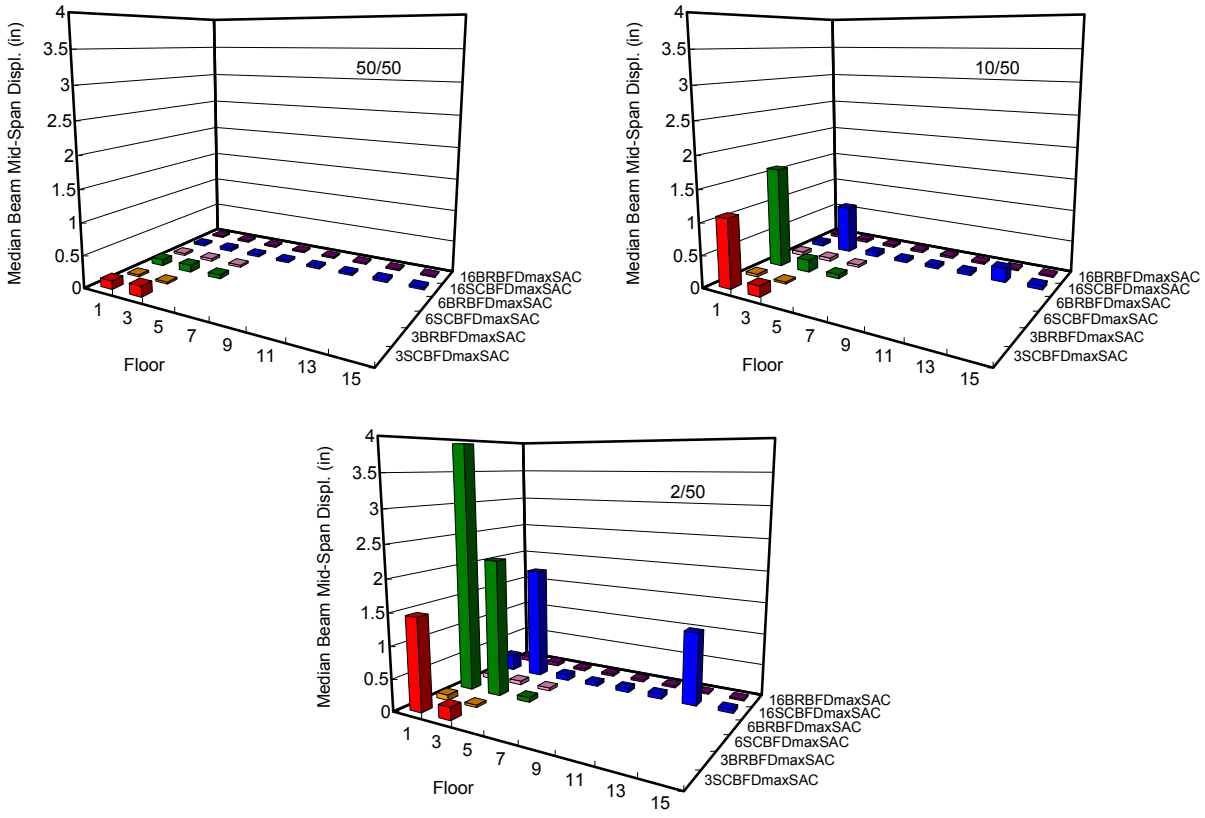

Figure 7.16 Median vertical deformations in the middle span of beams in odd stories in SCBF and BRBF archetypes under SAC ground motions corresponding to three hazard levels.

7.4 BEHAVIOR AND DEMANDS FOR COLUMNS

Columns are one of the most critical structural components that protect buildings from collapse. This section discusses column axial force demands (compression and tension), column moment demands, and P-M relationships.

7.4.1 Column Axial Force Demand

Axial force is one of the primary components of the ability of columns to resist lateral forces. Axial force demand usually governs the design of columns. Here we extract the column axial force demands from the responses to the combinations of gravity loads and lateral seismic loads, and isolate the responses to lateral seismic loads.

Figure 7.17 shows the median column axial force demands under various hazard levels. Positive values represent tensile axial force demands and negative ones represent compressive axial force demands. For all the 3-story and 6-story archetypes, the medians and maxima of column axial force demands were similar at the same story, and the values were almost identical for various hazard levels. Clearly, the column axial force demands of 3-story and 6-story archetypes were bounded as the medians and maxima coincided with each other. In 16SCBFDmaxSAC, while the maxima of column axial forces were similar to the capacity at all

hazard levels, the medians increased as the hazard level increased from the service-level event to the design-level and MCE-level events. The maximum axial force demands in 16SCBFDmaxSAC reached the capacity of the columns for the design-level and MCE-level events on almost all floors. In 16BRBFDmaxSAC, the maximum column axial force demands barely changed with the hazard levels and were about 40% of the column axial force capacity. Here, the median column axial force demands were smaller than the maximum column axial force demands for the service-level event, but similar to the maximum column axial force demands for the design-level and MCE-level events.

The profile of the column axial force demands shows that these demands change every two stories. The double-story X configuration contributes to this profile. More specifically, the column axial force demands are related to the force demands and capacity of braces.

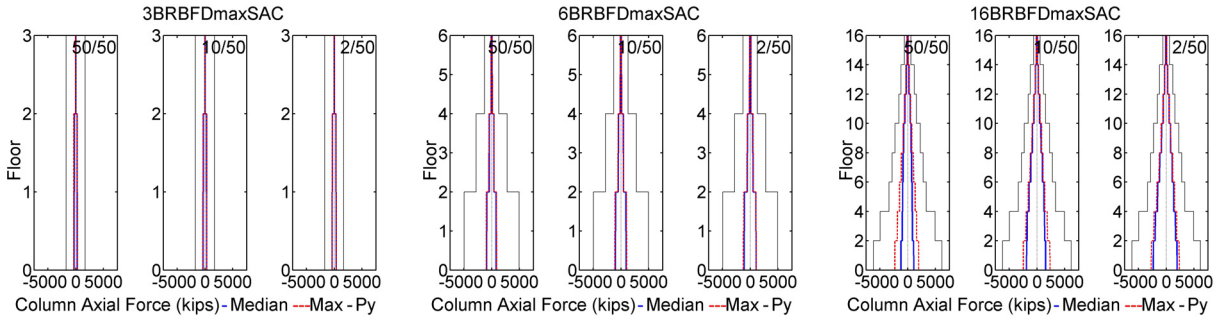

Figure 7.17 Profiles of axial forces in columns of SCBF and BRBF archetypes under SAC ground motions corresponding to three hazard levels.

7.4.2 Column Flexural Moment Demand

Figure 7.18 shows the column moment demands of all archetypes at different hazard levels, displaying only the maxima of the top and bottom ends of the column in the same story. In 3SCBFDmaxSAC and 3BRBFDmaxSAC at all hazard levels, the maxima of the column moment demands reached the capacity at the first story. For the 6- and 16-story archetypes, the median column moment demands increased, in general, as the hazard level changed from the service-level event to the design- and MCE-level events. For 3SCBFDmaxSAC for the service-level event, the median column moment demand in the third story was slightly greater than that measured in the second story. For 6SCBFDmaxSAC, the median and maximum column moment demands increased along with the hazard levels. For the MCE-level event, the maximum column moment demands reached capacity at odd stories, where the column section changed. In higher stories of 6SCBFDmaxSAC, the column moment demands were small but approached the column moment capacity for all three hazard levels. The trends for 6BRBFDmaxSAC and 6SCBFDmaxSAC were similar. In 16SCBFDmaxSAC and 16BRBFDmaxSAC, the median column moment demands were less than 800 kips-ft, which is about 40% of the column moment capacity, on the stories higher than the 5th story at all hazard levels. In the first stories of the 16-story archetypes, the maximum column moment demands were less than 80% of column moment capacity for the design-level event. The maximum column moment demands reached the 95% and 100% of column moment capacity in the first stories of 16SCBFDmax and 16BRBFDmax, respectively, for the MCE-level event.

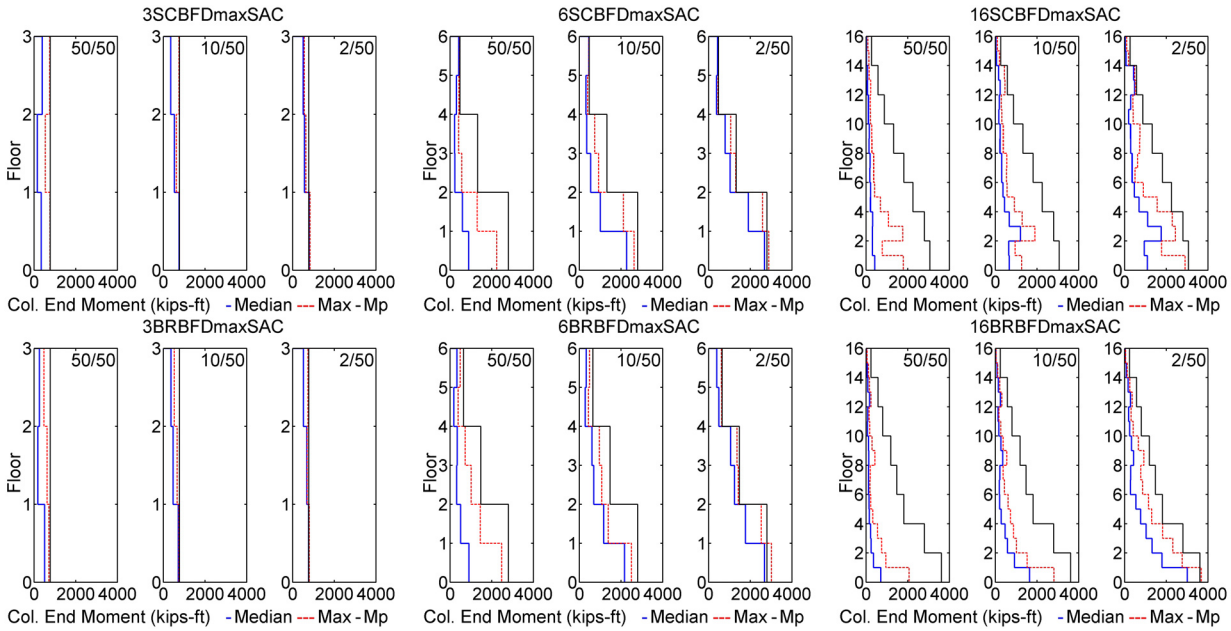

Figure 7.18 Profiles of column end moment of SCBF and BRBF archetypes under SAC ground motions corresponding to three hazard levels.

7.4.3 P-M Relationship of Columns

Figure 7.19 shows the P-M relationship of the columns in the first story of all archetypes under the LA09 excitation. For the SCBF archetypes, the column axial force demand was about 600 kips in 3SCBFDmaxSAC, 2000 kips in 6SCBFDmaxSAC, and 5000 kips in 16SCBFDmaxSAC. For 3SCBFDmaxSAC, the column axial force demand was about 30% of the column axial force capacity. The column moment demands of 3SCBFDmaxSAC reached the P-M envelope in both left and right columns at both top and bottom ends. For 6SCBFDmaxSAC, the column axial force demand was about 40% of the column axial force capacity. While the column moment demands at the bottom end of the columns of 6SCBFDmaxSAC reached the column moment capacity, those at the top ends were about 30% of the column moment capacity. For 16SCBFDmaxSAC, the P-M response obviously differed from those in 3SCBFDmaxSAC and 6SCBFDmaxSAC. The columns on the first story were subjected to large axial force demands to resist lateral forces in this high-rise building. The column moment demand was about 10% of column moment capacity.

In the BRBF archetypes, the column axial force demand was about 300 kips in 3BRBFDmaxSAC, 1000 kips in 6BRBFDmaxSAC, and 2500 kips in 16BRBFDmaxSAC. For 3BRBFDmaxSAC, the column moment demands reached the P-M envelope in both left and right columns at both the top and bottom ends. For 6BRBFdmaxSAC, the column axial force demand was about 20% of the column axial force capacity, and the column moment demands were all under the P-M envelope. For 16BRBFDmaxSAC, the column axial force demands of the columns were not as high as those found in 16SCBFDmaxSAC, but the column moment demand at the bottom of the column reached the P-M envelope. The 16-story BRBF archetype obviously had a greater column moment demand under the same ground motion excitation than its SCBF counterparts; the column responses of 16BRBFDmaxSAC exhibited greater flexural behavior and those of 16SCBFDmaxSAC exhibited greater tensile and compressive behavior.

Figure 7.20 shows the P-M relationships of the columns in the second story for all archetypes under LA09 ground motion excitation of. The axial force demands were about the same as those in the first story, as the axial force demands changed approximately every two stories. The column moment demands were lower than in the first story for most of the archetypes, except in the case of 16SCBFDmaxSAC. The responses show that the bottom of the columns usually had slightly greater moment demands than the top of the columns in all archetypes.

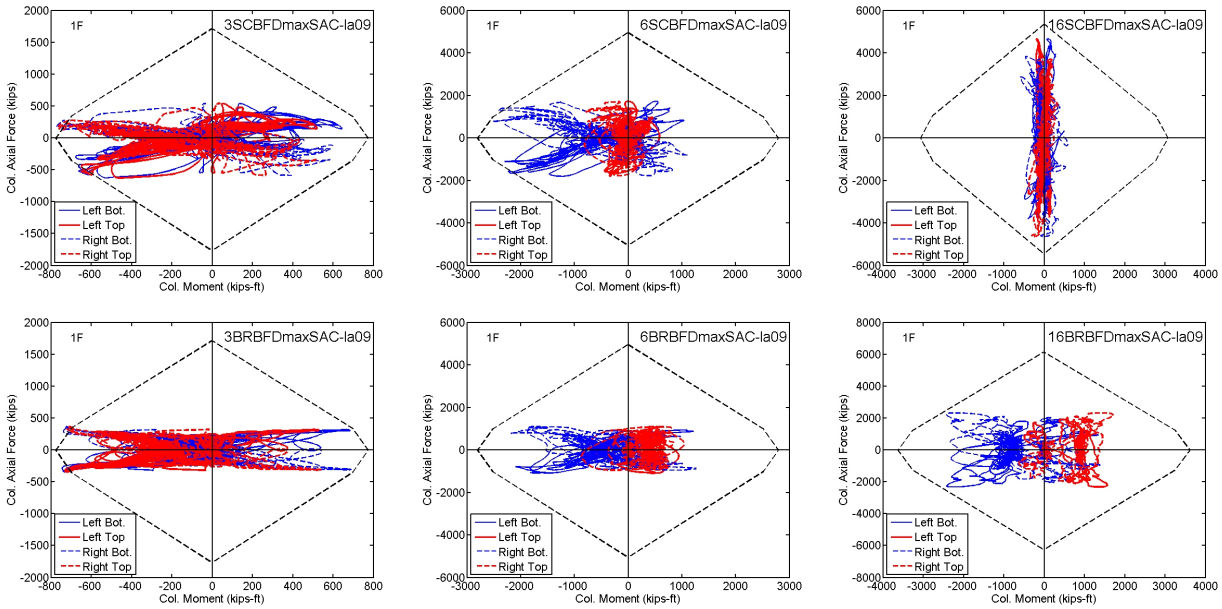

Figure 7.19 P-M interactions of the columns in the first story of SCBF and BRBF archetypes under the excitation of SAC ground motion LA09.

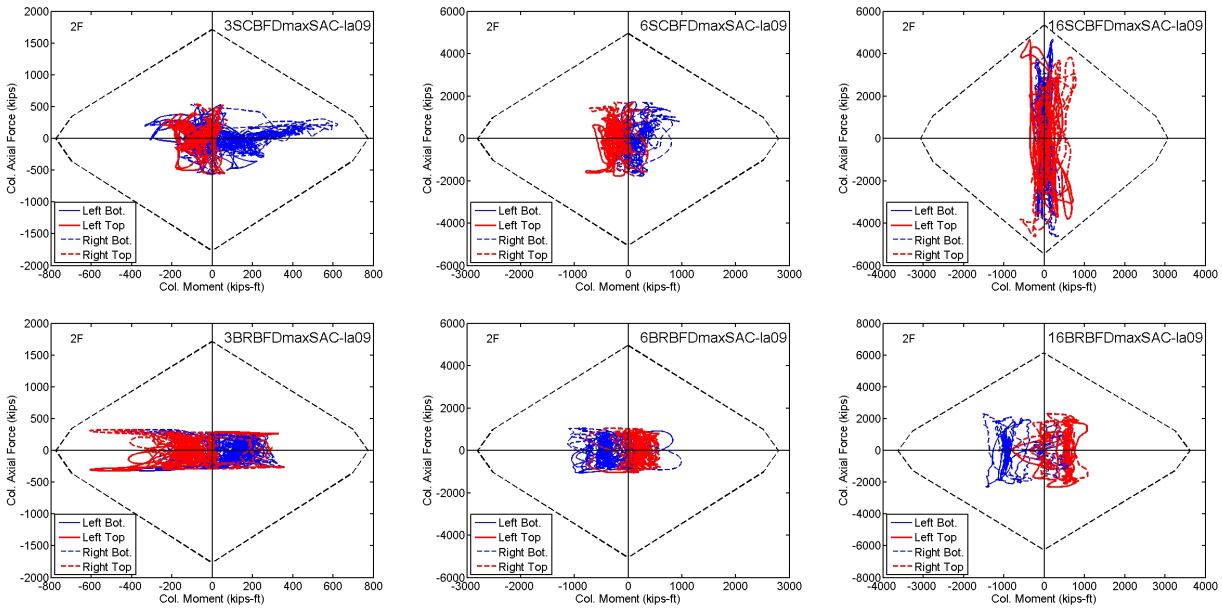

Figure 7.20 P-M interactions of the columns in the second story of SCBF and BRBF archetypes under the excitation of SAC ground motion LA09.

7.4.4 Estimation of Column Compression Force Demand

The column axial force demands were bounded and changed every two stories, as shown in Figure 7.17. Here we discuss the accurate estimation of the column demands based on the capacity and demands of the braces and beams. In the SCBF archetypes, the force demands in the braces reached the capacity in some stories and usually not in all stories. A conservative estimate of column axial demands for design would consider the full capacity of braces and beams in all stories. Figure 7.21 illustrates the design estimation of the upper bound of column force demand, which is the sum of the brace and the beam capacity of the upper floors. In the double-story X configuration, the estimate was calculated differently for the odd stories than for the even stories. The vertical component of brace in story j can be expressed as:

$$V_{br,j} = P_{br,j} \cdot \sin\theta \tag{7.8}$$

where $P_{br,j} = \begin{cases} P_{cr} & j = 1,3,5,... \\ P_y & j = 2,4,6,... \end{cases}$ and θ is the incline angle of the brace with respect to the horizontal.

Accordingly, the column axial force demand in story i was estimated as the sum of the demands of the braces and beams in all upper stories:

$$P_{col,i} = \begin{cases} \sum_{j=i+1}^{\#story} (V_{br,j} + V_{b,j}) + V_{b,i} & i = 1,3,5,... \\ \sum_{j=i}^{\#story} (V_{br,j} + V_{b,j}) & i = 2,4,6,... \end{cases} \tag{7.9}$$

Note that the difference between $P_{col,1}$ and $P_{col,2}$ was only $V_{b,1}$, that between $P_{col,3}$ and $P_{col,4}$ was only $V_{b,2}$, and so forth.

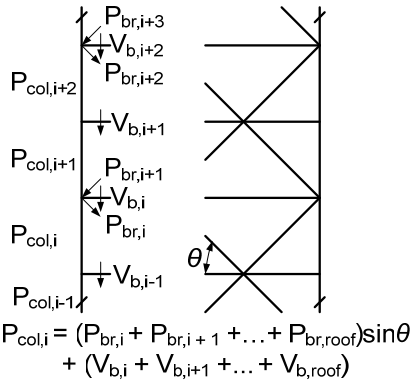

Figure 7.21 Estimation of column axial force demands.

The previous analysis of the demands in beams and braces demonstrated that the demands were usually smaller than the corresponding capacity, although the demands did reach the capacity in some stories under some ground motion excitations. To estimate the column axial force, the reduction factor in Equation 7.10 for the brace capacity of upper stories was adopted. To estimate the axial force demand of column on floor *i*, the reduction factor was applied to each upper story (from story *i* to the roof level). The reduction factor was proposed to account for the full brace capacity on the floor in question, while decreasing exponentially with the power of k for the higher floors (which varies depending on the archetypes).

For the 3- and 6-story archetypes, the k factor was taken as a large number such that the reduction factor ϕ_{ji} was 1.0 for all the upper floors to be considered, i.e., the full brace capacity of upper floors were used to estimate column axial demands. For the 16-story archetypes, the reduction factor changed along the height, reducing the brace capacity for estimation of column axial force demands for the higher floors. At the instant when the maximum column axial force demands occurred in a story, the force demands in the other upper stories were usually not the maximum demands. What was more common was that the force demands in some upper stories reached the corresponding force capacity but remained small in other stories. The reduction factor was assigned to maximize the possible braces strength but reduce the braces strength on some floors as necessary for estimating column demands. In other words, the reduction factor was greater for the braces in the lower stories (with larger capacity) and less in the higher stories:

$$\phi_{ji} = 1 - \left(\frac{j-i}{\#story} \right)^k \qquad j \geq i \,. \tag{7.10}$$

If we apply the reduction factor for the braces, the column axial force demands can be rewritten as:

$$P_{col,i} = \begin{cases} \sum_{j=i+1}^{\#story} (V_{br,j} \cdot \phi_{ji} + V_{b,j}) + V_{b,i} & i = 1,3,5,... \\ \sum_{j=i}^{\#story} (V_{br,j} \cdot \phi_{ji} + V_{b,j}) & i = 2,4,6,... \end{cases} \tag{7.11}$$

where V_b depends on the moment demands at beam ends. As demonstrated in the response of SCBF archetypes, most of the beam end moments were usually less than the beam moment capacity, and the corresponding beam shear was neglected when estimating the column axial force. For BRBF archetypes, the beam end moment demands were closer to the corresponding capacity, and therefore the cumulative beam shear acting on columns was more significant than in the SCBFs. As shown in Figure 7.22, by ignoring V_b in SCBF archetypes and including $V_{b,j} = 2M_{p,j} / span$ in BRBF archetypes, we obtained the estimated column axial force demands and percent errors. Note that the percent errors in top stories were large because the calculation was normalized by the values of the column axial force demands (which were small in top stories).

For the 3- and 6-story archetypes, reduction factor ϕ for all braces was taken as 1.0. This corresponded to a large value of k, and 100% of the brace capacity was considered to estimate the column axial forces. For the 16-story archetypes, the reduction factors for braces were calculated with k of 0.95. For example, when calculating the column axial force demand in the second story, 100% of the brace capacity was considered in the second story while 12% of the brace capacity was considered for the roof. With the appropriate reduction factors, the percentage errors for all archetypes were reduced to less than 10% except for the top stories, where the absolute errors were not greater than for the other stories.

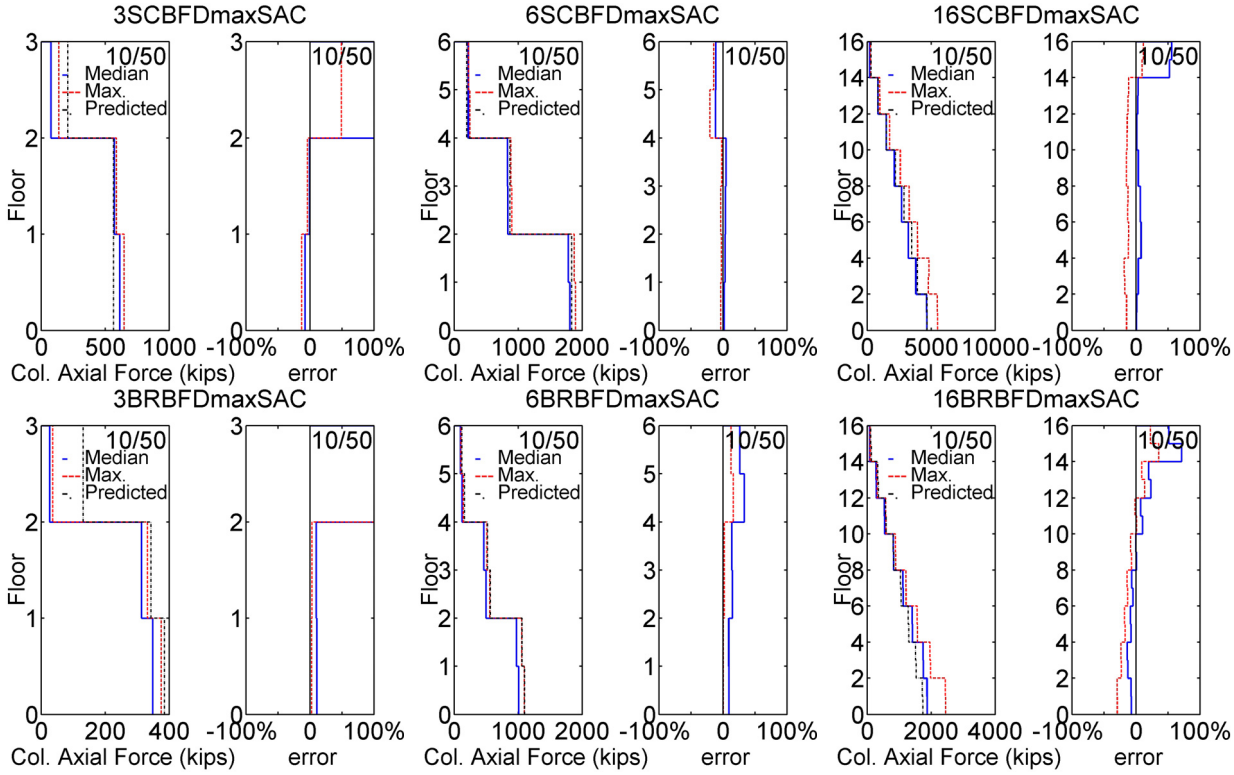

Figure 7.22 Estimated axial compressive forces in columns and percent errors of SCBF and BRBF archetypes under design-level SAC ground motions.

7.5 SUMMARY

We evaluated the EDPs of structural components in braced frame buildings, including the force and deformation demands in braces, beams, and columns. These demands at various hazard levels are expected to provide indices to improve the design criteria for structural components in steel braced frame buildings.

For braces, the out-of-plane deformation is approximately proportional to the square root of DR. Note that when the DR is less than the DR that initiates buckling of the brace, no out-of-plane deformation has occurred. The proposed relationship between out-of-plane deformation and DR estimates out-of-plane deformation accurately at various hazard levels.

Comparing the SCBF archetypes with their BRBF counterparts, the brace ductility demand of BRBFs is generally smaller at various hazard levels. The smaller brace ductility demand and better ductility performance of BRBF archetypes lead to a more reliable seismic resisting structural system compared to SCBFs.

The median damage indices (DI) of braces were approximately identical for two braces in the same story for most of the archetypes. While the maximum DI values of the BRBF archetypes were similar for the two braces in the same story, those of the SCBF archetypes showed differently shaped DI profiles. The drift concentration of a few ground motions resulted in an asymmetric profile of the brace damage for SCBF archetypes. The brace damage profile of BRBF archetypes showed uniform and symmetric response at various hazard levels. DI provides an index to monitor the fatigue life of braces. In most cases, braces were either 30% exhausted in terms of fatigue life or had nearly completely ruptured.

For beams, the axial force demands were slightly greater in the SCBF archetypes than in the BRBF archetypes. For designing beams for even stories, where the braces connect in beam-column connections, the estimation of beam axial force demand becomes very conservative if considering the full tensile capacity of braces and neglecting the compressive capacity of braces in adjacent stories. For designing beams for odd stories, where the braces connect in the mid-span of beams, the estimation of beam axial force demand is acceptable if considering the full capacity of braces in adjacent stories, unless severe drift concentration occurs.

For the beam moment demands, the analyses showed that most of the median beam moment demands in SCBF archetypes were less than the beam moment capacity. For BRBF archetypes, median and maximum beam moment demands reached the capacity in many stories for the design-level and MCE-level events. Our simulations showed that the beams in the BRBF archetypes experienced more nonlinear flexural behavior and, therefore, dissipated more energy through beam plastic rotations than their SCBF counterparts.

In all BRBF archetypes, the beam axial force demands were all about 20% of the capacity and beam moment demands all reached the capacity. The inelastic behavior and beam moment demands were concentrated at beam-column connections (left end of left beam and right end of right beam) rather than the middle span of the beams. The unbalanced loads had little effect on the beam moment demands in the middle span of beams, which were far less than those in the ends of the beams.

In SCBF archetypes, although the unbalanced load was reduced, its effects could not be ignored. Under the unbalanced load, the moment demands in the middle span of the beams were about the same magnitude as the moment demand in the ends of the beams. For the design-level event, the median vertical deformations in the middle span of beams were more than 1.0 inch for

the first story of 3SCBFDmaxSAC and 6SCBFDmaxSAC, increasing the deformation demands of the beam-column connections by 0.5% radian. This amount of deformation may not greatly increase the structural damage, but it may cause nonstructural damage that must be addressed. For the MCE-level event for 6SCBFDmaxSAC, the vertical deformation was as high as 3.93 inches at the first story, which corresponded to about 2% radian rotation of the beam-column connections. This greatly increased the deformation demands of the beam-column connections, increasing the risk of damage to them.

For columns, the profile of the column axial force demands showed that the demands along the height changed every two stories, a result of the double-story X configuration. It is expected that the axial force demands of columns are related to the brace demands and capacity.

For all 3-story and 6-story archetypes, the medians and maxima of column axial force demands were similar in the same story and did not change much with hazard levels. The axial force demands in 16SCBFDmaxSAC reached the capacity of the columns for the design-level and MCE-level events in almost all stories. The axial force demands for 16BRBFDmaxSAC were not as high as those in 16SCBFDmaxSAC. The 16-story BRBF archetype had higher column moment demands than their SCBF counterparts under the same ground motion excitation; the column responses of 16BRBFDmaxSAC exhibited more flexural behavior while those of 16SCBFDmaxSAC exhibited more tensile and compressive behavior. In all archetypes, the response of column moment demands also showed that the bottoms of the columns usually had slightly greater moment demands than the tops.

For the SCBF archetypes, the braces reached capacity in some levels but not all levels. It was conservative if the column axial demands were estimated using the full capacity of braces and beams in all upper stories. Reduction factors were used to determine the percentage of capacity of braces and beams for estimating column axial force demands. With the appropriate reduction factors, the percent errors were less than 10% except in the top stories, where the absolute errors were not greater than the other floors.

8 Conclusions and Recommendations

To design and utilize concentrically braced frames more efficiently and with more confidence, our numerical studies of several SCBF and BRBF archetypes were analyzed and interpreted on the basis of probability and statistics. Computationally efficient and accurate fiber-based models were constructed to perform an extensive set of nonlinear static and dynamic analyses. We investigated the seismic demands of concentrically braced and buckling-restrained braced frame systems for several ground motion records corresponding to various hazard levels. The results were used to assess performance and improve the design criteria of braced frame systems. The conclusions we reached are summarized below.

8.1 MODELING

- The force-based beam-column element demonstrates an acceptable degree of accuracy and is recommended to better estimate the nonlinear responses of braced frame systems.
- An appropriate working point at the column base should be defined so that the accurate height of the first story can be included in numerical models, thus reflecting realistic structural behavior.
- A finite-element model (LS-DYNA) satisfactorily captured the local buckling behavior and changed the strength gradually before and after peak strength was reached. The fiber-based OpenSees model exhibited a sudden drop in strength following buckling and when fracture criteria were met. The global buckling of braces occurred at about 0.3% radian drift ratio in the analyses.
- The OpenSees analyses suggest that statistically, the effect of low-cycle fatigue is not pronounced, but it is important to include when predicting the structural response under a single ground motion. The effect of fatigue is more important for predicting the residual displacement than it is for the peak displacement.
- Using inelastic rather than elastic spectrum displacement for the short-period SCBF systems significantly reduced the scatter in the statistical data, especially for large intensity events.

8.2 ANALYTICAL BEHAVIOR OF CONCENTRICALLY BRACED FRAMES

- From the analyses, the performance of 3-story SCBFs designed as per ASCE/SEI 7-05 and 1997 NEHRP are quite similar statistically. The responses of the top floor are different due to the change in design criteria for the roof beam of chevron braced frames.
- The expected median maximum story drift ratios of SCBFs with an R of 6 for the service-level event had more than 75% probability to be greater than 0.3%, which is close to the DR that results in buckling of braces. Thus, following an occasional earthquake, for which no structural damage is generally desired, it is necessary to replace one or more braces and repair nonstructural damage to adjacent elements. The expected median maximum story drift ratios had more than 70% probability of exceeding 2.5% radian for the MCE-level event, at which point the braces fractured due to low-cycle fatigue, but the integrity of the beam-to-column connections is likely adequate.
- The expected median maximum story drift ratios of SCBFs with an R of 3 were less than those needed to initiate buckling for the service-level event, and less than those likely to fracture the beam-to-column connections for the MCE-level event. Reducing the R-factor was effective in reducing the drift demand of braced frames.
- The BRBF model in Chapter 4 experienced large residual drifts at various hazard levels partly because of its relatively longer fundamental period. Because the elastic stiffness of BRBFs did not decrease dramatically after the braces yielded or were damaged, the braced frame required more force to swing back during a ground motion.
- For SCBFs, reducing the R-factor reduced the tendency to form a soft story. The cost of constructing SCBFs with smaller R-factors is higher and significant elastic response can be expected, but the demands are more consistent with the ductility capacity of the connections and buckling braces considered here.
- The analyses of the archetype buildings showed that the 3-story SCBF tended to concentrate deformation in the bottom story, the 6-story SCBF had greater story drift ratios at the roof level, and the largest drift ratio for the 16-story SCBF occurred in the middle stories. The BRBF archetypes generally had more uniform DRmax profiles than the SCBF archetypes.
- The story shear demands of all the archetypes were usually close to the yielding capacity of each story if the archetype had experienced nonlinear behavior.
- For the two-story SCBF archetype, R-factors of 3.3 and 3 for design were more consistent with the ductility capacity of the structural system, which also reduced the drift demand at various hazard levels and the probability of collapse for the MCE-level event.
- This research assumed that the energy dissipation profile over the height of the building during dynamic excitations was proportional to DCR distribution of the first-mode pushover analysis over the height. Under this assumption, the DR of each story was approximately proportional to D_i/C_i^2 (or $D_i \cdot V_y/C_i^2$). The analysis of the 16-story SCBF archetypes showed that the target DR at different hazard levels could be achieved by limiting the $D_i \cdot V_y/C_i^2$ ratios. We also found that the stiffness difference at adjacent levels should be limited to reduce damage concentration. A 30% difference of $D_i \cdot V_y/C_i^2$ ratio in adjacent stories was adopted in this case study, which successfully reduced the stiffness irregularity and damage concentration of the 16-story SCBF archetype.

- In general, median PFAs for the MCE-level event were greater than those at the other hazard levels, especially for the lower floor of all SCBF and BRBF archetypes. Because of the longer fundamental period and higher flexibility of BRBF archetypes, the median PFAs of SCBF archetypes were greater than those of BRBF archetypes along the height of the archetypes. Thus nonstructural damage associated with floor acceleration was expected to be more severe for the SCBF archetypes than for the BRBF archetypes.
- We propose a relationship in which out-of-plane deformation is approximately proportional to the square root of DR. The proposed estimate is accurate at various hazard levels.
- The low-cycle fatigue life of braces was monitored in the analyses. The analyses show that in most cases, the braces either exhausted 30% of their fatigue life or they nearly completely ruptured.
- The beam moment demands of SCBF and BRBF archetypes showed that the BRBF archetypes experienced more nonlinear flexural behavior of beams and, therefore, were expected to dissipate more energy through beam plastic rotations than their SCBF counterparts.
- For the SCBF archetypes, although the unbalanced load was reduced in the double-story configuration, its effects still could not be ignored in beams. Under the unbalanced load, the moment demands in the middle span of the beams were similar to the moment demand in the ends of the beams.
- For double-story X SCBFs, the middle-span vertical deformation of beams for the design-level event may not contribute to the structural damage to any large extent, but it may cause nonstructural damage that cannot be ignored. For the MCE-level event for the first story of 6SCBFDmaxSAC, the vertical deformation in the middle span of beams was as high as 3.93 inches, corresponding to about 2% rotation of the beam-column connection. This greatly increased the deformation demands of the beam-column connections and hence increased the risk of damaging them.
- For the double-story X configuration, the column axial force demands changed every two stories. The axial force demands of columns are presumably related to the brace demands and capacity. The 16-story BRBF archetypes had higher column moment demand than their SCBF counterparts under the same ground motion excitation; the column responses of 16BRBFDmaxSAC exhibited more flexural behavior while those of 16SCBFDmaxSAC exhibited more tensile and compressive behavior.
- To estimate the axial force demands of columns, it is conservative to consider the full capacity of braces and beams in all stories. Reduction factors were used in the capacity of braces and beams for estimating column axial force demands. With the appropriate reduction factors, the percent errors were less than 10% except for the top stories, where the absolute errors were not greater than the other stories.

8.3 EVALUATION OF DESIGN PARAMETERS USING FEMA P695 METHODOLOGY

Various archetypes of SCBF and BRBFs ranging from 2 to 16 stories were evaluated. The appropriateness of seismic performance factors was investigated according to the FEMA P695 (ATC-63) methodology.

- The BRBFs passed the evaluation, but the two-story SCBF designed for the upper bound of seismic design category D failed. Therefore the seismic performance factors of ASCE/SEI 7-05 seem appropriate for BRBFs based on FEMA P695 and the archetypes, but may need adjusting for the two-story SCBF.
- The taller archetypes were designed with the drift control criteria, and member sizes may be increased to obtain more stiffness to limit the drift. The strength is usually increased by increasing the stiffness accordingly. Low-rise archetypes typically satisfy drift requirements, and member sizes need not be increased beyond those required for strength. Thus they have less reserve capacity to resist collapse.
- The Equivalent Lateral Force Analysis (ELF) and Model Response Spectrum Analysis (RSA) resulted in greater differences in member sizes for higher-rise braced frames than lower-rise braced frames. For example, in the 6-story SCBFs, the difference of force demand in the members determined by ELF and RSA was within 10%. For the 16-story SCBFs, the difference increased to 50%. The displacement demand under RSA was much less than that of ELF.

8.4 RECOMMENDATIONS FOR FUTURE WORK

- Full-scale component and frame test data from large brace sizes will significantly improve the numerical models and increase the confidence of performance evaluations. Brace components with larger sections are usually stockier and tend to be used with smaller slenderness ratio (KL/r). Braces with smaller KL/r ratio usually have less ductility capacity, although they provide higher initial compression strength. Gusset plates and brace-to-framing connections adjacent to the braces, based on capacity design criteria, also have higher deformation and force demand due to the larger capacity of the heavy braces. The test data should be used to improve the confidence on the quality of the parameters to design the braced frame systems in a more rational manner.
- The evaluation of braced frames should be extended to different design choices, such as different floor plans, different vertical configurations, and different numbers of braced bays. Investigations of different brace configurations should cover a wider range of samples to improve the confidence of the evaluation.
- The torsional effect of the braced frames building is an important factor, especially when the structure is subject to near-field ground motions in two orthogonal directions, which may cause obvious asymmetric excursions. Future numerical simulations should be able to model the fracture of the braces and structural behavior under multidirectional force demand.
- Complex nonlinear behavior of buckling braces and the tendency to form weak stories in SCBFs increase the difficulty of designing such a structural system using PBEE. New strategies need to be developed to reduce or redistribute the engineering demand, so that

the demand can be compatible with the structural capacity by applying other engineering solutions, such as base-isolation systems, rocking mechanisms, or elastic back-up frame systems.

- While the performance-based design method is a powerful tool, it requires extensive nonlinear analyses. This complex and time-consuming analysis has limited appeal in practice, and more efforts are required to simplify the method.

REFERENCES

ABAQUS (2003). Version 6.4 online Documentation.

Aguero, A, Izvernari, C, Tremblay, R (2006). Modeling of the seismic response of concentrically braced steel frames using the OpenSees analysis environment, *Int. J. Advanced Steel Construc.*, 2(3):242–274.

AIJ (1995). *Reconnaissance Report on Damage to Steel Building Structures Observed from the 1995 Hyogoken-Nanbu (Hanshin/Awaji) Earthquake*, Steel Committee of Kinki Branch, Architectural Institute of Japan, Tokyo, pg. 167.

AISC (1997). *Seismic Provisions for Structural Steel Buildings*, American Institute of Steel Construction, Chicago, IL.

AISC (2002). *Seismic Provisions for Structural Steel Buildings*, American Institute of Steel Construction, Chicago, IL.

AISC (2005). *Seismic Provisions for Structural Steel Buildings*, American Institute of Steel Construction, Chicago, IL.

Annan, C, Youssef, M, El Naggar, M (2009). Experimental evaluation of the seismic performance of modular steel-braced frames, *Eng. Structures*, 31(7):1435–1446.

ANSYS. Inc. (2005). *Theory Reference*, South Pointe, 275 Technology Drive, Canonsburg, PA.

Anthes, RJ (1997). Modified rainflow counting keeping the load sequence, *Int. J. Fatigue*, 19(7):529–535.

ASCE/SEI 7-05 (2005). *Minimum Design Loads for Buildings and Other Structures*, American Society of Civil Engineers, Reston, VA.

Asgarian, B, Shojrgozar, HR (2009). BRBF response modification factor, *J. Constructional Steel Res.*, 65(2):290–298.

Astaneh-Asl, A (1998). *Seismic Behavior and Design of Gusset Plates*, Steel Tips, Structural Steel Educational Council, Moraga, CA.

ASTM (2003). Standard practices for cycle counting in fatigue analysis, *ASTM E 1049–85*, West Conshohocken, PA.

Baker, JW (2005). *Vector-Valued Ground Motion Intensity Measures for Probabilistic Seismic Demand Analysis*, Ph.D. Dissertation, Department of Civil and Environmental Engineering, Stanford University, Stanford, CA.

Baker, JW, Cornell, CA (2006). Spectral shape, epsilon and record selection, *Earthq. Eng. Struct. Dyn.*, 34 (10):1193–1217.

Balendra, T, Huang, X (2003). Overstrength and ductility factors for steel frames designed according to BS5950, ASCE, *J. Struc. Eng.*, 129(8):1019–1035.

Basquin, OH (1910). The exponential law of endurance tests, *Proceedings*, American Society for Testing and Materials, 10:625–630.

Bertero, VV, Uang, C-M, Llopiz, C, Igarashi, K (1989). Earthquake simulator testing of concentric braced dual system, ASCE, *J. Struc. Eng.*, 115(8):1877–1894.

BHRC (2005). *Iranian Code of Practice for Seismic Resistant Design of Buildings: Standard No. 2800,* 3rd ed., Building and Housing Research Center, Tehran, Iran.

Black, C, Makris, N, Aiken, ID (2004). Component testing, seismic evaluation and characterization of buckling-restrained braces, ASCE, *J. Struc. Eng.*, 130(6):880–894.

Black, GR, Wenger, BA, Popov, EP (1980). Inelastic buckling of steel struts under cyclic load reversals, *UCB/EERC-80/40*, Earthquake Engineering Research Center, Berkeley, CA.

Bonneville, D, Bartoletti, S (1996). Case Study 2.3: Concentric Braced Frame, Lankershim Boulevard, North Hollywood, *1994 Northridge Earthquake; Building Case Studies Project; Proposition 122: Product 3.2, SSC 94-06*, Seismic Safety Commission State of California, pp. 305–324.

Broderick, B, Elghazouli, A, Goggins, J (2008). Earthquake testing and response analysis of concentrically-braced sub-frames, *J. Constructional Steel Res.*, 64(9):997–1007.

BSI. (1990). *BS 5950: Structural Use of Steel Work in Building. Part 1*, British Standards Institution, London, U.K.

Chambers, JJ, Ernst, CJ (2005). *Brace Frame Gusset Plate Research: Phase I Literature Review*. American Institute of Steel Construction, Chicago, IL.

Chenouda, M, Ayoub, A (2009). Probabilistic collapse analysis of degrading multi-degree of freedom structures under earthquake excitation, *Eng. Structures*, 31:2909-2921.

Chopra, AK (2006). *Dynamics of Structures*, 2nd ed., Prentice Hall, New York.

Cochran, M, Honeck, W (2004). *Design of Special Concentric Braced Frames*, Steel TIPS Report, Structural Steel Educational Council, Moraga, CA, May.

Coffin, LF, Jr (1954). A study of the effects of cyclic thermal stresses on a ductile metal, ASME, *Trans.*, 76:931–950.

DASSE (2007). *Cost Advantages of Buckling Restrained Braced Frame Buildings*, DASSE Design, Inc.

Ding, X (2006). *Redundancy in Steel Braced Frames under Seismic Excitations*, Ph.D. dissertation, Department of Civil Engineering, University of Illinois at Urbana-Champaign, Urbana, IL.

Downing, SD, Socie, DF (1982). Simple rainflow counting algorithms, *Int. J. Fatigue*, 4:31–40.

Ellingwood, B, Galambos, TV, MacGregor, JG, Cornell, CA (1980), Development of a probability based load criteria for American National Standard Committee A58, *Special Publication No. 577*, National Bureau of Standards, Washington, D.C.

Fahnestock, LA, Ricles, JM. Sause, R (2007a). Experimental evaluation of a large-scale BRBF, ASCE, *J. Struc. Eng.*, 133(9):1205–1214.

Fahnestock, LA, Sause, R, Ricles, J.M. (2007b). Seismic response and performance of BRBFs, ASCE, *J. Struc. Eng.*, (9):1195–1204.

Fajfar, P (2000). A nonlinear analysis method for performance-based seismic design, *Earthq. Spectra*, 16:573–591.

Fell, BV, Kanvinde, AM, Deierlein, GG, Myers, AT (2009). Experimental investigation of inelastic cyclic buckling and fracture of steel braces, ASCE, *J. Struc. Eng.*, 135(1):19–32.

FEMA P695 (ATC-63) (2009), *Recommended Methodology for Quantification of Building System Performance and Response Parameters*, Applied Technology Council: Redwood City, CA.

FEMA (1997a). *FEMA 273: NEHRP Guidelines for the Seismic Rehabilitation of Buildings*, Federal Emergency Management Agency, Washington, DC.

FEMA (1997b). *FEMA 302: NEHRP Recommended Provisions for Seismic Regulations for New Buildings and Other Structures*, Building Seismic Safety Council, Washington D.C.

FEMA (1997c). *FEMA 303: Commentary to NEHRP Recommended Provisions for Seismic Regulations for New Buildings and Other Structures*, Building Seismic Safety Council, Washington D.C.

FEMA (2000a). *FEMA 351: Recommended Seismic Evaluation and Upgrade Criteria for Existing Welded Steel Moment Frame Buildings*, Federal Emergency Management Agency, Washington, DC.

FEMA (2000b). *FEMA 355C: State of the Art Report on Systems Performance of Steel Moment Frames Subject to Earthquake Ground Motion Shaking*. H. Krawinkler, ed., Federal Emergency Management Agency, Washington, D.C.

FEMA (2000c). *FEMA 355F: State of the Art Report on Performance Prediction and Evaluation of Steel Moment-Frame Buildings*, D. A. Foutch, ed., Federal Emergency Management Agency, Washington, D.C.

FEMA (2000d). *FEMA 356: Prestandard and Commentary for the Seismic Rehabilitation of Buildings*, Federal Emergency Management Agency, Washington, D.C.

Ferch, R (2004). Personal Communication, Berkeley, CA.

Fukuta, T, Nishiyama, I, Yamanouchi, H, Kato, B (1989). Seismic performance of steel frames with inverted v-braces, ASCE, *J. Struc. Eng.*, 155(8):2016–2028.

Glinka, G, Kam, JCP (1987). Rainflow counting algorithm for very long stress histories, *Int. J. Fatigue*, 9(3):223–228.

Gupta, A, Krawinkler, H. (1999). Seismic demands for performance evaluation of steel moment resisting frame structures (SAC Task 5.4.3), *Report No. 132*, John A. Blume Earthquake Engineering Center, Stanford University, Stanford, CA.

Hachem, M (2009). BiSpec 1.62, Berkeley, CA, *http://www.ce.berkeley.edu/~hachem/bispec/index.html*.

Hamburger, RO, Foutch, DA, Cornell, CA (2003). Translating research to practice. FEMA/SAC performance-based design procedures, *Earthq. Spectra*, 19(2):255–267.

Han, S-W, Kim, WT, Foutch, DA (2007). Seismic behavior of HSS bracing members according to width-thickness ratio under symmetric cyclic loading, ASCE, *J. Struc. Eng.*, 133(2):264–273.

Hanson, RD, Martin, HW (1987). Performance of steel structures in the September 19 and 20, 1985 Mexico earthquakes, *Earthq. Spectra*, 3(2):329–346.

Hines, EM, Appel, ME (2007). Behavior and design of low-ductility braced frames, *Proc*., *ASCE Structures Congress*, Long Beach, CA.

Hines, EM, Grynuik, MC (2006). Collapse performance of low-ductility chevron braced steel frames in moderate seismic regions, *http://engineering.tufts.edu/cee/people/hines/hinesappelcheever2008finsub.pdf*.

Hisatoku, T (1995). Reanalysis and repair of a high-rise steel building damaged by the 1995 Hyogoken-Nanbu earthquake, *Proc.*, *64th Annual Convention, Structural Engineers Association of California*, Structural Engineers Assn. of California, Sacramento, CA, pp. 21–40.

Hong, NA (1991). Modified rainflow counting method, *Int. J. Fatigue*, 13:465–469.

Huang, Y, Mahin, SA (2008). Evaluation of steel structure deterioration with cyclic damaged plasticity, *Proc.*, *14th World Conference on Earthquake Engineering*, Beijing, China.

Huang, Y, Mahin, SA (2010). Simulating the inelastic seismic behavior of steel braced frames including the effects of low cycle fatigue, *PEER-2010/104*, Pacific Earthquake Engineering Research Center, University of California, Berkeley, CA.

ICC (2000). *International Building Code*, International Code Council, Falls Church, VA

ICC (2003). *International Building Code*, International Code Council, Falls Church, VA

Kato, B, Tanaka, H, Yamanouchi, H (1980). Field work investigation of steel building damage due to the 1978 Miyagiken-oki earthquake, *Proc., Seventh World Conference on Earthquake Engineering*, Istanbul, Turkey, pp. 479–486.

Kelly, DJ, Bonneville, DR, Bartoletti, SJ (2000). 1994 Northridge earthquake: damage to a four-story steel braced frame building and its subsequent upgrade, *Proc., 12th World Conference on Earthquake Engineering*, New Zealand Society for Earthquake Engineering, Upper Hutt, New Zealand.

Khandelwal, K, El-Tawil, S, Sadek, F, (2009). Progressive collapse analysis of seismically designed steel braced frames, *J. Constructional Steel Res.*, 65(3):699–708.

Khatib, F, Mahin, SA, Pister, KS (1988). Seismic behavior of concentrically braced steel frames, *UCB/EERC-88/01*, Earthquake Engineering Research Center, University of California, Berkeley, CA.

Kim, H, Goel, S (1992). Seismic evaluation and upgrading of braced frame structures for potential local failures, *UMCEE 92-24*, Dept. of Civil Engineering and Environmental Engineering, University of Michigan, Ann Arbor, MI.

Kim, J, Choi, H (2004). Response modification factors of chevron-braced frames, ASCE, *J. Struc. Eng.*, 27:285–300.

Krawinkler, H, et al. (1996). Northridge earthquake of January 17, 1994: reconnaissance report, Vol. 2—steel buildings, *Earthq. Spectra*, Suppl. C, 11:25–47.

Lee, K, Bruneau, M (2005). Energy dissipation of compression members in concentrically braced frames: Review of experimental data, ASCE, *J. Struc. Eng.*, 131(4):552–559.

Lee, K, Foutch, DA (2006). Seismic evaluation of steel moment frame buildings designed using different R-values, ASCE, *J. Struc. Eng.*, 132(9):1461–1472.

Lehman, DE, Roeder, CW, Herman, D, Johnson, S, Kotulka, B (2008). Improved seismic performance of gusset plate connections, ASCE, *J. Struc. Eng.*, 134(6):890–901.

López, W, Sabelli R (2004). *Seismic Design of Buckling-Restrained Braced Frames*, Steel TIPS Report, Structural Steel Educational Council, Moraga, CA.

LSTC (2007). *LS-DYNA Keyword User's Manual*, Livermore Software Technology Corporation, Livermore, CA.

Mahmoudi, M, Zaree, M (2010). Evaluating response modification factors of concentrically braced steel frames, *J. Constructional Steel Res.*, 66:1196–1204.

Manson, SS (1953). Behavior of materials under conditions of thermal stress, *Heat Transfer Symposium*, University of Michigan Engineering Research Inst., pp. 9–75.

Matsuishi, M, Endo, T (1968). Fatigue of metals subjected to varying stress," *Proc.*, Kyushu Branch of Japan Society of Mechanics Engineering, Fukuoka, Japan (in Japanese), pp. 37–40.

McKenna, F (1997). *Object Oriented Finite Element Programming: Frameworks for Analysis, Algorithms and Parallel Computing*, University of California, Berkeley, CA.

Miner, MA (1945). Cumulative damage in fatigue, ASME, *J. Applied Mech.*, 12:159–164.

Miranda, E, Aslani, H (2003). Building-specific loss estimation for performance-based earthquake engineering, *Working Paper*, Stanford University, Stanford, CA.

Moehle, JP (2003). A framework for performance-based earthquake engineering,*: Report ATC–15–9*, Applied Technology Council, Redwood City, CA.

Moehle, JP, Stojadinovic, B, Der Kiureghian, A, Yang, T (2005). An application of PEER performance-based earthquake engineering mMethodology," *Research Digest 2005-1*, Pacific Earthquake Engineering Research Center, Berkeley, CA.

Naeim, F (1997). *Performance of Extensively Instrumented Buildings During the January 19, 1994 Northridge Earthquake*, John A Martin And Associates, Research and Development Department, Los Angeles, CA.

Naeim, F (1998). Performance of 20 extensively instrumented buildings during the 1994 Northridge earthquake, *The Structural Design of Tall Buildings*, 7(3):179–215.

Neuenhofer, A, Filippou, FC (1997). Evaluation of nonlinear frame finite-element models, ASCE, *J. Struc. Eng.*, 123(7):958–966.

Newell, J, Uang, C-M (2006). Cyclic behavior of steel columns with combined high axial load and drift demand, *SSRP-06/22*, University of California, San Diego, CA.

Newmark, NM, Hall, WJ (1982). *Earthquake Spectra and Design*, Earthquake Engineering Research Institute, Oakland, CA.

Osteraas J, Krawinkler, H (1989). The Mexico earthquake of September 19, 1985—behavior of steel buildings, *Earthq. Spectra*, 5(1):51–88.

Ousterhout, JK (1994). *Tcl and the Tk Toolkit*, Professional Computing Series. Addison-Wesley.

Packer, JA (2006). Tubular brace member connections in braced steel frames, *Proc., 11th international Symposium and IIW International Conference on Tubular Structures*, Taylor & Francis, Québec City (Canada), pp. 3–11.

Palmgren, A (1924). Die lebensdauer von kugellagern, *Zeitschrijt des Vereines Deutscher Ingenieure* (in German), 64:339–341.

Powell, J, Clark, K, Tsai, K-C, Roeder, C, Lehman, D. (2008). Test of a full scale concentrically braced frame with multi-story X-bracing, *Proc*., *ASCE 2008 Structures Congress*, Vancouver, BC, Canada.

Rai, D, Goel, S, Firmansjah. J (1996). SNAP-2DX (Structural Nonlinear Analysis Program). *Research Report UMCEE96-21*, Dept. of Civil Engineering, University of Michigan, Ann Arbor. MI.

Riddell, R, Hidalgo, P, Cruz, E (1989). Response modification factors for earthquake resistant design of short period buildings, *Earthq. Spectra*, 5(3):571–590.

Roeder,C, Lehman, D, Yoo, JH (2005). Improved design of steel frame connections, *Int. J. Steel Structures*, 5(2): 141–153.

Ruiz-Garcia, J, Miranda, E (2006). Evaluation of residual drift demands in regular multi-storey frames for performance-based seismic assessment, *Earthq. Eng. Struct. Dyn.*, 35(13):1609-1629.

Ruiz-García, J, Miranda, E (2009). Probabilistic estimation of residual drift demands for seismic assessment of multi-story framed buildings, *Eng. Structures*, 32:11–20.

Sabelli, R (2000). *Research on Improving the Design and Analysis of Earthquake Resistant Steel Braced Frames*, Earthquake Engineering Research Institute, Oakland, CA.

Sabelli, R, Mahin, SA, Chang, C (2003). Seismic demands on steel braced frame buildings with buckling-restrained braces, *Eng. Structures*, 25(5):655–666.

Scott, MH, Franchin, P, Fenves, GL, Filippou, FC (2004). Response sensitivity for nonlinear beam–column elements, ASCE, *J. Struc. Eng.*, 130(9):1281–1288.

Shaw, S, Kanvinde, A, Fell, B (2010). Earthquake-induced net section fracture in brace connections—e xperiments and simulations, *J. Constructional Steel Res.*, 66(12):1492–1501.

Somerville, PG (1997). *Development of Ground Motion Time Histories for Phase 2 of the FEMA /SAC Steel Project*, SAC BD/97-04, SAC Steel Joint Venture, Sacramento CA.

Tang, X, Goel, S (1989). Brace fractures and analysis of Phase I structure, ASCE, *J. Struc. Eng.*, 115(8):1960-1976.

Tremblay, R (2002). Inelastic seismic response of bracing members, *J. Constructional. Steel Res.*, 58:665–701.

Tremblay, R (2008). Influence of brace slenderness on the fracture life of rectangular tubular steel bracing members subjected to seismic inelastic loading, *Proc., ASCE 2008 Structures Congress*, Vancouver, BC, Canada.

Tremblay, R et al. (1995). Performance of steel structures during the 1994 Northridge earthquake, *Canadian J. Civil Eng.*, 22(2):338–360.

Tremblay R et al. (1996).Seismic design of steel buildings: lessons from the 1995 Hyogo-ken Nanbu earthquake, *Canadian J. Civil Eng.*, 23(3):727–756.

Tremblay, R, Archambault, M-H, Filiatrault, A (2003). Seismic response of concentrically braced steel frames made with rectangular hollow bracing members, ASCE, *J. Struc. Eng.*, 129(12):1626–1636.

Tremblay, R, Castonguay, PX, Guilini-Charette, K, Koboevic, S (2009). Seismic performance of conventional construction braced steel frames designed according to Canadian seismic provisions, *Proc., Structures Congress - Don't Mess With Structural Engineers: Expanding Our Role*, pp. 794–803.

Tremblay, R, Haddad, M, Martinez, G, Richard, J, Moffatt, K (2008). Inelastic cyclic testing of large size steel bracing members, *Proc., 14th World Conference on Earthquake Engineering*, Paper No. 05–05–0071, Beijing, China.

Tsai, KC, Hsiao, PC, Wang, KJ, Weng, YT, Lin, ML, Lin, KC, Chen, CH, Lai, JW, and Lin, SL (2008). Pseudo-dynamic tests of a full-scale CFT/BRB frame-Part I: Specimen design, experiment and analysis, *Earth. Eng. Struct. Dyn.*, 37(7):1081–1098.

Uang, C-M (1991). Establishing R (or R_w) and C_d factors for building seismic provisions, ASCE, *J. Struc. Eng.*, 117(1):19–28.

Uriz, P, Mahin, SA (2008). Towards earthquake resistant design of concentrically braced steel structures, *PEER-2008/08*, Pacific Earthquake Engineering Research Center, University of California, Berkeley, CA.

Wallace, BJ, Krawinkler, H (1989). Small-scale model tests of structural steel assemblies, ASCE, *J. Struc. Eng.*, 115(8):1999–2015.

Welch, B, Jones, K, Hobbs, J (2003), *Practical Programming in Tcl and Tk*, 4th Edition.

Wigle, VR, Fahnestock, LA (2010). Buckling-restrained braced frame connection performance, *J. Constructional Steel Res.*, 66(1): 65–74.

Willibald, S, Packer, JA, Martinez-Saucedo, G (2006). Behaviour of gusset plate to round and elliptical hollow structural section end connections, *Canadian J. Civil Eng.,* 33:373–383.

WJE (1998). *Oviatt Library, East and West Wings Investigation of Base Plate Damage Caused by the Northridge Earthquake*, Wiss, Janey, Elstner Associates, Inc., Emeryville, CA.

Yang, F, Mahin, SA (2005). *Limiting Net Section Fracture in Slotted Tube Braces*, Steel Tips Series, Structural Steel Education Council, Moraga, CA.

Yazgan, U, Dazio, A (2008). Utilization of residual displacements in the post-earthquake assessment, *Proc., 14th. World Conference on Earthquake Engineering*, Paper No. 05–01–0445, Beijing, China.

Yoo, JH, Roeder, CW, Lehman, DE (2008). FEM simulation and failure analysis of special concentrically braced frame tests, *J. Struc. Eng.,* 134(6):881–889.

Zayas, VA, Popov, EP, Mahin, SA (1980). Cyclic inelastic buckling of tubular steel braces, *UCB/EERC-80/16*, Earthquake Engineering Research Center, University of California, Berkeley, CA.

9 Appendix A: Design of SCBF and BRBF Archetype Buildings for Evaluation of Seismic Performance Factors

Index archetypes for SCBF and BRBF are designed by adopting the design requirements of ASCE/SEI 7-05 and the referenced standards. Test data are used to support the designs as necessary. The index archetype designs of SCBF and BRBF account for the significant design features that may affect the structural collapse behavior. Structural components such as beams, columns, and braces are designed to comply strictly with the code requirement.

There are a variety of archetype configurations and design choices. In the evaluation of the SCBF and BRBF, our objective is to give an overview of the performance of braced frame systems. Therefore, we adopted the most common options during the design. Regular structural layouts and typical loading conditions were used. The archetype designs were intended to cover a reasonable range of the practical designs, but not include those designs for extreme seismic performances. The seismic criteria, design loads, load combinations, and related requirements for the SCBF and BRBF archetypes are described in this appendix.

A.1 Archetype Design Information

All the archetypes have similar floor layouts with typical material properties and gravity loads. The material properties and gravity loads are modified from Steel TIPS [López and Sabelli 2004; Cochran and Honeck 2004] and SAC building designs [Gupta and Krawinkler 1999]. The design information is summarized as follows:

Structural Materials

- W sections — ASTM A992 (Fy = 50 ksi, Fu = 65 ksi)
- HSS sections — ASTM A500 Gr.B (Fy = 42 ksi for square tube sections, 46 ksi for circular pipe sections, Fu = 58 ksi)
- BRB Steel Core — ASTM A36 or JIS G3136 SN 400B with supplemental yield requirements: F_{ysc} = 42 ksi
- Gusset plates — ASTM A572, Grade 50 (Fyg = 50 ksi, Fu = 65 ksi)
- Weld electrodes — E70XX (notch toughness: 20 ft-lb at –20° Fahrenheit)

Gravity loading

Roof Loading:

Roofing and insulation:	7.0 psf
Metal deck and concrete fill:	47.0 psf
Steel framing and fireproofing:	8.0 psf
Ceiling:	3.0 psf
Mechanical/electrical:	2.0 psf
Total:	67.0 psf

Floor Weights:

Metal deck and concrete fill:	47.0 psf
Steel framing and fireproofing:	13.0 psf
Partition walls:	20.0 psf
Ceiling:	3.0 psf
Mechanical/electrical:	2.0 psf
Total:	85.0 psf

Average Exterior Curtain Wall Weight including Column and Spandrel Covers: 15.0 psf

Live Loads (reducible):

Roof:	20 psf
Floor:	50 psf

Based on these loadings, the design considerations and the member sizes of all the archetypes are summarized in the following sections.

A.2 Seismic Design Loading Criteria

The seismic loads and design criteria in ASCE/SEI 7-05 were specified based on the Seismic Design Category (SDC) of the structure. SDCs are determined from the ground motion intensity of the design earthquake and the Occupancy Category of the structure. FEMA P695 (ATC-63) assumes all structures to be either Occupancy Category I or II with a corresponding importance factor equal to unity. For the SCBFs and BRBFs we evaluated, the Occupancy Category was chosen to be II. The design spectral response acceleration short periods and 1-second period are shown in Table A.1. The site coefficients F_a and F_v and the response modification coefficient R are also listed in Table A.1.

Table A.1 Design parameters of SCBF and BRBF archetypes.

Seismic design category	D_{max}	D_{min}
Occupancy category	II (Office)	
Importance factor	1.0	
Design spectral acceleration at short periods, S_{DS}	1.0g	0.5g
Design spectral acceleration at 1-sec period, S_{D1}	0.6g	0.2g
F_a	1.0	1.36
F_v	1.5	2.27
R	6(SCBF), 8(BRBF)	

A.3 Seismic Load Resisting System Parameters

The seismic base shear varies depending on the analysis procedure. In the design of SCBF and BRBF archetypes, the analysis procedure was determined for each archetype from Section 12.6 in ASCE/SEI 7-05. The equivalent lateral force analysis (ELF) was used for most of the archetypes except for archetypes 16SCBFDmax, 16SCBFDmin, 12BRBFDmax, 12BRBFDmin, 16BRBFDmax, and 16BRBDmin, for which the modal response spectrum analysis (RSA) was used.

A.3.1 Equivalent Lateral Force Analysis

In the ELF procedure, the seismic base shear, V, in ASCE/SEI 7-05 is defined by

$$V = C_s W \tag{A.1}$$

where C_s is the seismic response coefficient and W is the effective seismic weight of the building. The seismic coefficient, C_s, is calculated for short-period and long-period archetypes.

For short-period archetypes ($T \leq T_s$):

$$C_s = \frac{S_{DS}}{R} \tag{A.2}$$

where S_{DS} is the design spectral response acceleration parameter in the short period range and R is the response modification factor. The occupancy importance factor, I, is unity and not shown in the equation.

For long-period archetypes ($T_s < T \leq T_L$):

$$C_s = \frac{S_{D1}}{TR} \tag{A.3}$$

where S_{D1} is the design spectral response acceleration parameter at a period of 1.0 sec, T is the fundamental period of the structure (sec), and T_L is the long-period transition period (sec) between the constant velocity and constant displacement response domains. Again, the occupancy importance factor is 1.0 and not shown in the equation.

In FEMA P695 (ATC-63), the calculation of seismic response coefficient from Equation A.3 is constrained by a lower bound value of 0.044 for S_{DS} which is used in many of the long-period archetypes, especially the higher-rise BRBFs.

In ASCE/SEI 7-05, the value of C_s is computed from another equation for very long period structures with a fundamental period $T > T_L$. It does not apply to the evaluation here. Due to possible limitations on the low-frequency content of the selected ground motion records, the FEMA P695 (ATC-63) methodology limits the index archetype designs to configurations with fundamental periods less than 4 sec.

The design story drift was computed by amplifying the story drift under elastic analysis and can be expressed in Equation A.4.

$$\delta_x = C_d \delta_{xe} \tag{A.4}$$

where C_d is the deflection amplification factor and δ_{xe} are the deflections determined by an elastic analysis. The elastic analysis is conducted by using the seismic base shear V. The elastic drifts, δ_{xe}, were determined by using seismic design forces based on the computed fundamental period of the structure without the upper limit of $(C_u)(T_a)$.

A.3.2 Modal Response Spectrum Analysis (RSA)

Some of the SCBF and BRBF archetypes were designed using the RSA procedure from ASCE/SEI 7-05. For those archetypes, the analyses included a sufficient number of modes so the combined modal mass participation was more than 90% of the actual mass. The force-related design parameters for each mode of response were computed from the response spectra divided by R. The value for displacement and drift quantities computed from the response spectra were multiplied by C_d, which equals R for the SCBF and BRBF archetype design. The combined responses from various modes were calculated by the SRSS method.

The base shear, V, of the archetype to be evaluated was calculated using $(C_u)(T_a)$ as prescribed in ASCE/SEI 7-05, since the calculated fundamental period T_1 of each archetype exceeds $(C_u)(T_a)$. The combined response for the modal base shear V_t for each archetype was less than 85% of the base shear V calculated from the ELF procedure. Therefore the forces in the RSA procedure were multiplied by $0.85(V/V_t)$, but according to ASCE/SEI 7-05, the drifts need not increase by the factor $0.85(V/V_t)$. The drift calculation was based on V_t, which can be much less than V, in the SCBF and BRBF archetypes. For the archetype designs that drift controls, the force demand is reduced dramatically if RSA is adopted instead of ELF.

A.4 Story Drift Limit

The design story drifts determined from either ELF or RSA are limited by the allowable story drift in ASCE/SEI 7-05. For the two- and 3-story archetypes, the maximum story drift ratio modified by C_d factor was limited to 2.5% radian; for the 6-, 12-, and 16-story archetypes, the maximum story drift ratio modified by C_d factor was limited by 2.0% radian. By changing the member sizes, the stiffness of the archetypes was increased to satisfy the code prescript drift limits.

A.5 P-Δ Effects

The P-Δ effects, which can be evaluated as per ASCE/SEI 7-05, are less likely to control the design of buildings in high seismic areas. In the SCBF and BRBF archetypes designed for SDC D_{max} and D_{min}, the P-Δ effects did not dominate the design as calculated. Instead, the force controls the design of lower-rise archetypes and drift controls the design of higher-rise archetypes in general.

A.6 Loads and Load Combinations

The archetypes were designed in accordance with the seismic load effects and load combinations of Section 12.4 of ASCE/SEI 7-05 and guidance provided in FEMA P695 (ATC-63). The designs ignore snow load S and foundation loads H, and the basic seismic load combinations are:

$$(1.2 + 0.2S_{DS})D + Q_E + L \tag{A.5}$$

$$(0.9 - 0.2S_{DS})D + Q_E \tag{A.6}$$

where D is dead loads including the structural self weight and superimposed dead loads, L is the live load including appropriate live load reduction factors, and Q_E is the effect of horizontal seismic forces resulting from the base shear V. The redundancy factor, ρ, is conservatively assumed to be 1.0 in all cases in FEMA P695 (ATC-63), so it is not shown in the load combination.

The overstrength is required for the seismic load effect for the design of some structural components, such as columns. Ignoring snow and foundation loads, the load combinations for strength design of such components are:

$$(1.2 + 0.2S_{DS})D + \Omega_O Q_E + L \tag{A.7}$$

$$(0.9 - 0.2S_{DS})D + \Omega_O Q_E \tag{A.8}$$

where Ω_o is the overstrength factor.

The load combinations for the design of SCBF and BRBF archetypes are summarized in Table A.2.

Table A.2 Load combination of SCBF and BRBF archetypes.

With or without Ω_o	SDC Dmax, SDS = 1.0g		SDC Dmin, SDS = 0.5g	
Where Ω_o is not required	SCBF and BRBF		SCBF and BRBF	
	$1.4D + Q_E + L$ $0.7D + Q_E$		$1.3D + Q_E + L$ $0.8D + Q_E$	
Where Ω_o is required	SCBF	BRBF	SCBF	BRBF
	$1.4D + 2.0Q_E + L$ $0.7D + 2.0Q_E$	$1.4D + 2.5Q_E + L$ $0.7D + 2.5Q_E$	$1.3D + 2.0Q_E + L$ $0.8D + 2.0Q_E$	$1.3D + 2.5Q_E + L$ $0.8D + 2.5Q_E$

A.7 Trial Values of Seismic Performance Factors

For the purpose of evaluating the appropriateness of seismic performance factors in current code, we chose the response modification coefficient R and the overstrength factor Ω_o based on ASCE/SEI 7-05. The displacement amplification coefficient C_d, however, was equal to R for most structural systems without damping devices. Section 7.7 in FEMA P695 (ATC-63) defines the value of the deflection amplification factor C_d to be the same as the value of the *R* factor, unless the system has increased damping (i.e., greater than nominal 5% of critical).

A.8 Structural Configurations and Member Sizes

The structural layouts of the archetypes are shown in Figures A.1 to A.3. Regular plan view is selected to avoid excessive torsional effects. The structural layouts of 3- and 6-story archetypes are similar to braced frames by others [DASSE 2007]. The braced bays (for both SCBFs and BRBFs) are located at the perimeter of the structures. For 2-, 3-, and 6-story archetypes, one bay of braced frame is used in each side of the perimeter. For 12- and 16-story archetypes, two bays of braced frame are used in each side of the perimeter. The floor plan is 180 ft by 120 ft. Beam spans are typically 30 ft, except in the 2-story archetypes where the span is 20 ft. The configuration of double-story X is used in the archetypes due to its benefit for design cost. The story height is 15 ft for all archetypes, except for the 2-story series, which has story height of 10 ft. The archetype of the 2-story SCBF designed for SDC Dmax is designed to comply with the design of the tested specimens [Uriz and Mahin 2008].

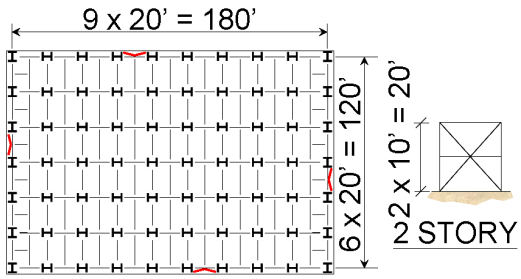

Figure A.1 Plan and elevation of 2-story braced frame archetypes.

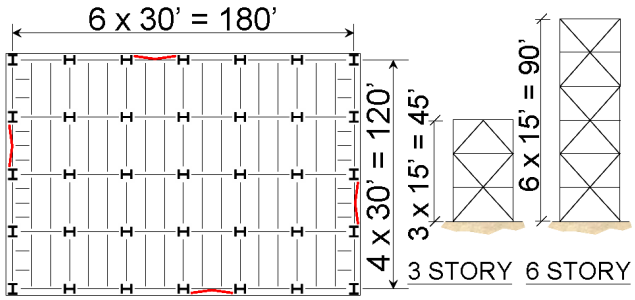

Figure A.2 Plan and elevation of 3-story and 6-story braced frame archetypes.

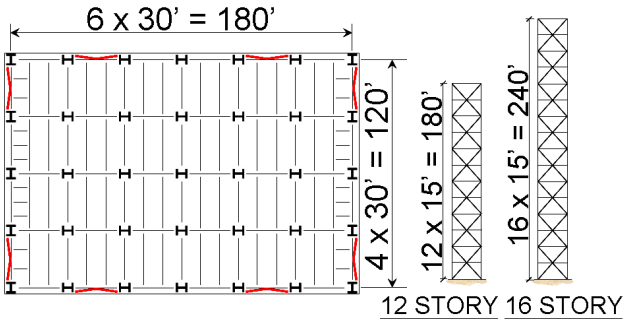

Figure A.3 Plan and elevation of 12-story and 16-story braced frame archetypes.

The gravity systems are simplified as leaning columns, which are pin-connected on each floor level to account for P-Δ effects in the design. The gravity systems are assumed to have no lateral resisting capacity, and their failure is not specially considered in analysis of the archetypes. Axial load on the leaning column is taken as the total dead load of the system tributary to a braced bay. The member sizes of the archetypes, shown in Table A-3 to Table A-12, are determined from the strength and drift requirements in ASCE/SEI 7-05 and the methodology of FEMA P695 (ATC-63).

Table A.3 Member sizes of 2-story SCBF archetypes.

2 STORY SCBF						
Floor	Columns		Braces		Beams	
	Dmax	Dmin	Dmax	Dmin	Dmax	Dmin
Roof	W10x45	W10x30	HSS6x6x3/8	HSS6x0.25	W24x117	W18x35
2F	W10x45	W10x30	HSS6x6x3/8	HSS6x0.25	W24x117	w18x50

Table A.4 Member sizes of 2-story BRBF archetypes.

2 STORY BRBF						
Floor	Columns		Braces		Beams	
	Dmax	Dmin	Dmax	Dmin	Dmax	Dmin
Roof	W10×39	W10×26	5 $in.^2$	2.5 $in.^2$	W18×35	W18×35
2F	W10×39	W10×26	5 $in.^2$	2.5 $in.^2$	W18×50	W18×35

Table A.5 Member sizes of 3-story SCBF archetypes.

3 STORY SCBF						
Floor	Columns		Braces		Beams	
	Dmax	Dmin	Dmax	Dmin	Dmax	Dmin
Roof	W12×120	W12×72	HSS8-3/4×0.312	HSS6-1/8×0.25	W30×173	W21×132
3F	W12×120	W12×72	HSS8-3/4×0.5	HSS6-7/8×0.312	W21×111	W18×76
2F	W12×120	W12×72	HSS9-5/8×0.5	HSS7-1/2×0.312	W18×65	W18×46

Table A.6 Member sizes of 3-story BRBF archetypes.

3 STORY BRBF						
Floor	Columns		Braces		Beams	
	Dmax	Dmin	Dmax	Dmin	Dmax	Dmin
Roof	W12×120	W14×82	3 $in.^2$	1 $in.^2$	W21×62	W21×62
3F	W12×120	W14×82	5.5 $in.^2$	2 $in.^2$	W18×76	W21×55
2F	W12×120	W14×82	6 $in.^2$	2 $in.^2$	W21×62	W21×62

Table A.7 Member sizes of 6-story SCBF archetypes.

6 STORY SCBF						
Floor	Columns		Braces		Beams	
	Dmax	Dmin	Dmax	Dmin	Dmax	Dmin
Roof	W14×68	W12×53	HSS7-1/2×0.312	HSS6×0.25	W18×97	W18×76
6F	W14×68	W12×53	HSS9x5/8×0.375	HSS6-5/8x0.25	W24×104	W18×76
5F	W14×176	W12×106	HSS9x5/8×0.5	HSS7×0.312	W24×131	W18×76
4F	W14×176	W12×106	HSS11-1/4×0.5	HSS7×0.375	W18×76	W21×68
3F	W14×342	W14×159	HSS12-1/2×0.5	HSS8-3/4×0.312	W24×146	W18×86
2F	W14×342	W14×159	HSS12-1/2×0.5	HSS8-3/4×0.312	W21×62	W21×62

Table A.8 Member sizes of 6-story BRBF archetypes.

6 STORY BRBF						
Floor	Columns		Braces			Beams
	Dmax	Dmin	Dmax	Dmin	Dmax	Dmin
Roof	W14×90	W14×53	2.5 $in.^2$	1 $in.^2$	W18×76	W21×55
6F	W14×90	W14×53	5 $in.^2$	1.5 $in.^2$	W21×62	W21×62
5F	W14×193	W14×90	5.5 $in.^2$	1.5 $in.^2$	W18×76	W21×55
4F	W14×193	W14×90	7 $in.^2$	2 $in.^2$	W21×62	W21×62
3F	W14×342	W14×176	8 $in.^2$	2 $in.^2$	W18×76	W21×55
2F	W14×342	W14×176	8 $in.^2$	2 $in.^2$	W21×62	W21×62

Table A.9 Member sizes of 12-story SCBF archetypes.

12 STORY SCBF (ELF)						
Floor	Columns		Braces		Beams	
	Dmax	Dmin	Dmax	Dmin	Dmax	Dmin
Roof	W12×45	W12×40	HSS6-5/8×0.312	HSS5×0.25	W18×55	W18×40
12F	W12×45	W12×40	HSS6-5/8×0.312	HSS5×0.25	W18×35	W18×35
11F	W14×99	W14×53	HSS8-3/4×0.312	HSS6-5/8×0.25	W18×60	W18×46
10F	W14×99	W14×53	HSS8-3/4×0.312	HSS6-5/8×0.25	W18×35	W18×35
9F	W14×193	W14×74	HSS10×0.375	HSS6-7/8×0.312	W18×65	W18×46
8F	W14×193	W14×74	HSS10×0.375	HSS6-7/8×0.312	W18×35	W18×35
7F	W14×283	W14×99	HSS10×0.375	HSS7×0.312	W18×65	W18×46
6F	W14x283	W14×99	HSS10×0.375	HSS7×0.312	W18×35	W18×35
5F	W14x398	W14×132	HSS9-5/8×0.5	HSS7×0.312	W18×71	W18×46
4F	W14x398	W14×132	HSS9-5/8×0.5	HSS7×0.312	W18×35	W18×35
3F	W14x550	W14×176	HSS9-5/8×0.5	HSS7×0.312	W18×71	W18×46
2F	W14x550	W14×176	HSS9-5/8×0.5	HSS7×0.312	W18×35	W18×35

Table A.10 Member sizes of 12-story BRBF archetypes.

12-STORY BRBF (RSA)						
Floor	Columns		Braces			Beams
	Dmax	Dmin	Dmax	Dmin	Dmax	Dmin
Roof	W12×40	W12×40	3	1.5	W18×46	W18×35
12F	W12×40	W12×40	3	1.5	W18×35	W18×35
11F	W14×74	W14×61	3.5	2	W18×46	W18×35
10F	W14×74	W14×61	3.5	2	W18×35	W18×35
9F	W14×99	W14×74	4	2.5	W18×46	W18×35
8F	W14×99	W14×74	4	2.5	W18×35	W18×35
7F	W14×145	W14×90	4.5	3	W18×46	W18×35
6F	W14×145	W14×90	4.5	3	W18×35	W18×35
5F	W14×176	W14×120	5.5	3.5	W18×50	W18×35
4F	W14×176	W14×120	5.5	3.5	W18×35	W18×35
3F	W14×257	W14×176	6	3.5	W18×50	W18×35
2F	W14×257	W14×176	6	3.5	W18×35	W18×35

Table A.11 Member sizes of 16-story SCBF archetypes

16-STORY SCBF (RSA)						
Floor	Columns		Braces		Beams	
	Dmax	Dmin	Dmax	Dmin	Dmax	Dmin
Roof	W12×45	W12×40	HSS9-5/8×0.375	HSS5×0.312	W18×65	W18×50
16F	W12×45	W12×40	HSS9-5/8×0.375	HSS5×0.312	W18×35	W18×35
15F	W14×82	W14×53	HSS8-5/8×0.5	HSS6x0.312	W18×71	W18×50
14F	W14×82	W14×53	HSS8-5/8×0.5	HSS6×0.312	W18×35	W18×35
13F	W14×120	W14×68	HSS11-1/4×0.5	HSS6×0.312	W18×86	W18×50
12F	W14×120	W14×68	HSS11-1/4×0.5	HSS6×0.312	W18×35	W18×35
11F	W14×176	W14×90	HSS10×0.625	HSS6×0.312	W18×86	W18×50
10F	W14×176	W14×90	HSS10×0.625	HSS6×0.312	W18×35	W18×35
9F	W14×233	W14×109	HSS11-1/4×0.625	HSS6-5/8×0.312	W18×97	W18×50
8F	W14×233	W14×109	HSS11-1/4×0.625	HSS6-5/8×0.312	W18×35	W18×35
7F	W14×283	W14×132	HSS11-1/4×0.625	HSS6-5/8×0.312	W18×97	W18×50
6F	W14×283	W14×132	HSS11-1/4×0.625	HSS6-5/8×0.312	W18×35	W18×35
5F	W14×342	W14×159	HSS11-1/4×0.625	HSS6-5/8×0.5	W21×93	W18×60
4F	W14×342	W14×159	HSS11-1/4×0.625	HSS6-5/8×0.5	W18×35	W18×35
3F	W14×370	W14×193	W12×96	HSS6-5/8×0.5	W24×146	W18×60
2F	W14×370	W14×193	W12×96	HSS6-5/8×0.5	W18×35	W18×35

Table A.12 Member sizes of 16-story BRBF archetypes.

16-STORY BRBF (RSA)						
Floor	Columns		Braces		Beams	
	Dmax	Dmin	Dmax	Dmin	Dmax	Dmin
Roof	W12×40	W12×40	3	1.5	W18×46	W18×35
16F	W12×40	W12×40	3	1.5	W18×35	W18×35
15F	W14×82	W14×61	3.5	2.5	W18×46	W18×35
14F	W14x82	W14x61	3.5	2.5	W18×35	W18×35
13F	W14×109	W14×82	4.5	3	W18×46	W18×35
12F	W14×109	W14×82	4.5	3	W18×35	W18×35
11F	W14×159	W14×99	4.5	3	W18×46	W18×35
10F	W14×159	W14×99	4.5	3	W18×35	W18×35
9F	W14×193	W14×120	5.5	3.5	W18×50	W18×40
8F	W14×193	W14×120	5.5	3.5	W18×35	W18×35
7F	W14×233	W14×145	6	3.5	W18×50	W18×40
6F	W14×233	W14×145	6	3.5	W18×35	W18×35
5F	W14×342	W14×176	6.5	4	W18×50	W18×40
4F	W14×342	W14×176	6.5	4	W18x35	W18x35
3F	W14×426	W14×233	7	4.5	W18×55	W18×40
2F	W14×426	W14×233	7	4.5	W18×35	W18×35

Braces in SCBFs and BRBFs are assumed to have pin connections to the framing. Rigid-in-plane offsets are assumed at the beam-column connections and brace-to-framing connections. The effective length of the braces corresponds to 70% of the workpoint-to-workpoint length. The braces are designed to resist more than 70% of the lateral forces. HSS round sections are used for most of the SCBF archetypes except for the locations where the demand is too large to use HSS round sections, in which case compact wide flange sections are used. For the buckling-restrained braces, only the steel core areas are determined in the design of the archetypes. The effective stiffness of the BRBs are modified to 1.4 times the stiffness computed using only the steel core to account for the stiffness contribution from tapered and connection areas of the BRBs.

Fully restrained connections are adopted in the design of beams. Beams are laterally supported at quarter points along the span. In SCBF and BRBF archetypes, the beams where the braces intersected at beam-column connections are also designed to carry the axial force from braces. The capacity design concept is adopted. The axial force from braces are conservatively estimated as $R_y F_y A_g$ in tension and zero in compression, where $R_y F_y$ is the expected yield strength of the braces and A_g is the brace gross area. For the beams where the braces intersected at the mid-span, the unbalanced loads due to the capacity difference of braces above and below

the beams are applied. The unbalanced loads in SCBFs are estimated based on $R_y F_y A_g$ for tension braces and $0.3P_n$ for compression braces, where P_n is the nominal compression capacity of the conventional buckling braces. In BRBFs, the capacity of braces is estimated as $\omega\beta P_{ysc}$ for compression and ωP_{ysc} for tension, where ω is the tension strength adjustment factor, β is the compression strength adjustment factor, and P_{ysc} is the yield strength of steel core. ω and $\omega\beta$ are estimated as 1.15 and 1.18, respectively, which are similar to the design in Steel Tips [López and Sabelli 2004]. Due to the configuration of double-story X in elevation, the unbalanced loads of the SCBF and BRBF archetypes cancel out and only a small portion of the unbalanced force is applied in the beams. The beams are also designed to carry the tributary gravity load distributed along the span.

Columns of the braced frames are fixed at the base. They are oriented to resist lateral force by strong-axis bending. The columns are designed to carry the appropriate load combinations including the overstrength factor, Ω_o. W14, and W12 sections with proper axial, shear, and flexural capacity are used for the columns. Generally, the column sections are changed every two stories and the splices are assumed to be on the floor level.

PEER REPORTS

PEER reports are available individually or by yearly subscription. PEER reports can be ordered at http://peer.berkeley.edu/publications/peer_reports.html or by contacting the Pacific Earthquake Engineering Research Center, 325 Davis Hall mail code 1792, Berkeley, CA 94720. Tel.: (510) 642-3437; Fax: (510) 665-1655; Email: peer_editor@berkeley.edu

PEER 2012/08 *Guidelines for Estimation of Shear Wave Velocity.* Bernard R. Wair, Jason T. DeJong, and Thomas Shantz. December 2012.

PEER 2012/07 *Earthquake Engineering for Resilient Communities: 2012 PEER Internship Program Research Report Collection.* Heidi Tremayne (Editor), Stephen A. Mahin (Editor), Collin Anderson, Dustin Cook, Michael Erceg, Carlos Esparza, Jose Jimenez, Dorian Krausz, Andrew Lo, Stephanie Lopez, Nicole McCurdy, Paul Shipman, Alexander Strum, Eduardo Vega. December 2012.

PEER 2012/06 *Fragilities for Precarious Rocks at Yucca Mountain.* Matthew D. Purvance, Rasool Anooshehpoor, and James N. Brune. December 2012.

PEER 2012/05 *Development of Simplified Analysis Procedure for Piles in Laterally Spreading Layered Soils.* Christopher R. McGann, Pedro Arduino, and Peter Mackenzie–Helnwein. December 2012.

PEER 2012/04 *Unbonded Pre-Tensioned Columns for Bridges in Seismic Regions.* Phillip M. Davis, Todd M. Janes, Marc O. Eberhard, and John F. Stanton. December 2012.

PEER 2012/03 *Experimental and Analytical Studies on Reinforced Concrete Buildings with Seismically Vulnerable Beam-Column Joints.* Sangjoon Park and Khalid M. Mosalam. October 2012.

PEER 2012/02 *Seismic Performance of Reinforced Concrete Bridges Allowed to Uplift during Multi-Directional Excitation.* Andres Oscar Espinoza and Stephen A. Mahin. July 2012.

PEER 2012/01 *Spectral Damping Scaling Factors for Shallow Crustal Earthquakes in Active Tectonic Regions.* Sanaz Rezaeian, Yousef Bozorgnia, I. M. Idriss, Kenneth Campbell, Norman Abrahamson, and Walter Silva. July 2012.

PEER 2011/10 *Earthquake Engineering for Resilient Communities: 2011 PEER Internship Program Research Report Collection.* Eds. Heidi Faison and Stephen A. Mahin. December 2011.

PEER 2011/09 *Calibration of Semi-Stochastic Procedure for Simulating High-Frequency Ground Motions.* Jonathan P. Stewart, Emel Seyhan, and Robert W. Graves. December 2011.

PEER 2011/08 *Water Supply in regard to Fire Following Earthquake.* Charles Scawthorn. November 2011.

PEER 2011/07 *Seismic Risk Management in Urban Areas. Proceedings of a U.S.-Iran-Turkey Seismic Workshop.* September 2011.

PEER 2011/06 *The Use of Base Isolation Systems to Achieve Complex Seismic Performance Objectives.* Troy A. Morgan and Stephen A. Mahin. July 2011.

PEER 2011/05 *Case Studies of the Seismic Performance of Tall Buildings Designed by Alternative Means.* Task 12 Report for the Tall Buildings Initiative. Jack Moehle, Yousef Bozorgnia, Nirmal Jayaram, Pierson Jones, Mohsen Rahnama, Nilesh Shome, Zeynep Tuna, John Wallace, Tony Yang, and Farzin Zareian. July 2011.

PEER 2011/04 *Recommended Design Practice for Pile Foundations in Laterally Spreading Ground.* Scott A. Ashford, Ross W. Boulanger, and Scott J. Brandenberg. June 2011.

PEER 2011/03 *New Ground Motion Selection Procedures and Selected Motions for the PEER Transportation Research Program.* Jack W. Baker, Ting Lin, Shrey K. Shahi, and Nirmal Jayaram. March 2011.

PEER 2011/02 *A Bayesian Network Methodology for Infrastructure Seismic Risk Assessment and Decision Support.* Michelle T. Bensi, Armen Der Kiureghian, and Daniel Straub. March 2011.

PEER 2011/01 *Demand Fragility Surfaces for Bridges in Liquefied and Laterally Spreading Ground.* Scott J. Brandenberg, Jian Zhang, Pirooz Kashighandi, Yili Huo, and Minxing Zhao. March 2011.

PEER 2010/05 *Guidelines for Performance-Based Seismic Design of Tall Buildings.* Developed by the Tall Buildings Initiative. November 2010.

PEER 2010/04 *Application Guide for the Design of Flexible and Rigid Bus Connections between Substation Equipment Subjected to Earthquakes.* Jean-Bernard Dastous and Armen Der Kiureghian. September 2010.

PEER 2010/03 *Shear Wave Velocity as a Statistical Function of Standard Penetration Test Resistance and Vertical Effective Stress at Caltrans Bridge Sites.* Scott J. Brandenberg, Naresh Bellana, and Thomas Shantz. June 2010.

PEER 2010/02 *Stochastic Modeling and Simulation of Ground Motions for Performance-Based Earthquake Engineering.* Sanaz Rezaeian and Armen Der Kiureghian. June 2010.

PEER 2010/01 *Structural Response and Cost Characterization of Bridge Construction Using Seismic Performance Enhancement Strategies.* Ady Aviram, Božidar Stojadinović, Gustavo J. Parra-Montesinos, and Kevin R. Mackie. March 2010.

PEER 2009/03 *The Integration of Experimental and Simulation Data in the Study of Reinforced Concrete Bridge Systems Including Soil-Foundation-Structure Interaction.* Matthew Dryden and Gregory L. Fenves. November 2009.

PEER 2009/02 *Improving Earthquake Mitigation through Innovations and Applications in Seismic Science, Engineering, Communication, and Response. Proceedings of a U.S.-Iran Seismic Workshop.* October 2009.

PEER 2009/01 *Evaluation of Ground Motion Selection and Modification Methods: Predicting Median Interstory Drift Response of Buildings.* Curt B. Haselton, Ed. June 2009.

PEER 2008/10 *Technical Manual for Strata.* Albert R. Kottke and Ellen M. Rathje. February 2009.

PEER 2008/09 *NGA Model for Average Horizontal Component of Peak Ground Motion and Response Spectra.* Brian S.-J. Chiou and Robert R. Youngs. November 2008.

PEER 2008/08 *Toward Earthquake-Resistant Design of Concentrically Braced Steel Structures.* Patxi Uriz and Stephen A. Mahin. November 2008.

PEER 2008/07 *Using OpenSees for Performance-Based Evaluation of Bridges on Liquefiable Soils.* Stephen L. Kramer, Pedro Arduino, and HyungSuk Shin. November 2008.

PEER 2008/06 *Shaking Table Tests and Numerical Investigation of Self-Centering Reinforced Concrete Bridge Columns.* Hyung IL Jeong, Junichi Sakai, and Stephen A. Mahin. September 2008.

PEER 2008/05 *Performance-Based Earthquake Engineering Design Evaluation Procedure for Bridge Foundations Undergoing Liquefaction-Induced Lateral Ground Displacement.* Christian A. Ledezma and Jonathan D. Bray. August 2008.

PEER 2008/04 *Benchmarking of Nonlinear Geotechnical Ground Response Analysis Procedures.* Jonathan P. Stewart, Annie On-Lei Kwok, Yousseff M. A. Hashash, Neven Matasovic, Robert Pyke, Zhiliang Wang, and Zhaohui Yang. August 2008.

PEER 2008/03 *Guidelines for Nonlinear Analysis of Bridge Structures in California.* Ady Aviram, Kevin R. Mackie, and Božidar Stojadinović. August 2008.

PEER 2008/02 *Treatment of Uncertainties in Seismic-Risk Analysis of Transportation Systems.* Evangelos Stergiou and Anne S. Kiremidjian. July 2008.

PEER 2008/01 *Seismic Performance Objectives for Tall Buildings.* William T. Holmes, Charles Kircher, William Petak, and Nabih Youssef. August 2008.

PEER 2007/12 *An Assessment to Benchmark the Seismic Performance of a Code-Conforming Reinforced Concrete Moment-Frame Building.* Curt Haselton, Christine A. Goulet, Judith Mitrani-Reiser, James L. Beck, Gregory G. Deierlein, Keith A. Porter, Jonathan P. Stewart, and Ertugrul Taciroglu. August 2008.

PEER 2007/11 *Bar Buckling in Reinforced Concrete Bridge Columns.* Wayne A. Brown, Dawn E. Lehman, and John F. Stanton. February 2008.

PEER 2007/10 *Computational Modeling of Progressive Collapse in Reinforced Concrete Frame Structures.* Mohamed M. Talaat and Khalid M. Mosalam. May 2008.

PEER 2007/09 *Integrated Probabilistic Performance-Based Evaluation of Benchmark Reinforced Concrete Bridges.* Kevin R. Mackie, John-Michael Wong, and Božidar Stojadinović. January 2008.

PEER 2007/08 *Assessing Seismic Collapse Safety of Modern Reinforced Concrete Moment-Frame Buildings.* Curt B. Haselton and Gregory G. Deierlein. February 2008.

PEER 2007/07 *Performance Modeling Strategies for Modern Reinforced Concrete Bridge Columns.* Michael P. Berry and Marc O. Eberhard. April 2008.

PEER 2007/06 *Development of Improved Procedures for Seismic Design of Buried and Partially Buried Structures.* Linda Al Atik and Nicholas Sitar. June 2007.

PEER 2007/05 *Uncertainty and Correlation in Seismic Risk Assessment of Transportation Systems.* Renee G. Lee and Anne S. Kiremidjian. July 2007.

PEER 2007/04 *Numerical Models for Analysis and Performance-Based Design of Shallow Foundations Subjected to Seismic Loading.* Sivapalan Gajan, Tara C. Hutchinson, Bruce L. Kutter, Prishati Raychowdhury, José A. Ugalde, and Jonathan P. Stewart. May 2008.

PEER 2007/03 *Beam-Column Element Model Calibrated for Predicting Flexural Response Leading to Global Collapse of RC Frame Buildings.* Curt B. Haselton, Abbie B. Liel, Sarah Taylor Lange, and Gregory G. Deierlein. May 2008.

PEER 2007/02 *Campbell-Bozorgnia NGA Ground Motion Relations for the Geometric Mean Horizontal Component of Peak and Spectral Ground Motion Parameters.* Kenneth W. Campbell and Yousef Bozorgnia. May 2007.

PEER 2007/01 *Boore-Atkinson NGA Ground Motion Relations for the Geometric Mean Horizontal Component of Peak and Spectral Ground Motion Parameters.* David M. Boore and Gail M. Atkinson. May. May 2007.

PEER 2006/12 *Societal Implications of Performance-Based Earthquake Engineering*. Peter J. May. May 2007.

PEER 2006/11 *Probabilistic Seismic Demand Analysis Using Advanced Ground Motion Intensity Measures, Attenuation Relationships, and Near-Fault Effects.* Polsak Tothong and C. Allin Cornell. March 2007.

PEER 2006/10 *Application of the PEER PBEE Methodology to the I-880 Viaduct.* Sashi Kunnath. February 2007.

PEER 2006/09 *Quantifying Economic Losses from Travel Forgone Following a Large Metropolitan Earthquake.* James Moore, Sungbin Cho, Yue Yue Fan, and Stuart Werner. November 2006.

PEER 2006/08 *Vector-Valued Ground Motion Intensity Measures for Probabilistic Seismic Demand Analysis*. Jack W. Baker and C. Allin Cornell. October 2006.

PEER 2006/07 *Analytical Modeling of Reinforced Concrete Walls for Predicting Flexural and Coupled–Shear-Flexural Responses*. Kutay Orakcal, Leonardo M. Massone, and John W. Wallace. October 2006.

PEER 2006/06 *Nonlinear Analysis of a Soil-Drilled Pier System under Static and Dynamic Axial Loading.* Gang Wang and Nicholas Sitar. November 2006.

PEER 2006/05 *Advanced Seismic Assessment Guidelines.* Paolo Bazzurro, C. Allin Cornell, Charles Menun, Maziar Motahari, and Nicolas Luco. September 2006.

PEER 2006/04 *Probabilistic Seismic Evaluation of Reinforced Concrete Structural Components and Systems.* Tae Hyung Lee and Khalid M. Mosalam. August 2006.

PEER 2006/03 *Performance of Lifelines Subjected to Lateral Spreading.* Scott A. Ashford and Teerawut Juirnarongrit. July 2006.

PEER 2006/02 *Pacific Earthquake Engineering Research Center Highway Demonstration Project.* Anne Kiremidjian, James Moore, Yue Yue Fan, Nesrin Basoz, Ozgur Yazali, and Meredith Williams. April 2006.

PEER 2006/01 *Bracing Berkeley. A Guide to Seismic Safety on the UC Berkeley Campus.* Mary C. Comerio, Stephen Tobriner, and Ariane Fehrenkamp. January 2006.

PEER 2005/16 *Seismic Response and Reliability of Electrical Substation Equipment and Systems.* Junho Song, Armen Der Kiureghian, and Jerome L. Sackman. April 2006.

PEER 2005/15 *CPT-Based Probabilistic Assessment of Seismic Soil Liquefaction Initiation.* R. E. S. Moss, R. B. Seed, R. E. Kayen, J. P. Stewart, and A. Der Kiureghian. April 2006.

PEER 2005/14 *Workshop on Modeling of Nonlinear Cyclic Load-Deformation Behavior of Shallow Foundations.* Bruce L. Kutter, Geoffrey Martin, Tara Hutchinson, Chad Harden, Sivapalan Gajan, and Justin Phalen. March 2006.

PEER 2005/13 *Stochastic Characterization and Decision Bases under Time-Dependent Aftershock Risk in Performance-Based Earthquake Engineering.* Gee Liek Yeo and C. Allin Cornell. July 2005.

PEER 2005/12 *PEER Testbed Study on a Laboratory Building: Exercising Seismic Performance Assessment.* Mary C. Comerio, editor. November 2005.

PEER 2005/11 *Van Nuys Hotel Building Testbed Report: Exercising Seismic Performance Assessment.* Helmut Krawinkler, editor. October 2005.

PEER 2005/10 *First NEES/E-Defense Workshop on Collapse Simulation of Reinforced Concrete Building Structures.* September 2005.

PEER 2005/09 *Test Applications of Advanced Seismic Assessment Guidelines.* Joe Maffei, Karl Telleen, Danya Mohr, William Holmes, and Yuki Nakayama. August 2006.

PEER 2005/08 *Damage Accumulation in Lightly Confined Reinforced Concrete Bridge Columns.* R. Tyler Ranf, Jared M. Nelson, Zach Price, Marc O. Eberhard, and John F. Stanton. April 2006.

PEER 2005/07 *Experimental and Analytical Studies on the Seismic Response of Freestanding and Anchored Laboratory Equipment.* Dimitrios Konstantinidis and Nicos Makris. January 2005.

PEER 2005/06 *Global Collapse of Frame Structures under Seismic Excitations*. Luis F. Ibarra and Helmut Krawinkler. September 2005.

PEER 2005//05 *Performance Characterization of Bench- and Shelf-Mounted Equipment.* Samit Ray Chaudhuri and Tara C. Hutchinson. May 2006.

PEER 2005/04 *Numerical Modeling of the Nonlinear Cyclic Response of Shallow Foundations.* Chad Harden, Tara Hutchinson, Geoffrey R. Martin, and Bruce L. Kutter. August 2005.

PEER 2005/03 *A Taxonomy of Building Components for Performance-Based Earthquake Engineering.* Keith A. Porter. September 2005.

PEER 2005/02 *Fragility Basis for California Highway Overpass Bridge Seismic Decision Making*. Kevin R. Mackie and Božidar Stojadinović. June 2005.

PEER 2005/01 *Empirical Characterization of Site Conditions on Strong Ground Motion.* Jonathan P. Stewart, Yoojoong Choi, and Robert W. Graves. June 2005.

PEER 2004/09 *Electrical Substation Equipment Interaction: Experimental Rigid Conductor Studies.* Christopher Stearns and André Filiatrault. February 2005.

PEER 2004/08 *Seismic Qualification and Fragility Testing of Line Break 550-kV Disconnect Switches.* Shakhzod M. Takhirov, Gregory L. Fenves, and Eric Fujisaki. January 2005.

PEER 2004/07 *Ground Motions for Earthquake Simulator Qualification of Electrical Substation Equipment.* Shakhzod M. Takhirov, Gregory L. Fenves, Eric Fujisaki, and Don Clyde. January 2005.

PEER 2004/06 *Performance-Based Regulation and Regulatory Regimes.* Peter J. May and Chris Koski. September 2004.

PEER 2004/05 *Performance-Based Seismic Design Concepts and Implementation: Proceedings of an International Workshop.* Peter Fajfar and Helmut Krawinkler, editors. September 2004.

PEER 2004/04 *Seismic Performance of an Instrumented Tilt-up Wall Building.* James C. Anderson and Vitelmo V. Bertero. July 2004.

PEER 2004/03 *Evaluation and Application of Concrete Tilt-up Assessment Methodologies.* Timothy Graf and James O. Malley. October 2004.

PEER 2004/02 *Analytical Investigations of New Methods for Reducing Residual Displacements of Reinforced Concrete Bridge Columns.* Junichi Sakai and Stephen A. Mahin. August 2004.

PEER 2004/01 *Seismic Performance of Masonry Buildings and Design Implications.* Kerri Anne Taeko Tokoro, James C. Anderson, and Vitelmo V. Bertero. February 2004.

PEER 2003/18 *Performance Models for Flexural Damage in Reinforced Concrete Columns.* Michael Berry and Marc Eberhard. August 2003.

PEER 2003/17 *Predicting Earthquake Damage in Older Reinforced Concrete Beam-Column Joints.* Catherine Pagni and Laura Lowes. October 2004.

PEER 2003/16 *Seismic Demands for Performance-Based Design of Bridges.* Kevin Mackie and Božidar Stojadinović. August 2003.

PEER 2003/15 *Seismic Demands for Nondeteriorating Frame Structures and Their Dependence on Ground Motions.* Ricardo Antonio Medina and Helmut Krawinkler. May 2004.

PEER 2003/14 *Finite Element Reliability and Sensitivity Methods for Performance-Based Earthquake Engineering.* Terje Haukaas and Armen Der Kiureghian. April 2004.

PEER 2003/13 *Effects of Connection Hysteretic Degradation on the Seismic Behavior of Steel Moment-Resisting Frames.* Janise E. Rodgers and Stephen A. Mahin. March 2004.

PEER 2003/12 *Implementation Manual for the Seismic Protection of Laboratory Contents: Format and Case Studies.* William T. Holmes and Mary C. Comerio. October 2003.

PEER 2003/11 *Fifth U.S.-Japan Workshop on Performance-Based Earthquake Engineering Methodology for Reinforced Concrete Building Structures.* February 2004.

PEER 2003/10 *A Beam-Column Joint Model for Simulating the Earthquake Response of Reinforced Concrete Frames.* Laura N. Lowes, Nilanjan Mitra, and Arash Altoontash. February 2004.

PEER 2003/09 *Sequencing Repairs after an Earthquake: An Economic Approach.* Marco Casari and Simon J. Wilkie. April 2004.

PEER 2003/08 *A Technical Framework for Probability-Based Demand and Capacity Factor Design (DCFD) Seismic Formats*. Fatemeh Jalayer and C. Allin Cornell. November 2003.

PEER 2003/07 *Uncertainty Specification and Propagation for Loss Estimation Using FOSM Methods.* Jack W. Baker and C. Allin Cornell. September 2003.

PEER 2003/06 *Performance of Circular Reinforced Concrete Bridge Columns under Bidirectional Earthquake Loading*. Mahmoud M. Hachem, Stephen A. Mahin, and Jack P. Moehle. February 2003.

PEER 2003/05 *Response Assessment for Building-Specific Loss Estimation.* Eduardo Miranda and Shahram Taghavi. September 2003.

PEER 2003/04 *Experimental Assessment of Columns with Short Lap Splices Subjected to Cyclic Loads.* Murat Melek, John W. Wallace, and Joel Conte. April 2003.

PEER 2003/03 *Probabilistic Response Assessment for Building-Specific Loss Estimation.* Eduardo Miranda and Hesameddin Aslani. September 2003.

PEER 2003/02 *Software Framework for Collaborative Development of Nonlinear Dynamic Analysis Program.* Jun Peng and Kincho H. Law. September 2003.

PEER 2003/01 *Shake Table Tests and Analytical Studies on the Gravity Load Collapse of Reinforced Concrete Frames.* Kenneth John Elwood and Jack P. Moehle. November 2003.

PEER 2002/24 *Performance of Beam to Column Bridge Joints Subjected to a Large Velocity Pulse.* Natalie Gibson, André Filiatrault, and Scott A. Ashford. April 2002.

PEER 2002/23 *Effects of Large Velocity Pulses on Reinforced Concrete Bridge Columns.* Greg L. Orozco and Scott A. Ashford. April 2002.

PEER 2002/22 *Characterization of Large Velocity Pulses for Laboratory Testing.* Kenneth E. Cox and Scott A. Ashford. April 2002.

PEER 2002/21 *Fourth U.S.-Japan Workshop on Performance-Based Earthquake Engineering Methodology for Reinforced Concrete Building Structures*. December 2002.

PEER 2002/20 *Barriers to Adoption and Implementation of PBEE Innovations.* Peter J. May. August 2002.

PEER 2002/19 *Economic-Engineered Integrated Models for Earthquakes: Socioeconomic Impacts.* Peter Gordon, James E. Moore II, and Harry W. Richardson. July 2002.

PEER 2002/18 *Assessment of Reinforced Concrete Building Exterior Joints with Substandard Details.* Chris P. Pantelides, Jon Hansen, Justin Nadauld, and Lawrence D. Reaveley. May 2002.

PEER 2002/17 *Structural Characterization and Seismic Response Analysis of a Highway Overcrossing Equipped with Elastomeric Bearings and Fluid Dampers: A Case Study.* Nicos Makris and Jian Zhang. November 2002.

PEER 2002/16 *Estimation of Uncertainty in Geotechnical Properties for Performance-Based Earthquake Engineering.* Allen L. Jones, Steven L. Kramer, and Pedro Arduino. December 2002.

PEER 2002/15 *Seismic Behavior of Bridge Columns Subjected to Various Loading Patterns.* Asadollah Esmaeily-Gh. and Yan Xiao. December 2002.

PEER 2002/14 *Inelastic Seismic Response of Extended Pile Shaft Supported Bridge Structures.* T.C. Hutchinson, R.W. Boulanger, Y.H. Chai, and I.M. Idriss. December 2002.

PEER 2002/13 *Probabilistic Models and Fragility Estimates for Bridge Components and Systems.* Paolo Gardoni, Armen Der Kiureghian, and Khalid M. Mosalam. June 2002.

PEER 2002/12 *Effects of Fault Dip and Slip Rake on Near-Source Ground Motions: Why Chi-Chi Was a Relatively Mild M7.6 Earthquake.* Brad T. Aagaard, John F. Hall, and Thomas H. Heaton. December 2002.

PEER 2002/11 *Analytical and Experimental Study of Fiber-Reinforced Strip Isolators*. James M. Kelly and Shakhzod M. Takhirov. September 2002.

PEER 2002/10 *Centrifuge Modeling of Settlement and Lateral Spreading with Comparisons to Numerical Analyses***.** Sivapalan Gajan and Bruce L. Kutter. January 2003.

PEER 2002/09 *Documentation and Analysis of Field Case Histories of Seismic Compression during the 1994 Northridge, California, Earthquake.* Jonathan P. Stewart, Patrick M. Smith, Daniel H. Whang, and Jonathan D. Bray. October 2002.

PEER 2002/08 *Component Testing, Stability Analysis and Characterization of Buckling-Restrained Unbonded Braces™.* Cameron Black, Nicos Makris, and Ian Aiken. September 2002.

PEER 2002/07 *Seismic Performance of Pile-Wharf Connections.* Charles W. Roeder, Robert Graff, Jennifer Soderstrom, and Jun Han Yoo. December 2001.

PEER 2002/06 *The Use of Benefit-Cost Analysis for Evaluation of Performance-Based Earthquake Engineering Decisions*. Richard O. Zerbe and Anthony Falit-Baiamonte. September 2001.

PEER 2002/05 *Guidelines, Specifications, and Seismic Performance Characterization of Nonstructural Building Components and Equipment*. André Filiatrault, Constantin Christopoulos, and Christopher Stearns. September 2001.

PEER 2002/04 *Consortium of Organizations for Strong-Motion Observation Systems and the Pacific Earthquake Engineering Research Center Lifelines Program: Invited Workshop on Archiving and Web Dissemination of Geotechnical Data, 4–5 October 2001*. September 2002.

PEER 2002/03 *Investigation of Sensitivity of Building Loss Estimates to Major Uncertain Variables for the Van Nuys Testbed.* Keith A. Porter, James L. Beck, and Rustem V. Shaikhutdinov. August 2002.

PEER 2002/02 *The Third U.S.-Japan Workshop on Performance-Based Earthquake Engineering Methodology for Reinforced Concrete Building Structures*. July 2002.

PEER 2002/01 *Nonstructural Loss Estimation: The UC Berkeley Case Study.* Mary C. Comerio and John C. Stallmeyer. December 2001.

PEER 2001/16 *Statistics of SDF-System Estimate of Roof Displacement for Pushover Analysis of Buildings.* Anil K. Chopra, Rakesh K. Goel, and Chatpan Chintanapakdee. December 2001.

PEER 2001/15 *Damage to Bridges during the 2001 Nisqually Earthquake.* R. Tyler Ranf, Marc O. Eberhard, and Michael P. Berry. November 2001.

PEER 2001/14 *Rocking Response of Equipment Anchored to a Base Foundation.* Nicos Makris and Cameron J. Black. September 2001.

PEER 2001/13 *Modeling Soil Liquefaction Hazards for Performance-Based Earthquake Engineering.* Steven L. Kramer and Ahmed-W. Elgamal. February 2001.

PEER 2001/12 *Development of Geotechnical Capabilities in OpenSees.* Boris Jeremić. September 2001.

PEER 2001/11 *Analytical and Experimental Study of Fiber-Reinforced Elastomeric Isolators*. James M. Kelly and Shakhzod M. Takhirov. September 2001.

PEER 2001/10 *Amplification Factors for Spectral Acceleration in Active Regions.* Jonathan P. Stewart, Andrew H. Liu, Yoojoong Choi, and Mehmet B. Baturay. December 2001.

PEER 2001/09 *Ground Motion Evaluation Procedures for Performance-Based Design.* Jonathan P. Stewart, Shyh-Jeng Chiou, Jonathan D. Bray, Robert W. Graves, Paul G. Somerville, and Norman A. Abrahamson. September 2001.

PEER 2001/08 *Experimental and Computational Evaluation of Reinforced Concrete Bridge Beam-Column Connections for Seismic Performance*. Clay J. Naito, Jack P. Moehle, and Khalid M. Mosalam. November 2001.

PEER 2001/07 *The Rocking Spectrum and the Shortcomings of Design Guidelines*. Nicos Makris and Dimitrios Konstantinidis. August 2001.

PEER 2001/06 *Development of an Electrical Substation Equipment Performance Database for Evaluation of Equipment Fragilities*. Thalia Agnanos. April 1999.

PEER 2001/05 *Stiffness Analysis of Fiber-Reinforced Elastomeric Isolators.* Hsiang-Chuan Tsai and James M. Kelly. May 2001.

PEER 2001/04 *Organizational and Societal Considerations for Performance-Based Earthquake Engineering.* Peter J. May. April 2001.

PEER 2001/03 *A Modal Pushover Analysis Procedure to Estimate Seismic Demands for Buildings: Theory and Preliminary Evaluation.* Anil K. Chopra and Rakesh K. Goel. January 2001.

PEER 2001/02 *Seismic Response Analysis of Highway Overcrossings Including Soil-Structure Interaction.* Jian Zhang and Nicos Makris. March 2001.

PEER 2001/01 *Experimental Study of Large Seismic Steel Beam-to-Column Connections.* Egor P. Popov and Shakhzod M. Takhirov. November 2000.

PEER 2000/10 *The Second U.S.-Japan Workshop on Performance-Based Earthquake Engineering Methodology for Reinforced Concrete Building Structures.* March 2000.

PEER 2000/09 *Structural Engineering Reconnaissance of the August 17, 1999 Earthquake: Kocaeli (Izmit), Turkey.* Halil Sezen, Kenneth J. Elwood, Andrew S. Whittaker, Khalid Mosalam, John J. Wallace, and John F. Stanton. December 2000.

PEER 2000/08 *Behavior of Reinforced Concrete Bridge Columns Having Varying Aspect Ratios and Varying Lengths of Confinement.* Anthony J. Calderone, Dawn E. Lehman, and Jack P. Moehle. January 2001.

PEER 2000/07 *Cover-Plate and Flange-Plate Reinforced Steel Moment-Resisting Connections.* Taejin Kim, Andrew S. Whittaker, Amir S. Gilani, Vitelmo V. Bertero, and Shakhzod M. Takhirov. September 2000.

PEER 2000/06 *Seismic Evaluation and Analysis of 230-kV Disconnect Switches.* Amir S. J. Gilani, Andrew S. Whittaker, Gregory L. Fenves, Chun-Hao Chen, Henry Ho, and Eric Fujisaki. July 2000.

PEER 2000/05 *Performance-Based Evaluation of Exterior Reinforced Concrete Building Joints for Seismic Excitation.* Chandra Clyde, Chris P. Pantelides, and Lawrence D. Reaveley. July 2000.

PEER 2000/04 *An Evaluation of Seismic Energy Demand: An Attenuation Approach.* Chung-Che Chou and Chia-Ming Uang. July 1999.

PEER 2000/03 *Framing Earthquake Retrofitting Decisions: The Case of Hillside Homes in Los Angeles.* Detlof von Winterfeldt, Nels Roselund, and Alicia Kitsuse. March 2000.

PEER 2000/02 *U.S.-Japan Workshop on the Effects of Near-Field Earthquake Shaking.* Andrew Whittaker, ed. July 2000.

PEER 2000/01 *Further Studies on Seismic Interaction in Interconnected Electrical Substation Equipment.* Armen Der Kiureghian, Kee-Jeung Hong, and Jerome L. Sackman. November 1999.

PEER 1999/14 *Seismic Evaluation and Retrofit of 230-kV Porcelain Transformer Bushings.* Amir S. Gilani, Andrew S. Whittaker, Gregory L. Fenves, and Eric Fujisaki. December 1999.

PEER 1999/13 *Building Vulnerability Studies: Modeling and Evaluation of Tilt-up and Steel Reinforced Concrete Buildings.* John W. Wallace, Jonathan P. Stewart, and Andrew S. Whittaker, editors. December 1999.

PEER 1999/12 *Rehabilitation of Nonductile RC Frame Building Using Encasement Plates and Energy-Dissipating Devices.* Mehrdad Sasani, Vitelmo V. Bertero, James C. Anderson. December 1999.

PEER 1999/11 *Performance Evaluation Database for Concrete Bridge Components and Systems under Simulated Seismic Loads.* Yael D. Hose and Frieder Seible. November 1999.

PEER 1999/10 *U.S.-Japan Workshop on Performance-Based Earthquake Engineering Methodology for Reinforced Concrete Building Structures.* December 1999.

PEER 1999/09 *Performance Improvement of Long Period Building Structures Subjected to Severe Pulse-Type Ground Motions.* James C. Anderson, Vitelmo V. Bertero, and Raul Bertero. October 1999.

PEER 1999/08 *Envelopes for Seismic Response Vectors.* Charles Menun and Armen Der Kiureghian. July 1999.

PEER 1999/07 *Documentation of Strengths and Weaknesses of Current Computer Analysis Methods for Seismic Performance of Reinforced Concrete Members.* William F. Cofer. November 1999.

PEER 1999/06 *Rocking Response and Overturning of Anchored Equipment under Seismic Excitations.* Nicos Makris and Jian Zhang. November 1999.

PEER 1999/05 *Seismic Evaluation of 550 kV Porcelain Transformer Bushings.* Amir S. Gilani, Andrew S. Whittaker, Gregory L. Fenves, and Eric Fujisaki. October 1999.

PEER 1999/04 *Adoption and Enforcement of Earthquake Risk-Reduction Measures.* Peter J. May, Raymond J. Burby, T. Jens Feeley, and Robert Wood.

PEER 1999/03 *Task 3 Characterization of Site Response General Site Categories.* Adrian Rodriguez-Marek, Jonathan D. Bray, and Norman Abrahamson. February 1999.

PEER 1999/02 *Capacity-Demand-Diagram Methods for Estimating Seismic Deformation of Inelastic Structures: SDF Systems.* Anil K. Chopra and Rakesh Goel. April 1999.

PEER 1999/01 *Interaction in Interconnected Electrical Substation Equipment Subjected to Earthquake Ground Motions.* Armen Der Kiureghian, Jerome L. Sackman, and Kee-Jeung Hong. February 1999.

PEER 1998/08 *Behavior and Failure Analysis of a Multiple-Frame Highway Bridge in the 1994 Northridge Earthquake.* Gregory L. Fenves and Michael Ellery. December 1998.

PEER 1998/07 *Empirical Evaluation of Inertial Soil-Structure Interaction Effects.* Jonathan P. Stewart, Raymond B. Seed, and Gregory L. Fenves. November 1998.

PEER 1998/06 *Effect of Damping Mechanisms on the Response of Seismic Isolated Structures.* Nicos Makris and Shih-Po Chang. November 1998.

PEER 1998/05 *Rocking Response and Overturning of Equipment under Horizontal Pulse-Type Motions.* Nicos Makris and Yiannis Roussos. October 1998.

PEER 1998/04 *Pacific Earthquake Engineering Research Invitational Workshop Proceedings, May 14–15, 1998: Defining the Links between Planning, Policy Analysis, Economics and Earthquake Engineering.* Mary Comerio and Peter Gordon. September 1998.

PEER 1998/03 *Repair/Upgrade Procedures for Welded Beam to Column Connections.* James C. Anderson and Xiaojing Duan. May 1998.

PEER 1998/02 *Seismic Evaluation of 196 kV Porcelain Transformer Bushings.* Amir S. Gilani, Juan W. Chavez, Gregory L. Fenves, and Andrew S. Whittaker. May 1998.

PEER 1998/01 *Seismic Performance of Well-Confined Concrete Bridge Columns.* Dawn E. Lehman and Jack P. Moehle. December 2000.

ONLINE REPORTS

The following PEER reports are available by Internet only at http://peer.berkeley.edu/publications/peer_reports.html

PEER 2012/103 *Performance-Based Seismic Demand Assessment of Concentrically Braced Steel Frame Buildings.* Chui-Hsin Chen and Stephen A. Mahin. December 2012.

PEER 2012/102 *Procedure to Restart an Interrupted Hybrid Simulation: Addendum to PEER Report 2010/103.* Vesna Terzic and Bozidar Stojadinovic. October 2012.

PEER 2012/101 *Mechanics of Fiber Reinforced Bearings.* James M. Kelly and Andrea Calabrese. February 2012.

PEER 2011/107 *Nonlinear Site Response and Seismic Compression at Vertical Array Strongly Shaken by 2007 Niigata-ken Chuetsu-oki Earthquake.* Eric Yee, Jonathan P. Stewart, and Kohji Tokimatsu. December 2011.

PEER 2011/106 *Self Compacting Hybrid Fiber Reinforced Concrete Composites for Bridge Columns.* Pardeep Kumar, Gabriel Jen, William Trono, Marios Panagiotou, and Claudia Ostertag. September 2011.

PEER 2011/105 *Stochastic Dynamic Analysis of Bridges Subjected to Spacially Varying Ground Motions.* Katerina Konakli and Armen Der Kiureghian. August 2011.

PEER 2011/104 *Design and Instrumentation of the 2010 E-Defense Four-Story Reinforced Concrete and Post-Tensioned Concrete Buildings.* Takuya Nagae, Kenichi Tahara, Taizo Matsumori, Hitoshi Shiohara, Toshimi Kabeyasawa, Susumu Kono, Minehiro Nishiyama (Japanese Research Team) and John Wallace, Wassim Ghannoum, Jack Moehle, Richard Sause, Wesley Keller, Zeynep Tuna (U.S. Research Team). June 2011.

PEER 2011/103 *In-Situ Monitoring of the Force Output of Fluid Dampers: Experimental Investigation.* Dimitrios Konstantinidis, James M. Kelly, and Nicos Makris. April 2011.

PEER 2011/102 *Ground-motion prediction equations 1964 - 2010.* John Douglas. April 2011.

PEER 2011/101 *Report of the Eighth Planning Meeting of NEES/E-Defense Collaborative Research on Earthquake Engineering.* Convened by the Hyogo Earthquake Engineering Research Center (NIED), NEES Consortium, Inc. February 2011.

PEER 2010/111 *Modeling and Acceptance Criteria for Seismic Design and Analysis of Tall Buildings.* Task 7 Report for the Tall Buildings Initiative - Published jointly by the Applied Technology Council. October 2010.

PEER 2010/110 *Seismic Performance Assessment and Probabilistic Repair Cost Analysis of Precast Concrete Cladding Systems for Multistory Buildlings.* Jeffrey P. Hunt and Božidar Stojadinovic. November 2010.

PEER 2010/109 *Report of the Seventh Joint Planning Meeting of NEES/E-Defense Collaboration on Earthquake Engineering. Held at the E-Defense, Miki, and Shin-Kobe, Japan, September 18–19, 2009.* August 2010.

PEER 2010/108 *Probabilistic Tsunami Hazard in California.* Hong Kie Thio, Paul Somerville, and Jascha Polet, preparers. October 2010.

PEER 2010/107 *Performance and Reliability of Exposed Column Base Plate Connections for Steel Moment-Resisting Frames.* Ady Aviram, Božidar Stojadinovic, and Armen Der Kiureghian. August 2010.

PEER 2010/106 *Verification of Probabilistic Seismic Hazard Analysis Computer Programs.* Patricia Thomas, Ivan Wong, and Norman Abrahamson. May 2010.

PEER 2010/105 *Structural Engineering Reconnaissance of the April 6, 2009, Abruzzo, Italy, Earthquake, and Lessons Learned.* M. Selim Günay and Khalid M. Mosalam. April 2010.

PEER 2010/104 *Simulating the Inelastic Seismic Behavior of Steel Braced Frames, Including the Effects of Low-Cycle Fatigue.* Yuli Huang and Stephen A. Mahin. April 2010.

PEER 2010/103 *Post-Earthquake Traffic Capacity of Modern Bridges in California.* Vesna Terzic and Božidar Stojadinović. March 2010.

PEER 2010/102 *Analysis of Cumulative Absolute Velocity (CAV) and JMA Instrumental Seismic Intensity (I_{JMA}) Using the PEER–NGA Strong Motion Database.* Kenneth W. Campbell and Yousef Bozorgnia. February 2010.

PEER 2010/101 *Rocking Response of Bridges on Shallow Foundations.* Jose A. Ugalde, Bruce L. Kutter, and Boris Jeremic. April 2010.

PEER 2009/109 *Simulation and Performance-Based Earthquake Engineering Assessment of Self-Centering Post-Tensioned Concrete Bridge Systems.* Won K. Lee and Sarah L. Billington. December 2009.

PEER 2009/108 *PEER Lifelines Geotechnical Virtual Data Center.* J. Carl Stepp, Daniel J. Ponti, Loren L. Turner, Jennifer N. Swift, Sean Devlin, Yang Zhu, Jean Benoit, and John Bobbitt. September 2009.

PEER 2009/107 *Experimental and Computational Evaluation of Current and Innovative In-Span Hinge Details in Reinforced Concrete Box-Girder Bridges: Part 2: Post-Test Analysis and Design Recommendations.* Matias A. Hube and Khalid M. Mosalam. December 2009.

PEER 2009/106 *Shear Strength Models of Exterior Beam-Column Joints without Transverse Reinforcement.* Sangjoon Park and Khalid M. Mosalam. November 2009.

PEER 2009/105 *Reduced Uncertainty of Ground Motion Prediction Equations through Bayesian Variance Analysis.* Robb Eric S. Moss. November 2009.

PEER 2009/104 *Advanced Implementation of Hybrid Simulation.* Andreas H. Schellenberg, Stephen A. Mahin, Gregory L. Fenves. November 2009.

PEER 2009/103 *Performance Evaluation of Innovative Steel Braced Frames.* T. Y. Yang, Jack P. Moehle, and Božidar Stojadinovic. August 2009.

PEER 2009/102 *Reinvestigation of Liquefaction and Nonliquefaction Case Histories from the 1976 Tangshan Earthquake.* Robb Eric Moss, Robert E. Kayen, Liyuan Tong, Songyu Liu, Guojun Cai, and Jiaer Wu. August 2009.

PEER 2009/101 *Report of the First Joint Planning Meeting for the Second Phase of NEES/E-Defense Collaborative Research on Earthquake Engineering.* Stephen A. Mahin et al. July 2009.

PEER 2008/104 *Experimental and Analytical Study of the Seismic Performance of Retaining Structures.* Linda Al Atik and Nicholas Sitar. January 2009.

PEER 2008/103 *Experimental and Computational Evaluation of Current and Innovative In-Span Hinge Details in Reinforced Concrete Box-Girder Bridges. Part 1: Experimental Findings and Pre-Test Analysis.* Matias A. Hube and Khalid M. Mosalam. January 2009.

PEER 2008/102 *Modeling of Unreinforced Masonry Infill Walls Considering In-Plane and Out-of-Plane Interaction.* Stephen Kadysiewski and Khalid M. Mosalam. January 2009.

PEER 2008/101 *Seismic Performance Objectives for Tall Buildings.* William T. Holmes, Charles Kircher, William Petak, and Nabih Youssef. August 2008.

PEER 2007/101 *Generalized Hybrid Simulation Framework for Structural Systems Subjected to Seismic Loading.* Tarek Elkhoraibi and Khalid M. Mosalam. July 2007.

PEER 2007/100 *Seismic Evaluation of Reinforced Concrete Buildings Including Effects of Masonry Infill Walls.* Alidad Hashemi and Khalid M. Mosalam. July 2007.

The Pacific Earthquake Engineering Research Center (PEER) is a multi-institutional research and education center with headquarters at the University of California, Berkeley. Investigators from over 20 universities, several consulting companies, and researchers at various state and federal government agencies contribute to research programs focused on performance-based earthquake engineering.

These research programs aim to identify and reduce the risks from major earthquakes to life safety and to the economy by including research in a wide variety of disciplines including structural and geotechnical engineering, geology/seismology, lifelines, transportation, architecture, economics, risk management, and public policy.

PEER is supported by federal, state, local, and regional agencies, together with industry partners.

PEER Core Institutions:
University of California, Berkeley (Lead Institution)
California Institute of Technology
Oregon State University
Stanford University
University of California, Davis
University of California, Irvine
University of California, Los Angeles
University of California, San Diego
University of Southern California
University of Washington

PEER reports can be ordered at http://peer.berkeley.edu/publications/peer_reports.html or by contacting

Pacific Earthquake Engineering Research Center
University of California, Berkeley
325 Davis Hall, mail code 1792
Berkeley, CA 94720-1792
Tel: 510-642-3437
Fax: 510-642-1655
Email: peer_editor@berkeley.edu

ISSN 1547-0587X